UvA-DARE (Digital Academic Repository)

Transverse momentum distributions with recoil-free jets

Zoppi, L.

Publication date
2020
Document Version
Final published version
License
Other

Link to publication

Transverse Momentum Distributions with Recoil-Free Jets

TMDs with Recoil-Free Jets
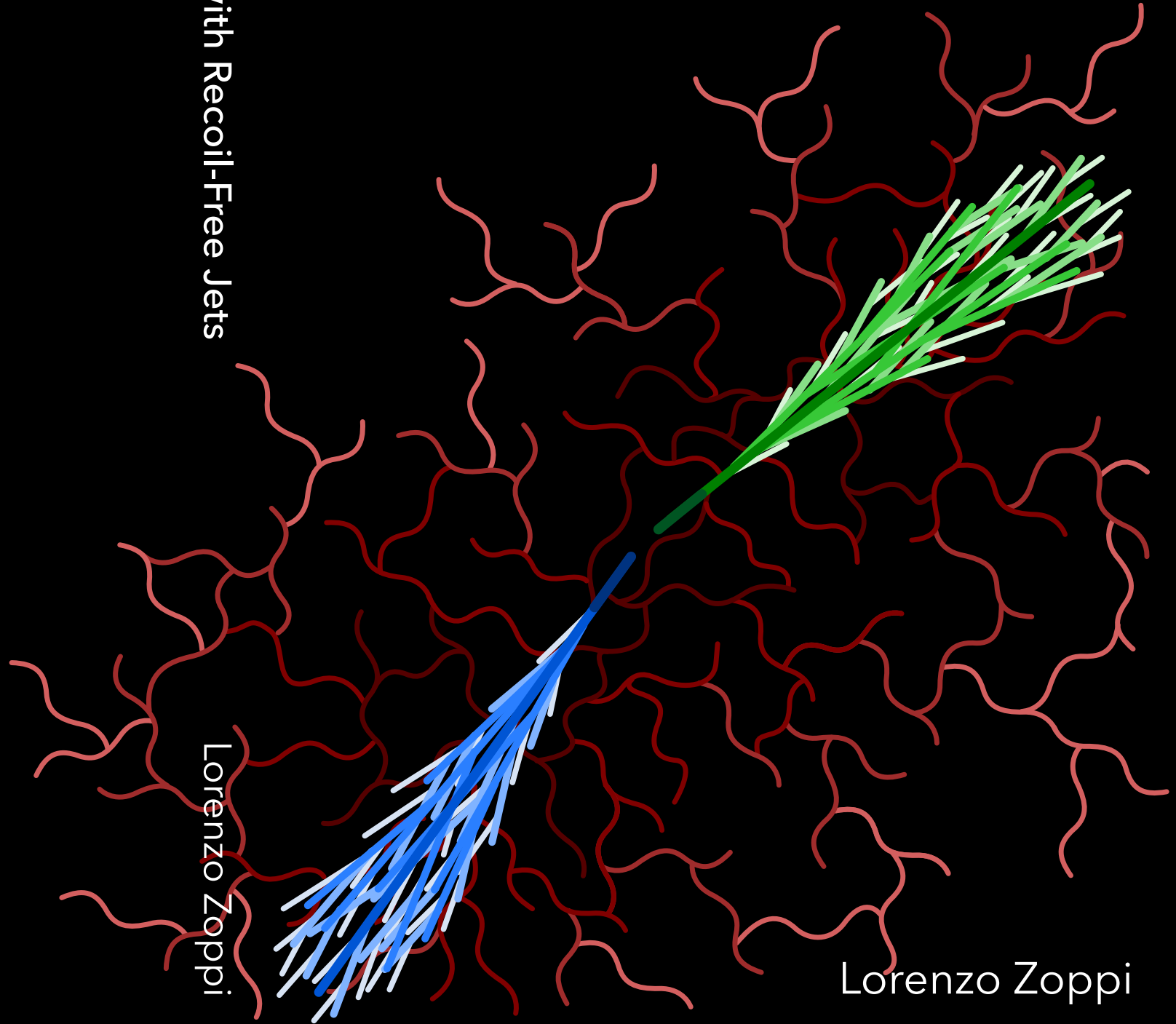
Lorenzo Zoppi

Lorenzo Zoppi

Transverse Momentum Distributions with Recoil-Free Jets

Lorenzo Zoppi

Title: Transverse Momentum Distributions with Recoil-Free jets
Printed by: pixartprinting

UNIVERSITEIT VAN AMSTERDAM

Nik[hef

erc

European Research Council
Established by the European Commission

Transverse Momentum Distributions with Recoil-Free Jets

ACADEMISCH PROEFSCHRIFT

ter verkrijging van de graad van doctor
aan de Universiteit van Amsterdam
op gezag van de Rector Magnificus
prof. dr. ir. K.I.J. Maex
ten overstaan van een door het College voor Promoties ingestelde
commissie, in het openbaar te verdedigen in de Agnietenkapel
op maandag 28 september 2020, te 14:00 uur

door

Lorenzo Zoppi

geboren te Turijn

Promotiecommissie:

Promotor:	prof. dr. E.L.M.P. Laenen	Universiteit van Amsterdam
Copromotor:	dr. W.J. Waalewijn	Universiteit van Amsterdam
Overige leden:	prof. dr. D.D. Baumann	Universiteit van Amsterdam
	prof. dr. L. Magnea	Università di Torino
	dr. M.E.J. Postma	Nikhef
	dr. R.M. Rahn	Universiteit van Amsterdam
	prof. dr. I.W. Stewart	Massachusetts Institute of Technology
	prof. dr. W. Verkerke	Universiteit van Amsterdam

Faculteit der Natuurwetenschappen, Wiskunde en Informatica

The material presented in this thesis is based on the following publications:

[1] D. Gutierrez-Reyes, I. Scimemi, W. J. Waalewijn and L. Zoppi
Transverse momentum dependent distributions with jets, *Phys. Rev. Lett.*
121 (2018) 162001 [1807.07573].

[2] D. Neill, A. Papaefstathiou, W. J. Waalewijn and L. Zoppi
Phenomenology with a recoil-free jet axis: TMD fragmentation and the jet shape, *JHEP* **01** (2019) 067 [1810.12915].

[3] D. Gutierrez-Reyes, I. Scimemi, W. J. Waalewijn and L. Zoppi
Transverse momentum dependent distributions in e^+e^- and semi-inclusive deep-inelastic scattering using jets, *JHEP* **10** (2019) 031 [1904.04259].

[4] D. Gutierrez-Reyes, Y. Makris, V. Vaidya, I. Scimemi and L. Zoppi
Probing Transverse-Momentum Distributions With Groomed Jets, *JHEP* **08** (2019) 161 [1907.05896].

Contents

Introduction

Fundamental physics aims at unraveling Nature at its deepest level. Its driving principle is reductionism, and its holy grail is a theory of everything. Not surprisingly, searching for the ultimate constituents of matter is one of its main focuses.

The status of particle physics is encompassed by the Standard Model (SM), which is a triumph of fundamental physics: with the important exception of gravity, this theory underlies every physical phenomenon whose origin we know. Much more than a catalog of particles and interactions, the SM achieves a complete description of electromagnetic and nuclear phenomena through a complex and elegant interplay between its parts. Its formal language is Quantum Field Theory (QFT), which describes particle dynamics complying to special relativity and quantum mechanics. Among its experimental tools, particle accelerators play a leading role: the large majority of fundamental particle discoveries, as well as the measurements of their key properties, were accomplished through high-energy scattering experiments.

QFT might be theoretically unsatisfactory: its path-integral formulation lacks a formal mathematical definition, and its predictions are based on asymptotic expansions. In addition, it is perhaps disappointing that such a comprehensive theory as the SM should eventually reduce to computing and measuring cross sections for scattering processes. However, this practice finds justification in the spectacular level of agreement within theory and experiment, spanning across several orders of magnitude in energy: very few fields of science may afford setting a 5σ deviation as their standard for new discoveries.

Despite this remarkable agreement, there are facts that the SM does not explain. Besides the inclusion of gravity, the most striking examples are perhaps the nature of dark matter and the origin of baryon asymmetry. Because of these and other theoretical considerations, the search for physics beyond the Standard Model is an extremely active topic. In absence of obvious places where to look, and without conclusive evidence of new physics at the Large Hadron Collider (LHC), there is consensus on the need of *precision* physics. Rather than with the sudden discovery of a new particle, it is likely that the SM will be falsified by an increasing number of small but significant discrepancies.

This thesis focuses on Quantum Chromodynamics (QCD), the theory de-

scribing the strong sector of the SM through the interplay of quarks and gluons. Besides providing one of the fundamental building blocks of nature, QCD is indispensable to present-day collider phenomenology. First, the most powerful accelerator in action, the LHC, accelerates and scatters protons, and protons are described by QCD. Second, the strong interaction was named so for a reason, and virtual QCD corrections have a large impact on cross sections; in an age of precision physics, these corrections cannot be ignored.

The most prominent feature of QCD is color confinement, the fact that quarks and gluons cannot be observed directly, but only inside bound states named hadrons. Investigating the internal structure of hadrons will be the main goal of this thesis: the aim will be studying initial-state colliding protons, as well as final-state hadrons fragmenting from high-energy particles. Specifically, I will focus on the transverse momentum of these hadrons, where *transverse* is with respect to the direction of motion. Historically, collider analyses mainly focus on longitudinal physics: extending the description to the transverse direction is a relevant generalization, that allows for mapping the hadron structure with a higher level of detail. The main result that makes this study possible is *factorization*, the separation of high-energy from hadronic physics.

The strategy I will follow, and the main element of originality of my doctoral work, is studying the transverse momentum dependence of hadrons using alternative definitions of *jets*. Jets are collimated sprays of particles that, because of the nature of QCD, populate the final state of a collision: before reaching the detectors, highly energetic quarks and gluons produced in a hard scattering will undergo a large number of splittings, showering into a collection of hadrons. By describing sprays of final-state hadrons as a single object, one attempts at reverting this description, and extract precious information about the early stage of a collision. This task is complicated for a number of reasons, not least the quantum nature of the system. A relevant issue is the presence of low-energy (*soft*) radiation. Soft radiation can communicate between different jets and between jets and proton beams, exposing a jet to multiple sources of contamination. As I will clarify later, this effect has a larger impact for measurements in the transverse direction. Using *recoil-free* jets – whose direction is insensitive to soft radiation – reduces the contamination due to this source, while achieving a considerable simplification of the theoretical framework.

The thesis is structured as follows: the first two chapters provide the theoretical grounds, while the last three present applications. In ch. 1 I review the main aspects of perturbative QCD relevant to the present work: although this is mainly textbook material, I will use this opportunity to present the topic in a functional way for the rest of the thesis. The focus will be on the soft and

collinear limit of the theory, which underlies the physics discussed here. In particular, the last section introduces Soft Collinear Effective Theory (SCET), the framework on which my results build upon. Ch. 2 bridges between theory and phenomenology, complementing the picture with a discussion of jets and transverse momentum dependence. On the first topic, the emphasis will be on recoil-free jets and *soft drop*, another established technique to cut down soft contamination inside jets. The second part introduces Transverse Momentum dependent Distributions, one of the main subjects of study of this work. The next three chapters will present the results of my research: besides the intrinsic relevance to collider phenomenology, I will use them to show some of the SCET methodologies in action. Ch. 3 carries on a study of transverse-momentum-dependent fragmentation of hadrons inside recoil-free jets. The work described here was one of the first applications of the Winner-Take-All jet recombination scheme, and we left large room to elucidating its properties. Moving on to ch. 4, I will discuss the application of WTA jets to the extraction of proton TMDs. This study is highly promising in view of the future Electron-Ion Collider; in this chapter, I also expand in detail the one-loop calculation of a transverse-momentum dependent jet function. Finally, ch. 5 discusses soft drop as a valid alternative to the extraction of proton TMDs. Besides remarking on differences and similarities with respect to recoil-free jets, I give some discussion of hadronization effects. Each of these applications strongly relies on factorization; although I will not rigorously give a factorization proof for these processes, I will argue for it and amply discuss its physical meaning.

The main result of the thesis is that the absence of recoil largely simplifies the theoretical framework in a number of transverse momentum dependent processes, allowing for a cleaner extraction of the relevant collinear physics. I will try to convince the reader that reconstructing jets using these alternative jet definitions is advantageous for LHC and EIC studies.

1

Quantum Chromodynamics for multi-scale processes

Quantum Chromodynamics (QCD), the theory of the strong interaction, is a pillar of modern physics. Governing the elaborate interplay of color-charged particles from the extreme temperatures of the quark-gluon plasma to the low energies of protons and nuclei, QCD has shaped the history of the universe. Imposing its strength over other fundamental interactions, it dominates a multitude of collision and decay processes that consolidate our confidence in the Standard Model (SM) or guide the search for physics beyond it.

To a novice of perturbative Quantum Field Theory (QFT), QCD appears as a self-standing, slightly cumbersome analog of Quantum Electrodynamics whose non-abelian nature brings technical complications into the game. At the Lagrangian level, its interplay with the rest of the SM is limited: QCD does not participate in the spectacular symmetry breaking and electroweak mixing that established the SM as a comprehensive theory of particle physics, and one could imagine a consistent universe where the strong interaction is the only actor on stage. However, rather than its purely theoretical aspects, what makes QCD special is the rich phenomenology, since virtually every relevant scattering process involves gluons and quarks or receives dominant quantum corrections from them. If we collide two protons at high energies, we need some knowledge of their inner structure to formulate quantitative predictions about the final state, even when the latter is leptonic and the leading interaction electromagnetic (such as Drell-Yan scattering, DY); the same occurs if we smash the proton with an electron probe (Deep Inelastic Scattering, DIS). The dominant mechanism to produce Higgs bosons at the Large Hadron Collider (LHC) is gluon fusion mediated by a top-quark loop, and a colliding electron-positron pair will preferentially annihilate into a colored state, eventually showering into hadrons. In addition to these examples, measurements that select hadrons or jets in the final state, like Semi-Inclusive Deep Inelastic Scattering (SIDIS) or Higgs + jet production, deal with intrinsic QCD objects.

Ultimately, what makes QCD phenomenology so relevant and varied is the peculiar dependence (or *running*) of the strong coupling constant on the energy scale at which the system is probed. As a three-fold charge allows gluons to proliferate, the effective strength of the interaction between colored particles increases with their distance. At very high energies we can think of quarks and gluons as weakly-interacting, well-defined entities (asymptotic freedom), while at ordinarily low energies the strong force segregates them into color-neutral hadrons (color confinement). This fact determines the predominance of QCD over other fundamental interactions, but at the same time seems to foreshadow the death of the perturbative QFT approach, since the particles whose degrees of freedom appear in the Lagrangian differ from the objects that we accelerate and detect in a collider experiment.

The picture above anticipates why a major theoretical result in QCD is factorization. Separating low-energy and high-energy dynamics, factorization overcomes the need to simultaneously describe quarks as confined into hadrons and asymptotically free. Low-energy, non-perturbative physics is isolated in hadronic matrix elements, that are universal and fitted to data, while the high-energy, process-dependent physics is still calculable in terms of Feynman diagrams, saving the predictive power of field theory in QCD. Furthermore, factorization paves the road to resummation, a technique to supplement cross sections with dominant terms at all orders in perturbation theory. Factorized observables involve multiple, largely separated physical energies (or *scales*); Renormalization Group Evolution (RGE) bridges this separation, and resummation captures the relevant physics between them, including it in our predictions. Very often, when studying differential cross sections, the agreement with experimental data is spectacularly enhanced by resummation.

The present chapter aims to give an overview of some of the main theoretical aspects of QCD relevant to multi-scale collider phenomenology. I will start from the Lagrangian and its renormalization: not only does this allow me to introduce the relevant notation, but it also serves as reminder of the vast technology that underlies the theory. I will then discuss how the description of soft and collinear dynamics in QCD leads to the factorization and resummation of physical observables. There exist two different, well-established approaches to the field: the first one dates back to the early '80s, with the original work of Collins, Soper and Sterman, and builds on a systematic study of the infrared singularities of QCD amplitudes to prove factorization at the level of Green functions (and subsequently, physical observables). Following common terminology, I will refer to this approach as *diagrammatic*. The second one, Soft Collinear Effective Theory, was formulated in the early 2000s and sets up the description at the Lagrangian level. In SCET, soft and collinear particles

correspond to different fields, with factorization directly following from a field redefinition. The results presented in this thesis were obtained within SCET, and this is the preferred language that I will use throughout. Nonetheless, I find it instructive to include a very brief discussion of the diagrammatic approach to resummation, as many of the concepts and tools are common to the two schools. It is useful to keep in mind that SCET and the diagrammatic approach are different languages to describe the same physics, and provide the exact same predictions when it comes to any observable.

1.1 QCD beyond tree level

1.1.1 The Lagrangian

If we accept the rules of perturbative QFT, then in principle all we need to know to describe QCD is the Lagrangian,

$$\mathcal{L}_{\text{QCD}} = -\frac{1}{4} F_a^{\mu\nu} F_{a,\mu\nu} + \sum_f \overline{\psi}_{f,i} \big(i \slashed{D}_{ij} - m_f \, \delta_{ij} \big) \psi_{f,j} + \mathcal{L}_{\text{FP}} + \mathcal{L}_{gh} \,. \qquad (1.1)$$

This explicitly features a set of n_f spin-$\frac{1}{2}$ fermions ψ_f (quark fields of flavor f), while the spin-1 boson A (gluon field) hides in the field strength tensor

$$F_a^{\mu\nu} = \partial^\mu A_a^\nu - \partial^\nu A_a^\mu - g_s f_{abc} \, A_b^\mu A_c^\nu \qquad (1.2)$$

and in the covariant derivative

$$D_{ij}^\mu = \delta_{ij} \, \partial^\mu + i g_s (t_a)_{ij} A_a^\mu \,. \qquad (1.3)$$

The strong coupling parameter g_s sets the strength of quark-gluon and gluon-gluon interactions. The t_a are the generators of the Lie group $SU(3)$, and f_{abc} its structure constants. The quark fields live in the fundamental representation of the group, thus their excitations over the vacuum state come in three *colors*, indexed by $\{i, j \dots\}$; the gluon field lives in the adjoint representation, so there exist $3^2 - 1 = 8$ independent gluons, indexed by $\{a, b \dots\}$. To comply with special relativity, the Lagrangian is invariant under the Lorentz group, whose metric is chosen $g^{\mu\nu} = \text{diag}(+, -, -, -)$. Greek indices denote Lorentz components and follow the Einstein summation convention; unless explicitly stated, $SU(3)$ indices are also understood to be summed over.

The Lagrangian in eq. (1.1) is invariant under the gauge transformations (here in infinitesimal form)

$$A_a^\mu(x) \to A_a^\mu(x) - \partial^\mu \theta_a(x) - g_s f_{abc} \, \theta_b(x) A_c^\mu(x) \,,$$

$$\psi_i(x) \to \psi_i(x) + ig_s\theta_a(x)(t_a)_{ij}\psi_j(x)\,, \tag{1.4}$$

parametrized by the set θ_a. For *global* transformations $\theta(x) = $ constant, Noether's theorem translates the symmetry into conservation of color charge, thus making color a well-defined quantum number. However, eq. (1.4) is valid also for *local* transformations, enforcing the theory to obey the principle of locality through the presence of interactions. Gauge invariance has the further consequence that the theory is redundant, since infinite field configurations describe the same physics. In order to define the gluon propagator and be able to compute physical quantities, it is necessary to solve this degeneracy by fixing the gauge to a particular value. The Faddeev-Popov mechanism implements this in a Lorentz-covariant way, at the price of introducing non-physical *ghost* fields. Different choices of gauge result in different, arbitrary definitions of the gluon propagator, and ghosts couple to physical fields in such a way to remove the arbitrariness, enforcing the consistency of the theory. The most popular choice of gauge is

$$\mathcal{L}_{\mathrm{FP}} = -\frac{1}{2\xi}\big(\partial_\mu A_a^\mu\big)\big(\partial_\nu A_a^\nu\big)\,, \tag{1.5}$$

and the corresponding ghost Lagrangian is

$$\mathcal{L}_{gh} = \big(\partial_\mu \bar{c}_a\big)\big(D_{ab}^\mu c_b\big)\,. \tag{1.6}$$

The ghost field c couples to the gluon field through the covariant derivative in adjoint representation, $D_{ab}^\mu = \delta_{ab}\partial_\mu + g_s f_{abc}A_{\mu,c}$. Setting $\xi = 1$ in eq. (1.5) defines the Feynman-'t Hooft gauge and will be the default in the thesis.

Having specified the meaning of every term in the Lagrangian, one can use standard QFT techniques to generate Feynman rules in the quantized theory, and computing physical observables becomes a matter of drawing Feynman diagrams, calculating amplitudes and performing phase-space integrations. Unfortunately, this plan would fail very soon for two distinct reasons. The first issue, of technical nature, is the presence of ultraviolet (UV) divergences in loop diagrams. This is common to every physical QFT, but particularly relevant for QCD, where g_s is large and the tree level approximation is often extremely poor. The second problem, conceptual and specific of QCD, is that our predictions for quark and gluon processes are meaningless unless we translate them to the level of hadrons, the objects we actually collide and detect. Renormalization is the procedure to fix the former issue, but also clarifies why the latter arises, so I will shortly have a look at it in the next section.

1.1.2 Renormalization

The main need for renormalization is dealing with UV divergences in loop diagrams. Still, its physical meaning is not necessarily linked to divergences, but is found in the quantum-relativistic nature of the theory. Let us ignore for a moment that quarks and gluons are undetectable objects, and imagine to test the Lagrangian in eq. (1.1) against experiment (in fact, the following reasoning applies directly to QED). We would first select a set of measurements to fix the free parameters m_f and g_s, and only then would the theory provide genuine predictions for independent processes. However, beyond tree level, Lagrangian parameters would differ from measured quantities.

Let me argue for this, focusing for definiteness on the fermion mass. Consider the two-point fermion correlator in momentum space,

$$G_2(p) = \int \frac{\mathrm{d}^4 x}{(2\pi)^4} e^{-ip\cdot x} \langle 0|T\big[\overline{\psi}(x)\psi(0)\big]|0\rangle, \tag{1.7}$$

which at tree level simply coincides with the fermion propagator,

$$G_2^{[0]}(p) \;=\; \longrightarrow \;=\; \frac{i}{\slashed{p} - m}. \tag{1.8}$$

It is the presence of a pole at $\slashed{p} = m$ that allows, at tree level, to interpret the Lagrangian parameter m as the fermion mass: if quarks were free entities, we would experimentally observe this as a resonance in cross sections, as it actually occurs for leptons. Beyond tree level, the correlator receives corrections from virtual particles. The first correction comes from a single amputated diagram, a virtual gluon loop on the fermion line, $\Sigma(\slashed{p}, m)$ in the following. Accounting for an arbitrary number of uncorrelated insertions yields

$$
\begin{aligned}
G_2^{[1]}(p) \;&=\; \sum_{n=0}^{\infty} \Big[\underbrace{\longrightarrow \cdots \longrightarrow}_{n\ \text{gluons}} \Big] \\
&=\; \frac{i}{\slashed{p} - m} \sum_{n=0}^{\infty} \Big[-i\Sigma(\slashed{p}, m) \frac{i}{\slashed{p} - m} \Big]^n \\
&=\; \frac{i}{\slashed{p} - m - \Sigma(\slashed{p}, m)}.
\end{aligned}
\tag{1.9}
$$

The last equality in eq. (1.9) is purely formal (as obtained taking the geometric series of an inverse Dirac operator), but one can foresee that loop corrections may shift the pole in the correlator, which in general differs from the Lagrangian parameter m. Specifically, as I will show in a moment, the one-loop

two-point function takes the form

$$G_2^{[1]}(p) = \frac{iR}{\not{p} - m_{\text{pole}}} + \text{finite}\,, \qquad (1.10)$$

where *finite* refers to regular terms in $\not{p}$. This clarifies that in a theory allowing for virtual pair production and annihilation, physical constants are not an input, but rather the dynamical product of particle interactions. The same reasoning applies to the coupling parameter g_s; in particular, loop corrections change their size with the energy of a process, turning coupling constants to functions of the energy.

Having accepted that Lagrangian parameters differ from physical constants because of loop corrections, one introduces *renormalization* factors Z that reabsorb such corrections in a redefinition of the parameters,

$$m_f = m_f^R Z_m\,, \qquad g_s = g_s^R Z_g^{\frac{1}{2}}\,, \qquad (1.11)$$

where the superscript R denotes *renormalized* quantities. We can write analogous relations for the fields, as their norm is also modified by quantum corrections,

$$\psi = Z_\psi^{\frac{1}{2}} \psi^R\,, \qquad A_a^\mu = Z_A^{\frac{1}{2}} A_a^{R\mu}\,, \qquad c_a = Z_c^{\frac{1}{2}} c_a^R\,, \qquad (1.12)$$

and substitute them in eq. (1.1) to rewrite the Lagrangian in terms of renormalized quantities,

$$
\begin{aligned}
\mathcal{L}_{\text{QCD}} = \mathcal{L}_{\text{QCD}}^R + {} & \tfrac{1}{4}(Z_A - 1)\big(\partial^\mu A_a^{R\nu} - \partial^\nu A_a^{R\mu}\big)\big(\partial_\mu A_{a,\mu}^R - \partial_\nu A_{a\mu}^R\big) \\
& + (Z_g Z_A^{\frac{3}{2}} - 1)g_s^R f_{abc}(\partial_\mu A_{a,\nu}^R)A_b^{R\mu} A_c^{R\nu} \\
& - \tfrac{1}{4}(Z_g^2 Z_A^2 - 1)(g_s^R)^2 f_{abc} f_{ade} A_{\mu b}^R A_{\nu c}^R A_d^{R\mu} A_e^{R\nu} \\
& + (Z_\psi - 1)\sum_f \overline{\psi}_{f,i}^R i\not{\partial} \psi_{f,i}^R - (Z_\psi Z_m - 1)\sum_f m_f^R \overline{\psi}_{f,i}^R \psi_{f,i}^R \\
& - (Z_c - 1)\overline{c}_a^R \partial_\mu \partial^\mu c_a^R - (Z_g Z_A^{\frac{1}{2}} Z_c - 1)g_s^R f_{abc}(\partial_\mu \overline{c}_a^R)A_b^{R\mu} c_c^R \\
& - (Z_g Z_\psi Z_A^{\frac{1}{2}} - 1)g_s^R \overline{\psi}_i^R \not{A}_a^R (t_a)_{ij} \psi_j^R\,. \qquad (1.13)
\end{aligned}
$$

Here $\mathcal{L}_{\text{QCD}}^R$ is the renormalized Lagrangian, i.e. a copy of the original (*bare*) Lagrangian where the parameters and fields have been replaced by the renormalized counterparts. What follows is a list of *counterterms*, combinations of fields (*operators*) that also appear in the bare Lagrangian, but weighted with a combination of renormalization factors. Eq. (1.13) states that we can include loop corrections in a redefinition of constants and fields, at the price of supplementing the Lagrangian with additional terms.

The renormalization factors in (1.11) need to be updated order by order in perturbation theory; in the example of eq. (1.9), including higher-loop diagrams will further shift the pole of the propagator. Therefore,

$$Z_\kappa = 1 + \sum_{n=1}^{\infty} \left(\frac{\alpha_s}{4\pi}\right)^n Z_\kappa^{[n]} \,, \tag{1.14}$$

where $\alpha_s = g_s^2/(4\pi)$. Superscripts in square brackets will denote coefficients in the $\alpha_s/(4\pi)$ expansion throughout the whole thesis. From now on I will manipulate only renormalized objects and drop the R superscript. At tree level the renormalization factors are just one, and because the Lagrangian parameters coincide with the physical constants.

The formalism becomes essential in presence of UV divergences. The one-loop quark self-energy in d spacetime dimensions yields

$$\Sigma(\not{p}, m) = i \;\vdash\!\!\!\!\!\!\overset{\text{\tiny◯◯◯}}{\longrightarrow}\!\!\!\!\!\dashv\; = \int \frac{\mathrm{d}^d\ell}{(2\pi)^d} \frac{-ig_s^2 C_F\, \gamma^\mu(\not{p} - \not{\ell} + m)\gamma_\mu}{(\ell^2 + i\eta)\left[(p-\ell)^2 - m^2 + i\eta\right]} \,, \tag{1.15}$$

where $C_F = (t_a)_{ij}(t_a)_{ij} = \frac{4}{3}$, the trace of the generators in the fundamental representation of $SU(3)$, arises when summing over loop color, and the infinitesimal positive quantity η locates the poles in the denominators relative to the integration path. For $d = 4$ the integrand has a logarithmic singularity at $\ell \to \infty$, hence the UV divergence. Loosely speaking, because of virtual particles carrying arbitrarily high energies, the Lagrangian parameters differ from the physical parameters by an *infinite* amount. Still, we now that physical parameters must be finite, which is possible if the counterterms in eq. (1.13) cancel the divergence. To make this quantitative, one needs to parameterize the divergence within a *regularization scheme*. Although many of these exist, in practice only dimensional regularization works systematically for perturbative QFT, as it simultaneously preserves Lorentz and Gauge symmetry while keeping the analytic complexity under control.

The method requires to work in a generic $d = 4 - 2\varepsilon$ dimensional space, with $\varepsilon \to 0$ delivering the physical limit. In the following, I will assume basic knowledge of d-dimensional integration; provided with this tool, for positive ε the integral converges to

$$\begin{aligned}
\Sigma(\not{p}, m) &= \frac{\alpha_s}{\pi} C_F \left(\frac{4\pi\mu^2}{m^2}\right)^\varepsilon \Gamma(-\varepsilon)\left[\left(m - \frac{\not{p}}{4}\right) + \mathcal{O}(\varepsilon)\right] \\
&= \frac{\alpha_s}{\pi} C_F \left[\frac{1}{\varepsilon} + \ln\left(\frac{4\pi\mu^2}{m^2}\right) - \gamma_E\right]\left[\left(m - \frac{\not{p}}{4}\right) + \mathcal{O}(\varepsilon)\right] \,, \tag{1.16}
\end{aligned}$$

and the divergence manifests itself through the ε pole. The *renormalization scale* μ is required for dimensional consistency: if we want the regularized

Lagrangian to be homogeneous in mass dimensions while keeping the physical coupling constant dimensionless, we must replace eq. (1.11) with

$$m_f = m_f^R Z_m \,, \qquad g_s = \mu^\varepsilon g_s^R Z_g^{\frac{1}{2}} \,. \tag{1.17}$$

The value of μ is arbitrary; the renormalized Lagrangian parameters will also depend on μ, so that the dependence cancels out in physical observables. The result in eq. (1.16) allows one to fix the one-loop renormalization factors Z_ψ and Z_m, as the two counterterms in the fourth line of eq. (1.13) yield effective vertices (here symbolized by boxes) with respective Feynman rules

$$\longrightarrow\!\square\!\!\longrightarrow = i(1 - Z_\psi)\,\slashed{p}\,, \qquad \longrightarrow\!\diamond\!\!\longrightarrow = i(1 - Z_\psi Z_m)m \;: \tag{1.18}$$

in order for the ε pole to cancel,

$$Z_\psi^{[1]} = -\left(\frac{1}{\varepsilon} + k_\psi^{[1]}\right), \qquad Z_m^{[1]} = -3\left(\frac{1}{\varepsilon} + k_m^{[1]}\right). \tag{1.19}$$

The finite parts $k_i^{[1]}$ are unconstrained, and making a choice specifies the *renormalization scheme*. Minimal schemes set them to a constant; in particular, *modified minimal subtraction* ($\overline{\text{MS}}$) fixes $k_i^{[1]} = \ln(4\pi e^{\gamma_E})$ and will be used in the rest of this thesis. Practically, it is convenient to substitute

$$\mu = \frac{e^{-\gamma_E}\bar{\mu}}{4\pi}\,, \tag{1.20}$$

so renormalization amounts to subtracting all and only the poles and relabeling $\bar{\mu} \to \mu$ at the end of the calculation.

The freedom in the choice of scheme is already implicit in the arbitrary separation between counterterms and renormalized terms in eq. (1.13) and is due to the lack of a unique definition for the constants (α_s, m_f). The latter are not directly measurable, but are extracted from some observable O (e.g., a cross section) whose theoretical prediction is also sensitive to the choice of scheme. These constants will enter genuine predictions for new observables O' computed in the same scheme:

$$\mathcal{L}(\{k_i\}, \alpha_s, m_f) \to O(\{k_i\}, \alpha_s, m_f) \equiv O_{\text{meas}} \to (\alpha_s, m_f) \to O'(\{k_i\}, \alpha_s, m_f)\,. \tag{1.21}$$

The implicit scheme dependence in the extraction of (α_s, m_f) will then compensate for the explicit scheme dependence when generating predictions for the new observables. Applying the same reasoning to the choice of renormalization scale poses the basis to renormalization group evolution, which will be the subject of the next section.

To make renormalization systematic, one can first map all the possible sources of UV divergences by *UV power counting*. This amounts to tracking how many powers of loop momenta each element (line of vertex) brings to a given diagram $\mathcal{G}$ in the UV limit. The answer is the superficial degree of divergence

$$\omega_{\mathcal{G}} = 4L - 2I_b - I_q + V_3 \,, \tag{1.22}$$

where L is the number of loops, I_b and I_q the number of internal boson (including ghosts) and quark lines, V_3 the number of three-particle vertices. Positive, null or negative $\omega_{\mathcal{G}}$ correspond respectively to power divergent, logarithmically divergent or convergent integrals. Basic graph identities and the knowledge of the vertex content of the theory allow one to rewrite eq. (1.22) in terms of only the number of external lines (E_b and E_q for respectively bosons and quarks),

$$\omega_{\mathcal{G}} = 4 - E_b - \frac{3}{2} E_q \,. \tag{1.23}$$

This form is much more insightful, because it makes evident that in QCD a finite number of correlators diverge, regardless of the number of loops. Were this not the case it would be impossible to renormalize the theory, as starting at some perturbative order we would run out of counterterms in eq. (1.13)[1]. It is further reassuring that all the divergent correlators resemble by number and type of legs one of the Lagrangian interactions (fig. 1.1), since these are the only counterterms that the theory delivers. For this to be true, it is important to notice that the superficial degree of divergence gives only an upper bound to the scaling behavior of the loop integrals. Eventually, symmetries can mitigate the divergence, as occurs to the four-ghost correlator. Specifically, the symmetry of the correlator under interchanges of external momenta, combined with the ghost Feynman rule derived from eq. (1.6), forces the numerator to be proportional to two powers of loop momenta, so loop integrals converge. This is fundamental for the theory to be renormalizable, since QCD lacks four-point ghost interactions to start with. The same effect applies to the two-ghost, two-gluon correlator.

A further, fundamental condition that guarantees the consistency of the theory is that gauge invariance survives renormalization, so that color charge is conserved beyond tree level. This requirement is implicit in eq. (1.13), where the eight coefficients of the counterterm operators are written in terms of only five renormalization factors, while a priori we could expect each correlator to

---

[1] As I will discuss in sec. 1.3.1, this condition is looser in Effective Field Theories, where an infinite number of divergent correlator still allows the theory to be renormalized order by order in a power expansion.
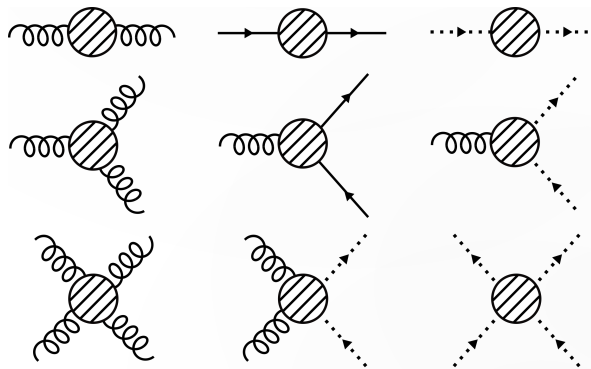
Figure 1.1 UV-divergent QCD correlators, as predicted by the superficial degree of divergence (dotted lines represent ghosts). The last two correlators in the bottom row actually converge, as renormalizability of QCD requires.

renormalize independently. The result that all-order renormalization preserves gauge invariance is known as Ward-Takahashi identities (or Slavnov-Taylor identities in the specific instance of QCD) and constitute a proof that the theory is renormalizable.

1.1.3 Renormalization Group Evolution

Renormalization Group Evolution (RGE) is a powerful tool that turns the ambiguity in the definition of renormalized quantities into an advantage. It plays a crucial role in resummation, so underlies most of the results presented in this thesis. RGE studies variations with respect to the renormalization scale, building a dictionary between different values of μ.

The starting point is noticing that the logic of eq. (1.21) also applies to the choice of renormalization scale. Different choices of μ lead one to extract different physical constants $\alpha_s(\mu), m_f(\mu)$. The implicit dependence of a physical observable O on μ through the constants must then cancel the explicit dependence, yielding

$$\mu\frac{\mathrm{d}}{\mathrm{d}\mu}O\big(\mu, \alpha_s(\mu), m_f(\mu)\big) = 0\,. \tag{1.24}$$

Eq. (1.24) is an example of Renormalization Group Equation (also RGE), and is valid at all orders in perturbation theory. Truncating the perturbative expansion poses a practical issue, because varying μ affects the expansion parameter $\alpha_s(\mu)$, reshuffling contributions between perturbative orders and potentially impacting the convergence of the series.

To clarify this, let me go back to the quark self-energy result of eq. (1.16) and focus on the logarithmic scale dependence. Logarithms of the ratio μ/m would appear at every perturbative order n, since each loop integral contributes in general an extra $1/\varepsilon$ and

$$\frac{1}{\varepsilon^n}(g_s\mu^\varepsilon)^{2n}m^{-2n\varepsilon} = (4\pi\alpha_s)^n \sum_{k=0}^{n} \frac{1}{\varepsilon^{n-k}}\frac{n^k}{k!}\ln^k\left(\frac{\mu^2}{m^2}\right) + \mathcal{O}(\varepsilon) \qquad (1.25)$$

(the mass is the available physical scale to make the argument of the logarithm dimensionless). This implies the all-order schematic form

$$\Sigma(\not{p}, m) = \sum_{n=0}^{\infty}\sum_{k=0}^{n}\sigma_{n,k}\,\alpha_s^n\ln^k\left(\frac{\mu^2}{m^2}\right). \qquad (1.26)$$

Choosing $\mu \gg m$ compromises the convergence of the perturbative series, because the expansion effectively occurs in terms of

$$\alpha_s\ln\frac{\mu^2}{m^2}\,,$$

which is now large because of the logarithm. Clearly, $\mu \sim m$ guarantees a much better convergence. Generalizing, fixing $\mu = E$ optimizes the convergence of the perturbative series for observables measured at the scale E. One can foresee that in presence of multiple, largely-separated physical scales choosing μ becomes a problem; this is where resummation will become important.

The same two-point fermion correlator offers the opportunity to examine an RGE more closely. The bare quantity is independent of μ, thus

$$\mu\frac{\mathrm{d}}{\mathrm{d}\mu}G_2(p, m_f, \alpha_s) = 0\,. \qquad (1.27)$$

From the definition in eq. (1.7) and eq. (1.12) (here explicitly denoting renormalized quantities with R for clarity),

$$G_2(p, m_f, \alpha_s) = Z_\psi\big(\alpha_s^R(\mu)\big)G_2^R\big(p, m_f^R(\mu), \alpha_s^R(\mu), \mu\big)\,. \qquad (1.28)$$

Note that the renormalization factors depend on μ through the coupling constant (because they admit perturbative expansion) but are constant functions of the kinematics (because of working in a minimal scheme). Entering eq. (1.28) in eq. (1.27) returns a Callan-Symanzik equation,

$$\left[\mu\frac{\partial}{\partial\mu} + \mu\frac{\mathrm{d}\alpha_s}{\mathrm{d}\mu}\frac{\partial}{\partial\alpha_s} + \mu\frac{\mathrm{d}m_f}{\mathrm{d}\mu}\frac{\partial}{\partial m_f} + \mu\frac{\mathrm{d}\ln Z_\psi}{\mathrm{d}\mu}\right]G_2\big(p, m_f(\mu), \alpha_s(\mu), \mu\big) = 0\,.$$
$$(1.29)$$

Its fomal solution in terms of an *evolution kernel U* is

$$G_2\big(p, m_f(\mu), \alpha_s(\mu), \mu\big) = U(\mu, \mu_0)\, G_2\big(p, m_f(\mu_0), \alpha_s(\mu_0), \mu_0\big)\,, \qquad (1.30)$$

and relates the correlator at two different renormalization scales. Evolution kernels satisfy

$$U(\mu_0, \mu_0) = 1\,, \qquad U(\mu_0, \mu_1)U(\mu_1, \mu) = U(\mu_0, \mu)\,, \qquad (1.31)$$

thus they have the algebraic structure of semigroup (they are in general not invertible), whose action on the correlators is parametrized by μ. This is referred to as *Renormalization Group* (RG).

Rather than finding a specific expression for the evolution kernel of this correlator by solving eq. (1.29), it is interesting to focus on some of the terms that appear there. The quantities

$$\gamma_\psi\big(\alpha_s(\mu)\big) = \mu\frac{\mathrm{d}\ln Z_\psi}{\mathrm{d}\mu}, \qquad \gamma_{m_f}\big(\alpha_s(\mu)\big) = \frac{\mu}{m_f}\frac{\mathrm{d}m_f}{\mathrm{d}\mu} \qquad (1.32)$$

take the name *anomalous dimensions*, because they govern the scaling of physical quantities due to loop effects (anomalies). The importance of the objects defined in eq. (1.32) resides in their universality, as they enter every correlator involving fermion fields. Even more important is the *beta function*,

$$\beta\big(\alpha_s(\mu)\big) = \mu\frac{\mathrm{d}\alpha_s}{\mathrm{d}\mu}\,, \qquad (1.33)$$

describing the evolution of the coupling constant at different reference scales. This is an ingredient in every RGE and also shows the existence of asymptotic freedom. It can be computed from differentiating the second equation of (1.17),

$$\beta(\alpha_s, \varepsilon) = -\alpha_s\Big(2\varepsilon + \mu\frac{\mathrm{d}\ln Z_g}{\mathrm{d}\mu}\Big) \qquad (1.34)$$

and further be expressed in terms of the coefficient of the simple ε pole of the renormalization factor,

$$\beta(\alpha_s) = 4\alpha_s^2\frac{\mathrm{d}}{\mathrm{d}\alpha_s}\Big(\mathrm{Res}\, Z_g\big|_{\varepsilon=0}\Big)\,. \qquad (1.35)$$

Given the expansion

$$\beta(\alpha_s) = -\frac{\alpha_s^2}{2\pi}\sum_{n=0}^{\infty}\beta_n\Big(\frac{\alpha_s}{4\pi}\Big)^n\,, \qquad (1.36)$$

the first coefficient β_0 is then determined from the one-loop renormalization factor,

$$\beta_0 = -2 \operatorname{Res} Z_g^{[1]}\big|_{\varepsilon=0}\,. \tag{1.37}$$

Gauge invariance offers various ways to access Z_g, but none of them is direct. For instance, one could compute the gluon self-energy and vertex corrections to extract

$$\text{rooo}\bigcirc\text{ooo} + \text{rooo}\otimes\text{ooo} + \text{rooo}\cdots\text{ooo} \rightarrow Z_A^{[1]}\,, \tag{1.38}$$

$$\text{rooo} + \text{rooo} \rightarrow Z_g^{[1]} + Z_\psi^{[1]} + \tfrac{1}{2} Z_A^{[1]}\,, \tag{1.39}$$

while $Z_\psi^{[1]}$ is known from the first equation in (1.19), leading to

$$Z_g^{[1]} = \frac{1}{6\varepsilon}\left(11 C_A - 4 n_f T_F\right) + \mathcal{O}(\varepsilon^0)\,. \tag{1.40}$$

In the standard choice of group basis, C_A and T_F are

$$C_A = f_{abc} f_{abc} = \frac{N_c^2 - 1}{2 N_c} = 3\,, \qquad T_F \delta_{ab} = (t_a)_{ij} (t_b)_{ji} = \frac{1}{2}\delta_{ab}\,, \tag{1.41}$$

and arise when tracing over respectively a gluon-to-boson and a gluon-to-quark splitting. Since color is always traced over, these are the only group factors (together with C_F) that physical observables depend on. In particular, T_F is always accompanied by the number of fermions n_f, as all active flavors circulate in fermion loops. This, and the knowledge that every QCD loop comes with a color factor, offers a helpful tool to organize and check QCD calculations.

From eq. (1.37) one gets the famous one-loop result

$$\beta_0 = \frac{11}{3} C_A - \frac{4}{3} n_f T_F\,. \tag{1.42}$$

The most striking features of QCD come from the evidence that β_0 is positive. This makes the coupling constant is a monotonically decreasing function of the energy,

$$\mu \frac{\mathrm{d}\alpha_s}{\mathrm{d}\mu} = -\frac{\beta_0}{2\pi} \alpha_s^2(\mu) < 0\,, \tag{1.43}$$

predicting asymptotic freedom at high energies. Since the first prediction by Gross, Politzer and Wilczek [5, 6], asymptotic freedom has received precise
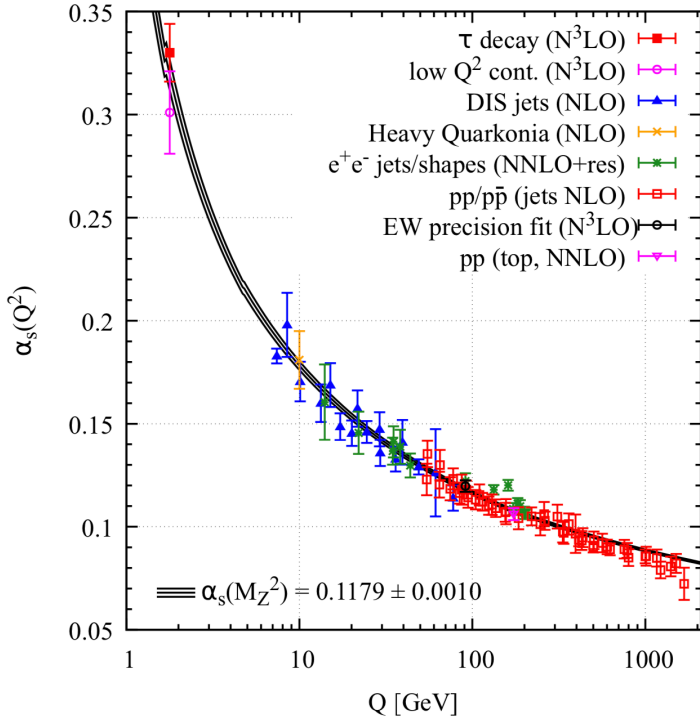
Figure 1.2 Running of the QCD coupling constant with the energy scale Q, from the 2019 update of the Particle Data Group Collaboration [7]. The various colors label results from different classes of experiments, and black curves correspond to analytic predictions for the schemes $n_f = (3, 4, 5)$. NLO to N³LO refer to the precision of the fixed-order QCD ingredients employed in the analysis.

experimental confirmation, see fig. 1.2. The differential equation (1.43) has solution

$$\alpha_s(\mu) = \frac{\alpha_s(\mu_0)}{1 + \frac{\beta_0}{2\pi}\alpha_s(\mu_0)\ln\frac{\mu}{\mu_0}} \, , \tag{1.44}$$

explicitly showing that the coupling constant goes to 0 in the limit $\mu \to \infty$. On the other hand, the (Landau) pole at

$$\mu_{\text{pole}} = \mu_0 \exp\left[- \frac{2\pi}{\beta_0 \alpha_s(\mu_0)} \right] \tag{1.45}$$

clearly shows that perturbative QCD fails at low energy, thus providing a justification for color confinement. Substituting the world average value from [7],

$$\alpha_s(M_Z = 91.1876\,\text{GeV}) = 0.1179 \tag{1.46}$$

in eq. (1.45), and evaluating β_0 with $n_f = 5$, yields

$$\mu_{\text{pole}} = 87\,\text{MeV}\,. \tag{1.47}$$

This is a rough estimate for Λ_{QCD}, the energy where confinement takes over and hadronization occurs. The precise value in eq. (1.47) is not particularly meaningful, because higher order corrections will sensitively affect it and the use of perturbative QFT itself becomes unjustified. In practical analyses, Λ_{QCD} is often assumed to be order of few hundreds MeV.

In general, one can wonder whether the conclusions of the one-loop analysis survive higher order corrections. In fact, the series in eq. (1.36) has been computed up to four [8] and five loop [9], making it the most accurate QCD calculation and providing an even more robust check of asymptotic freedom. The strong coupling constant is one of the most studied quantities in QCD from both the high-energy and lattice perspective, see e.g. [10] for a recent review.

Asymptotic freedom offers a window on quarks and gluons, and a hope to perturbative QCD. Still, this a quantum mechanical window, meaning that our glimpsing through it will distort the vision. At the typical center-of-mass energy of a collision, the value of α_s is small enough that we can safely describe the system with perturbative QCD; however, particle detection occurs at much lower energies, where color confinement is already active. Some trick is needed to separate the two phases of the process. In the early times of QFT, this was done within the *parton model*, treating colliding protons as the incoherent sum of point-like constituents (partons) and postulating the high-energy scattering to probe a single parton a time. This is clearly an approximation, as quantum mechanics in fact entangles the various partons, but it proved very successful to describe data. Factorization gives the parton model a theoretical basis.
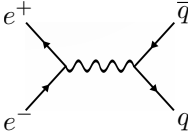
1.2 Soft and collinear QCD

1.2.1 The physical picture: on-shell intermediate states

According to the path-integral formulation of quantum mechanics, we can imagine a dynamical process as the superposition of all the stories that could have occurred to the system from a known initial configuration to its measurement. No matter how bizarre a trajectory is from the classical perspective; it will nonetheless get a weight in the path integral. Still, those paths that give the largest contribution to the action are the ones that are allowed even classically, while destructive interference will dampen the most unlikely trajectories.

The same reasoning applies in Quantum Field Theory, where we model the story of a process as a collection of steps of particle creation and annihila-

tion. The role of each propagator $i/(p^2 - m^2)$ is suppressing configurations with large virtuality. Since by construction the theory enforces momentum conservation at each vertex, virtuality manifests itself through violation of the on-shell condition $p^2 = m^2$. As a side remark, it is interesting to consider an alternative formulation (Time-Ordered Perturbation Theory) where virtual particles are on shell and propagators parametrize the violation of energy-momentum conservation. Either way, whenever the process allows for propagation of intermediate-state low-virtuality particles, we expect these configurations to dominate the path integral. This is the principle behind the detection of new particles via resonances: in the example of an e^+e^- collider[2], when the center-of-mass energy $\sqrt{s}$ of a collision is tuned to the mass M of a particle, then the latter is produced on shell and we observe a peak in the cross section.

As it will turn out useful in ch. 4, it is worth looking at the example of the Z boson resonance in $e^+e^- \to q\bar{q}$. The process by itself is non-physical (we cannot observe the final-state pair) but provides the leading order result for *inclusive* hadron production (meaning that we sum over all hadrons in the final state). The tree level amplitude in QED, Feynman gauge, in the limit of negligible fermion masses is

$$= -ie^2 Q_f \frac{1}{s} \bar{v}(p_+)\gamma_\mu u(p_-)\bar{u}(p)\gamma^\mu v(\bar{p}) \,, \qquad (1.48)$$

where Q_f is the charge of the quark of flavor f in units of e. Squaring, averaging (summing) over inital (final) spin, color and flavor, integrating over the phase space, and including the flux factor, returns the cross section

$$\sigma_{e^+e^- \to X} = \frac{4\pi\alpha^2 N_c}{3s} \sum_f Q_f^2 \equiv \sigma_0 \,, \qquad (1.49)$$

where $\alpha = e^2/4\pi$ is the fine structure constant. Famously, measuring this quantity played an important role in setting the number of colors N_c to three and confirming the fractionary charge of quarks. A way to account for the Z boson and its interference with the photon is the effective replacement

$$Q_f^2 \to Q_f^2 + \frac{(v_f^2 + a_f^2)(v_e^2 + a_e^2) - 2Q_f v_f v_e(1 - M_Z^2/s)}{(1 - M_Z^2/s)^2 + M_Z^2\Gamma_Z^2/s^2} \,, \qquad (1.50)$$

---

[2]Because of the composite nature of protons, a *pp* collider probes a whole range of energies. In this case it is of course still possible to detect particles via resonances, but not to tune the energy to one value.

where the relevant EW parameters are collected in appx. A.4, eq. (A.27) and following. By substituting the numerical values, one can easily see that the Z boson contribution is negligible at low (few tens GeV) center of mass energies, but becomes dominant around M_Z, where it enhances the cross section by almost three orders of magnitude.

Something conceptually similar occurs in massless gauge theories, and in particular in the high-energy limit of QCD. In this case propagators can go on shell not due to resonant particle production, but because of simple kinematics. Take for definiteness a $q \to qg$ splitting,

$$\text{(diagram)} \quad = \quad \frac{it_a\gamma^\mu(\slashed{p} + \slashed{k})}{(p + k)^2} \quad = \quad \frac{it_a\gamma^\mu(\slashed{p} + \slashed{k})}{2E_k E_p(1 - \cos\vartheta)}\,, \tag{1.51}$$

where E are the energies of the two products and ϑ their relative angle. The virtual particle goes on shell if one of the products[3] is *soft*, meaning its energy vanishes, or if the two are *collinear*, namely they move in the same direction, $\vartheta = 0$. As both limits correspond to vanishing sqared momentum, they concern the low-energy behavior of the theory and are collectively referred to as infrared (IR). These are the kinematical configurations allowed also classically, thus we expect them to dominate QCD observables. This indeed leaves a signature in high-energy collisions, where collimated sprays of hadrons (jets) typically carry a large fraction of the center-of-mass energy.

Physical intuition suggests that studying small kinematical perturbations around the soft and collinear configurations should simplify the problem while retaining most of the relevant QCD physics. In the diagrammatic approach this is called *eikonal approximation*; the name reminds of taking the classical, infrared limit of infinite wavelength when studying light propagation, and in a way we are applying the same idea to QCD. On the other hand, having identified the relevant IR degrees of freedom, effective field theories provide a natural language to systematically incorporate perturbations from the high-energy completion into their dynamics. I will postpone the discussion of SCET to sec. 1.3 and take a full QCD viewpoint for the time being.

A consequence of having taken the fermion masses to zero is that we lost any characteristic energy scale in the IR (we are not involving Λ_{QCD} for the moment). Virtual particles are then allowed to carry arbitrarily low (or "arbitrarily collimated") momentum, which generates IR divergences in loop integrals.

---

[3]In fact, at leading power, only a soft gluon (not a soft quark) generates a singularity. Showing this requires considering the interplay with phase-space integration and adjacent propagators, and is not evident by simply looking at eq. (1.51).

The same issue affects phase-space integrals: whenever final-state kinematics allows for soft or collinear emissions, the integral diverges in the IR. The solution is that sensible observables always involve both real and virtual contributions, and divergences cancel when the two effects are accounted for. The idea behind the cancellation is that every virtual state that is allowed on-shell should also be included as real final state, or there will be a mismatch in the physical content of the theory. Quantities that are free of IR divergences are called *infrared safe*. Even if physical observables can be IR unsafe, a direct comparison between QCD parton-level predictions and measured quantities is possible only for infrared-safe quantities. A practical way to confirm the IR safety of a candidate observable O involving a set of final-state particles j with momenta p_j, is checking whether soft and collinear splittings leave it unchanged,

$$
\begin{aligned}
O\big(\ldots(j, p_j)\ldots\big) &= O\big(\ldots(j, p_j), (j', 0)\ldots\big) \\
O\big(\ldots(j, p_j)\ldots\big) &= O\big(\ldots(j, x p_j)(j', (1-x)p_j)\ldots\big),
\end{aligned}
\tag{1.52}
$$

where $x \in [0, 1]$ represents the energy fraction of one of the collinear products. This requirement is consistent with the impossibility of detect a zero-energy particle in experiments, or tell a single particle from a perfectly collimated pair. Trivial examples are the number of particles (not infrared safe) or the total energy or momentum (infrared safe), but (dis)proving the IR safety of more complicated observables can be rather subtle.

If IR divergences ultimately cancel, intermediate stages of the calculation still require a regulator. Dimensional regularization proves itself fundamental in fixing divergences arising from the scaling behavior of loop integrals at high momentum, while holding the symmetries of the problem; it seems natural to apply the same technique to the other end of the energy spectrum. Working in $4 - 2\varepsilon$ dimensions with $\varepsilon < 0$, IR divergences show up again as poles in ε. In presence of both UV and IR divergences, one can imagine a conflict in the choice of ε. I will comment on this point in the following, where I show a specific instance of what discussed here while introducing resummation.

1.2.2 Example: hadron production with a cut on thrust

To familiarize with the role of soft and collinear physics in QCD it is useful to consider a specific example. I will sketch the calculation of the next-to-leading order QCD corrections to the $e^+e^- \to$ hadrons cross section in eq. (1.49), starting with imposing a cut on thrust. Thrust is a typical example of *event shape*, a class of observables that characterizes the global properties of an event through the spatial distribution of final-state energy and momentum. Event

shapes (and thrust in particular) have been a testing ground for resummation techniques, see e.g. [11–15], and lead precise determinations of the strong coupling constant [16–18]. In this section, I will consider imposing a cut on thrust as an intuitive way to regulate IR divergences, but this procedure has also phenomenological relevance, see refs. [19–21].

Thrust is defined by maximizing the scalar sum of the particle three-momenta projected on a reference vector $\hat{t}$ [22],

$$T = \max_{\hat{t} \in S_2} \frac{\sum_i |\vec{p}_i \cdot \hat{t}|}{\sum_i |\vec{p}_i|} \,. \tag{1.53}$$

The direction $\hat{t}$ that determines the maximum is called *thrust axis*. One can check the IR safety of eq. (1.53) from eq. (1.52). The definition is frame dependent, and for e^+e^- collisions the natural choice is the center-of-mass frame. When all final-state particles are aligned then $T = 1$, while an isotropic momentum distribution corresponds to the lower bound $T = \frac{1}{2}$. Therefore, thrust is a measure of how "pencil-like" or "two-particle-like" an event is. At tree level, the $q\bar{q}$ pair is always produced back to back, so the thrust is one,

$$\frac{\mathrm{d}\sigma_{e^+e^- \to X}}{\mathrm{d}T}(T) = \sigma_0 \, \delta(1 - T) \,, \tag{1.54}$$

where σ_0 is the inclusive tree-level cross section from eq. (1.49). Higher order corrections smear the distribution, but soft and collinear splittings do not, so the limit $T \to 1$ coincides in fact with the IR limit. This makes thrust a useful probe of soft and collinear dynamics.

I will now move on to the calculation of the inclusive cross section. At order α_s five diagrams contribute to the process: two radiative emissions and three virtual loop corrections (fig. 1.3). If a cut on thrust is imposed, $T < T_c$, only
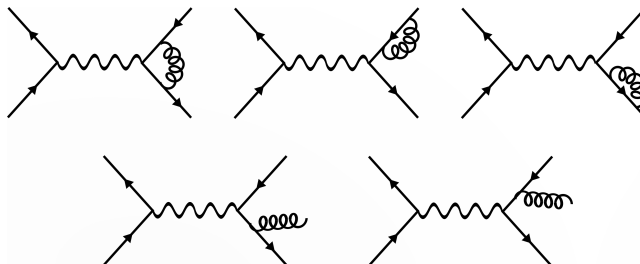

Figure 1.3 Next-to-leading order (NLO) diagrams for $e^+e^- \to$ hadrons.

real diagrams contribute, as the virtual ones have a two-particles final state

(thus $T = 1$). Summing the two amplitudes yields

$$M_{\mathrm{R}} = \frac{e^2 g_s Q_f}{2s} \overline{v}(p_+) \gamma_\mu u(p_-) \, \overline{u}(p) t_a \left[\not\epsilon(k) \frac{\not p + \not k}{p \cdot k} \gamma^\mu - \gamma^\mu \frac{\not{\overline{p}} + \not k}{\overline{p} \cdot k} \not\epsilon(k) \right] v(\overline{p}) \,, \tag{1.55}$$

where k is the gluon momentum and $\epsilon(k)$ its polarization vector. Using Dirac algebra and momentum conservation, one can write the squared amplitude averaged over spin, flavor, color and polarizations as

$$\langle |M_{\mathrm{R}}|^2 \rangle = \frac{512\pi^3 \alpha_s \alpha^2 C_F N_c}{3s} \sum_f Q_f^2 \frac{(p \cdot k)^2 + (\overline{p} \cdot k)^2 + 2(p_+ \cdot p_-)\,(p \cdot \overline{p})}{(p \cdot k)\,(\overline{p} \cdot k)} \,. \tag{1.56}$$

The three-particle phase space involves a twelve-dimensional integral,

$$\int_{2\to 3} \{\mathrm{d}P_s\} = \frac{1}{(2\pi)^5} \int \mathrm{d}^4 p \int \mathrm{d}^4 \overline{p} \int \mathrm{d}^4 k \, \delta^+(p^2)\delta^+(\overline{p}^2)\delta^+(k^2)\,\delta^{(4)}(p + \overline{p} + k - q) \,, \tag{1.57}$$

but on-shell conditions, momentum conservation and angular symmetry reduce the number of nontrivial integrations to two. In other words, we can specify the final-space kinematics with

$$p = (E, 0, 0, -E) \,, \qquad \overline{p} = (\overline{E}, \overline{E} \sin \vartheta, 0, \overline{E} \cos \vartheta) \,, \tag{1.58}$$

and let momentum conservation fix k. The on-shell condition for the latter relates then the angle

$$\cos \vartheta = \frac{E^2 + \overline{E}^2 - (\sqrt{s} - E - \overline{E})^2}{2E\overline{E}} \tag{1.59}$$

to the quark/antiquark energies, taken as independent variables. It is convenient to further introduce the energy fractions

$$x = \frac{2E}{\sqrt{s}} \,, \qquad \overline{x} = \frac{2\overline{E}}{\sqrt{s}} \,, \tag{1.60}$$

in terms of which eq. (1.56) takes the simple form

$$\langle |M_{\mathrm{R}}|^2 \rangle = 128\pi^2 \alpha_s C_F \sigma_0 \frac{x^2 + \overline{x}^2}{(1-x)(1-\overline{x})} \tag{1.61}$$

and the radiative cross section (including the flux factor $1/(2s)$) reads

$$\sigma_R = \frac{\alpha_s C_F}{2\pi} \sigma_0 \int_0^1 \mathrm{d}x \int_0^{1-x} \mathrm{d}\bar{x}\, \frac{x^2 + \bar{x}^2}{(1-x)(1-\bar{x})}\,. \qquad (1.62)$$

The bound $\bar{x} < 1 - x$ arises because also the gluon energy fraction $2 - x - \bar{x}$ cannot exceed 1. This expression is purely formal: as expected, the integral has infrared logarithmic divergences when $x \to 1$ and $\bar{x} \to 1$.

Nonetheless, eq. (1.62) becomes well-defined if we apply a cut on thrust. To see this, one can use the result that in a three-particle configuration the thrust axis aligns to the most energetic, and

$$T = \max(x, \bar{x}, 2 - x - \bar{x})\,. \qquad (1.63)$$

One can therefore split the integration domain depending on what particle has larger enrgy (fig. 1.4), and perform the substitution (1.63) region by region (in fact, one can assume $x > \bar{x}$ by symmetrizing the integration domain). This yields

$$\sigma_R = \frac{\alpha_s C_F}{\pi} \sigma_0 \int_{\frac{2}{3}}^1 \mathrm{d}T \left[\int_T^{1-T} \mathrm{d}\bar{x}\, \frac{T^2 + \bar{x}^2}{(1-T)(1-\bar{x})} + \int_{2-2T}^{1-T/2} \mathrm{d}\bar{x}\, \frac{(2 - \bar{x} - T)^2 + \bar{x}^2}{(T + \bar{x} - 1)(1 - \bar{x})} \right]\,. \qquad (1.64)$$

This form makes it clear that the IR divergences arise from the limit $T \to 1$,
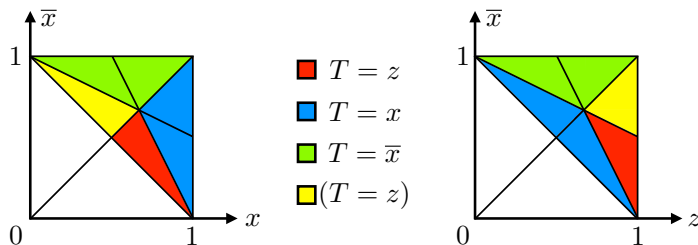

Figure 1.4 Three-particle massless phase space in terms of the energy fractions $x, \bar{x}, z = 2 - x - \bar{x}$. Different colors correspond to the thrust axis lying on different particles. The green (yellow) domain is related to the blue (red) one by $x \to \bar{x}$.

thus a cut $T < T_c$ acts as a physical IR regulator. Performing the $\bar{x}$ integral allows one to extract the cross section differential in thrust,

$$\frac{\mathrm{d}\sigma}{\mathrm{d}T} = \frac{\alpha_s C_F}{\pi} \sigma_0 \left[\ln\left(\frac{2T - 1}{1 - T}\right)\left(\frac{2}{1 - T} + \frac{2}{T} - 3\right) - \frac{3}{2(1 - T)} + \frac{15}{2} - \frac{9}{2}T \right]\,, \qquad (1.65)$$

while the cumulant yields

$$\sigma(T < T_c) = \int_{\frac{2}{3}}^{T_c} \mathrm{d}T \, \frac{\mathrm{d}\sigma}{\mathrm{d}T} = \frac{\alpha_s C_F}{\pi} \sigma_0 \left[\ln^2\left(\frac{1 - T_c}{T_c}\right) + \frac{3}{2}(1 - 2T_c) \ln\left(\frac{2T_c - 1}{1 - T_c}\right) \right.$$

$$\left. + 2\mathrm{Li}\left(\frac{1 - T_c}{T_c}\right) - 4 - \frac{\pi^2}{6} + \frac{15}{2}T_c - \frac{9}{4}T_c^2 \right], \tag{1.66}$$

where Li_2 is the dilogarithm. In the limit $T_c \to 1$, it simplifies as

$$\sigma(T < T_c) = \frac{\alpha_s C_F}{\pi} \sigma_0 \left[\ln^2(1 - T_c) + \frac{3}{2}\ln(1 - T_c) - \frac{\pi^2}{6} + \frac{5}{4} \right] + \mathcal{O}(1 - T_c). \tag{1.67}$$

A characteristic feature of this observable is the quadratic logarithmic dependence on $1 - T_c$. I will comment extensively on this in sec. 1.2.4, where eq. (1.67) will be the starting point to discuss resummation.

1.2.3 Inclusive hadron production

The previous example considered a simple observable where IR divergences are cut off by a physical regulator. To see dimensional regularization at work in the infrared, one can repeat the calculation removing the cut on thrust.

The squared amplitude for the radiative diagrams in $4 - 2\varepsilon$ dimension reads

$$\langle |M_{\mathrm{R}}|^2 \rangle = 128\pi^2 \alpha_s \mu^{4\varepsilon} C_F \sigma_0 \frac{(1 - \varepsilon)^2}{1 - \frac{2}{3}\varepsilon} \frac{x^2 + \bar{x}^2 - \varepsilon(2 - x - \bar{x})^2}{(1 - x)(1 - \bar{x})}, \tag{1.68}$$

where the scale μ is needed in view of renormalization. Integrating over the three-particle phase space in $4 - 2\varepsilon$-dimensions yields

$$\sigma_R = \frac{\alpha_s C_F}{2\pi} \sigma_0 \frac{(1 - \varepsilon)^2}{1 - \frac{2}{3}\varepsilon} \left(\frac{4\pi\mu^2}{s}\right)^{2\varepsilon} \frac{1}{\Gamma(2 - 2\varepsilon)}$$

$$\times \int_0^1 \mathrm{d}x \int_{1-x}^1 \mathrm{d}\bar{x} \left[\frac{x^2 + \bar{x}^2 - \varepsilon(2 - x - \bar{x})^2}{(1 - x)^{1+\varepsilon}(1 - \bar{x})^{1+\varepsilon}(x + \bar{x} - 1)^{1+\varepsilon}} \right]. \tag{1.69}$$

The limit $x, \bar{x} \to 0$ is now safe since $\varepsilon < 0$, and the integral evaluates to

$$\sigma_R = \frac{\alpha_s C_F}{\pi} \sigma_0 \left(\frac{\bar{\mu}^2 e^{\gamma_E}}{s}\right)^{2\varepsilon} \frac{3(2 - 2\varepsilon + \varepsilon^2)(1 - \varepsilon)^2}{3 - 2\varepsilon} \frac{\Gamma(1 - \varepsilon)\Gamma^2(-\varepsilon)}{\Gamma(1 - 2\varepsilon)\Gamma(3 - 3\varepsilon)}, \tag{1.70}$$

whose expansion reads

$$\sigma_R = \frac{\alpha_s C_F}{\pi} \sigma_0 \left[\frac{1}{\varepsilon^2} + \frac{1}{\varepsilon}\left(2\ln\frac{\bar{\mu}^2}{s} + \frac{13}{6}\right) + 2\ln^2\frac{\bar{\mu}^2}{s} + \frac{13}{3}\ln\frac{\bar{\mu}}{s} - \frac{5}{6}\pi^2 + \frac{259}{36} \right]. \tag{1.71}$$

The limit $x \to 1, \bar{x} \to 1$ where the gluon is soft and collinear at the same time produces the double infrared pole (hence, the double logarithms). The argument of the logarithms is the renormalization scale over the center-of-mass energy. This is inevitable, as μ comes in powers of ε and $\sqrt{s}$ is the only available scale in the problem, and is a common feature to every calculation involving soft and collinear physics.

Next comes the virtual amplitude, the first diagram in fig. 1.3

$$
\begin{aligned}
M_{\mathrm{V}} &= e^2 Q_f g_s^2 C_F \mu^{2\varepsilon} \bar{v}(p_+) \gamma_\mu u(p_-) \, \bar{u}(p) \int \frac{\mathrm{d}^d \ell}{(2\pi)^d} \frac{\gamma_\nu (\slashed{p} + \slashed{\ell}) \gamma^\mu (\slashed{\bar{p}} - \slashed{\ell}) \gamma^\nu}{\ell^2 (p+\ell)^2 (\bar{p}-\ell)^2} v(\bar{p}) \\
&= \frac{i e^2 g_s^2 Q_f}{32\pi^2 s} \left(\frac{4\pi\mu^2}{-s} \right)^\varepsilon \frac{\Gamma(\varepsilon)\Gamma^2(-\varepsilon)}{\Gamma(-2\varepsilon)} \frac{(2 - \varepsilon + 2\varepsilon^2)}{(1 - 2\varepsilon)} \bar{v}(p_+) \gamma_\mu u(p_-) \, \bar{u}(p) \gamma^\mu v(\bar{p}) \,.
\end{aligned}
$$
(1.72)

At order α_s, this interferes with the tree-level diagram to give

$$
\begin{aligned}
\langle 2\mathrm{Re}\big(M_{\mathrm{V}} M_{\mathrm{tree}}^*\big) \rangle = {}& \frac{32\pi\alpha^2 \alpha_s C_F N_c}{s^2} \sum_f Q_f^2 \left(\frac{4\pi\mu^4}{s} \right)^\varepsilon \cos(\pi\varepsilon) \frac{\Gamma(\varepsilon)\Gamma^2(-\varepsilon)}{\Gamma(-2\varepsilon)} \\
&\times \frac{(2 - \varepsilon + 2\varepsilon^2)}{(1 - 2\varepsilon)} \big[p_+ \!\cdot\! p \, p_- \!\cdot\! \bar{p} + p_- \!\cdot\! p \, p_+ \!\cdot\! \bar{p} - \varepsilon s/4 \big] \,.
\end{aligned}
$$
(1.73)

Integrating over the $4 - 2\varepsilon$ dimensional $2 \to 2$ phase space finally yields

$$
\sigma_V = \sigma_0 \frac{\alpha_s C_F}{\pi} \left(\frac{4\pi\mu^2}{s} \right)^\varepsilon \frac{3\Gamma(\varepsilon)\Gamma^3(-\varepsilon)(2 - \varepsilon + 2\varepsilon^2)}{8(1 - 2\varepsilon)^\varepsilon (3 - 2\varepsilon)\Gamma^2(-2\varepsilon)} \cos(\pi\varepsilon) \,,
$$
(1.74)

and expanding

$$
\sigma_V = \frac{\alpha_s C_F}{\pi} \sigma_0 \left[-\frac{1}{\varepsilon^2} - \frac{1}{\varepsilon} \left(2\ln\frac{\bar{\mu}^2}{s} + \frac{13}{6} \right) - 2\ln^2\frac{\bar{\mu}^2}{s} - \frac{13}{3}\ln\frac{\bar{\mu}}{s} + \frac{5}{6}\pi^2 - \frac{58}{9} \right] \,.
$$
(1.75)

While the poles in eq. (1.71) are clearly of IR origin (it is a tree-level graph), eq. (1.75) contains a mix or IR and UV poles. Explicitly labeling their origin,

$$
-\frac{1}{\varepsilon^2} - \frac{1}{\varepsilon} \left(2\ln\frac{\bar{\mu}^2}{s} + \frac{13}{6} \right) = -\frac{1}{\varepsilon_{\mathrm{IR}}^2} + \frac{1}{\varepsilon_{\mathrm{UV}}} - \frac{1}{\varepsilon_{\mathrm{IR}}} \left(2\ln\frac{\bar{\mu}^2}{s} + \frac{19}{6} \right) \,.
$$
(1.76)

The distinction can be seen for instance by repeating the calculation with a different infrared regulator, so that all the remaining poles would be UV. However, ultraviolet poles in the final result would mean that QCD corrections require counterterms in QED, spoiling the renormizablity of the latter.

This potential issue is fixed by the second and third diagrams in fig. 1.3, virtual corrections on a single quark/antiquark leg.[4] In a massless theory these graphs are *scaleless*, as the loop has no reference energy (by contrast, connecting the two outgoing legs, the loop in eq. (1.72) knows about $p \cdot \bar{p} = s$). The loop integral that appears here has the form

$$\int \frac{\mathrm{d}^{4-2\varepsilon}\ell}{(2\pi)^{4-2\varepsilon}} \ell^2 (\ell - p)^2 = \int_0^1 \mathrm{d}x \int \frac{\mathrm{d}^{4-2\varepsilon}\ell}{(2\pi)^{4-2\varepsilon}} \frac{1}{(\ell^2 - 2x\ell \cdot p)^2} = \int \frac{\mathrm{d}^{4-2\varepsilon}\ell}{(2\pi)^{4-2\varepsilon}} \frac{1}{\ell^4}$$

$$= \frac{(4\pi)^\varepsilon}{8\pi^2 \Gamma(2-\varepsilon)} \int_0^\infty \mathrm{d}\ell\, \ell^{-1-\varepsilon} = \frac{(4\pi)^\varepsilon}{8\pi^2 \Gamma(2-\varepsilon)} \left[\frac{1}{\varepsilon_{\mathrm{UV}}} - \frac{1}{\varepsilon_{\mathrm{IR}}} \right]. \quad (1.77)$$

The second step involves a shift in the integration momentum, and in the final step the different origin of the poles is clear since they regulate opposite ends of the momentum spectrum. In dimensional regularization, scaleless integrals are formally vanishing, but in fact they bridge between UV and IR physics, converting the relative poles. The presence of a numerator alters the final coefficient in eq. (1.77), but does not affect the logic. Summing over the three virtual diagrams in fig. 1.3 the UV pole in eq. (1.76) is effectively replaced by an IR one: eq. (1.75) is formally unaffected, but all the poles are now infrared.

At this point, one can appreciate the cancellation of infrared divergences and unphysical μ dependence delivering one of the neatest QFT results,

$$\sigma_{e^+e^- \to \mathrm{hadrons}} = \sigma_0 + \sigma_R + \sigma_V = \sigma_0 \left(1 + \frac{3\alpha_s C_F}{4\pi} \right) = \sigma_0 \left(1 + \frac{\alpha_s}{\pi} \right). \quad (1.78)$$

1.2.4 Resummation

I will now use the calculations in the previous two sections to motivate for resummation, and show its effects in a simple setting. Let me consider to this aim the cross section with a *lower* cut on thrust, $T_c < T < 1$, which in the limit of large T_c follows from the difference of eq. (1.78) and eq. (1.67),

$$\sigma(T > T_c) = \sigma_0 \left\{ 1 + \frac{\alpha_s C_F}{\pi} \left[-\ln^2(1-T_c) - \frac{3}{2}\ln(1-T_c) + \frac{7\pi^2}{12} - \frac{5}{4} \right] \right\}. \quad (1.79)$$

This simple quantity already exhibits some characteristic features of IR physics relevant to phenomenology. The cross section is free of soft and collinear

---

[4]In fact, being one-particle reducible, these diagrams do not enter the cross section directly, but they do it through replacement factors for the external spinors in the Lehmann-Symanzik-Zimmermann reduction formula, see e.g. [23]. This subtlety does not impact the logic of what presented here.

singularities, but the logarithms of $1 - T_c$ are reminiscent of their existence. In particular, eq. (1.79) contains *double* logarithms, terms of the kind
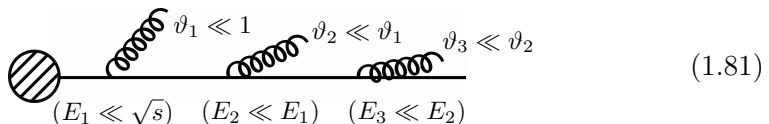
$$\alpha_s^n \ln^{2n}(1 - T_c)$$

that arise whenever an emission can be soft and collinear at the same time. To practical purpose, it could be useful to set a large cut $T_c \lesssim 1$, as most of the events in a real collider occur very close to $T = 1$ [24]. In this case, the power corrections that were dropped passing from eq. (1.66) to eq. (1.67) are mostly negligible, but in turn the logarithms become large. The size of the logarithms is not per se a problem, but it becomes worrying since their power grows with the perturbative order. Indeed, the all-order structure of the cross section would be

$$\sigma(T > T_c) = \sum_n \alpha_s^n \Big[\sigma_{n,2n} \underbrace{\ln^{2n}(1 - T_c)}_{\text{LL}} + \sigma_{n,2n-1} \underbrace{\ln^{2n-1}(1 - T_c)}_{\text{NLL}} + \dots \Big],$$

(1.80)

so the presence of the logarithms would spoil the convergence of the perturbative series. In particular one can distinguish *Leading Logarithms* (LL), *Next-to-Leading Logarithms* (NLL), and so on, depending on the power of the logarithms relative to the power of the coupling constant.[5]

Although I have not proven the structure (1.80), there is a powerful physical argument while this should be the case. First, in the IR limit, subsequent emissions are uncorrelated. The idea is that we are describing a radiative process as the succession of splittings of on-shell particles, any splitting corresponding to a decay that occurs with some rate P. This is formalized by introducing *splitting functions*, and I will come back to this point in sec. 2.2.1. Second, infrared emissions are not associated with any particular energy, so nothing prevents them to become even more soft and collinear. We can thus consider the *strongly ordered* limit in which each emission has angle and energy much smaller than the previous one,

(1.81)

---

[5] Often the series exponentiates, see eq. (1.84), and the terminology LL, NLL, etc. refers to the logarithms in the exponent, rather than in the cross section itself. However, the logic is unaltered.

The leading logarithms in eq. (1.80) come then from n uncorrelated strongly ordered emissions. Relenting the strong ordering condition for one of the emissions would generate the next-to-leading logarithms, and so on.

The presence of such an iterative structure suggests that it must be possible to predict the coefficients of the logarithms at every order in perturbation theory by performing a finite-order calculation. In fact, if the emissions are truly uncorrelated, the order-n coefficient is simply (up to a common normalization, and including the combinatorial factor $1/n!$ for identical particles) the n-th power of some Δ_1, and the whole LL series exponentiates,

$$\Delta = \sum_{n=0}^{\infty} \left(\frac{4\alpha_s C_F}{\pi}\right)^n \frac{\Delta_1^n}{n!} = \exp\left[\frac{4\alpha_s C_F}{\pi} \Delta_1\right]. \tag{1.82}$$

the exponential defined in eq. (1.82) is called Sudakov form factor. To understand the coefficient of Δ_1 and the link between double logarithms and strongly ordered limit, switch coordinates to the gluon energy fraction $z = 2 - x - \overline{x}$ and the angle between the gluon and the emitting (anti)quark in eq. (1.62). The soft *and* collinear limit now reads $z \to 0, \vartheta \to 0$, yielding

$$\sigma_R = \sigma_0 \frac{4\alpha_s C_F}{\pi} \int \frac{\mathrm{d}z}{z} \int \frac{\mathrm{d}\vartheta}{\vartheta}. \tag{1.83}$$

This expression is generally valid for $q \to qg$ splittings in the strongly ordered limit. Imposing a measurement fixes the integration bounds, and determines the specific form of Δ_1. In the case of lower cut on thrust, entering $\theta(T - T_C)$ under integral in eq. (1.83) allows one to fix $\Delta_1 = -\frac{1}{4}\ln^2(1 - T_C)$, thus retrieving the double logarithms in eq. (1.79).[6] The prediction for $e^+e^- \to$ hadrons with a cut on thrust including LL becomes

$$\sigma^{\mathrm{LL}}(T > T_c) = \sigma_0 \Delta = \sigma_0 \exp\left[-\frac{\alpha_s C_F}{\pi} \ln^2(1 - T_c)\right]. \tag{1.84}$$

This process of including a whole class of logarithms in our predictions is called resummation. One could also include in the form factor the single logarithms in eq. (1.67), but to achieve full NLL accuracy one would need to perform a two-loop calculation. Eq. (1.84) is now well-behaved for $T_c \to 1$, and in this limit, even without including the full α_s correction, it will describe data much better than the fixed-order result. In fact, for the purpose of extracting the LL behavior in eq. (1.84), the full NLO result in eq. (1.66) was largely superfluous. One could have aimed from the beginning at just the coefficient

---

[6]To do so, one uses $\theta(T - T_C) = 1 - \theta(T_C - T)$. The first term produces a formally infinite integral, that cancellation of IR divergences sets to zero; in other words, we know the total cross section to be free of large logarithms.

of the logarithms, for example by performing an expansion under integral. This is indeed a valid strategy in practical situations where the full calculation becomes too complicated.

The resummation example that I sketched here is perhaps misleadingly simple, since it hides the central role played by factorization. Systematically performing resummation requires in general to factorize the observable and evolving the various factorization ingredients up to a common energy scale using Renormalization Group Equations. Practical situations often require a choice between retaining power corrections, of the kind I dropped from eq. (1.66) to eq. (1.67), or including resummation. In ch. 3 I will give a first example of this interplay.

Before moving on, let me note that the strong ordering picture (1.81) is a key ingredient of the event generators commonly used in particle physics simulations, such as PYTHIA [25] and HERWIG [26]. These Monte Carlo programs are a fundamental tool to benchmark both theoretical predictions and experimental analyses. Event generators model the infrared QCD dynamics through parton showers: quarks and gluons generated in an initial subprocess undergo multiple branchings, assuming independent splitting probability and ordering in either angle or transverse momentum. A hadronization model converts the final-state quarks and gluons into hadrons. At the time of writing, the accuracy of parton showers is currently limited to LL (and leading color), although relevant steps are being made to overcome these limits, see e.g. [27–31].

1.2.5 Factorization in diagrammatic language

Before discussing Soft Collinear Effective Theory, I will sketch how factorization was first derived from a systematic study of soft and collinear singularities at the diagrammatic level. I will keep the discussion very brief, and the interested reader can look for instance at the textbook [32] or some of the original papers [33–36] for details. I will focus on an inclusive $1 \rightarrow N$ process. Imposing a measurement on the final state (e.g., the transverse momentum of one of the products) may change the picture; this is related to the difference between $\mathrm{SCET_I}$ and $\mathrm{SCET_{II}}$, and I will comment on this point in sec. 1.3.2 from that perspective.

The goal is making a systematic approximation that captures the IR limit of the theory, and showing that amplitudes (and observables) factorize in this limit. The key steps are the following: first, one classifies all the IR singularities by looking at the general structure of Feynman diagrams; next introduces IR power counting to tell truly divergent singularities from spurious ones. This tool provides us with the most generic IR-divergent graphs and with a practical way to implement the eikonal approximation; finally, one shows that in

this limit the general graph reduces to the product of subdiagrams, each describing either soft or collinear divergences, or hard high-energy physics. An important ingredient are Wilson lines, that loosely speaking represent a high-energy parton from the perspective of soft and collinear radiation. Showing that the phase space also factorizes extends factorization from amplitudes to observables. I will now quickly comment on these steps in turn.

Following an analysis first due to Landau, to identify the IR singularities a generic Feynman diagram $\mathcal{G}$, one describes it as a function of external momenta p_i and loop momenta ℓ_j. The denominators can be recombined through (for definiteness) Feynman parameters x_k,

$$\mathcal{G}(p_i \cdot p_{i'}) = \left(\prod_k \int_0^1 \mathrm{d}x_k\right) \delta(1 - \sum_k x_k) \left(\prod_j \int \frac{\mathrm{d}^d \ell_j}{(2\pi)^d}\right) \frac{\mathcal{N}(p_i, \ell_j, x_k)}{\mathcal{D}^\alpha(p_i, \ell_j, x_k)}, \quad (1.85)$$

where the numerator $\mathcal{N}$ includes Dirac structures and overall constants, and the denominator $\mathcal{D}$ is quadratic in the loop momenta,

$$\mathcal{D}(p_i, \ell_j, x_k) = a_{jj'}(x_k)\ell_j \cdot \ell_{j'} + q_j(x_k, p_i) \cdot \ell_j + m^2(x_k, p_i \cdot p_{i'}) + i\eta, \quad (1.86)$$

for some functions a, q, m^2 linear in their arguments. The indices j, j' are understood to be summed over, and the infinitesimal imaginary phase $i\eta$ specifies the position of the poles relative to the integration path. While UV divergences are simply related to the overall $\ell^2 \to \infty$ limit of the integral, IR singularities require specific configurations of the denominator, where the integration path cannot be deformed away from poles. Specifically, the integrand must either have a pole at the endpoint of some integration path (if the latter is an open interval), or a pair of poles pinching the path at some value $\ell_j^2 = c^2(p_i, k_{j'}, x_k) - i\eta$. These requirements are formalized by *Landau equations*, which although fully general, are a rather cumbersome way to tackle the problem.

A much more intuitive picture was given by Coleman and Norton [37], that mapped the solutions of Landau equation to graph identities. They essentially state: given a conjugate Feynman diagram in position space, an IR singularity occurs when each line either is on shell, or connects two points with zero space-time separation (fig. 1.5). This formalizes the physical intuition that on-shell states dominate the path integral, giving the largest contribution to physical observables. Off-shell particles are still allowed, but they are effectively seen as a single, large-momentum dot. Let me note that this picture already suggests an effective field theory description, with low-energy particles propagating and high-energy physics collapsed to an effective vertex.

The Coleman-Norton picture allows one to identify the most general graph affected by IR singularities: for a $1 \to N$ QCD process, this involves a bunch
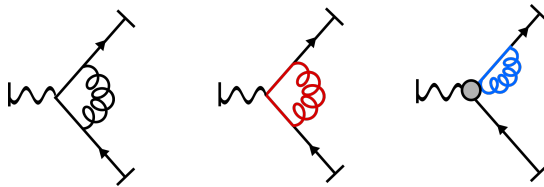
Figure 1.5 Coleman-Norton picture in an example graph. Lines and vertices should be thought of in Minkowski space rather than momentum space. IR singularities occur when each line is on shell (red, blue) or collapses to a point (grey dot). The picture does non exhausts the possible configurations.

of off-shell interactions close to the innermost vertex, after which a number of on-shell emissions recombine into the N-particle final state. To understand what configurations actually diverge and identify soft and collinear particles, the following step is introducing *infrared power counting*, which I now discuss.

Formally, one parametrizes each singular surface in the multi-dimensional loop momentum space with a set of *intrinsic coordinates* $\{k_a\}$. The remaining integration variables $\{n_b\} = \{\ell_j\} - \{k_a\}$ are called *normal coordinates*, and vanish at the singular surface. To study small perturbations around the singular configuration, one introduces a power counting parameter λ and rescales each normal coordinate as

$$n_b \to \lambda^{\omega_b} n_b \,, \tag{1.87}$$

for some power ω_b to be determined. The eikonal approximation consists in dropping subleading powers of λ,

$$\left(\prod_a \int \frac{\mathrm{d}^d k_a}{(2\pi)^d}\right)\left(\prod_b \int \frac{\mathrm{d}^d n_b \, \lambda^{\omega_b d}}{(2\pi)^d}\right) \frac{\mathcal{N}(p_i, k_a, \lambda^{\omega_b} n_b, x_k)}{\mathcal{D}^\alpha(p_i, k_a, \lambda^{\omega_b} n_b, x_k)} \sim \lambda^{\omega_{\mathcal{G}}} \mathcal{I}\Big[1 + \mathcal{O}(\lambda)\Big] \,, \tag{1.88}$$

where the resulting integral has homogeneous scaling in λ and $\omega_{\mathcal{G}}$ is called IR degree of divergence, in analogy with the UV counterpart of eq. (1.22).

Practically, finding normal coordinates reduces to identifying independent loop momentum components that vanish when intermediate lines go on shell. Because of collinear configurations, this is best done in *lightcone coordinates*: for each direction i, one introduces two lightlike vectors $n_i, \overline{n}_i$, representing parallel and antiparallel propagation relative to i. Each momentum is thus decomposed along the two vectors and the plane perpendicular to them. I will use the convention $n \cdot \overline{n} = 2$, with further conventions for lightcone vectors collected in appx. A.1. Given such decomposition, momentum conservation

and the requirement that intermediate states are on shell when $\lambda \to 0$ force the propagator momenta to scale as either

$$p_{\mathrm{c}} \equiv (p_+, p_-, \vec{p}_\perp) \sim Q(\lambda^2, 1, \lambda), \quad \text{or} \quad p_{\mathrm{us}} \sim Q(\lambda^2, \lambda^2, \lambda^2), \qquad (1.89)$$

where Q is the hard momentum scale (for definiteness, the center of mass energy in e^+e^- collisions). Eq. (1.89) defines soft and collinear scaling; I use the subscript *us* for consistency with the standard SCET notation, where radiation with such scaling is called *ultrasoft*.

Off-shell hard lines simply scale as $Q(1, 1, 1)$. Each of the N collinear directions has its own scaling, but the sum of a soft and a collinear momentum is still collinear, thus soft radiation is allowed to communicate between different collinear sectors without spoiling the power counting. This leads to the picture in fig. 1.6.
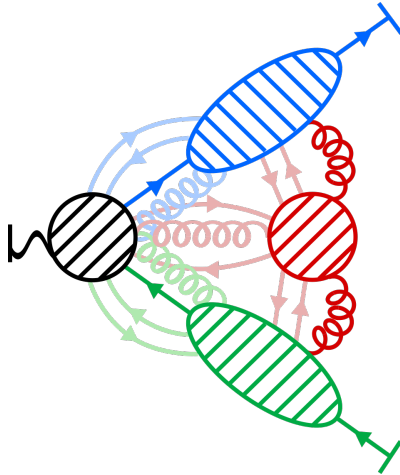

Figure 1.6 Generic graph resulting from applying power counting to the Coleman-Norton picture. At leading power only one collinear line connects the hard blob (black) to each collinear sector (blue, green) while soft radiation (red) can communicate between collinear sectors with an arbitrary number of gluon emissions. Light colors denote connections that do not contribute at leading power.

Equipped with IR power counting, one can systematically tell which singularities contribute at a definite order in λ, and in particular which diagrams are logarithmically divergent, $\lambda = 0$. The degree of divergence of each graph is determined as a function of the number of lines between the hard, soft and collinear subgraphs. Phrasing the scaling of a diagram in terms of connections between the various subgraphs is very convenient, because it gives relations that hold regardless of the number of loops. Furthermore, it is a fundamental

step in view of factorization, as shows that one needs to worry about a finite number of connections between the elements we wish to separate. This operation is done analogously to the UV case by counting how many powers of λ each line or vertex brings,

$$\longrightarrow \propto \frac{\not p_c}{p_c^2} \sim \lambda^{-2}, \qquad \text{\color{red}00000} \propto \frac{1}{p_s^2} \sim \lambda^{-4}, \qquad \ldots \qquad (1.90)$$

and simplifying the overall sum by means of graph identities. In ref. [38] I did this for QED. There I found

$$\omega_{\mathcal{G}} = 2S_\gamma + 3S_f + \sum_{i=1}^{N} \left(s_f^i + C_f^i + C_\gamma^i - 1 \right), \qquad (1.91)$$

where S_κ, C_κ^i and s_κ^i are respectively the number of soft-to-hard, collinear-to-hard and soft-to-collinear connections, κ is either fermion or photon, and i labels the collinear sector. Since every collinear subgraph (or *jet*) has at least one connection to the hard function, the lower bound for eq. (1.91) is zero, which corresponds to configurations with no lines connecting soft and hard subdiagrams, only gauge bosons between the soft subdiagram and jets, and no further link from jets to the hard subgraph. These are the IR divergent, *leading power* configurations, the only ones retained by eikonal approximation.

Among the scaling relations of the kind (1.90) one is rather subtle,

$$\longrightarrow\hspace{-1em}\text{\color{red}}\sim \lambda^0, \qquad \longrightarrow\hspace{-1em}\text{\color{red}}\sim \lambda. \qquad (1.92)$$

If k is the gauge boson momentum and p the fermion one, the Dirac structure corresponding to these configurations is

$$(\not p + \not k)\gamma^\mu \not p = -(\not p + \not k)\not p \gamma^\mu - 2(p+k)^\mu \not p. \qquad (1.93)$$

The first factor on the right hand side is order λ, because the leading term $\frac{1}{4}p_-^2 \not n \not n = 0$; the second factor is order λ^0, and for soft emissions from collinear lines this determines the overall scaling. For collinear emissions from collinear lines, one can show that the latter structure vanishes upon summing over physical, transverse polarizations, thus explaining the scaling $\sim \lambda$. This is an important step to derive eq. (1.91), which then is evident on a diagram-by-diagram basis only when working in a gauge that explicitly suppresses unphysical polarizations, like axial gauge. In Feynman gauge, single diagrams would exhibit a different scaling, but when summing over a gauge-invariant set, suitable cancellations would result in an extra suppression. Although in

deriving eq. (1.91) we had QED in mind, the same leading-order picture applies to QCD. A practical consequence is that fig. 1.6 in Feynman gauge allows for extra gluon connections between jets and hard subdiagrams, as long as they carry longitudinal polarization. The effect of these extra emissions is described by a *Wilson line* in the respective collinear direction,

$$W_n = P \exp\left[-ig_s \int_0^\infty \mathrm{d}s\, \overline{n} \cdot A(\overline{n}s) \right], \qquad (1.94)$$

where the path ordering operator P arranges the group generators to preserve causality. Physically, Wilson lines describe a cluster of collimated radiation from the point of view of an IR probe: the latter cannot resolve single soft emissions and collinear splittings, but knows only about the direction of the energetic parton that originated them. As the discussion above suggests, Wilson lines are essential to enforce gauge invariance in the theory. I will try to elucidate this in sec. 1.3.4 from the SCET perspective.

The fundamental result of factorization theorems is that the soft and collinear subgraphs in fig. 1.6 can be computed in fact as separate matrix elements,

$$S(\hat{p}_i \cdot \hat{p}_j) = \langle 0| \prod_{i=1}^N W_{\hat{p}_i} |0\rangle, \qquad J_i(p_i \cdot n_i, \mu^2) = \langle 0| W_{n_i} \psi(0) |p_i\rangle, \qquad (1.95)$$

and the amplitude in the eikonal limit reduces to their product,

$$\mathcal{M}(p_i \cdot p_j, \mu^2) = H(Q^2, p_i \cdot n_i, \mu^2) S(\hat{p}_i \cdot \hat{p}_j) \prod_{i=1}^N \frac{J_i(p_i \cdot n_i, \mu^2)}{J_{Si}(\hat{p}_i \cdot n_i)}. \qquad (1.96)$$

The jet functions J describe collinear radiation[7], and their soft limit J_S need to be subtracted to avoid double-counting the overlap between soft and collinear emissions. In SCET language, the same concept is referred to as *zero-bin subtraction* [39]. The directions $\hat{p}_i$ are determined by the external momenta, while the reference vectors n_i are unphysical and their dependence must ultimately cancel. In sec. 1.3.4, I will describe this through *reparametrization invariance*. The hard function H depends on the specific process, but since it lives at the hard scale Q, it is guaranteed to be calculable in perturbation theory.

Sketching a diagrammatic proof of factorization theorems is largely beyond the scope of this thesis, but to get a little flavor one can go back to the radiative

---

[7]To avoid any confusion, let me note that the word *jet function* is used here with a different meaning than in the rest of the thesis. In ch. 2, jets will describe sprays of particles within a definite angular distance, built with a specific jet algorithm. Here, I use "jet function" as a synonym "collinear function".

amplitude in eq. (1.55) and notice that in the soft limit the rightmost spin structure simplifies as

$$\bar{u}(p)t_a\gamma^\mu v(\bar{p})\left[\frac{\hat{p}\cdot\epsilon}{\hat{p}\cdot k} - \frac{\hat{\bar{p}}\cdot\epsilon}{\hat{\bar{p}}\cdot k}\right]. \tag{1.97}$$

The factor in brackets is universal, is independent of the spin of the fermion, and knows about the kinematics only through the directions $\hat{p}, \hat{\bar{p}}$. The emission of a soft gluon factors with respect to the $q\bar{q}$ pair production, which has the same spin structure as the tree-level cross section.

The factorization in eq. (1.96) is one of the greatest theoretical achievements of QCD, and in the following I will further comment on its importance. To begin with, it trades one complicated object for a bunch of simpler ones, making calculations easier. The universal ingredients describing IR physics are computed once and for all and reused for different processes by matching them onto different hard functions. Moreover, in the eikonal limit the phase space also factorizes, extending this result to cross sections.

Second, although I considered an inclusive process, factorization applies to a large class of more *exclusive* observables; one just needs to make sure that the measurement also factorizes. This is perhaps where factorization proves itself the most important: in inclusive hadron production, we use the fact that quarks and gluons would eventually shower into some hadron to overcome the impossibility to detect free partons. If instead we measure single hadrons or make protons collide, we cannot rely on this effect and QCD loses its predictive power. In such cases factorization comes to the rescue, because an analog of eq. (1.96) is still valid where the inclusive jet function is replaced by an exclusive counterpart describing hadron production or the extraction of a quark and gluon from a proton. The most common example is given by Parton Distribution Functions and Fragmentation Functions, that will be the subject of sec. 2.2.1. These collinear ingredients are non-perturbative, but still universal: once measured from experiment, they are used in different processes, and the predictive power of perturbative QCD is restored.

Finally, different ingredients in eq. (1.96) depend on the renormalization scale. If physical observables do not, it means that the μ dependence of separate ingredients is related. This observation provides the key for systematically implementing resummation, and the applications presented in the following chapters will illustrate this point.

In this section I tried to make clear that already within QCD systematic tools exist to study its IR limit. Still, it is a natural question whether rather then expanding away subleading powers on a diagram-by-diagram basis, an IR approximation could not be implemented directly in the Lagrangian. If soft and collinear particles approximately behave as separate entities, why not

encode this separation at the deepest level of the theory? It turns out that effective field theories are an ideal language to do so, and in the next section I will elaborate on this topic.

1.3 Soft Collinear Effective Theory

1.3.1 Effective Field Theories

Effective Field Theories (EFTs) are a powerful and systematic tool to model physical phenomena in terms of a minimal number of degrees of freedom. The main idea is that to make physics at an energy scale Q we do not need to know *in detail* what happens at $\Lambda \gg Q$. In support of this claim, classical mechanics works well for everyday-life systems even if they are made of quantum constituents; atomic physics does not require the details of QED; but rather than adding examples, one can just take it as an EFT working assumption. To be more precise, consider two sets of degrees of freedom

$$\big(\{\phi_i\}, Q\big), \qquad \big(\{\Phi_J\}, \Lambda\big),$$

where Q and Λ denote the order of typical energy scales within the set. EFTs postulate that the effect of the Φ_J's at the scale Q is described by supplementing the Lagrangian with effective interactions

$$C_a(\{\Phi_J\}) \, O_a\big[\phi_i(x)\big],$$

where the *operators O* are functionals of the fields ϕ_i while the *Wilson coefficients C* are dimensionful constants suppressed by powers of the ratio $1/\Lambda$. In practical cases, one may know what the Φ_J are and use this knowledge to fix the Wilson coefficients (top-down EFTs), or ignore their nature and just fit the coefficients to experiment (bottom-up EFTs). However, from the theory perspective the distinction doesn't really matter, because in both cases we want a description where only the ϕ_i's are dynamical fields.

The spirit of an EFT is giving up the pretense of having the ultimate theory of nature in favor of delivering precise predictions through an effective approximate description. In this sense, EFTs are a quite modest approach to physics, and not surprisingly their popularity is reflorishing in a time where particle physics does not foresee specific revolutionary discoveries. Still, they provide a highly valuable tool to make model-independent predictions and systematically implement approximations in the Lagrangian.

Many introductions to EFTs are available in the literature, see for instance [40, 41]. To show a standard example of EFT at work, I will make an excursion to

the electroweak sector of the SM and have a look at the Fermi theory of electroweak interactions. Fermi had in mind the nuclear beta decay $n \rightarrow p + e^- + \overline{\nu}_e$, that corresponds at the fundamental level to a valence down quark converting into an up quark. Since it violates isospin, it must be driven by weak interaction, and in fact in the Standard Model it is mediated at tree level by a W^- boson. However, for illustration purpose it is more convenient to consider instead the muon decay (fig. 1.7 left), because the initial muon is a well-defined state in QFT and its large mass $m_\mu = 105.7$ MeV allows one to neglect in turn the electron mass.
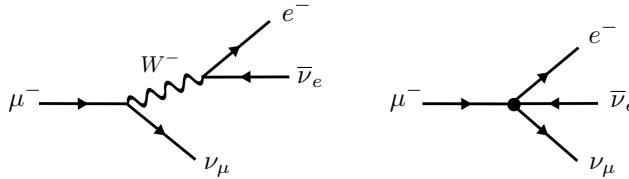

Figure 1.7 Tree-level muon decay diagrams in the SM (left) and in Fermi theory (right), where the heavy W boson is replaced by an effective four-point interaction.

The charged electroweak current responsible for the decay is described in the SM by the interaction term

$$\mathcal{L}_{cc} = -\frac{ig}{2\sqrt{2}} \sum_\ell \left[\overline{\psi}_\ell W\!\!\!\!/^{\,-}(1-\gamma_5)\psi_{\nu_\ell} + \overline{\psi}_{\nu_\ell} W\!\!\!\!/^{\,+}(1-\gamma_5)\psi_\ell \right], \qquad (1.98)$$

where the index ℓ runs over lepton families. The weak coupling parameter $g = e/\sin\vartheta_W$ is related to the electric charge by the weak mixing angle, and the spin structure $\frac{1}{2}(1-\gamma_5)$ selects fermion states of left chirality, enforcing maximal CP violation in the charged sector. The corresponding tree-level amplitude reads

$$M_{\text{EW}} = \frac{ig^2}{8} \frac{g_{\lambda\rho} - \frac{q_\mu q_\lambda}{M_W^2}}{q^2 - M_W^2} \overline{u}(p)\gamma^\lambda(1-\gamma_5)\overline{u}(p_\mu)\,\overline{v}(\overline{p})\gamma^\rho(1-\gamma_5)u(p_e), \qquad (1.99)$$

where p_μ, p_e, p, $\overline{p}$ are the momenta of respectively μ, e, ν_μ and $\overline{\nu}_e$ and $q = p_\mu - p_e$ flows through the W propagator. In the rest frame of the muon $p_\mu = (m_\mu, 0, 0, 0)$, and $\sqrt{p_\mu^2} = m_\mu$ sets the energy available for the process. This is much smaller than $M_W \sim 80$ GeV, so a good approximation is

$$M_{\text{EW}} = \frac{-ig^2}{8M_W^2} \overline{u}(p)\gamma^\lambda(1-\gamma_5)\overline{u}(p_\mu)\,\overline{v}(\overline{p})\gamma_\lambda(1-\gamma_5)u(p_e)\left[1 + \mathcal{O}\!\left(\frac{m_\mu^2}{M_W^2}\right)\right].$$
$$(1.100)$$

After performing the Clifford algebra taking the spin average, this yields

$$\langle|M_{\rm EW}|^2\rangle = \frac{g^4}{32M_W^4}\, p\cdot p_\mu\, \bar{p}\cdot p_e \left[1+\mathcal{O}\!\left(\frac{m_\mu^2}{M_W^2}\right)\right],\tag{1.101}$$

and further integrating over the $1\to 3$ massless phase space and including the flux factor $1/(2m_\mu)$ one gets the decay width

$$\Gamma_\mu = \frac{g^4 m_\mu^5}{6144\pi^3 M_W^4}\left[1+\mathcal{O}\!\left(\frac{m_\mu^2}{M_W^2}\right)\right].\tag{1.102}$$

This tree-level, approximate prediction is already in good agreement with experiment, because the EW coupling constant is small, the electron mass tiny, and neglected W mass power corrections have weight $\sim 10^{-6}$ from the ratio in brackets.

The same prediction was in fact obtained within the Fermi model of weak interactions, more than thirty years before the formulation of the SM. Fermi postulated a four-point contact interaction between leptons and neutrinos, that for our case of interest is described by

$$\mathcal{L}_F = \frac{G_F}{\sqrt{2}}\overline{\psi}_{\nu_\mu}\gamma^\lambda(1-\gamma_5)\psi_\mu\,\overline{\psi}_{\nu_e}\gamma_\lambda(1-\gamma_5)\psi_e + h.c.\,,\tag{1.103}$$

yielding the amplitude

$$M_F = \frac{-iG_F}{\sqrt{2}}\overline{u}(p)\gamma^\lambda(1-\gamma_5)\overline{u}(p_\mu)\,\overline{v}(\bar{p})\gamma_\lambda(1-\gamma_5)u(p_e)\,.\tag{1.104}$$

Carrying on the same calculation again one concludes

$$\Gamma_\mu = \frac{G_F^2\, m_\mu^5}{192\,\pi^3}\tag{1.105}$$

and by looking at eq. (1.103) identifies the Fermi constant,

$$G_F = \frac{g^2}{4\sqrt{2}M_W^2}\,.\tag{1.106}$$

From the point of view of the Standard Model, Fermi theory is an EFT where the weak gauge bosons have been *integrated out*. The interaction Lagrangian in eq. (1.102) consists of an four-fermion effective operator, with G_F its Wilson coefficient. The role of high-energy scale Λ is played by M_W, and the Wilson coefficient (1.106) is suppressed by two powers of the scale. This is inevitable, because the mass dimension $4\cdot\frac{3}{2}=6$ of the operator exceeds by two units

the mass dimension of a Lagrangian. The effective theory works well as long as we consider processes at energies $Q \ll M_W$ and power corrections Q^2/M_W^2 are under control. This happens automatically for the muon decay where $Q = m_\mu$ is fixed, but in a scattering process (e.g. $e\nu \to e\nu$) would depend on $Q = \sqrt{s}$, with the description gradually losing accuracy when approaching the W resonance.

A point to stress is that the Lagrangian (1.102) fails to provide a correct theory of the EW interactions not only because it is disproved by data, but even a priori because it lacks theoretical consistency. To name two major problems, it is not unitary nor renormalizable. Ultimately, the issues come from the coupling constant G_F being dimensionful; in other words, the theory allows for interactions involving too many fields. In the following I will try to clarify this point, focusing on the issue of renormalizability.

It is interesting to look back at the QCD UV superficial degree of divergence of eq. (1.23), $\omega = 4 - \frac{3}{2}E_q - E_b$, and notice that the coefficients of the external lines E_i are exactly the mass dimensions of the respective fields. This means that logarithmically divergent correlators ($\omega = 0$) have mass dimension four. Four is also the mass dimension of the Lagrangian, and in presence of only dimensionless constants, the mass dimension of operators: provided that the Lagrangian contains *all* possible dimension-4 operators compatible with the symmetries of the theory, every logarithmically divergent correlator is therefore guaranteed to match a counterterm. What happens in the case of (1.102)? Instead of eq. (1.23), we would find

$$\omega_{\mathcal{G}} = 4 + 2V_4 - \frac{3}{2}E_f \,, \tag{1.107}$$

where V_4 is the number of effective four-fermion vertices in the diagram $\mathcal{G}$. Inserting two four-fermion vertices generates logarithmically divergent six-fermion correlators, but the theory lacks six-point interactions to build the corresponding counterterms. We could then try to fix the problem by supplementing the Lagrangian with six-fermion vertices, but this would not suffice[8] if $V_4 = 3$. In brief, as soon as the theory involves just one operator of mass dimension higher than four, we are forced to include in the Lagrangian infinite operators with arbitrarily high dimension. This not only largely complicates the theory, but also destroys its predictive power, because we need infinite measurements to fix all the Lagrangian parameters.

What condemns Fermi theory to fail as ultimate description of nature makes in fact perfect sense according to the logic of EFTs. In general, effective theories

---

[8]It would actually make the problem worse, as the power counting formula would get an additional term proportional to V_6.

do allow for operators with arbitrary mass dimension D,

$$\mathcal{L}_{\text{EFT}} = \mathcal{L}_{\text{kin}}[\phi_i] + \sum_{D=4}^{\infty} \mathcal{L}_D[\phi_i], \qquad (1.108)$$

but simply because of dimensional analysis these are suppressed by more and more powers of the scale of high-energy physics,

$$\mathcal{L}_D[\phi_i] = \sum_a \frac{c_a}{\Lambda^{\overline{D}}} O_a[\phi_i], \qquad (1.109)$$

where I introduced the reduced mass dimension $\overline{D} = D - 4$ and redefined the Wilson coefficients $C_a \to \Lambda^{-\overline{D}} c_a$ to make their scaling explicit. Either multiple insertions of operators $\overline{D} > 0$ or single insertions of higher-dimensional operators enhance the suppression by bringing additional powers of $1/\Lambda$ into the game (fig. 1.8). Truncating the series in $1/\Lambda$ at some $\overline{D}$ delivers a perfectly consistent theory, because this causes violation of unitarity, renormalizability, etc. only at order $\overline{D} + 1$. Fermi theory at power $1/M_W^2$ allows for only one four-point vertex, and eq. (1.107) predicts only four-point divergent correlators. This generalizes at every power [42]. Two four-point insertions generate $\mathcal{O}(1/M_W^4)$ corrections, but at this point we should include anyway dimension-8 operators in the Lagrangian, that also contribute the same power.
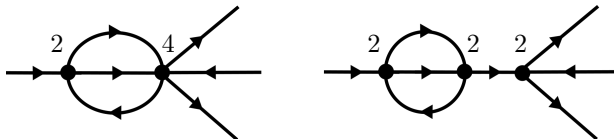

Figure 1.8 Example diagrams at power $1/M_W^6$ in Fermi theory. Both higher-dimensional operators (left) or multiple insertions (right) increase the power. The numbers on vertices are the reduced dimensions of the corresponding operators.

In conclusion, EFTs provide a systematic way to implement an approximate theory in presence of a hierarchy of energies. Whether the high-energy completion of the theory is known or not, one can follow the steps:

1. Determine the degrees of freedom ϕ_i of the theory. These are described by dynamical fields.

2. To reach power accuracy $\overline{D}$, list all the independent D-dimensional operators compatible with the symmetries of the ϕ_i's. The effective Lagrangian is the sum of these operators weigthed by Wilson coefficients.

3. Compute a set of independent order $\overline{D}$ processes within the EFT. Comparison with experiment (bottom-up) or the high-energy completion (top-down) allows one to fix the Wilson coefficients.

This grand plan can be challenging in practice. Finding a basis of independent operators for a given EFT is nontrivial [43, 44]: higher dimension operators involve higher powers of fields and their derivatives, and integration by parts, equations of motion and symmetries of the theory may relate operators in a subtle way. The problem is particularly relevant for bottom-up EFTs like the Standard Model Effective Field Theory, where a basis is known up to dimension 8 but an efficient determination of the operators is still an open problem [45–49]. In addition, the Wilson coefficients could be in general too many to be fixed from a limited number of experiments.

1.3.2 Degrees of freedom in SCET

Soft Collinear Effective Theory applies (or rather, extends) the general ideas of EFTs to describe the IR limit of QCD in this intuitive language. It was first formulated in refs. [50–53] using the *label formalism* and later complemented in refs. [54–56] with the alternative (but equivalent) position-space formulation. Besides dedicated reviews, the subject is also covered by lecture notes, see for instance [57].

The main difference from the example of Fermi theory is the nature of the degrees of freedom of the EFT. The dynamical fields of SCET are the IR degrees of freedom of QCD, while high-energy QCD (as the rest of the SM) is described through effective interactions: one does not integrate out a particle, but high-virtuality dynamical modes. The top-down process of building SCET from QCD requires then the additional step of identifying and isolating such modes. An interesting consequence is that the quantity suppressing higher-dimensional SCET operators is not a mass scale $1/\Lambda$, but the dimensionless IR power counting parameter λ. Moreover, the relevant degrees of freedom, effective operators and power counting parameters vary with the physical process. To describe an event invoving N well-separated directions n_i, SCET introduces N different sets of dynamical collinear modes. The effective operators involve fields along various n_i and depend on the high-energy QCD dynamics through the large momentum ω_i flowing along these directions. Schematically, the Lagrangian reads

$$\mathcal{L}_{\text{SCET}} = \mathcal{L}_{\text{kin}}[\phi_{n_i}] + \sum_a \Big(\prod_j \int d\omega_j \Big) C_a(\{\omega\})\, \mathcal{O}_a[\phi_{n_i}](\{\omega\})\,, \qquad (1.110)$$

with the standard product between Wilson coefficients C and operators $\mathcal{O}$ replaced by a convolution. The precise form of the convolution depends on the

operator and will be discussed in sec. 1.3.4. Rather than a single effective theory of QCD, SCET can be thought of as a collection of EFTs for different QCD processes: each application to phenomenology requires identifying the relevant modes and setting up a dedicated analysis, within the general framework provided by the theory.

Ultimately, what determines the relevant directions and modes is the type and energy of the colliding particles or the measurement imposed on the final state. To illustrate this, I will consider a simplified picture for three QCD processes of main relevance to this thesis (fig. 1.9) and argue for the modes that arise there. These processes involve *jets*, collimated sprays of final-state hadrons. The precise definition will be given in sec. 2.1, but for now one can roughly think of a collection of final-state particles within a cone of aperture R centered in the collision vertex, collectively described as a single spray of radiation moving along the *jet axis*.
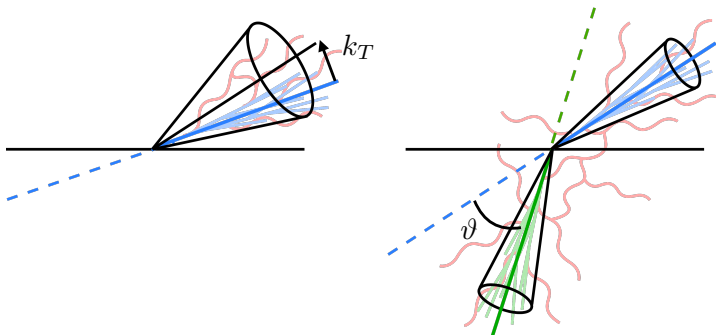

Figure 1.9 Two processes related to the ones considered in this thesis. In-jet fragmentation (left) is described by one collinear mode along the direction of the fragmenting hadron (blue) and – with a standard jet definition – soft radiation (red). Dijet production (right) involves one collinear mode along each of the two jets, and soft modes that communicate between the two jets: measuring thrust or rather the relative angle of the jet pair changes the relative scaling of soft and collinear modes.

Consider first *fragmentation*, the process of hadron production from a high-energy quark or gluon, and imagine measuring the transverse momentum k_T between the hadron and the hard particle producing it. I will take the relative transverse momentum to be much larger than the hadronization scale, $k_T \sim \omega \gg \Lambda_{\text{QCD}}$, and roughly the same size as the energy of the parton ω, since we want the perturbative description to be valid. Of course one cannot directly measure k_T by detecting the initiating parton, but we can reconstruct a jet and use the direction of the jet as a proxy for the direction of the parton (I

will do this explicitly in ch. 3). There is only one relevant direction in the problem, the one of the hadron relative to the parton/jet. To describe low-energy fluctuations induced by IR QCD dynamics around this direction, SCET introduces the collinear mode

$$p_{\mathrm{c}} = (p_+, p_-, p_\perp) \sim \omega(\lambda^2, 1, \lambda)\,, \qquad \lambda = \frac{\Lambda_{\mathrm{QCD}}}{\omega}\,, \qquad (1.111)$$

where the lightcone decomposition is along the direction of the parton/jet. Here I defined the power counting parameter λ with respect to ω, but I could have used k_T as well, as it is only indicative of the parametric size of the scaling. One can argue for eq. (1.111) as follows: in the rest frame of the hadron, fluctuations are isotropic and of the typical size of the hadronization scale, $p \sim (\Lambda_{\mathrm{QCD}}, \Lambda_{\mathrm{QCD}}, \Lambda_{\mathrm{QCD}})$. However, since the initiating parton carries large energy, in the frame of the collision the hadron will be highly boosted along the direction of parton, $\sim (0, \omega, 0_\perp)$. In lightcone coordinates, a boost with rapidity y reads $p_\pm \to p_\pm e^{\mp y}$, hence eq. (1.111).

On the other hand, we know that QCD has also IR divergences corresponding to homogeneous momentum scaling, which advocate for the soft mode

$$p_{\mathrm{s}} \sim \omega(\lambda, \lambda, \lambda)\,, \qquad \lambda = \frac{\Lambda_{\mathrm{QCD}}}{\omega}\,. \qquad (1.112)$$

In absence of additional constraints, the scaling with a single power of λ naturally follows from Λ_{QCD} setting the scale for IR physics, and the EFT featuring this hierarchy of modes is referred to as SCET$_{\mathrm{II}}$. Fig. 1.10, left panel, illustrates the corresponding mode picture in the lightcone plane. Soft and collinear modes lie on the same hyperbola, which is a line of constant virtuality λk_T, while the hard mode has virtuality $\omega \sim k_T$; points on the same hyperbola are connected by a boost.

The scaling in eq. (1.112) contrasts with the one of hadron production shown in eq. (1.89) in the diagrammatic language. The difference is due to the number of collinear directions being fixed in that case, as the next example will help clarify.

To show an example of SCET$_{\mathrm{I}}$ scaling, one can take dijet production in e^+e^- collisions, meaning that we consider events where the number of jets is limited to two. There is a natural way to do so, namely considering events where the thrust defined in eq. (1.53) is $T \sim 1$. The natural power-counting parameter is therefore $1 - T$, and SCET introduces the two collinear modes

$$p_{\mathrm{c}}^{(i)} \sim \sqrt{s}\,(\tau^2, 1, \tau)^{(i)}\,, \qquad i \in \{1, 2\}\,, \qquad \tau = 1 - T\,. \qquad (1.113)$$

The two sectors employ in principle a different lightcone decomposition in terms of $(n^{(i)}, \overline{n}^{(i)})$. In practice, since the two directions are back to back up

to power corrections, it suffices to have a single set $(n, \bar{n})$ with one of the jets along the anti-collinear direction,

$$p_{\mathrm{c}} \sim \sqrt{s}\,(\tau^2, 1, \tau)\,, \qquad p_{\bar{\mathrm{c}}} \sim \sqrt{s}\,(1, \tau^2, \tau)\,. \qquad (1.114)$$

This choice exploits reparametrization invariance, the fact that changing reference vectors should not affect the theory up to power corrections. In the leading-power description, the initial $q\bar{q}$ pair produces the dijet and further splittings are not allowed to carry large momentum away from these directions: an additional hard prong would result in a third jet. This forces the soft mode to take the dominant scaling that does not alter the collinear power counting in eq. (1.114),

$$p_{\mathrm{us}} \sim \sqrt{s}\,(\tau^2, \tau^2, \tau^2)\,. \qquad (1.115)$$

To emphasize the different scaling with respect to eq. (1.112), it is common to call this modes *ultrasoft*. The central panel of fig. 1.10 shows the mode picture for this case: ultrasoft and collinear modes lie on different hyperbolae, as they are hierarchically separated in virtuality ($\tau\sqrt{s} \gg \tau^2\sqrt{s}$). This relative scaling defines the SCET$_\mathrm{I}$ regime.
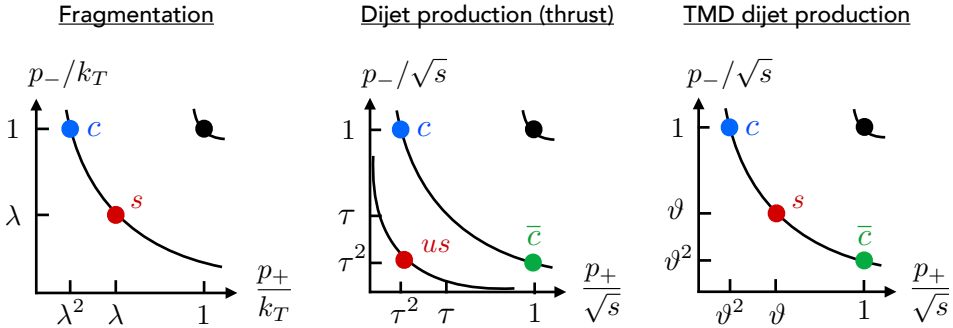

Figure 1.10 Mode picture in the lightcone plane in the three cases discussed in the text. The central configuration defines SCET$_\mathrm{I}$, while the left and right panels show instances of SCET$_\mathrm{II}$. Black dots represent non-dynamical, hard modes.

To emphasize the fundamental role played by the measurement in determining the mode picture, let me consider a third example. Take again dijet production in e^+e^- collisions, but now measuring the relative angle ϑ between the two jets (defined with respect to π, so the dijet pair is back to back if $\vartheta = 0$). This quantity is assumed small for factorization to hold, and determines the power counting of collinear modes,

$$p_{\mathrm{c}} \sim \sqrt{s}\,(\vartheta^2, 1, \vartheta)\,, \qquad p_{\bar{\mathrm{c}}} \sim \sqrt{s}\,(1, \vartheta^2, \vartheta)\,. \qquad (1.116)$$

By assumption, measuring ϑ displaces the jets from the back-to-back configuration of a small but finite amount. Fixing the angle corresponds to measuring the relative transverse momentum of the jets, as the two variables are proportional for small angles. Since transverse momenta are additive, soft radiation contributes to the measurement only if its transverse component has the same size as the collinear one

$$p_{\text{s}} \sim \sqrt{s}\,(\vartheta, \vartheta, \vartheta)\,, \qquad (1.117)$$

so we are back to the SCET_{II} description (fig. 1.10, right). In summary, when measuring thrust the cross section is dominated by back-to-back jets, and the scaling of soft radiation is suppressed not to spoil this configuration. Instead, measuring the angle pins soft radiation to be energetic enough to shift the jets slightly away from the back-to-back limit.

In the examples above, the derivation of the modes was entirely driven by physical intuition, and this is often how such analyses are set up. Since physical intuition is certainly not infallible and modes proliferate in presence of multiple scales, one may desire more robust checks. One possibility is relying on complementary information from the diagrammatic approach; another powerful tool is the *method of regions* [58–60][9]. In addition, Renormalization Group Evolution allows nontrivial consistency checks, since it provides all-order predictions on the scale dependence of the factorization ingredients that can be checked against fixed-order results. Finally, nothing prevents one from trying adding more modes in the analysis, as long as the overlap with existing modes is removed. If a newly-introduced mode overlaps entirely with existing ones, the former does not describe any physics. Throughout this thesis I will assume the validity of the mode picture derived by physical arguments. Consistency under RGE and factorization will provide the framework with robust checks at the perturbative order and resummation accuracy I consider, but I will not attempt at proving the all-order validity of our descriptions.

Before moving to the SCET Lagrangian, let me note that SCET_{I} and SCET_{II} describe the most common physical situations, but are not exhaustive. Extensions exist to account for e.g. Glauber gluons [61, 62] or modes with intermediate virtuality [63]. The phenomenological applications presented here focus on transverse momentum dependence, and can be thought of as SCET_{II} applications.

---

[9]In brief, this technique expands QCD integrands at all orders in ratios of the physical scales, decomposing the integral into contributions from single modes. Misidentifying modes would originate a mismatch between QCD integrals and the sum of the regions.

1.3.3 Building the SCET Lagrangian

Deriving the SCET Lagrangian requires one to define the dynamical fields and determine their mutual interactions, starting from full QCD. This step is not present in the standard EFT construction and has to be done prior to looking for effective operators, which encode instead the interaction of soft and collinear fields with hard QCD interactions and the EW sector of the Standard Model. One needs to

- identify from QCD fields components with definite scaling;

- integrate out hard-scaling, off-shell terms;

- depending on the order in the EFT expansion, expand away subleading terms;

- disentangle large- and small-scaling momentum component through a multipole expansion.

This task is complicated by the fact that the symmetries of the theory are hidden at intermediate stages of the construction. On the other hand, the final result has the advantage of having amplitude factorization explicitly written in the Lagrangian. I will go through this process without presenting calculations in detail, but try to show the main steps and ingredients of the leading-power derivation. Extending the construction beyond leading power and applying it to a variety of processes is a highly active topic, but beyond the scope of the thesis. I will just mention that the framework (both in SCET and diagrammatic approach) is mature enough to produce the first next-to-leading power resummed predictions for QCD [64–67].

It is a common choice in the literature to explicitly derive the SCET_I Lagrangian rather than the SCET_II counterpart, since the construction for ultrasoft scaling is more general. In fact, one can derive SCET_II from further expanding SCET_I: because of the harder scaling of soft radiation, some of the QCD interactions that are integrated out in the former are kept in the latter (but never the opposite). I will describe the SCET_I derivation, but point out differences at intermediate stages. I will focus for brevity on quark-gluon interactions, which still contain most of the complexity of the full analysis.

As first step, one replaces the QCD fields with the sum of their (ultra)soft and collinear counterparts,

$$\psi(x) \to \sum_i \psi_{n_i}(x) + \psi_{\text{us}}(x) + \dots$$

$$A^\mu(x) \to \sum_i A^\mu_{n_i}(x) + A^\mu_{\text{us}}(x) + \dots, \tag{1.118}$$

which affects the covariant derivative as well,

$$D^\mu \to \partial^\mu - ig_s \sum_i A_{n_i}^\mu(x) - ig_s A_{\text{us}}^\mu(x) + \dots . \tag{1.119}$$

The replacement does not involve hard-scaling fields, since these are integrated out and are described by the Wilson coefficients instead. The dots denote subleading corrections that would mix different fields already at this stage. From the point of view of one collinear direction, different collinear sectors appear as hard radiation (the sum of two momenta collinear to different directions has hard scaling) and their mutual interactions are always integrated out, so additional sectors are just replicas. For this reason, from now on, I will restrict the analysis to only one collinear sector, labeled by its reference direction n. The corresponding fermion Lagrangian has the form

$$\mathcal{L}_\psi \;\to\; i\overline{\psi}_{\text{us}}\slashed{D}_{\text{us}}\psi_{\text{us}} \;+\; g_s\overline{\psi}_{\text{us}}\slashed{A}_n\psi_{\text{us}} \;+\; i\overline{\psi}_n\slashed{D}\,\psi_n \;+\; i\overline{\psi}_{\text{us}}\slashed{D}\,\psi_n \;+\; i\overline{\psi}_n\slashed{D}\,\psi_{\text{us}} , \tag{1.120}$$

where the ultrasoft covariant derivative is

$$D_{\text{us}}^\mu = \partial^\mu - ig_s A_{\text{us}}^\mu . \tag{1.121}$$

The way terms in eq. (1.120) are organized looks arbitrary at this stage, but will be justified by the manipulations that I will introduce shortly.
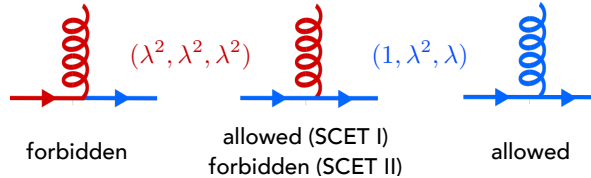

Figure 1.11 Examples of quark-gluon vertices involving different combinations of (ultra)soft (red) or collinear (blue) fields. Configurations where momentum conservation forces one of the lines off shell are integrated out from the Lagrangian.

To begin with, many interactions in eq. (1.120) are explicitly incompatible with power counting, namely momentum conservation at vertices forces one of the lines to be off shell. Fig. 1.11 shows examples for the quark-gluon vertex, but this is a kinematical property that applies regardless of the nature of fields. Off-shell configurations are safely integrated out the SCET Lagrangian; this allows us to drop from eq. (1.120) every term that contains one and only one collinear field, as its large momentum component is unmatched at the vertex,

$$\mathcal{L}_\psi \to i\overline{\psi}_{\text{us}}\slashed{D}_{\text{us}}\psi_{\text{us}} + i\overline{\psi}_n\slashed{D}\,\psi_n + i\overline{\psi}_{\text{us}}\slashed{D}_n\psi_n + i\overline{\psi}_n\slashed{D}_n\,\psi_{\text{us}} , \tag{1.122}$$

where

$$D_n^\mu = \partial^\mu - ig_s A_n^\mu \,. \tag{1.123}$$

In SCET_{II} we can also drop interactions that contain one and only one soft field, because its $+$ component spoils collinear power counting. An interesting consequence is that in this regime only two terms survive,

$$\mathcal{L}_\psi^{\text{II}} \to i\overline{\psi}_{\text{s}} \slashed{D}_{\text{s}} \psi_{\text{s}} + i\overline{\psi}_n \slashed{D}_n \psi_n \ : \tag{1.124}$$

at least in the fermion sector, SCET_{II} exhibits soft-collinear factorization even at this preliminary stage!

The following step is assigning a scaling to fields, which allows to tell leading from subleading interactions. This is straightforward for bosons, and can be argued by looking at the QCD propagator in a generic Feynman gauge,

$$\int \mathrm{d}^4 x \, e^{ip\cdot x} \langle 0|A^\mu(x)A^\nu(0)|0\rangle = \frac{i}{p^2}\Big[g^{\mu\nu} - (1-\xi)\frac{p^\mu p^\nu}{p^2}\Big] \,, \tag{1.125}$$

and comparing the two sides of the equations in the ultrasoft and collinear limits. For instance, the collinear measure scales as λ^{-4}, collinear squared momentum as λ^2, so we conclude $A_n^+ A_n^- \sim A_n^- A_n^+ \sim A_{n,\perp}^2 \sim \lambda^2$. This reasoning shows that gluon fields take component by component the same scaling of the corresponding momenta,

$$A_{\text{us}} \sim (\lambda^2, \lambda^2, \lambda^2)\,, \quad A_n \sim (\lambda^2, 1, \lambda)\,, \quad A_{\text{s}} \sim (\lambda, \lambda, \lambda)\,, \tag{1.126}$$

consistent with the fact that covariant derivatives should be homogeneous.

Power counting follows the same logic for (ultra)soft fermions, but is less immediate for collinear ones, as different spin components can in principle scale differently depending on their orientation with respect to the reference vector. One introduces the operators

$$P_n = \frac{\slashed{n}\slashed{\overline{n}}}{4}\,, \qquad P_{\overline{n}} = \frac{\slashed{\overline{n}}\slashed{n}}{4}\,, \tag{1.127}$$

which being idempotent and summing up to unity provide a projection onto two complementary spin subspaces. Since the Dirac equation in lightcone components reads

$$\big(\slashed{n}p_- + \slashed{\overline{n}}p_+ + \slashed{p}_\perp\big)u(p) = 0\,, \tag{1.128}$$

it follows from collinear scaling that $\slashed{n}u(p_n) \sim \lambda$ while $\slashed{\overline{n}}u(p_n) \sim 1$. This means from the definition 1.127 that P_n selects the leading spin components

over external spinors, while $P_{\overline{n}}$ projects them out. One thus defines[10]

$$\hat{\xi}_n(x) = P_n \, \psi(x) \,, \quad \varphi_{\overline{n}}(x) = P_{\overline{n}} \, \psi(x) \,, \tag{1.129}$$

so that

$$\psi_n(x) = \hat{\xi}_n(x) + \varphi_{\overline{n}}(x) \,, \tag{1.130}$$

where the second field carries spin components which are suppressed on external, on-shell states. Analogous to eq. (1.125), it is now possible to determine the scaling for the leading spin component from the collinear expansion of the fermion propagator,

$$\int \mathrm{d}^4 x \, e^{ip \cdot x} \langle 0 | \hat{\xi}_n(x) \overline{\hat{\xi}}_n(0) | 0 \rangle = \frac{i \slashed{p}}{p^2} \sim \frac{i \slashed{n}}{2 n \cdot p + \frac{p_\perp^2}{\overline{n} \cdot p}} \,, \tag{1.131}$$

ultimately concluding

$$\hat{\xi}_n \sim \lambda \,, \qquad \psi_{\mathrm{us}} \sim \lambda^3 \,, \qquad \psi_{\mathrm{s}} \sim \lambda^{\frac{3}{2}} \,. \tag{1.132}$$

Having derived the scalings in eqs. (1.126) and (1.132) one can isolate leading interactions in eq. (1.122). Rather than in the Lagrangian, we actually seek the leading terms in the action

$$S = \int \mathrm{d}^4 x \, \mathcal{L}(x) \,. \tag{1.133}$$

The difference does not matter in standard EFTs, but is relevant in SCET, where coordinates have their own scaling because of the dynamical nature of the degrees of freedom. Ultrasoft and collinear phase space yield respectively λ^{-8} and λ^{-4}; the former compensates for the higher suppression of ultrasoft fields and saves interactions among only such fields. Terms mixing ultrasoft and collinear fields receive the collinear enhancement λ^{-4}, as the sum of collinear and soft momenta has still collinear scaling: this allows for dropping the last two terms in eq. (1.122), which feature ψ_{us} among collinear fields. Besides purely ultrasoft interactions, the interesting term left is

$$\mathcal{L}_n = \overline{\psi}_n \, i \slashed{D} \psi_n = i \overline{\psi}_n \left(\frac{\slashed{\overline{n}}}{2} n \cdot D + \frac{\slashed{n}}{2} \overline{n} \cdot D + \slashed{D}_\perp \right) \psi_n \,, \tag{1.134}$$

where it is now more convenient to expand the covariant derivative in terms of lightcone components, rather than type of field (D still contains both ultrasoft

---

[10]The hat on the leading spin component $\hat{\xi}_n$ is convenient in label formalism to leave the symbol ξ_n free in view of a future transformation.

and collinear gluons). Further employing the spin decomposition of eq. (1.130) we can rewrite this as

$$\mathcal{L}_n = i\left(\bar{\hat{\xi}}_n \frac{\bar{\slashed{n}}}{2} n\cdot D\,\hat{\xi}_n + \overline{\varphi_{\overline{n}}}\, \slashed{D}_\perp \hat{\xi}_n + \bar{\hat{\xi}}_n\, \slashed{D}_\perp \varphi_{\overline{n}} + \overline{\varphi_{\overline{n}}}\, \frac{\slashed{n}}{2}\overline{n}\cdot D\,\varphi_{\overline{n}}\right), \quad (1.135)$$

which is still completely unexpanded. Terms involving the subleading spin component $\varphi_{\overline{n}}$ are not in directly suppressed by power counting, but the equation of motion (1.128) causes the corresponding fields to never appear as external states. Therefore, $\varphi_{\overline{n}}$ does not propagate, but still contributes to the Lagrangian via effective interactions. To integrate it out, one could perform a matching calculation in a QCD process along the lines of the Fermi theory example, but at leading power it suffices to solve the equations of motion

$$\frac{\delta\mathcal{L}_n}{\delta\varphi_{\overline{n}}} - \partial_\mu \frac{\delta\mathcal{L}_n}{\delta(\partial_\mu\varphi_{\overline{n}})} = 0 \qquad (1.136)$$

for the subleading spin component

$$\varphi_{\overline{n}} = \frac{1}{\overline{n}\cdot D}\slashed{D}_\perp \frac{\bar{\slashed{n}}}{2}\hat{\xi}_n\,, \qquad (1.137)$$

and plug the solution back in the Lagrangian,

$$\mathcal{L}_{n\xi} = i\bar{\hat{\xi}}_n\left(n\cdot D + \slashed{D}_\perp \frac{1}{\overline{n}\cdot D}\slashed{D}_\perp\right)\frac{\bar{\slashed{n}}}{2}\,\hat{\xi}_n\,. \qquad (1.138)$$

At this stage of the derivation, the Lagrangian contains only dynamical SCET fields with a definite scaling in position space. As QFT preferentially uses momentum-space Feynman rules, the next step is providing a consistent and general translation of the picture in terms of momenta. To simplify the issue here, consider Fourier transforming the derivative of a collinear field,

$$\int \mathrm{d}^4x\,\partial_\mu\xi_n(x)\,e^{ip\cdot x} = \int \mathrm{d}^4x\,(ip_\mu)\xi_n(x)\,e^{ip\cdot x}\,, \qquad (1.139)$$

and note that this operation reinstates some subleading terms through the small momentum components of the collinear momentum p. It is preferable to set up a formalism where we can separately address small and large momentum components without the need of further expansions. A solution is carrying out a position-space multipole expansion, that would naturally lead to position-space Feynman rules. The alternative is provided by performing a multiple expansion directly in momentum space: this is called *label formalism*, which I'll briefly describe.

The idea, inspired by Heavy Quark Effective Theory [68], is separating momenta into a large-scaling *label* momentum p_ℓ and a *residual* order λ^2 perturbation r around it,

$$p^\mu = p_\ell^\mu + r^\mu, \quad p_\ell \sim Q(0, 1, \lambda), \quad r \sim Q(\lambda^2, \lambda^2, \lambda^2), \qquad (1.140)$$

such that the small component of label momenta is exactly zero. The space $(p_-, p_\perp)$ of label momenta is discretized into a two-dimensional grid, with the physical case retrieved in the continuum limit, while the space of residual momenta is unconstrained (fig. 1.12). The grid spacing in the two directions reflects the power counting of the respective components. We can imagine residual momenta to live in a box centered in the node of the grid, labeled by a pair of indices ℓ; to address a point in momentum space, we first specify the box through p_ℓ, then move within the box by a small amount r. Momentum
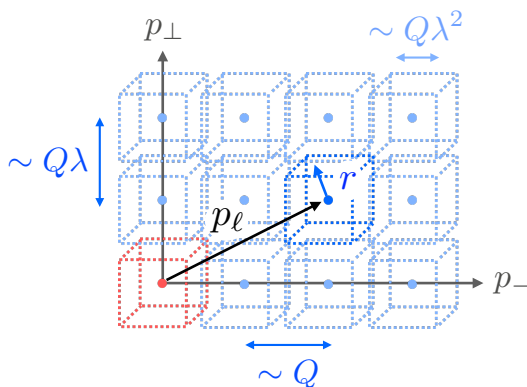

Figure 1.12 Label formalism. Large-scaling momentum directions are discretized, and a four-dimensional box assigned to each node of the grid. Every point in momentum space is specified by a node (label momentum p_ℓ) and a small shift within the corresponding box (residual momentum r).

integration is now performed by summing over boxes and integrating within the box,

$$\int \frac{\mathrm{d}^4 p}{(2\pi)^4} \to \sum_{\ell \neq 0} \int \frac{\mathrm{d}^4 r}{(2\pi)^4}. \qquad (1.141)$$

That one integrates on an infinite domain on each node is a possible source of confusion, but the paradox is solved by taking the $\lambda \to 0$ limit before the continuum limit, so every box shrinks to a point. In other words, we can

think of all the contribution to the integral coming from a neighborhood of the node with size $\sim Q\lambda^2$. The box centered in the grid origin and labeled $\ell = 0$ should not enter the integral over collinear momentum, because if the large components vanish the momentum scaling is in fact ultrasoft.

With this setup, one can separate forward- and backward-propagating modes in the collinear field,

$$\hat{\xi}_n(x) = \hat{\xi}_n^+(x) + \hat{\xi}_n^-(x) \,, \tag{1.142}$$

so that the $+$ term creates particles and the $-$ one annihilates antiparticles, and apply the label/residual decomposition (here represented by a arrow) to their Fourier transformed, momentum space counterparts,

$$\int \mathrm{d}^4x \, e^{\pm ip \cdot x} \, \hat{\xi}_n^\pm(x) \;=\; \tilde{\xi}_n^\pm(p) \to \tilde{\xi}_{n,p_\ell}^\pm(r) \,. \tag{1.143}$$

When transforming back to position space, using eq. (1.141), one can explicitly solve the integral over the residual momentum and get

$$\hat{\xi}_n^\pm(x) = \sum_{\ell \neq 0} e^{\mp ip_\ell \cdot x} \xi_{n,p_\ell}^\pm(x) \tag{1.144}$$

where the position-space fields

$$\xi_{n,p_\ell}^\pm(x) = \int \frac{\mathrm{d}^4r}{(2\pi)^4} e^{\mp ir \cdot x} \tilde{\xi}_{n,p_\ell}^\pm(r) \tag{1.145}$$

still depend explicitly on the large momentum component, while the argument x contains only residual dependence. It is convenient to express the Lagrangian in terms of these collinear fields, rather than the hatted counterparts; this is because one wants the dependence on the hard momentum scale to be non-dynamical. After recombining the $\pm$ terms,

$$\xi_{n,p_\ell}(x) = \xi_{n,p_\ell}^+(x) + \xi_{n,-p_\ell}^-(x) \,, \tag{1.146}$$

one defines the label momentum operator whose action on a field extracts its large component,

$$\mathcal{P}^\mu \, \xi_{n,p_\ell}(x) = p_\ell^\mu \, \xi_{n,p_\ell}(x) \,. \tag{1.147}$$

The relations between the hatted fields and the new ones become

$$\hat{\xi}_n(x) = e^{i\mathcal{P} \cdot x} \xi_n(x) \,, \quad \partial_\mu \hat{\xi}_n(x) = e^{i\mathcal{P} \cdot x} (-i\mathcal{P}_\mu + \partial_\mu) \, \xi_n(x) \,, \tag{1.148}$$

where

$$\xi_n(x) = \sum_{\ell \neq 0} \xi_{n,p_\ell}(x) \,. \tag{1.149}$$

The expressions (1.148) come in handy because they are formally identical in the limit of continuum label momenta.

The same manipulations apply to collinear gluon fields, and after dropping subleading terms, the collinear Lagrangian (1.138) reads in terms of the redefined fields

$$\mathcal{L}_{n\xi}^{(0)} = ie^{-ix\cdot\mathcal{P}} \, \overline{\xi}_n \left(n \cdot D + \slashed{\mathcal{D}}_{n\perp} \frac{1}{\overline{n} \cdot \mathcal{D}_n} \slashed{\mathcal{D}}_{n\perp} \right) \frac{\overline{n}}{2} \, \xi_n \,, \tag{1.150}$$

where the collinear covariant derivative

$$\mathcal{D}_n^\mu = -i\mathcal{P}^\mu - ig_s A_n^\mu \tag{1.151}$$

should not be confused with the object defined in (1.123). Eq. (1.150) is the SCET$_{\rm I}$ leading power collinear fermion Lagrangian. It has homogeneous scaling λ^4 and involves soft–collinear interactions through the full covariant derivative $n \cdot D$. The latter was not altered by rewriting the Lagrangian in terms of ξ_n, since $\mathcal{P} \cdot n = 0$. The SCET$_{\rm II}$ Lagrangian is similar, but as already noted the soft gluon field would not appear there.

For brevity I will not investigate the gluon sector, which undergoes the same steps: after integrating out off shell terms, expanding subleading ones away, and introducing label momenta, the leading power collinear gluon Lagrangian in Feynman-'t Hooft gauge yields

$$\mathcal{L}_{ng}^{(0)} = \frac{1}{2g_s^2} \mathrm{tr}\left(\left[\mathcal{D}^\mu, \mathcal{D}_\mu \right]^2 \right) - i\,\mathrm{tr}\left(\left[\mathcal{D}_{\rm us}^\mu, A_{n\mu} \right]^2 \right) - 2\overline{c}_n \mathrm{tr}\left(\left[\mathcal{D}_{\rm us}^\mu, \left[\mathcal{D}_\mu, c_n \right] \right] \right) \,, \tag{1.152}$$

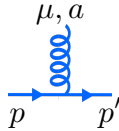where the leading-power covariant derivative and its ultrasoft analogs are

$$\mathcal{D}^\mu = \frac{\overline{n}^\mu}{2} n \cdot D + \frac{n^\mu}{2} \overline{n} \cdot \mathcal{D}_n + \mathcal{D}_{n\perp}^\mu \,,$$

$$\mathcal{D}_{\rm us}^\mu = \frac{\overline{n}^\mu}{2} n \cdot D_{\rm us} - i\frac{n^\mu}{2} \overline{n} \cdot \mathcal{P} - i\mathcal{P}_\perp^\mu \,. \tag{1.153}$$

Besides the collinear quark and gluon terms, the final SCET Lagrangian would contain an ultrasoft term,

$$\mathcal{L}_{\rm SCET}^{(0)} = \mathcal{L}_{n\xi}^{(0)} + \mathcal{L}_{ng}^{(0)} + \mathcal{L}_{\rm us}^{(0)} \,. \tag{1.154}$$

Because of homogeneous scaling of (ultra)soft radiation, the latter is just a copy of the original QCD Lagrangian where every field is replaced by its (ultra)soft counterpart.

From the Lagrangian one can systematically derive SCET Feynman rules. The beauty of this construction is that every vertex and propagator comes with a definite scaling, so there is no need for further expanding. The price we pay is that some of the rules look fairly cumbersome compared to the QCD analog. In the example of a collinear gluon-fermion vertex,

$$= ig_s t^a \left[n^\mu + \frac{\overline{n} \cdot p' \gamma_\perp^\mu \slashed{p}_\perp + \overline{n} \cdot p \, \slashed{p}'_\perp \gamma_\mu^\perp - \slashed{p}'_\perp \slashed{p}_\perp \overline{n}^\mu}{\overline{n} \cdot p \, \overline{n} \cdot p'} \right] \frac{\slashed{\overline{n}}}{2} \, , \quad (1.155)$$

and there is a similar collinear vertex involving two gluons. In practical situations, it is often advantageous to compute SCET observables by replacing collinear fields with the full QCD analog in the SCET matrix elements, which (at least at leading power) is proven to give the same result. This does not mean that SCET was derived for nothing, and I will show some of its useful properties in the next section. In particular, if one accepts the EFT description, then factorization follows almost automatically.

1.3.4 Symmetries, operators and factorization in SCET

One of the main advantages of EFTs is that they are systematic. In the past section I showed how dynamical fields and their mutual interactions are determined, which (for a given scaling of modes) is done once and for all. Equipped with this, one can select a specific process and describe the interactions of soft and collinear degrees of freedom with the rest of the SM via effective operators. In the example of dijet production from e^+e^- collision of sec. 1.3.2, it is evident from tree-level kinematics that there must be some operator of the kind

$$\mathcal{O} \approx \overline{\xi}_n \, \Gamma \, \xi_{\overline{n}} \qquad (1.156)$$

responsible for producing the $q\overline{q}$ pair showering in the dijet. Now given the scalings in eq. (1.126) and eq. (1.132), it is clear that every other combination of fields compatible with basic kinematics[11] would be power suppressed compared to (1.156): this already concludes that at leading power in λ hard interactions are described by tree-level kinematics at every perturbative order!

---

[11]Here we just need that two particles cannot annihilate in a single massless one.

In order to make the search for operators systematic and understand (for instance) how the Γ structure in eq. (1.156) looks like, one needs to study the symmetries of the theory. These make it possible to constrain the form of effective operators and find a complete set for the process of interest. Ultimately, one identifies *gauge-invariant building blocks* that automatically fulfill this task.

Besides spin symmetry, parity and charge conjugation, in which SCET does not differ from full QCD, the symmetries of the former are gauge invariance and reparametrization invariance. Gauge symmetry is of course inherited from QCD, but looks different from the point of view of the dynamical fields: different sectors transform under subsets of the original $SU(3)$. Reparametrization invariance deals instead with the freedom in the choice of reference vectors, related to the Lorentz invariance of the original theory. I will briefly examine the two in turn.

In the EFT, symmetries apply in general order by order in the power-counting expansion. The general gauge transformations in eq. (1.4) mix soft and collinear fields of SCET and dynamical fields with hard interactions that we integrated out, so the full $SU(3)$ cannot be an explicit symmetry of the effective theory. One should instead look for those subsets of transformations that preserve power counting within each sector. In SCET I, these are collinear gauge transformations (one for each collinear sector),

$$
\mathcal{U}_n : \left\{
\begin{array}{ll}
\xi_n(x) & \to U_n(x)\xi_n(x) \\
A_n^\mu(x) & \to U_n(x)\big[A_n^\mu(x) + \frac{i}{g_s}\mathcal{D}_{\text{us}}\big]U_n^\dagger(x) \\
\psi_{\text{us}}(x) & \to \psi_{\text{us}}(x) \\
A_{\text{us}}^\mu(x) & \to A_{\text{us}}^\mu(x)
\end{array}
\right.
\tag{1.157}
$$

and ultrasoft gauge transformations,

$$
\mathcal{U}_{\text{us}} : \left\{
\begin{array}{ll}
\xi_n(x) & \to U_{\text{us}}(x)\xi_n(x) \\
A_n^\mu(x) & \to U_{\text{us}}(x)A_n^\mu(x)U_{\text{us}}^\dagger(x) \\
\psi_{\text{us}}(x) & \to U_{\text{us}}(x)\psi_{\text{us}}(x) \\
A_{\text{us}}^\mu(x) & \to U_{\text{us}}(x)\big[A_{\text{us}}^\mu(x) + \frac{i}{g_s}\mathcal{D}_{\text{us}}\big]U_{\text{us}}^\dagger(x)
\end{array}
\right.
\tag{1.158}
$$

Collinear gauge transformations act essentially as a copy of the full gauge group on the collinear sector, but they do not impact ultrasoft fields, as they would spoil their power counting. In other words, the long-wavelength ultrasoft modes do not resolve the short-distance collinear gauge transformations. For the same reason, transformations in different collinear sectors do not talk to each other. Contrarily, the small components of collinear fields are affected by ultrasoft transformations, consistent with the two fields dialoguing in the collinear Lagrangian. This does not happen with the soft scaling of SCET$_{\text{II}}$.

It is convenient at this point to introduce the collinear Wilson line operator (here in position space),

$$W_n(x) = P \exp\left(ig_s \int_{-\infty}^{0} ds\, \overline{n} \cdot A_n(\overline{n}s + x) \right), \qquad (1.159)$$

which alternatively can be implicitly defined as

$$i\overline{n} \cdot \mathcal{D}_n W_n(x) = 0\,, \quad W_n^\dagger W_n = 1\,, \qquad (1.160)$$

featuring the collinear covariant derivative (1.151). This should be understood in the sense of label formalism: the dependence on the coordinate (x) is obtained by Fourier transforming the residual components, but W_n still depends on the label momentum. The definition (1.160 allows for rewriting the inverse derivative operator appearing in the quark collinear Lagrangian (1.150 as

$$\frac{1}{\overline{n} \cdot \mathcal{D}_n} = -W_n \frac{i}{\overline{n} \cdot \mathcal{P}} W_n^\dagger \qquad (1.161)$$

and the Lagrangian itself as

$$\mathcal{L}_{n\xi}^{(0)} = e^{-ix\cdot\mathcal{P}} \,\overline{\xi}_n \left(in \cdot D + \not{\mathcal{P}}_{n\perp} W_n \frac{1}{\overline{n} \cdot \mathcal{P}} W_n^\dagger \not{\mathcal{P}}_{n\perp} \right) \frac{\overline{n}}{2} \,\xi_n\,. \qquad (1.162)$$

Under SCET gauge transformations,

$$\mathcal{U}_n : W_n(x) \to U_n(x) W_n(x)\,,$$
$$\mathcal{U}_{\text{us}} : W_n(x) \to U_{\text{us}}(x) W_n(x) U_{\text{us}}^\dagger(x)\,. \qquad (1.163)$$

Wilson lines have therefore a fundamental role in enforcing gauge invariance: in the case of eq. (1.162), they compensate for the terms generated by transforming the transverse covariant derivatives. In the EFT, Wilson lines act as gauge proxies for the fields that are integrated out, reinstating the correct factors $U, U^\dagger$ which these would generate in the full theory.

The second important SCET symmetry is reparametrization invariance (RPI). This states that a change of reference basis $(n, \overline{n})$ will not alter the Lagrangian as long as it does not spoil the power counting of fields, consistent with the physical intuition that collinear and anticollinear kinematic regions do not have exact bounds. There are three different classes of RPI transformations (here in infinitesimal form),

$$i : \begin{cases} n^\mu \to n^\mu + \delta_\perp^\mu \\ \overline{n}^\mu \to \overline{n}^\mu \end{cases} \qquad ii : \begin{cases} n^\mu \to n^\mu \\ \overline{n}^\mu \to \overline{n}^\mu + \epsilon_\perp^\mu \end{cases} \qquad iii : \begin{cases} n^\mu \to (1+\alpha)n^\mu \\ \overline{n}^\mu \to (1-\alpha)\overline{n}^\mu \end{cases}$$
$$(1.164)$$

depending on the parameters $\delta_\perp$, $\epsilon_\perp$ and α. The $\perp$ subscript specifies that only the two perpendicular components of these vectors are nonzero, $\delta_\perp \cdot n = \delta_\perp \cdot \overline{n} = 0$ (and similarly for ϵ), so the group of RPI is parametrized by five real numbers. The idea is that the arbitrary choice of reference direction broke down the explicit Lorentz invariance of the theory, and RPI reinstates the missing degrees of symmetry. The request that eq. (1.164) does not alter the scaling of SCET fields fixes the scalings

$$\delta_\perp \sim \lambda, \quad \epsilon_\perp \sim \lambda^0, \quad \alpha \sim \lambda^0. \tag{1.165}$$

The first two transformations change the direction of the reference vectors in the transverse lightcone plane. The scaling of the shift in n is such to preserve the scaling of label momenta. The third transformation combines the first two effects with a boost along the lightcone direction; in particular, it reduces to a boost with the standard choice of back-to-back reference vectors. Transformations i and ii also alter momenta, affecting collinear fields and Wilson lines through their dependence on the label momentum,

$$i : \begin{cases} \xi_n & \to (1 + \frac{1}{4}\slashed{\delta}_\perp \slashed{\overline{n}})\xi_n \\ W_n & \to W_n \end{cases} \qquad ii : \begin{cases} \xi_n & \to (1 + \frac{1}{2}\slashed{\epsilon}_\perp \frac{1}{\overline{n}\cdot\mathcal{D}}\slashed{\mathcal{P}}_{n\perp})\xi_n \\ W_n & \to (1 - \frac{1}{\overline{n}\cdot\mathcal{D}}\epsilon_\perp \cdot \mathcal{D}_{n\perp})W_n \end{cases} \tag{1.166}$$

Combining gauge and Lorentz symmetries and RPI makes it possible to constrain the general form of the operators that enter the SCET Lagrangian. In particular, one can prove at every order in λ [52] that collinear fields enter SCET operators only through the combinations

$$\chi_n = W_n^\dagger \xi_n, \qquad \mathcal{B}_{n\perp}^\mu = \frac{1}{g_s}\left(\frac{1}{\overline{n}\cdot\mathcal{P}}W_n^\dagger\left[\mathcal{D}_{n\perp}^\mu, \overline{n}\cdot\mathcal{D}_n\right]W_n\right). \tag{1.167}$$

These are sometimes referred to as *quark jet* and *gluon jet* fields or simply as the collinear SCET fields. They can be thought of as an improved version of the Lagrangian fields that are automatically gauge invariant. Together with the perpendicular component of the label operator $\mathcal{P}_{n\perp}^\mu$, they can be assembled into every operator in the collinear sector. In fact (without including weak corrections) the correct expression for the leading order dijet operator (1.156) reads

$$\overline{\chi}_{n_1}\gamma^\mu \chi_{n_2}, \tag{1.168}$$

where I kept the two collinear directions generic (rather than fixing $n_1 \equiv \overline{n}_2 \equiv n$), and the current must be vector because it matches to an electromagnetic vertex.

As last topic of this section, I will describe how factorization appears in SCET language. In the EFT, the separation of ultrasoft and collinear modes looks quite different from the factorization of hard modes from IR. This is not surprising, since this first property involves an interplay of dynamical fields, while the second one concerns the non-dynamical fields through the Wilson coefficients of effective operators.

The key observation to show soft–collinear factorization is that soft and collinear SCET fields communicate only via covariant derivative terms of the kind $n \cdot D$ in the collinear sector, and such terms can be rephrased in terms of Wilson lines. The trick is then reabsorbing the Wilson lines in a redefinition of the collinear fields. In analogy with (1.159) one defines *(ultra)soft* Wilson lines,

$$Y_n(x) = P \exp \left(i g_s \int_{-\infty}^{0} \mathrm{d}s \, n \cdot A_{\mathrm{us}}(ns + x) \right), \qquad (1.169)$$

satisfying

$$i n \cdot D \, Y_n(x) = 0, \quad Y_n^\dagger Y_n = 1. \qquad (1.170)$$

The difference from the collinear counterpart is the ultrasoft gluon field in place of the collinear one, and the direction n instead of $\bar{n}$. Note that ultrasoft Wilson lines still know about the collinear direction, and in fact there is a different Y_n for each of the collinear sectors. The n-component of the ultrasoft covariant derivative satisfies the operator equation

$$n \cdot D_{\mathrm{us}} = Y_n \, n \cdot \partial \, Y_n^\dagger, \qquad (1.171)$$

and the expanded leading power collinear fermion Lagrangian in eq. (1.150) yields

$$\mathcal{L}_{n\xi}^{(0)} = e^{-x \cdot \mathcal{P}} \overline{\xi}_n \bigg(i Y_n n \cdot \partial Y_n^\dagger + g_s n \cdot A_n$$
$$+ (\slashed{\mathcal{P}}_\perp + g_s \slashed{A}_{n\perp}) W_n \frac{1}{\bar{n} \cdot \mathcal{P}} W_n^\dagger (\slashed{\mathcal{P}}_\perp + g_s \slashed{A}_{n\perp}) \bigg) \frac{\slashed{\bar{n}}}{2} \xi_n. \quad (1.172)$$

The fact that at this stage the interaction between soft and collinear particles occurs only through ultrasoft Wilson lines is the SCET equivalent of the diagrammatic statement that at leading power an arbitrary number of longitudinal gluons (but nothing else) can connect the soft and collinear subdiagrams in fig. 1.6. Now one can perform the Bauer-Pirjol-Stewart field redefinitions

$$\xi'_{n,p_\ell}(x) = Y_n^\dagger(x) \xi_{n,p_\ell}(x), \qquad A'^\mu_{n,p_\ell}(x) = Y_n^\dagger(x) A^\mu_{n,p_\ell}(x) Y_n(x). \qquad (1.173)$$

These apply for each separate label momentum component, but extend to the fields ξ_n, A_n, as the ultrasoft Wilson lines (1.169) commute with the label momentum operator $\mathcal{P}$. As a consequence, the collinear Wilson lines (1.159) also obey the relation

$$W_n'(x) = Y_n^\dagger(x)W_n(x)Y_n(x)\,. \tag{1.174}$$

Inverting the definitions and expressing the Lagrangian in terms of the new fields, all the ultrasoft Wilson lines cancel out, leaving

$$\mathcal{L}_{n\xi}^{(0)} = e^{-x\cdot\mathcal{P}}\overline{\xi}_n'\left(in\cdot\partial + g_s n\cdot A_n'\right.$$
$$\left. + (\mathcal{P}_\perp + g_s A\!\!\!/\,'_{n\perp})W_n'\frac{1}{\overline{n}\cdot\mathcal{P}}W_n'^\dagger(\mathcal{P}_\perp + g_s A\!\!\!/\,'_{n\perp})\right)\frac{\overline{n}\!\!\!/}{2}\xi_n'\,, \tag{1.175}$$

and soft fields completely decoupled from the collinear Lagrangian. The same result would follow in the gluon sector. To be consistent, effective SCET operators also need to be written in terms of redefined fields, which in general will thus contain ultrasoft Wilson lines. BPS redefinitions replaced the original collinear particles with collinear particles dressed up with longitudinal gluon emissions. These new degrees of freedom only see soft radiation mediated by high energy physics through effective operators.

If soft–collinear factorization is achieved through a field redefinition, hard factorization occurs at this stage automatically: this is the statement that QCD hard dynamics has been integrated out and confined in the Wilson coefficients of effective operators, $C(\overline{n}_i\cdot\mathcal{P})$, depending on the $\mathcal{O}(\lambda^0)$ momentum component flowing along each collinear direction. The delicate point is that some dependence on $\overline{n}_i\cdot\mathcal{P}$ is also present in operators; this can occur explicitly, through the label momentum of the fields, or through the collinear derivatives $\overline{n}_i\cdot\mathcal{D}_{n_i}$. Thus in general

$$C(\overline{n}_i\cdot\mathcal{P})O(\overline{n}_i\cdot\mathcal{P}) \tag{1.176}$$

has to be read as the action of C over O, rather than a product. This is somewhat vague, but one can rephrase it in full generality in terms of convolutions. In the example of the dijet operator (1.177) all the dependence on $\mathcal{P}$ is hidden in the fields, and

$$\overline{\chi}_{n_1}\gamma^\mu\chi_{n_2}C(\overline{n}_1\cdot\mathcal{P},\overline{n}_2\cdot\mathcal{P}) =$$
$$\int d\omega_1 d\omega_2\, C(\omega_1,\omega_2)\,\chi_{n_1}\delta(\omega_1 - \overline{n}_1\cdot\mathcal{P}^\dagger)\gamma^\mu\delta(\omega_2 - \overline{n}_2\cdot\mathcal{P})\chi_{n_2}^\dagger\,. \tag{1.177}$$

The first operator is daggered, because it refers to a field $\overline{\chi}$ rather than χ, so the physical momentum flows counter-arrow. In this form, Wilson coefficients are ordinary functions of the large momentum components, and they appear in convolution with differential operators whose large momentum component is fixed by delta functions. The structure of eq. (1.177) is completely general: in presence of N directions one introduces N Dirac functions. Under the assumption that the Wilson coefficients smoothly depend on $\overline{n_i} \cdot \mathcal{P}$, the explicit dependence is converted to ω_i while in presence of collinear derivatives, eq. (1.161) implies

$$f(i\overline{n} \cdot \mathcal{D}) = W_n f(\overline{n} \cdot \mathcal{P}) W_n^\dagger = \int d\omega \, f(\omega) W_n \delta(\omega - \overline{n} \cdot \mathcal{P}) W_n^\dagger. \qquad (1.178)$$

This concludes amplitude factorization. Provided that the phase space and additional measurements over the final state also factorize, this would result in factorized cross sections. The squared Wilson coefficient would yield a hard function

$$|C(\omega_i)|^2 \;\rightarrow\; H(Q^2, \mu^2) \qquad (1.179)$$

to be determined from a QCD matching calculation, while collinear field operators and delta functions would enter jet operators. I will give examples in the following chapters, where factorization of cross sections will be crucial to phenomenological applications.

2

Jets and transverse momentum

Since the Rutherford experiment showed – more than one century ago – the existence of atomic nuclei, collider experiments have established themselves as the preferential way to unveil the nature of fundamental interactions. From the small equipment, easily manageable by a few people, of the early days of particle physics, accelerators evolved into tremendous machines like the Large Hadron Collider, which is by itself a masterpiece of engineering and employs several thousands of physicists just within the four main collaborations AT-LAS, CMS, LHCb and ALICE. Back then, the same people developing a theoretical model were often the ones who physically operated the experimental apparatus. This is almost unthinkable nowadays, when the need for precision pushed experimental and theoretical analyses to unmatched heights of sophistication, sometimes slowing down the dialogue between the two communities.

In parallel to this process, the field has observed a constant expansion of phenomenology. This is the branch of theoretical particle physics that rather than studying the general properties of the existing theories (or their extensions) focuses on improving the predictions for specific observables. Backed by the growing confidence in the predictive power of the Standard Model, many different subfields developed to detailedly study some of its aspects, often evolving their own tools and terminology. Examples within QCD are small-x, heavy-meson, or quark-gluon plasma physics. These communities interact with SCET, benefiting from the effective formulation and providing in turn new testing ground for the theory.

The phenomenological applications presented in this thesis mainly concern the use of alternative jet definitions to study cross sections differential in transverse momentum. Before proceeding in this direction, it is convenient to introduce some of the main objects that will appear later on: this chapter can be thought of as a small phenomenological toolbox to complement the theoretical picture of ch. 1 in view of applications. The first section focuses on jets, sprays of collimated hadrons described as a single object. The large amount of freedom to do so turns into an advantage, as it can be adapted to probe rele-

vant physics in a variety of contexts. The second section deals with Transverse Momentum dependent Distributions (TMDs), generalizations of the Parton Distribution Functions and Fragmentation Functions that carry additional information on the transverse plane relative to direction of motion. Both topics are well integrated with the SCET formalism, and I will describe them from this point of view.

2.1 Jets

2.1.1 Jet algorithms

At the LHC, the high center-of-mass energy implies that a large number of particles is produced per event. The final state of a collision contains a large amount of information, from which one wants to extract the relevant physics. Setting up a description that simultaneously accounts for each and every detected particle is teoretically impossible, but also largely uninteresting, since most of the final-state particles are just byproducts of well-known interactions. An obvious way to overcome the problem is tagging specific particles, selecting events where these have been produced. Event shapes like thrust implement an opposite strategy, ignoring single constituents and focusing on the global properties of the event.

Jets lie between these two extremes, as they aim at describing a bunch of collimated hadrons as a single object. The reason for doing this is precisely given by IR QCD dynamics: energetic quarks and gluons preferentially shower through soft and collinear emissions, so sprays of hadrons are good proxies for single high-energy partons. For instance, detecting two jets in an e^+e^- collision is suggestive of the high-energy reaction $e^+e^- \to q\bar{q}$, while a three-jet event would point in the direction of $e^+e^- \to q\bar{q}g$, with the radiated energetic gluon originating a third prong. The effective description gives a rigorous meaning to these vague qualitative statements, as the identifications are valid up to power corrections described by subleading operators.

Once we decide to describe a collection of hadrons as a single pseudo-particle, we still need to specify the rules; we need a *jet algorithm*. Clearly one disposes of a lot of freedom, since all the information on the particles in a jet is collapsed into one four-vector. First of all, there is no intrinsic angular distance above which particles stop being collimated and start being spread out. This is controlled by the *jet radius R*, which is a free parameter of the analysis and can be roughly thought of as half the maximum angular separation[1] between particles within a jet. Although one has in mind collimated radiation, the jet

---

[1]This is exact only for e^+e^- collisions, while the pp case involves pseudorapidities.

radius does not have to be small: for instance, CMS and ATLAS experiments use for Run2 default values of $R = 0.4$ and $R = 0.7$ [69]. One can also consider hemisphere jets, $R \sim \pi/2$, where every final-state particle is assigned to one of the hemispheres.

Second, one needs a rule to combine particles into the jet. An intuitive way is provided by *cone algorithms*, that identify geometrical cones of radius R and assign to the jet all the particles within the cone. The first jet definition by Sterman and Weinberg [70] belongs to this category. Emissions close to the cone boundary can potentially violate the IR safety condition in eq. (1.52), and one needs to consider only *stable* cones, unaffected by such emissions. Finding all IR safe stable cones and consistently dealing with their overlap is not simple, and was fully achieved only with the modern Seedless Infrared Safe Cone algorithm (SIScone, [71]). An alternative is provided by the eXclusive cone algorithm (Xcone, [72]), based on N-jettiness [73].

Recombination (or *sequential*) algorithms provide a successful alternative. The idea is to define a distance measure between particles, and sequentially merge them, starting from the closest pairs. The limitations of the first recombination algorithm proposed by the JADE collaboration in [74] were overcome by the k_T algorithm [75], that works as follows (fig. 2.1). For a given jet radius
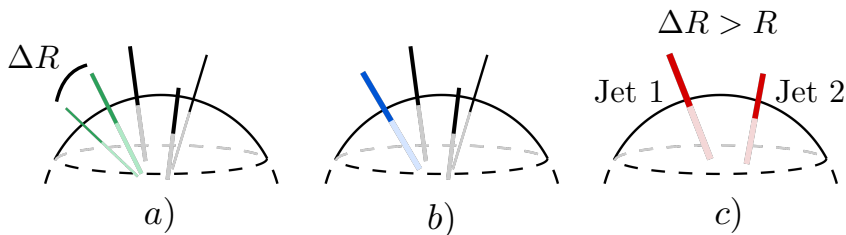

Figure 2.1 Main steps of a k_T-type recombination algorithm. A distance between particles is defined based on their separation in solid angle, ΔR; the algorithm identifies the pair with the smallest distance (*a*), green) and merges them into a single pseudo-particle (*b*), blue). The process continues until the distance between remaining pseudo-particles is larger than the jet radius parameter R (*c*), and such objects (red) are declared jets.

R, define a distance between two particles and a "single-particle distance" as respectively

$$ d_{ij} = \min\left(k_{Ti}^{2p}, k_{Tj}^{2p}\right) \frac{\vartheta_{ij}^2}{R^2}, \quad d_i = k_{Ti}^{2p}, \tag{2.1} $$

where

$$\vartheta_{ij} = \sqrt{(\eta_i - \eta_j)^2 + (\varphi_i - \varphi_j)^2} \tag{2.2}$$

is the geometrical angular distance expressed in pseudorapidity and azimuthal coordinates. The exponent p allows for weighting the distance with the smallest transverse momentum within the pair. The original k_T algorithm sets $p = 1$, meaning that energetic particles will be merged with lower priority; the alternative choices $p = 0$ and $p = -1$ define respectively the Cambridge-Aachen (C/A) [76, 77] and anti-k_T [78] algorithms. These are collectively referred to as k_T-type algorithms. Starting from a list of particles $I = \{i\}$, the algorithm loops over the following steps: as long as I is not empty,

1. determine the minimum distance $d_{\min}$ among the set $\{d_{ij}, d_i\}$;

2. if $d_{\min} = d_i$, declare i a jet; remove it from the list;

3. if instead $d_{\min} = d_{ij}$, merge i and j.

The missing ingredient is of course the definition of *merge*. Standard k_T-type algorithms simply add the four-momenta,

$$\begin{cases} E_{(ij)} & = E_i + E_j \\ \vec{p}_{(ij)} & = \vec{p}_j + \vec{p}_j \,. \end{cases} \tag{2.3}$$

The final direction of the jet is called *jet axis*. A consequence of eq. (2.3) is that, for standard jets, the jet axis balances between the four-momentum of all the constituents, a behavior that will be contrasted by recoil-free jets. Another consequence is that even if all the initial particles are massless, the final jet is not. This is inevitable with $1 \to 2$ recombination schemes, since it is kinematically impossible to simultaneously conserve four-momentum and on-shellness. The jet mass

$$m_J = \sqrt{\sum_{i \in \text{jet}} p_i^2} \tag{2.4}$$

is in fact a measure of how collimated the jet is, because it reduces to zero if all the energetic particles are aligned and grows with their spread.[2] In SCET applications it is usually assumed small compared to the jet energy, for the soft/collinear approximation to hold.

A point to stress is that a priori all IR-safe jet definitions are equally valid. In perturbative QCD, jet algorithms run over final-state quarks and gluons,

---

[2]This is much similar to thrust, but the sum runs over only the particles in the jet.

while in experimental analyses they run over energy deposits in calorimeter cells or reconstructed particles[3]. Different choices of radius and algorithm produce different observables, but this is perfectly consistent as long as theory and experiment use the same definition. In practice, some definitions meet better physical requirements. For instance, the anti-k_T algorithm has the advantage of generating neat cone-shaped jets, making it the experimental choice of preference. In general, the best definition to tackle one problem may not be optimal for another.

   The implementation of jet algorithms in SCET calculations was studied in [80, 81], which also discuss their compatibility with power counting and factorization. Factorization formulae for cross sections involve jet operators of the kind (here for quark-initiated jets)

$$J_n(\omega, \Phi) = \frac{1}{2N_c} \sum_X \mathrm{tr}\left[\langle 0| \frac{\overline{n}}{2} \chi_n(0) \delta_{\mathrm{meas}}(\Phi)|J_{\mathrm{alg}}X\rangle \langle J_{\mathrm{alg}}X|\chi(0)|0\rangle\right], \qquad (2.5)$$

where ω is the large momentum component, Φ collectively denotes dependence on kinematical variables (e.g. transverse momentum of one of the products) arisen from the measurement $\delta_{meas}(\Phi)$, and the sum/average over spin and color introduces the trace and color factor. LO jet production is trivial, as no splitting occurs and each jet consists of only the initial particle, regardless of the jet definition. Starting at NLO, the jet measurement imposes final-space cuts depending on the algorithm. One-loop quark jet functions require computing the SCET diagrams

$$\qquad (2.6)$$

where all the lines are collinear, crosses denote insertions of the gauge invariant jet fields χ_n, and as a result of phase-space integration, diagrams are understood to be cut through the loops (virtual diagrams are scaleless and vanish). The jet algorithm determines whether both particles enter a single jet or they define two separate jets. In terms of the momentum k of the emitted gluon and the large momentum component ω of the initiating quark, the one-loop condition of single jet takes the form

$$\theta\left(\tan\frac{R}{2} - \sqrt{\frac{k_+}{k_-}\frac{\omega}{\omega - k_-}}\right) \qquad (2.7)$$

---

[3]Finally, in event generators, the standard implementation of jet algorithms is provided by Fastjet [79].

for every recombination algorithm, and

$$\theta \left(\tan \frac{R}{2} - \sqrt{\frac{k_+}{k_-}} \right) \tag{2.8}$$

for every cone algorithm. At this level of perturbative accuracy the dependence on the jet definition is still very limited, and in particular all the three k_T-type algorithms yield the same predictions for every observable, compatible with the clustering order being trivial for only two particles. Differences arise starting at two loop, and ch. 4 will provide an example.

2.1.2 Recoil-free jets

Standard recombination algorithms employ a merging prescription, eq. (2.3), that gives equal weight to the momentum of each constituent. This has some interesting side effects for differential measurements, and transverse momentum measurements in particular. In the effective-theory description, the jet contains in general soft and collinear radiation. We can imagine the jet to originate via subsequent splittings from an initial quark or gluon of large momentum component ω, and choose a frame where the light-cone momentum of this initial particle reads $(0, \omega, 0_\perp)$. By construction, the transverse momentum of the jet in this frame will be zero, resulting from balancing soft and collinear transverse momentum within the jet:

$$k_{\perp s}^\mu + k_{\perp c}^\mu = 0 \,. \tag{2.9}$$

If we assume the SCET$_{\text{II}}$ picture, where soft radiation scales $(\lambda, \lambda, \lambda)$, soft and collinear transverse momenta are parametrically of the same size and the transverse direction of the standard jet axis is affected by soft radiation. This is a source of contamination, because soft radiation communicates between all the collinear sectors of the event, making each jet sensitive to other jets and the initial state of the collision. In proton-proton collisions, it introduces a sensitivity to underlying event and pileup, that experimentally causes the jet picture to be blurred. Theoretically, soft radiation inside the jet can complicate factorization due for instance to to non-global logarithms [82].[4]

The problem discussed above motivated the search for alternative jet definitions. The main solution investigated in this work are *recoil-free* jets, whose direction is by construction insensitive to soft radiation. A precise definition

---

[4]In summary, non-global observables involve arbitrary space cuts, for instance when dividing the space into hemispheres. If the hemispheres are connected via soft radiation, the ratio of the characteristic energy scales of the two will show up in calculations through large logarithms, whose resummation is more involved than standard logarithms.
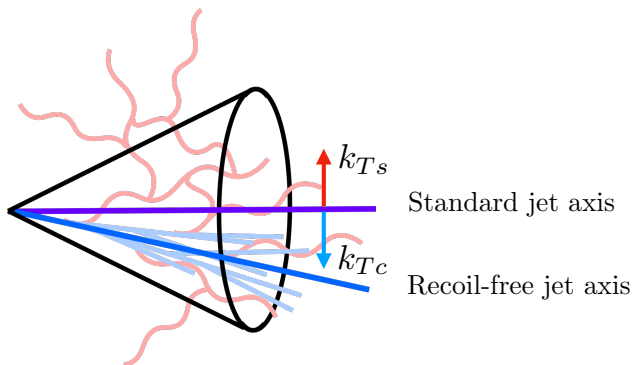
Figure 2.2 By construction, standard jet axes balance the transverse momentum of soft (red) and collinear (blue) radiation within a jet. This makes them sensitive to the other directions in the event. Instead, recoil-free jet axes are unaffected by soft emissions and track the bulk of collinear splittings.

of recoil-free jet J was given in [83], but the idea is that a soft emission with transverse momentum $k_\perp$ should only alter the jet function of an amount which is power suppressed with respect to the jet energy, $\mathcal{O}(k_\perp/E_J)$.

A specific instance of a recoil-free jet is achieved with the *winner-take-all* (WTA) recombination scheme [84]. It employs the same distance measure as standard algorithms, eq. (2.1), but changes the merging prescription from eq. (2.3) to

$$
\left\{
\begin{array}{ll}
E_{(ij)} & = E_i + E_j \\
\vec{p}_{(ij)} & = (E_i + E_j)\big[\vartheta(E_i - E_j)\vec{p}_i/E_i + \vartheta(E_j - E_i)\vec{p}_j/E_j\big] \,,
\end{array}
\right.
\tag{2.10}
$$

meaning that the three-momentum of the pair is aligned with the more energetic particle, and its mass null by definition. In other words, at any recombination step the most energetic particle of the pair "seizes control" of the jet axis, that at the end of the process by construction lies on a particle (the "winner"). Note that the winner is not necessarily the most energetic among the final-state particles, as depending on their relative distance, lower-energy particles could be clustered first, and accumulate enough energy to ultimately prevail. This makes it clear that the clustering ordering is still relevant, and in particular one can still choose between the three definitions of distance given by k_T-type algorithms. In the EFT picture, WTA jets are clearly insensitive to soft radiation, since the latter always loses to collinear. Therefore, measuring transverse momenta with respect to the WTA axis makes the jets recoil-free.

The WTA recombination scheme provides an intuitive way to achieve insensitivity to soft radiation: it is easy to implement and requires a minimal

modification with respect to the standard merging prescription. As I will show in sec. 3.1.3, it has the further advantage of obeying a very simple RGE. Still, it is not the only choice. The first systematic phenomenological analysis using recoil-free jets [85] mainly focused on the *broadening axis* [86]. Broadening is an event shape, like thrust in eq. (1.53), whose definition is

$$B_{\hat{n}} = \frac{\sum_i |\vec{p}_i \times \hat{n}|}{\sum_i |\vec{p}_i|} \, , \tag{2.11}$$

where the unit vector $\hat{n}$ needs to be specified. In fact, the common choice for $\hat{n}$ is the thrust axis, the unit vector $\hat{t}$ that defines thrust. Broadening is by itself a powerful observable, see e.g. [87–89]. If the sum is restricted to the particles in a jet, $i \in$ jet, one obtains *jet* broadening, which is an example of *jet shape*. Jet shapes are a whole class of observables that characterize the energy and momentum distribution within a jet, with several applications in jet substructure (see for instance [90] for a recent review of the latter field). In fact, the jet mass of eq. (2.4) is also a jet shape.

So far, eq. (2.11) defines a jet observable, which in general *is* sensitive to recoil. The idea is now taking as jet axis the direction $\hat{b}$ that minimizes broadening,

$$\hat{b} \, : \, B_{\hat{b}} = \min_{\hat{n} \in S_2} B_{\hat{n}} \, . \tag{2.12}$$

To get some intuition why the axis 2.12 has no recoil, it is instructive to compare jet thrust and jet broadening in the limit of small angles,

$$T_{\hat{n}} \simeq \sum_{i \in \text{jet}} z_i \vartheta_{i,\hat{n}}^2 \, , \qquad B_{\hat{n}} \simeq \sum_{i \in \text{jet}} z_i \vartheta_{i,\hat{n}} \, , \tag{2.13}$$

where $z_i = 2E_i/\omega$ is the energy fraction of the particle i, and $\vartheta_{i,\hat{n}}$ its angle relative to the generic unit vector $\hat{n}$. The specific $\hat{n}$ that minimizes T (B) is the thrust (broadening) axis. In the simple case of two particles, the problem becomes planar and the position of $\hat{n}$ is specified by an angle φ. Letting θ be the angle between the two particles, and setting the angular origin on the particle with energy fraction $1 - z$,

$$T(\varphi) = (1 - z)\varphi^2 + z(\theta - \varphi)^2 \, , \tag{2.14}$$

which is minimized by $\varphi = z\theta$. Instead, the broadening axis simply lies on the most energetic of the pair. In the EFT, if one particle is collinear and the other one soft, the latter will not affect the position of the broadening axis, while the thrust axis would receive a shift which is small ($z \sim \lambda$), but still of the same order as the measured transverse momenta. The above argument is

extended to the case of three or more particles by effectively describing soft and collinear radiation as two pseudoparticles, showing that the broadening axis is recoil-free [85].

Recoil-free axes have several potential advantages. Generally speaking, factorization theorems separate soft and collinear physics in different sectors, and each jet aims at describing one collinear sector. If the jet definition is affected by soft radiation, then the separation is inexact and the factorization structure more involved. In the following chapters, I will show examples where the absence of recoil considerably simplifies the theoretical framework. The WTA axis will be the privileged choice, mainly because of simplicity of implementation, but my analysis in sec. 3.1.4 also shows a theoretical limit of the broadening axis. It has to be noted that at the time of writing no experimental analysis reconstructs WTA jets. One of the main goals of this thesis is showing the potential of this tool, and it is our future responsibility to keep providing solid evidence of their advantages.

2.1.3 Jet grooming

Recoil-free algorithms elegantly address the problem of soft contamination in jets by a careful separation of soft and collinear effects. A more drastic approach is to take a recoil-sensitive jet and "manually" remove soft radiation at a later stage. This class of techniques goes under the name of *jet grooming*, and has proven itself highly successful in a broad range of situations. The are many examples of jet groomers, the most relevant including jet trimming [91], pruning [92], mass drop tagging [93], and modified mass drop tagging [94]. In the following I will focus on *soft drop* [95], a generalization of the latter that has established itself as the standard grooming technique, becoming subject of dedicated experimental measurements, see [96,97] in the case of jet mass.

The main goal achieved by jet grooming is to mitigate the effects of *pileup*, the contamination induced by simultaneous proton-proton collisions. This is an important issue at the LHC, where the high luminosity increases the average number or interactions per bunch crossing. Even when primary vertices are reconstructed and the hard physics isolated, soft radiation produced in secondary collisions will still affect the rest of the event. (See for instance ref. [98] for a review from theoretical perspective). At the same time, grooming significantly reduces the contamination from multi-parton interactions (MPI) and hadronization effects. As the name suggests, MPI are multiple fundamental collisions taking place in the same proton-proton scattering. Although they are formally power corrections, they play an important role in kinematic regions where single-parton scattering is suppressed, and their theoretical description reached a mature stage (see for example [99] for a recent short review). How-

ever, when MPI occur at low energy they provide a source of contamination.

All the phenomenological analyses I will present deal to some extent with hadronization effects, which I briefly turn to commenting on. These are final-state effects due to the conversion of quarks and gluons into hadrons, which (contrarily from pileup and MPI) impact also on e^+e^- collisions. Since every colored particle in a jet ultimately goes into some hadron, to first approximation these corrections are suppressed when summing over all hadron species within the jet. However, they can still interfere with the clustering process and directly affect differential distributions. In the example of a transverse momentum measurement, they will alter the cross section by a typical amount $\mathcal{O}(\Lambda_{\mathrm{QCD}}^2/k_T^2)$ and become therefore relevant at small transverse momenta. An advantage of event generators is that they allow for switching on and off the various effects (pileup, MPI, hadronization) that I just discussed, thus estimating the size of contaminating effects induced by soft radiation. The simulation in fig. 2.3 shows the impact of grooming on hadronization corrections in case of $e^+e^- \to$ dijet, providing important motivation for the application I will discuss in ch. 5. The figure shows hadronic to partonic ratios, namely the number
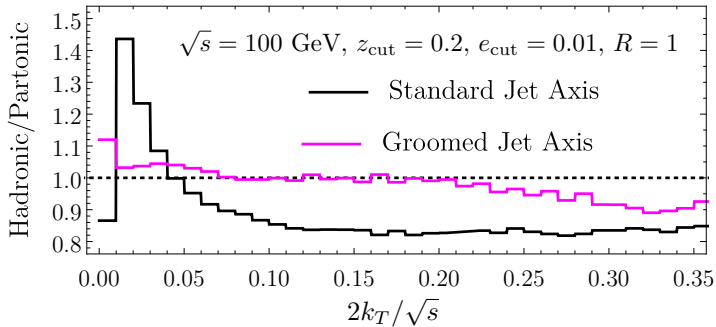

Figure 2.3 Effect of jet grooming on hadronization corrections for dijet production in e^+e^- collisions, simulated with Pythia 8. The soft drop parameter $\beta = 0$, and an upper cut on groomed jet mass $m_J^2 < e_{\mathrm{cut}}s$ is applied. Soft drop dramatically reduces hadronization effects over the whole plotted range in the relative transverse momentum of the dijet, k_T.

of events obtained switching on/off the hadronization model of the event generator, as a function of the transverse momentum of the dijet. I will define the parameters that enter there in a moment, but one can see that applying soft drop (magenta line) drastically reduces the impact of hadronization effects over the whole range in transverse momentum, compared to the counterpart without grooming (black).

The soft-drop procedure works as follows: given all the particles in a jet, one reclusters them using the C/A algorithm ($p = 0$ in eq. (2.1), independent of the original jet definition). Then, the clustering tree is opened up and the clustering history navigated backwards (fig. 2.4, left). At each node, the
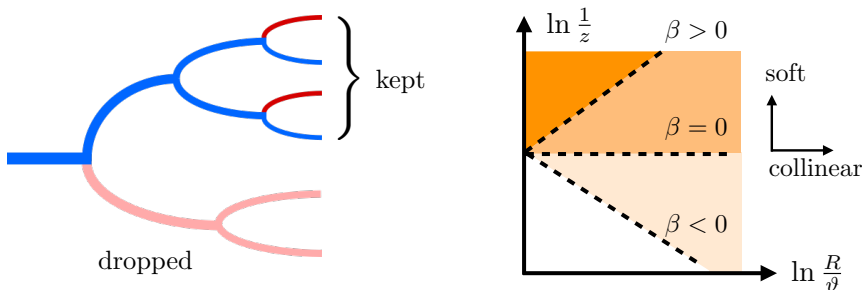

Figure 2.4 Soft drop. The algorithm goes backwards through the jet clustering history (left) testing the soft drop condition at each node. When a branch fails the test, it is dropped (light red) and the algorithm moves to the next node. As soon as one node passes the test, the algorithm stops; further soft splittings (red) are kept. The area corresponding to dropped emissions is displayed on the right (shades of orange) in a $\ln \frac{1}{z} / \ln \frac{1}{\vartheta}$ plane, for different values of the exponent β.

algorithm tests the condition

$$\frac{\min(k_{Ti}, k_{Tj})}{k_{Ti} + k_{Tj}} > z_{\text{cut}} \left(\frac{\vartheta_{ij}}{R}\right)^{\beta}, \tag{2.15}$$

where ϑ_{ij} is the angular distance defined in eq. (2.2), R the jet radius, and z_{cut}, β are soft-drop parameters to be specified. If (2.15) fails, the branch with minimum k_T is dropped from the jet, and the algorithm moves to testing the following node. As soon as one node passes the test, the procedure stops and the remaining jet is declared the groomed jet. The parameter z_{cut} sets a threshold in transverse momentum fraction below which emissions are dropped. As the purpose is eliminating low-energy radiation, it is chosen small, typically around $z_{\text{cut}} \simeq 0.1$. Note that soft drop does not remove *all* the soft radiation, because as soon as a node passes the test, the remaining branches are kept in their entirety, without further testing the condition on subsequent splittings. In particular, since by definition the jet has been reclustered with C/A, the clustering history is entirely based on the angular distance, thus soft drop removes in fact *wide-angle* soft radiation. The exponent β adjusts the threshold with an angular weight, and corresponds to a different level of tolerance when dealing with radiation that is soft *and* collinear (fig. 2.4, right). A positive

β effectively lowers the threshold for small-angle splittings, keeping a larger fraction of soft radiation that is also collinear. Contrarily, a negative β aggressively removes soft radiation even at low angles. In this regime, it is possible that a whole jet is dropped, and soft drop works as a *tagger*, discriminating those events where the jets pass the condition.

The soft drop definition in eq. (2.15) is the default for pp collisions. In case of e^+e^- collisions, one uses instead

$$\frac{\min(E_i, E_j)}{E_i + E_j} > z_{\text{cut}} \left(\sqrt{2} \, \frac{\sin(\vartheta_{ij}/2)}{\sin(R/2)} \right)^{\beta} , \qquad (2.16)$$

testing the condition with energies instead of transverse momenta. In fact, the same modifications occur in the definition of distance in eq. (2.1).[5]

Like for the jet radius R, there is no obvious choice for the soft-drop parameters z_{cut} and β; different values may be advantageous in describing different observables, and every choice is consistent as long as one compares the same value in theory and experiment. Similar to recoil-free jets, soft drop can sometimes simplify the theoretical picture, for example by removing non-global logarithms. However, the additional parameters z_{cut}, β may complicate the factorization picture by leading to new modes. In particular, the assumption $z_{\text{cut}} \ll 1$ introduces a new hierarchy, and the parameter z_{cut} can compete with other small quantities in the problem. Ch. 4 and 5 study the same physical processes with respectively WTA jets and soft drop. The comparison will show that soft drop trades a neat factorization picture for a stronger suppression of soft contamination.

2.2 Transverse Momentum dependent Distributions

2.2.1 Integrated parton distributions

As already remarked, the fundamental degrees of freedom of QCD, quarks and gluons, differ from the physical objects that we handle in experiments. In e^+e^- collisions, this limitation can be overcome by considering inclusive hadron production, as discussed in sec. 1.2.3. Clustering hadrons into jets goes in a similar direction, because the average properties of a jet computed from quarks and gluons well resemble the ones of the hadron counterpart, at least in those kinematical regions where hadronization corrections are under control. However, in

---

[5]It may look disturbing at first that different collisions use different definitions. The reason is that, at the level of the fundamental interaction, the electron-positron pair carries fixed energy, while two colliding quarks (or gluons) inside the proton receive a boost in the longitudinal direction. Transverse momenta and differences in pseudorapidities η are boost invariants, which makes them a privileged choice in this case.

most of the relevant QCD applications following this strategy is not possible. First, in proton-proton or electron-proton colliders one cannot avoid dealing with single initial-state protons. Second, one may want to measure the properties of a specific final-state hadron. In these cases, the problem inevitably involves non-perturbative physics and some notion of factorization is fundamental. The basic factorization ingredients describing hadronic physics are named Parton Distribution Functions (PDFs) and Fragmentation Functions (FFs). PDFs describe the distribution in longitudinal momentum of quarks and gluons inside an initial-state hadron, while FFs describe the longitudinal momentum distribution of quarks and gluons fragmenting into a final-state hadron [100–102]. I will refer to these distributions as *collinear* or *integrated*, in contrast with the more differential Transverse Momentum dependent Distributions (TMDs) to be introduced in the next section. In this thesis, I will always consider unpolarized parton distributions, i.e. averaged over spin, but polarized parton distributions are a very active field.

In factorization theorems, PDFs and FFs replace the jet functions describing collinear physics when the collinear directions are set by proton beams or detected final-state hadrons. For definiteness, consider the example of Deep Inelastic Scattering (fig. 2.5), that will also play an important role in ch. 4 and ch. 5. DIS is one of the most studied processes in particle physics, and the
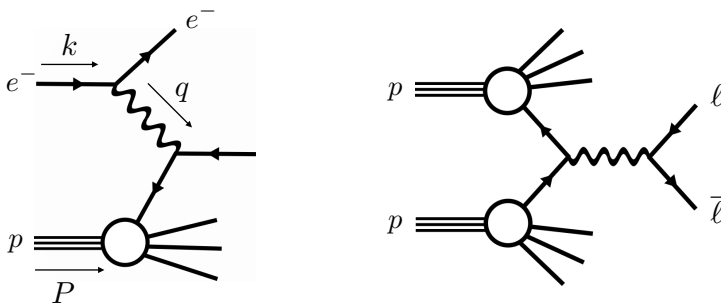

Figure 2.5 Deep Inelastic Scattering (left) is a preferential channel to extract PDFs. As a first approximation (leading power in SCET), the high-energy electron probes a single, free (anti)quark, while the rest of the proton does not interact. Drell-Yan scattering (right) describes lepton pair production from a proton-proton collision. By universality of non-perturbative physics, the same PDFs enter both processes.

preferential channel to extract information on the structure of the proton. *Deep inelastic* refers to the collision energy being sufficiently high for the electron to break the proton apart and probe its internal composition. Labeling momenta as in fig. 2.5, and neglecting the proton mass, the tree-level kinematics is

specified by two of the three dependent variables

$$Q^2 = -q^2, \qquad x = \frac{Q^2}{2P \cdot q}, \qquad y = \frac{P \cdot q}{P \cdot k}, \qquad (2.17)$$

named respectively *virtuality*, *Bjorken x* and *elasticity*.[6] Given the center-of-mass energy $\sqrt{s}$, these are related by

$$s = x\,y\,Q^2. \qquad (2.18)$$

Since the electron-proton collision is asymmetric and the virtuality Q^2 varies event by event, there is no obvious choice of reference frame. In the following I will consider the Breit frame, where by definition the momentum transfer is

$$q = (0, 0, 0, Q), \qquad (2.19)$$

so the scattering electron inverts its three-momentum as a result of the collision. The bottom half of fig. 2.5 is not a QCD Feynman diagram, since perturbative QFT does not provide rules for amplitudes involving protons, but acquires meaning thanks to factorization. Well before the theorization of quarks and asymptotic freedom, Feynman postulated the existence of *partons* as elementary constituents of the proton and assumed that at high energies the electron scatters in fact on a single parton, whose transverse momentum can be neglected. This ansatz motivates the formula

$$\frac{\mathrm{d}\sigma_{ep \to eX}}{\mathrm{d}x\,\mathrm{d}Q^2}(x, Q^2) = \sum_a \int_0^1 \mathrm{d}\xi\, f_{p \to a}(\xi, \mu) \frac{\mathrm{d}\sigma_{ea \to ea}}{\mathrm{d}x\,\mathrm{d}Q^2}(x, Q^2, \xi P, \mu), \qquad (2.20)$$

where the sum a runs in reality over quark and antiquark flavors. It states that the cross section for scattering on a proton is obtained from an incoherent sum of elementary scatterings on partons that carry a fraction ξ of the proton energy, convoluted with an energy fraction distribution $f_{p \to a}$. The latter is the Parton Distribution Function, which also depends on the factorization scale.

In the light of factorization, Eq. (2.20) acquires a new meaning. In SCET, quark PDFs in momentum space are defined by evaluating collinear quark fields on a proton state,

$$f_{p \to q}(\xi, \mu) = \mathrm{tr} \Big\{ \langle p | \overline{\chi}_n(0) \frac{\overline{n}}{2} \delta(\overline{n} \cdot \mathcal{P} - \xi\,\overline{n} \cdot P) \chi_n(0) | p \rangle \Big\}, \qquad (2.21)$$

and the partonic cross section plays the role of hard function, obtained by squaring a Wilson coefficient that depends only on the large (longitudinal)

---

[6]To be precise, the second is defined as the *Feynman x*, but there is no difference when neglecting proton mass corrections. Note that the sign convention for Q^2 makes it positive.

momentum component. The factorization formula does not involve a soft func-
tion, since the PDF operator is already a color singlet; in other words, there are
no other sectors of the theory that the soft radiation can communicate with.
The definition in position space, based on ref. [103], is shown in eq. (B.1) in
the appendix.

Being genuinely non-perturbative objects, PDFs set the limit of perturbative
QCD and can only be measured from experiment[7]. Their great importance
is in their universality, as they can be extracted from (in principle) a single
experiment and used in a variety of applications. Another major example
is Drell-Yan scattering, the production of a lepton pair from proton-proton
collisions (fig. 2.5 right), that involves two PDFs,

$$\frac{\mathrm{d}\sigma_{pp\to\ell\bar{\ell}X}}{\mathrm{d}Q^2} = \sum_f \int_0^1 \mathrm{d}x_1 \int_0^1 \mathrm{d}x_2 \, f_{p\to f}(x_1,\mu) f_{p\to\bar{f}}(x_2,\mu) \frac{\mathrm{d}\sigma_{f\bar{f}\to\ell\bar{\ell}}}{\mathrm{d}Q^2}(x_1 x_2 s, Q^2, \mu) \,,$$

(2.22)

but PDFs feature in every process involving initial-state protons where a notion
of factorization is present. Universality of non-perturbative physics is essential
to the predictive power of perturbative QCD: were this not the case, one would
need to perform a different measurement to fix the non-perturbative physics
for each process, nullifying the advantages of factorization.

Before moving on, I will comment on two properties of the PDFs. First of
all, being distributions in energy fraction, they satisfy the momentum sum rule

$$\sum_{i=f,\bar{f},g} \int_0^1 \mathrm{d}x \, x \, f_{p\to i}(x,\mu) = 1$$

(2.23)

enforcing energy conservation within the proton. In addition, valence sum
rules constrain the flavor number of each quark species in accordance to the
composition $p = (uud)$ of a proton. Another fundamental property of PDF
concerns their RGE, namely their dependence on the renormalization scale.
PDFs satisfy the Dokshitzer-Gribov-Lipatov-Altarelli-Parisi (DGLAP) evolu-
tion equations [105–107]

$$\frac{\mathrm{d}}{\mathrm{d}\mu} f_{p\to i}(x,\mu) = \int_x^1 \frac{\mathrm{d}x'}{x'} f_{p\to j}\left(\frac{x}{x'},\mu\right) P_{ji}(x',\mu) \,.$$

(2.24)

The QCD *splitting kernels* P_{ji} are the anomalous dimensions for parton distri-
butions. In $\overline{\text{MS}}$ scheme they depend on μ only through the coupling constant;
their perturbative expansions starts at one loop, and results are known up to

---

[7]Although an alternative approach is computing them on lattice, see [104].

three [108, 109] and partially four loop [110]. One-loop results are shown in eq. (B.39) in the appendix, and they can be computed from the amplitude of emission of a parton i from j in the collinear limit: we can imagine the PDF evolution as a process of energy loss through subsequent collinear emissions. The structure of eq. (2.24) involves a Mellin convolution, which comes from the energy fraction x being a multiplicative variable.

Since the LHC collides protons, the determination of PDFs is a highly active topic, see for instance the recent review [111]. PDF uncertainty dominates the theoretical error for many QCD processes, so a more accurate extraction of PDFs plays a vital role in precise tests of the SM, and provides one of the motivations for the future Electron-Ion collider (EIC). Recent determinations can be found in [112–116].

Most of what described for PDFs also holds for Fragmentation Functions $d_{i\to h}(z, \mu)$, whose main properties can be obtained by time reversal from the initial-state counterpart. The definition from SCET operators is given in eq. (B.2), and they are interpreted as the distributions in energy fraction z of a hadron h produced from the parton i. They enter factorization formulae describing exclusive hadron production; an example relevant to this thesis is Semi-Inclusive Deep Inelastic Scattering (SIDIS), where specific final-state hadron is detected on top of the electron in the final state of a $e - p$ collision. The factorization formula reads

$$\frac{\mathrm{d}\sigma_{ep\to ehX}}{\mathrm{d}x\,\mathrm{d}Q^2\,\mathrm{d}z}(x, Q^2, z) = \sum_{i=f,\bar{f},g} \int_0^1 \mathrm{d}\xi\, f_{p\to i}(\xi, \mu) d_{i\to h}(z, \mu) \frac{\mathrm{d}\sigma_{ei\to ei}}{\mathrm{d}x\,\mathrm{d}Q^2}(\xi P, \mu)\,,$$

$$(2.25)$$

where for brevity I omit the arguments Q, x^2. With respect to inclusive DIS, eq. (2.20), features the additional fragmentation function. The sum rule for FFs enforces energy conservation for a fragmenting hadron,

$$\sum_h \int_0^1 \mathrm{d}z\, z\, d_{i\to h}(z, \mu) = 1\,.$$

$$(2.26)$$

In ch. 3, I will take advantage of this rule to drop the dependence of our results on the specific set of FFs. DGLAP equations from FFs read

$$\frac{\mathrm{d}}{\mathrm{d}\mu} d_{i\to h}(z, \mu) = \int_z^1 \frac{\mathrm{d}z'}{z'} P_{ij}(z', \mu) d_{j\to h}\left(\frac{z}{z'}, \mu\right)\,.$$

$$(2.27)$$

Because of crossing symmetry, the one-loop splitting kernels for FFs are just the transpose (in the sense of matrices) relative to the ones of eq. (2.24), although starting at two-loop the relation is more involved.

Extracting FFs from experiments is harder than PDFs. SIDIS is a preferential channel, but the task is complicated by the simultaneous presence of initial- and final-state non-perturbative distributions. Because of the light mass, most of the final-state fragmenting hadrons are pions and to a smaller extent kaons, and the corresponding FFs are the most studied [117–120]. Refs. [121] and [122] provide the most up-to-date global fits for respectively π and K mesons.

2.2.2 TMDs and rapidity divergences

If integrated parton distributions already encode a large amount of information on hadrons, these clearly do not provide a complete description of their structure. A natural generalization is obtained by accounting for the momentum component perpendicular to the direction of motion, thus obtaining Transverse Momentum dependent Distributions (TMDs). Their operator definition is in eq. (B.3). First studied in Ref. [102], they are a more differential version of the collinear counterparts,

$$f_{p\to i}(x,\mu) = \int \mathrm{d}\boldsymbol{q}\, F_{p\to i}(x,\boldsymbol{q},\mu,\zeta)\,,$$

$$d_{i\to h}(z,\mu) = \int \mathrm{d}\boldsymbol{q}\, D_{i\to h}(x,\boldsymbol{q},\mu,\zeta)\,, \tag{2.28}$$

where the functions $F_{p\to i}$ and $D_{i\to h}$ are respectively TMDPDFs and TMDFFs. In addition to the energy fraction and the transverse momentum[8] $\boldsymbol{q}$, they depend on a *rapidity scale* ζ, that plays a similar role as the renormalization scale and is related to a new class of divergences. For practical reasons, it is often convenient to work in the space of impact parameter $\boldsymbol{b}$, the Fourier conjugate of transverse momentum, and define

$$F_{p\to i}(x,\boldsymbol{b},\mu,\zeta) = \int \mathrm{d}\boldsymbol{q}\, e^{i\boldsymbol{b}\cdot\boldsymbol{q}}\, F_{p\to i}(x,\boldsymbol{q},\mu,\zeta)\,, \tag{2.29}$$

and similarly for TMDFFs. I will use the same symbol for momentum space quantities and their Fourier conjugate, and always denote the argument for clarity.

TMDs enter factorization formulae for cross sections differential in transverse momentum, in processes like Drell-Yan scattering, SIDIS and dihadron production in e^+e^- collisions [123–125]. Once again, their relevance lies in their process-independence. To introduce the main complications that enter factorization formulae involving TMDs, it is useful to look at a specific example. I will explore SIDIS in some detail, since in ch. 4 the same formalism will

---

[8]In this chapter and in the rest of this thesis, I will use bold font to denote 2-vectors in the transverse plane, and the subscript T for their norm.

be largely reused to describe DIS+jet production. Working in the Breit frame, one defines the transverse momentum as

$$\boldsymbol{q} = \frac{\boldsymbol{P}_h}{z} + \boldsymbol{q}_{in} \,, \tag{2.30}$$

where $\boldsymbol{P}_h$ is the transverse momentum of the detected hadron, and $\boldsymbol{q}_{in}$ the one of the incoming parton in the proton. In order for factorization to hold, the transverse momentum needs to be much smaller than the virtuality of the process, $q_T = |\boldsymbol{q}| \ll Q$. This is intuitive, since to have some notion of collinear scaling we need the transverse component of the measured momentum to be small with respect to the longitudinal component. With the definition (2.30), the TMD factorization formula for SIDIS reads

$$\frac{\mathrm{d}\sigma_{ep \to ehX}}{\mathrm{d}Q^2\,\mathrm{d}x\,\mathrm{d}z\,\mathrm{d}\boldsymbol{q}} = \sum_q \sigma_{0,q}^{\mathrm{DIS}}(x,Q^2)\, H^{\mathrm{DIS}}(Q^2,\mu) \int \mathrm{d}\boldsymbol{q}\, \delta^{(2)}\!\left(\boldsymbol{q} - \sum_{i=1}^{3} \boldsymbol{q}_i\right)$$

$$S(\boldsymbol{q}_1,\mu)\widehat{F}_{p \to q}(x,\boldsymbol{q}_2,\mu)\,\widehat{D}_{q \to h}(z,\boldsymbol{q}_3,\mu)\left[1 + \mathcal{O}\!\left(\frac{q_T^2}{Q^2}\right)\right]. \tag{2.31}$$

Here $\sigma_{0,q}^{\mathrm{DIS}}$, the tree-level cross section for DIS, is explicitly factored, so that the hard function H^{DIS} is just 1 at leading order. Since transverse momenta are additive, the factorization structure takes the form of a Laplace convolution between the soft and collinear elements. In impact parameter space it reduces to an ordinary product, hence the convenience of working in the Fourier conjugate space. Differently from DIS, at leading power (but every loop order), the sum over eq. (2.31) does not include the gluon, since in presence of the transverse momentum measurement, the lepton-gluon interaction would be mediated by additional collinear operators.

One of the most salient features of eq. (2.31) is the presence of rapidity divergences [126–130], which escape dimensional regularization. Even if the TMDs entering there are made free of IR and UV divergences (the latter accounted for by renormalization), they are still ill-defined unless a new regulator is introduced. The hats over the TMDs refer to this fact. Once regulated, rapidity divergences in TMDs cancel against the soft function. To understand their origin, it is convenient to go back to the SCET$_{\mathrm{II}}$ mode picture in fig. 1.10, right panel. Analogous to the examples discussed in sec. 1.3.2, measuring the transverse momentum imposes the soft modes to scale as $(\lambda, \lambda, \lambda)$, so the observable is described by SCET$_{\mathrm{II}}$. Different from dijet production, in the case of SIDIS one of the two collinear modes refer to an incoming direction (rather than outgoing), and the role of $\sqrt{s}$ is now played by Q, but the mode picture is unaltered in its essence. In general, in the lightcone plane represented there, each hyperbola is a line of constant virtuality, while different points on the

same hyperbola are identified by their rapidity, $y = \frac{1}{2} \ln(p_-/p_+)$. Boosting the system along one of the collinear directions corresponds to moving along the hyperbola. In SCET_{II}, soft and collinear modes live on the same hyperbola, so it is not possible to discriminate them with a gap in virtuality, hence the additional divergence. Instead, the separation between soft and collinear modes needs to be specified through a rapidity scale ζ.

In the applications I will employ two different regularization schemes, based respectively on refs. [128] and [129]. I will give the practical definitions later, but for now, following the first reference, let me assume the existence of a regulator δ, with rapidity divergences arising in the $\delta \to 0$ limit. In fact, we can choose different (dimensionless) regulators $\delta, \overline{\delta}$ for the two collinear sectors, with the soft function depending on both, and the combination of soft and collinear ingredients in impact parameter space yields

$$
\begin{aligned}
S(\boldsymbol{b}, \mu, \delta, \overline{\delta}) \widehat{F}_{p\to q}(x, \boldsymbol{b}, \mu, \delta) \, \widehat{D}_{q\to h}(z, \boldsymbol{b}, \mu, \overline{\delta}) \\
= F_{p\to q}(x, \boldsymbol{b}, \mu, \zeta) \, D_{q\to h}(z, \boldsymbol{b}, \mu, \overline{\zeta}) \,.
\end{aligned} \tag{2.32}
$$

On the right hand side, a square root of the soft function has been reabsorbed in a redefinition of each TMD[9],

$$
\begin{aligned}
F_{p\to q}(x, \boldsymbol{b}, \mu, \zeta) &= S^{1/2}(\boldsymbol{b}, \mu, \delta\zeta) \, \widehat{F}_{p\to q}(x, \boldsymbol{b}, \mu, \delta) \,, \\
D_{q\to h}(x, \boldsymbol{b}, \mu, \zeta) &= S^{1/2}(\boldsymbol{b}, \mu, \overline{\delta}\,\overline{\zeta}) \, \widehat{D}_{q\to h}(x, \boldsymbol{b}, \mu, \overline{\delta}) \,,
\end{aligned} \tag{2.33}
$$

where the separation of the two regulators is allowed since S depends on them only through logarithms,

$$
S\left(\boldsymbol{b}, \ln\left(\frac{\mu^2}{\delta\overline{\delta}Q^2}\right)\right) = S^{1/2}\left(\boldsymbol{b}, \frac{1}{2}\ln\left(\frac{\mu^2}{\delta^2\zeta}\right)\right) S^{1/2}\left(\boldsymbol{b}, \frac{1}{2}\ln\left(\frac{\mu^2}{\overline{\delta}^2\overline{\zeta}}\right)\right), \tag{2.34}
$$

and the rapidity scales $\zeta, \overline{\zeta}$ emerge from the arbitrariness of the splitting, with $\zeta\overline{\zeta} = Q^4$. This redefinition yields the factorization formula for SIDIS in its final form,

$$
\frac{\mathrm{d}\sigma_{ep\to ehX}}{\mathrm{d}Q^2\,\mathrm{d}x\,\mathrm{d}z\,\mathrm{d}\boldsymbol{q}} = \sum_q \sigma^{\text{DIS}}_{0,q}(x, Q^2)\, H^{\text{DIS}}(Q^2, \mu)
$$

$$
\int \frac{\mathrm{d}\boldsymbol{b}}{(2\pi)^2}\, e^{-i\boldsymbol{b}\cdot\boldsymbol{q}} F_{p\to q}(x, \boldsymbol{b}, \mu)\, D_{q\to h}(z, \boldsymbol{b}, \mu) \left[1 + \mathcal{O}\left(\frac{q_T^2}{Q^2}\right)\right]. \tag{2.35}
$$

---

[9]Depending on the rapidity regulator, one may need to subtract the zero bin, removing double-counting of soft and collinear degrees of freedom. To keep the discussion simple, here I assume that the zero bins of both collinear sectors have already been accounted for in a redefinition of the soft function.

The TMDs that appear here are free of divergences, providing a definition comparable with experiments. The hard function is simply related to the quark form factor, and is known up to three loops [131], while the soft function has been computed at two loop [132–134].

The additional perturbative ingredients needed to describe TMDs are the coefficients for matching onto integrated distributions. When the transverse momentum is much larger than the hadronization scale, TMDs refactorize as

$$
F_{p\to i}(x, \boldsymbol{q}, \mu, \zeta) = \sum_j \int_x^1 \frac{\mathrm{d}x'}{x'} \mathcal{C}_{i\leftarrow j}(x', \boldsymbol{q}, \mu, \zeta) f_{p\to j}\left(\frac{x}{x'}, \mu\right) \left[1 + \mathcal{O}\left(\frac{\Lambda_{\mathrm{QCD}}^2}{q_T^2}\right)\right],
$$

$$
D_{i\to h}(z, \boldsymbol{q}, \mu, \zeta) = \sum_j \int_z^1 \frac{\mathrm{d}z'}{z'} \mathbb{C}_{i\to j}(z', \boldsymbol{q}, \mu, \zeta) d_{j\to h}\left(\frac{z}{z'}, \mu\right) \left[1 + \mathcal{O}\left(\frac{\Lambda_{\mathrm{QCD}}^2}{q_T^2}\right)\right],
$$

$$
\tag{2.36}
$$

meaning that the transverse momentum dependence is perturbatively calculable and the hadronic physics is entirely described by the collinear distributions. The matching coefficients are known at two loops [103,135], see also [136–140]. In general, *refactorization* means a further decomposition of one of the factorization ingredients in terms of simpler functions, valid up to power corrections. In SCET, this is described with multiple nested modes, hierarchically separated,

$$
p_F \sim Q(\lambda^2, 1, \lambda), \quad \lambda = \frac{q_T}{Q}, \qquad p_f \sim Q(\lambda^2\lambda'^2, 1, \lambda\lambda'), \quad \lambda' = \frac{\Lambda_{\mathrm{QCD}}}{q_T},
$$

$$
\tag{2.37}
$$

where p_F is the collinear mode of the TMDPDFs and p_f the collinear mode of the integrated PDFs. Loosely speaking, the typical fluctuations around the reference direction described with the PDF are "even more collinear". From the theoretical point of view, we can achieve refactorization starting from the SCET Lagrangian and performing a further expansion in λ', by just repeating the steps described in sec. 1.3.3.

Before moving on to discuss their evolution, let me comment that TMDs admit further generalizations. For polarized beams, the interplay of transverse momentum and spin gives rise to angular correlations between the produced particles that contain a large amount of interesting physics. In that case, besides the unpolarized TMD that I discussed, one introduces several functions corresponding to different Dirac structures, like the Boer-Mulders [141] or Sivers [142] functions. Finally, including information on the small (plus) momentum component leads to defining Generalized Parton Distributions as

well as Generalized TMDs, which carry in principle the most general informa-tion about the proton structure. These generalizations are beyond the scope of this thesis, see for instance [143–145] for introductory reviews.

2.2.3 TMD evolution

In the following, I will discuss the Renormalization Group Evolution of TMDs. This is more complicated than the evolution of integrated distributions, since they depend on both the renormalization scale and the rapidity scale. I will base my discussion on [146] and describe in some detail the formalism of refs. [147, 148] to define the so-called *optimal TMDs*, as this method underlies the numerical results that we obtained in refs. [3,4]. See in particular [129] for a common alternative approach using on the Rapidity Renormalization Group. The following equations refer to TMDFFs for definiteness, but TMDPDFs obey identical equations (meaning in particular that the anomalous dimensions are the same). In this section I'll suppress the argument z, since in contrast to DGLAP evolution this variable does not participate in the RGE.

The RGEs of TMDs in impact parameter space are

$$\mu \frac{\mathrm{d}}{\mathrm{d}\mu} D_{\kappa \to h}(\boldsymbol{b}, \mu, \zeta) = +\gamma_\kappa(\mu, \zeta) D_{\kappa \to h}(\boldsymbol{b}, \mu, \zeta) \,,$$

$$\zeta \frac{\mathrm{d}}{\mathrm{d}\zeta} D_{\kappa \to h}(\boldsymbol{b}, \mu, \zeta) = -\mathcal{D}_\kappa(\mu, \boldsymbol{b}) D_{\kappa \to h}(\boldsymbol{b}, \mu, \zeta) \,, \tag{2.38}$$

where $\mathcal{D}_\kappa$ and γ_κ are respectively the rapidity anomalous dimension and UV anomalous dimension, and κ can be any of the quark flavors, or gluon. In analogy with eq. (1.32),

$$\gamma_\kappa(\mu, \zeta) = \mu \frac{\mathrm{d}}{\mathrm{d}\mu} \ln Z_\kappa(\mu, \zeta) \,, \tag{2.39}$$

where Z_i is the renormalization factor for the TMDs, responsible for subtract-ing the UV divergences. Because of the presence of Sudakov double logarithms, it takes the form

$$\gamma_\kappa(\mu, \zeta) = \Gamma_\kappa(\mu) \ln \left(\frac{\mu^2}{\zeta} \right) - \gamma_\kappa^V(\mu) \,. \tag{2.40}$$

Γ_κ and γ_κ^V are referred to as respectively the *cusp* and *non-cusp* parts of the UV anomalous dimension, and in minimal schemes depend on the renormaliza-tion scale only through the strong coupling constant. The rapidity anomalous dimension is defined as

$$\mathcal{D}_\kappa(\boldsymbol{b}, \mu) = -\zeta \frac{\mathrm{d}}{\mathrm{d}\zeta} \ln S_\kappa^{1/2}(\boldsymbol{b}, \mu, \zeta) \,. \tag{2.41}$$

where the soft function includes the zero-bin contribution and has already been renormalized, so is free of UV poles. The definition is the analog – for rapidity divergences – of eq. (2.40), since the square root of the soft function acts as a rapidity renormalization factor, eq. (2.33), canceling rapidity divergences in TMDs. The anomalous dimensions that appear here are known up to three loops [108, 149–152], and the cusp anomalous dimension is known numerically at fourth order [153], and I show explicit expressions in appx. B.3.2. This allows for resummation of logarithms of small transverse momentum at N^3LL, a remarkable level of accuracy.

From eq. (2.38) and commutativity of second derivatives, it follows

$$\mu \frac{\mathrm{d}}{\mathrm{d}\mu} \mathcal{D}_\kappa(\mu, \boldsymbol{b}) = -\zeta \frac{\mathrm{d}}{\mathrm{d}\zeta} \gamma_\kappa(\mu, \zeta) = \Gamma_\kappa(\mu), \qquad (2.42)$$

with Γ_κ the cusp anomalous dimension. This is the starting point for the definition of "optimal TMDs", which I will briefly describe in the following. The anomalous dimensions $\big(\gamma_\kappa(\mu, \zeta), \mathcal{D}(\mu, b)\big)$ can be thought of as two components of a vector field in the plane $(\ln \mu^2, \ln \zeta)$. Eq. (2.42) provides an integrability condition, stating that the field is locally conservative. This allows for defining a scalar potential and guarantees that the evolution between two points in the $(\ln \mu^2, \ln \zeta)$ plane is independent of the path; in particular, no evolution occurs along equipotential lines. Among these, two special lines cross to determine a saddle point, see fig. 2.6, corresponding to

$$\mathcal{D}_\kappa(\mu_{\text{saddle}}, \boldsymbol{b}) = 0, \qquad \zeta_{\text{saddle}} = \mu_{\text{saddle}}^2 \exp\left(-\frac{\gamma_\kappa^V}{\Gamma_\kappa}\right). \qquad (2.43)$$

In practice, truncating the perturbative expansion breaks path independence, with effects that are numerically relevant. This problem is overcome by the *improved γ scenario*, that enforces path invariance by supplementing γ_κ with higher-order terms. The evolution kernel R, defined as

$$D_{\kappa \to h}(\boldsymbol{b}, \mu_f, \zeta_f) = R_\kappa(\boldsymbol{b}; \mu_f, \zeta_f; \mu_i, \zeta_i) D_{\kappa \to h}(\boldsymbol{b}, \mu_i, \zeta_i), \qquad (2.44)$$

and explicitly determined by solving eq. (2.38), within the improved γ scenario yields

$$R_\kappa(\boldsymbol{b}; \mu_f, \zeta_f; \mu_i, \zeta_i) = \exp\left\{ \mathcal{D}_\kappa(\mu_f, \boldsymbol{b}) \ln\left(\frac{\mu_f^2}{\zeta_f}\right) - \mathcal{D}_\kappa(\mu_\kappa, \boldsymbol{b}) \ln\left(\frac{\mu_i^2}{\zeta_i}\right) \right.$$
$$\left. - \int_{\mu_i}^{\mu_f} \frac{d\mu}{\mu} \left[2\mathcal{D}_\kappa(\mu, \boldsymbol{b}) + \gamma_\kappa^V(\mu)\right] \right\}. \quad (2.45)$$

Path independence allows one to apply the *ζ-prescription*. The idea is setting the initial rapidity scale $\zeta = \zeta(\mu_i)$ as a function of the initial virtuality scale
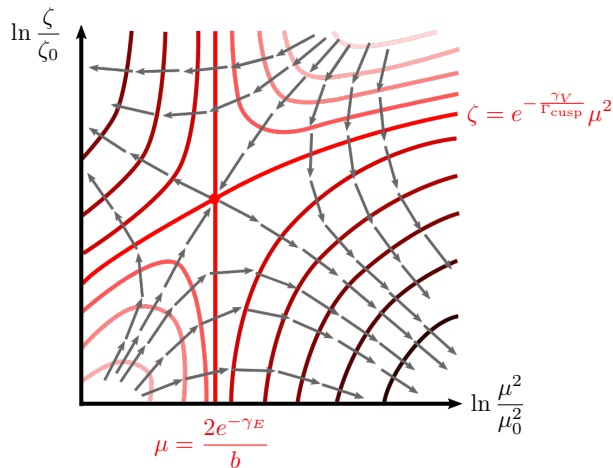
Figure 2.6 Sketch of the geometry relevant to double-scale evolution. The anomalous dimensions determine a conservative field (grey arrows) in the $(\ln \mu^2, \ln \zeta)$ plane, and the evolution is null among equipotential lines (shades of red). The zeta-prescription selects the saddle point at the intersection of two special equipotential lines (bright red) to define and evolve TMDs. The quoted equations are the one-loop analytic result for such lines.

μ_i such that the scale-dependence of the initial TMDs vanishes completely. At one loop, this simply amounts to

$$\zeta(\mu) \equiv \zeta_{\text{saddle}} = \mu^2 \exp\left(-\frac{\gamma_\kappa^V}{\Gamma_\kappa}\right) + \mathcal{O}(\alpha_s), \qquad (2.46)$$

and the two loop expression is given in eq. (B.49). In practice, it is common to choose the saddle point as initial point of the evolution, $\mu_i = \mu_{\text{saddle}}$.

The remarkable fact with the ζ prescription is that, contrarily from standard evolution, the cancellation of large rapidity logarithms occurs internally to each TMD. This fact allows for a clear separation of the uncertainty coming from evolution from other sources of uncertainty (perturbative, or related with the non-perturbative model). Of course, constraining the initial value of ζ_i removes one source of uncertainty in the evolution, reducing the theoretical error. Ref. [148] argued that this additional uncertainty is spurious, since it is unlinked with evolution.

In this section I tried to show how TMDs are a mature field, well integrated with the factorization framework, and where the ingredients to perform (re)factorization and resummation are known to a very high level of precision. In ch. 4 in particular, I will largely build on the results presented here to build

a formalism for DIS+jet. Our main finding in [1] was that the Winner-Take-All jet axis allows to largely reuse most of the results presented here, bringing that process on par with SIDIS.

3
In-jet fragmentation without recoil

Having reviewed the theoretical picture of soft and collinear QCD and introduced the main ingredients, I will now turn to presenting in detail some specific applications of recoil-free jets to describe processes involving a transverse momentum measurement. The common thread will be the investigation of the properties of recoil-free jets, and their relation with jet grooming. The main message I will try to convey is that besides reducing sensitivity to contamination, the Winner-Take-All algorithm largely simplifies the theoretical framework in many relevant processes. Not only is this simplification convenient to theoretical analyses, but it also proves itself advantageous when it comes to obtaining predictions to compare with data.

In this chapter I will extensively describe a first application of recoil-free jets, studying the transverse momentum distribution of hadrons fragmenting inside jets. Fragmentation in jets is a natural way to probe their substructure: from the way hadrons distribute (for example, in energy and momentum), one can reconstruct details of the initial parton, with the ultimate purpose of extracting precise information on the nature of QCD. For this reason, the theory of in-jet fragmentation (without accounting for the transverse momentum dependence) has been studied extensively. A possibility is considering hemisphere jets [19–21, 154–156], in practice defining an event shape. The alternative relevant to this work is using a jet algorithm, as in refs. [157–164]. These studies led to a variety of phenomenological applications and extensions, including predictions on spectra of charge hadrons, quarkonium spectroscopy, multi-hadron fragmentation, and generation of quark masses, [21, 165–171].

Recently, the framework was extended to study transverse momentum dependent (TMD) hadron fragmentation, where the transverse momentum is measured relative to the standard jet axis [172–175] or groomed jet axis [176, 177]. The applications considered in these works were the study of TMDFFs in pp and ep collisions, in both the unpolarized and polarized case, and quarkonium production.

The theoretical framework to describe TMD in-jet fragmentation *without*

recoil was developed in ref. [83]. This work showed how the absence of re-
coil delivers a purely collinear observable, described by a "Collinear Effective
Theory" rather than full SCET. In ref. [2], we investigated the framework in
the case study of e^+e^- collisions, and compared numerical predictions to par-
ton and hadron-level simulations obtained with PYTHIA 8.2 [25] and HERWIG
7.1 [178]. This analysis illustrated some of the intuitive properties of the WTA
scheme, and showed that in absence of recoil the distribution exhibits radically
different and interesting features. To summarize some of the main findings:
in contrast to the Sudakov double logarithms that appear for the standard jet
axis, the dependence of the TMD cross section is given by an (approximate)
power law for the WTA axis, see fig. 3.1. This remains true when taking
into account the limited angular resolution, as long as the angle ϑ between the
hadron and the axis is larger than the angular resolution scale. Furthermore, it
also persists when restricting to charged particles, which allows one to exploit
the finer angular resolution of the tracker. Due to these features, the WTA
observable looks promising for constraining α_s, since it only involves collinear
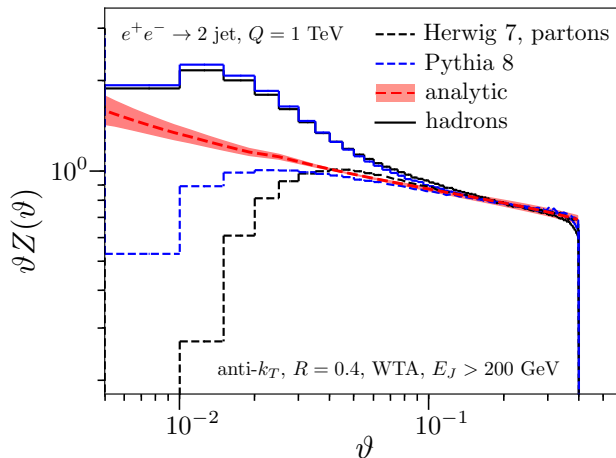physics and can in principle be calculated to high orders in perturbation theory.

Figure 3.1 The average energy fraction of hadrons fragmenting in jets, as a func-
tion of the angle between the hadron and the jet axis. The plot exhibits the striking
features of using recoil-free jets: the absence of soft contamination results in an ap-
proximate power-law behavior, and at low angles the observable is highly sensitive to
hadronization corrections.

The MC analysis also showed that at small angles the distribution is rather
sensitive to non-perturbative physics. This provides a new opportunity to

constrain non-perturbative collinear dynamics experimentally, which could be used to improve hadronization models. For the standard jet axis this is harder, as the relevant features are washed out due to smearing from soft radiation. Finally, a promising application is studying the jet shape modification (quenching) in the quark-gluon plasma originated from heavy-ion collisions. Since this environment is heavily contaminated by soft radiation, the absence of recoil could provide a significant advantage.

Following a common structure for the rest of the thesis, the chapter will be split in three sections. The first one presents the framework: it discusses the kinematics of the process and the consequent mode analysis; how the cross section factorizes in terms of these modes; resummation of large logarithms. Rather than a derivation of the ingredients (already known from [83]), the main focus will be on the evolution properties of the WTA and broadening axes, that I will study from a parton-shower perspective. The comparison between the two will argue in favor of using the WTA scheme. The second section moves from theory to phenomenology: here I introduce the jet shape, our privileged observable; briefly describe how I got numerical predictions; finally, show and discuss Monte Carlo predictions and numerical results. Last, I present a short outlook. Besides the intrinsic relevance, I believe that the extensive study of a recoil-free observable can help develop some physical intuition about the physics captured by this tool. Most of the material presented here is based on ref. [2].

3.1 Theoretical framework

3.1.1 Kinematics and modes

In the following I will define the physical quantities that enter our analysis of in-jet fragmentation. The definitions refer to e^+e^- collisions, the main focus of the analysis of sec. 3.2. Extending our analysis to pp collisions would be a relevant generalization and interesting step towards comparison with LHC data. The proton-proton kinematics is slightly different and is discussed in ref. [83].

The transverse momentum $\boldsymbol{k}$ is defined as

$$\boldsymbol{k} = \frac{\boldsymbol{p}_h}{z_h}, \tag{3.1}$$

where $z_h = E_h/E_J$ is the fraction of the jet energy carried by the hadron and $\boldsymbol{p}_h$ its transverse momentum measured relative to the WTA axis, fig. 3.2. Normalizing to the energy fraction ensures that $\boldsymbol{k}$ is a partonic variable, thus calculable for $\boldsymbol{k} \gg \Lambda_{\text{QCD}}$. I will also show results using the angle ϑ between
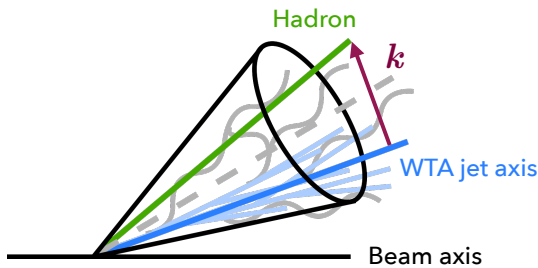
Figure 3.2 Sketch of the relevant directions for TMD in-jet hadron fragmentation. Defining the transverse momentum relative to a recoil-free jet axis makes the observable insensitive to soft radiation.

the hadron and the axis, which is related to $\boldsymbol{k}$ by

$$k_T \equiv |\boldsymbol{k}| = E_J \sin \vartheta \approx E_J \, \vartheta \,. \tag{3.2}$$

Much of the time I will consider the average energy due to all hadrons as function of ϑ or k_T, rather than the z_h spectrum of an individual hadron species h. This is known in the literature as the jet shape [179–183], but here it is defined with respect to the WTA axis instead of the standard jet axis.

The other relevant variables are the center-of-mass energy $\sqrt{s}$, jet scale $E_J R$, the transverse momentum k_T and the scale Λ_{QCD} of nonperturbative physics. I will always assume the hierarchy of scales

$$\sqrt{s} \gg E_J R > k_T \gg \Lambda_{\text{QCD}} \,. \tag{3.3}$$

The leftmost condition corresponds to the assumption of small jet radius, $R \ll \pi/2$, which was shown in previous analyses [163, 164] to hold surprisingly well up to relatively large values of the jet radius, $R \sim 0.4 - 0.5$. The rightmost condition in eq. (3.3) is the assumption of perturbative transverse momentum, meaning that our perturbative predictions are meaningful only where hadronization effects are under control. The central inequality simply follows from $\vartheta < R$ and eq. (3.3) , and I will consider in turn the two cases $E_J R \sim k_T$ and $E_J R \ll k_T$. Getting predictions across the whole transverse momentum spectrum will require interpolating between the two regimes.

The process considered here is *inclusive* in-jet fragmentation, namely we do not constrain the number of jets in the final state. At leading power, collinear splittings dress an initial back-to-back $q\bar{q}$ pair generated in the hard collision, but since the jet radius is assumed small, the products of a collinear splitting may or may not be clustered in the same jet. Therefore, in general, there are

more than two jets per event even at leading power. The hierarchy in eq. (3.3) implies the existence of the two modes

$$p_c \sim \sqrt{s}\left(R^2, 1, R\right), \qquad p_{c,h} \sim k_T\left(\frac{\Lambda_{\mathrm{QCD}}^2}{k_T^2}, 1, \frac{\Lambda_{\mathrm{QCD}}}{k_T}\right), \qquad (3.4)$$

describing collinear fluctuations around respectively the initial $q\bar{q}$ pair and the direction of the hadron, the latter carrying much lower virtuality. As discussed in sec. 2.1.2, the WTA axis simply tracks the bulk of energetic radiation within the jet, ignoring soft emissions. Since the transverse momentum $\boldsymbol{k}$ is measured relative to the recoil-free jet axis, it probes a single collinear sector and there is no soft mode. Contrarily, the standard jet axis balances soft and collinear radiation within the jet, introducing a sensitivity to all other collinear directions. In particular, it forces one to discriminate soft emissions *inside* and *outside* the jet, making the observable sensitive to non-global logarithms [183].

Building on collinear factorization, the mode picture eq. (3.4) naturally translates into a factorized description, which I now turn to presenting.

3.1.2 Factorization

In the following, I will describe the factorization picture induced by the hierarchy (3.3), discussing the various steps of refactorization and emphasizing their physical meaning. Further details are shown in [83], where the formulae were first derived.

The cross section for producing a hadron h with energy fraction z_h and transverse momentum $\boldsymbol{k} = \boldsymbol{p}_h/z_h$ inside a jet with energy E_J and radius R is given by

$$\frac{\mathrm{d}\sigma_h}{\mathrm{d}E_J\,\mathrm{d}\boldsymbol{k}\,\mathrm{d}z_h} = \sum_i \int \frac{\mathrm{d}x}{x}\, H_i\!\left(\frac{E_J}{x},\mu\right) \mathcal{G}_{i\to h}(x, E_J R, \boldsymbol{k}, z_h, \mu)\left[1 + \mathcal{O}(R^2)\right].$$
$$(3.5)$$

Here the collinear approximation $R \ll 1$ is exploited to factorize the cross section into a partonic cross section H, that describes the hard scattering, and the fragmenting jet function $\mathcal{G}$, that captures the formation of the jet. Specifically, the parton i with energy E_J/x produced in the hard scattering emits radiation, resulting in a jet with energy E_J that contains the hadron h. As already noted, collinear emissions may produce multiple jets even at leading power in SCET, thus i can be either quark or gluon, although in e^+e^- collisions gluon jets are only produced starting at NLO. The hard coefficients are the same as for inclusive jet production (integrated over transverse momentum), and the NLO expressions are therefore well known [184–187]. In presence of

multiple emissions, the energy fraction of the final parton is the product of
the energy fractions of each emission, hence the Mellin convolution over the
jet energy fraction. Compared to the full QCD result, eq. (3.5) misses power
corrections in R, but allows for resummation of large logarithms of the small
jet radius. The factorization formula does not involve a soft function, implying
in particular that the framework is free of rapidity divergences.

   When the hadron is produced close to the center of the jet, i.e. $k_T \ll E_J R$,
the effects of the jet boundary B furthermore separate from the fragmentation,

$$\mathcal{G}_{i \to h}(x, E_J R, \boldsymbol{k}, z_h, \mu) = \sum_j \int_{z_h}^1 \frac{\mathrm{d}y}{y} \, B_{ij}\Big(x, E_J R, \frac{z_h}{y}, \mu\Big) \mathcal{D}_{j \to h}(\boldsymbol{k}, y, \mu)$$
$$\times \big[1 + \mathcal{O}\big(k_T^2/(E_J R)^2\big)\big]. \quad (3.6)$$

This does not follow directly from collinear factorization, but requires that the
jet finding also factorizes. In other words, the effect of clustering particles at a
distance $d_{ij} \sim \vartheta \approx k_T/E_J$ must also be power suppressed by an amount ϑ/R.
This was argued to hold for the Cambridge/Aachen and anti-k_T with the WTA
axis in ref. [83]. The basic reasoning (which may fail for the k_T algorithm) is
that particles separated by $\sim \vartheta$ are clustered first, while recombination at the
scale $\sim R$ occurs only at a later stage.

   In eq. (3.6), non-perturbative physics has been confined in the coefficients
$\mathcal{D}_{j \to h}$, which must not be confused with the TMDFFs discussed in sec. 2.2.2.
Contrary to the TMDFFs, $\mathcal{D}_{j \to h}$ do not carry rapidity divergences, and they
will therefore obey a completely different evolution. However, similarly to
those, they involve an interplay of non-perturbative physics in energy fraction
and transverse momentum. Calculating the transverse momentum dependence
in perturbation theory requires the additional assumption $k_T \gg \Lambda_{\mathrm{QCD}}$. Under
this condition,

$$\mathcal{D}_{j \to h}(\boldsymbol{k}, z_h, \mu) = \sum_k \int_{z_h}^1 \frac{\mathrm{d}z}{z} \, C_{jk}\Big(\boldsymbol{k}, \frac{z_h}{z}, \mu\Big) d_{k \to h}(z, \mu) \bigg[1 + \mathcal{O}\bigg(\frac{\Lambda_{\mathrm{QCD}}^2}{k_T^2}\bigg)\bigg],$$
$$(3.7)$$

where by universality of collinear physics, $d_{k \to h}(z, \mu)$ are the integrated FFs
discussed in sec. 2.2.1. This is formally identical to the matching of TMDFFs
in eq. (2.36), with different matching coefficients C_{jk}.

   I will also consider the case $E_J R \sim k_T \gg \Lambda_{\mathrm{QCD}}$, where the hadron is pro-
duced fairly close to the jet boundary. Here $\mathcal{O}(k_T^2/(E_J R)^2)$ power corrections
cannot be neglected, resummation of logarithms of the corresponding ratio of
scales becomes irrelevant, and eq. (3.7) delivers a poor approximation. The
factorization formula for this regime is given by

$$\mathcal{G}_{i \to h}(x, E_J R, \boldsymbol{k}, z_h, \mu) = \sum_k \int_{z_h}^1 \frac{\mathrm{d}z}{z} \, J_{ik}\Big(x, E_J R, \boldsymbol{k}, \frac{z_h}{z}, \mu\Big) \, d_{k \to h}(z, \mu)$$

$$\times \big[1 + \mathcal{O}\big(\Lambda_{\mathrm{QCD}}^2/(E_J^2 R^2)\big)\big]. \quad (3.8)$$

The coefficients J_{ik} (together with C_{ij} and B_{jk}) were computed at one loop in ref. [83]. When $k_T \ll E_J R$, they refactorize as

$$J_{ik}(x, E_J R, \boldsymbol{k}, z, \mu) = \sum_j \int_z^1 \frac{\mathrm{d}z'}{z'} B_{ij}\Big(x, E_J R, \frac{z}{z'}, \mu\Big) C_{jk}(\boldsymbol{k}, z', \mu)$$

$$\times \big[1 + \mathcal{O}\big(k_T^2/(E_J R)^2\big)\big], \quad (3.9)$$

as required by consistency with eq. (3.5) and eq. (3.6): when simultaneously neglecting powers of k_T/E_J and $\Lambda_{\mathrm{QCD}}/k_T$, the order in which the corrections are expanded away should not matter. Using J_{ik} when $k_T \sim E_J R$, instead of the factorized form on the right-hand side, captures the $k_T^2/(E_J^2 R^2)$ corrections that are crucial in this region. Appx. B.2.1 collects the expressions for the various functions that appear in eq. (3.9), from which refactorization evident.

The logarithms in the cross section in eq. (3.5) become large when there are hierarchies between the scales of the hard scattering $\sqrt{s}$, the jet transverse momentum $E_J R$ and the transverse momentum $\boldsymbol{k}$. In the most factorized scenario, they can be resummed by evaluating each ingredient at its natural scale

$$\mu_H \sim \sqrt{s}\,, \qquad \mu_B \sim E_J R\,, \qquad \mu_C \sim k_T\,, \quad (3.10)$$

and running the renormalization group evolution (RGE) up to a common scale, as I will discuss in the next section.

3.1.3 Evolution: parton shower LL derivation

The RGEs required to implement resummation were derived in [83, 163, 188],

$$\mu \frac{\mathrm{d}}{\mathrm{d}\mu} \, \mathcal{G}_{i \to h}(x, E_J R, \boldsymbol{k}, z_h, \mu) = \sum_j \int_x^1 \frac{\mathrm{d}x'}{x'} \, P_{ij}\Big(\frac{x}{x'}, \mu\Big) \, \mathcal{G}_{j \to h}(x', E_J R, \boldsymbol{k}, z_h, \mu)\,,$$

$$\mu \frac{\mathrm{d}}{\mathrm{d}\mu} \, \mathcal{D}_{i \to h}(\boldsymbol{k}, z_h, \mu) = \sum_j \int_{z_h}^1 \frac{\mathrm{d}z}{z} \, P'_{ij}\Big(\frac{z_h}{z}, \mu\Big) \, \mathcal{D}_{j \to h}(\boldsymbol{k}, z, \mu)\,, \quad (3.11)$$

where P_{ij} are the usual QCD splitting kernels and P'_{ij} involve an additional Heaviside function

$$P'_{ij}(z, \mu) = P_{ij}(z, \mu)\, \theta\big(z - \tfrac{1}{2}\big)\,. \quad (3.12)$$

(Expressions in Mellin space are collected in appx. B.3.1). Together with the DGLAP evolution of the FFs, eq. (2.27), these allow to bridge the separation between any pair of scales in eq. (3.10). The fragmenting jet function $\mathcal{G}$ also has DGLAP evolution, but in the jet energy fraction x rather than in the hadron fraction. This is already clear from the factorization formula in eq. (3.5), because the hard function H is known to have DGLAP evolution from inclusive jet production, and the total cross section does not depend on the scale μ, so the dependence of $\mathcal{G}$ on μ must cancel the one of H. In general, RGE consistency is a very powerful tool to check the validity of a factorization framework: the anomalous dimensions of all the ingredients of a factorized cross section must ultimately add up to zero, which strongly constrains the logarithmic μ dependence of the individual ingredients.

The modified kernels in eq. (B.41) are particular to the fragmenting function $\mathcal{D}$. The additional $\theta(z - \frac{1}{2})$ is due to the WTA axis, and was argued in [83] to hold for the C/A and anti-k_T algorithms. I now turn to showing a derivation of this evolution equation which is limited at LL accuracy, but covers also the k_T case.

As already noted in sec. 1.2.2, at this level of logarithmic accuracy the structure of the evolution can be determined from a parton shower. Specifically, the radiation emitted by the parton produced in the hard interaction is described by a binary tree, see fig. 3.3, where each mother splits into two daughters with (relative) momentum fractions z_i and $1 - z_i$ and angle ϑ_i between them. The tree is strongly ordered in angle, meaning that angles of subsequent emissions are parametrically smaller, $\vartheta_{i+1} \ll \vartheta_i$. Before addressing TMD fragmentation with the WTA axis, let me first consider inclusive fragmentation in a jet. At LL order, the corresponding fragmenting jet function $\mathcal{G}^{\mathrm{incl}}$ (which differs from the TMD jet function $\mathcal{G}$ in eq. (3.5), but has the same evolution) reduces to the fragmentation function

$$\mathcal{G}^{\mathrm{incl}}_{i \to h}(x, E_J R, z_h, \mu) = \delta(1 - x)\, d_{i \to h}(z_h, \mu)\,, \tag{3.13}$$

evaluated at $\mu \sim E_J R$ to minimize higher-order corrections. The amplitude for inclusive hadron production in a jet follows from summing over an arbitrary number of emissions and integrating over their phase space. In terms of a parton shower, this is described by

$$A(z_h, R_0) = d_h(z_h, R_0) + \sum_{n=1}^{\infty} A_n(z_h, R_0)\,, \tag{3.14}$$

where the first term describes an initial parton that does not undergo any
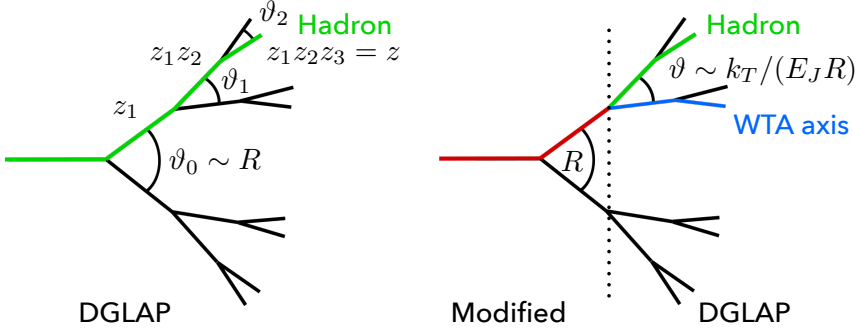
Figure 3.3 Parton shower picture for inclusive in-jet fragmentation (left) and TMD in-jet fragmentation with the WTA axis (right). In absence of other constraints, strong angular ordering yields DGLAP evolution. Measuring the transverse momentum forces the hadron and the WTA axis to follow the same branch (red) before the splitting that sets the measurement, resulting in the modified evolution of eq. (B.41).

perturbative splitting, while the amplitude for n emissions reads

$$A_n(z_h, R_0) = \left(\prod_{i=1}^{n} \int_0^1 \mathrm{d}z_i \, P(z_i) \int_{R_0}^{\vartheta_{i-1}} \frac{\mathrm{d}\vartheta_i}{\vartheta_i} \right) \int_0^1 \mathrm{d}z' \, d_h(z', R_0) \, \delta \left(z_h - z' \prod_{j=1}^{n} z_j \right).$$
(3.15)

The splitting fraction z_i and angle ϑ_i of each emission are integrated over, with the splitting function $P(z_i)$ providing a weight (for simplicity, I ignore parton flavors). This follows from a repeated application of the collinear approximation, where the quantity

$$\int_0^1 \mathrm{d}z_i \, P(z_i) \int \frac{\mathrm{d}\vartheta_i}{\vartheta_i}$$
(3.16)

gives the probability of one splitting. The upper bound on the ϑ_i integration follows from the angular ordering, which for the angle ϑ_1 of the first splitting is the jet radius R. The cutoff R_0 regulates the collinear singularity, and subsequent (nonperturbative) splittings are described by the fragmentation function d_h. Note that instead of traversing all branches of the binary tree, we can follow the branch with splitting fraction z_i (rather than $1 - z_i$), up to a symmetry factor absorbed in a redefinition of P. The measurement delta function fixes the observed momentum fraction to the product of all z_i.

To show that eq. (3.14) reproduces eq. (3.13), one solves the angular integrals

$$\prod_{i=1}^{n} \int_{R_0}^{\vartheta_{i-1}} \frac{\mathrm{d}\vartheta_i}{\vartheta_i} = \frac{1}{n!} \ln^n \frac{R}{R_0},$$
(3.17)

and since $\mu = E_J R$ in eq. (3.13), uses $\mathrm{d}\ln\mu = \mathrm{d}\ln R$ to obtain

$$
\begin{aligned}
\frac{\mathrm{d}A}{\mathrm{d}\ln\mu} &= \int_0^1 \mathrm{d}z \sum_{n=1}^{\infty} \left(\prod_{i=1}^{n-1} \int_0^1 \mathrm{d}z_i\, P(z_i) \right) \frac{1}{(n-1)!} \ln^{n-1} \frac{R}{R_0} \\
&\quad \times \int_0^1 \mathrm{d}z'\, d_h(z', R_0)\, \delta\!\left(z - z' \prod_{j=1}^{n-1} z_j \right) \int_0^1 \mathrm{d}z_n\, P(z_n)\, \delta(z_h - z z_n) \\
&= \int_{z_h}^1 \frac{\mathrm{d}z}{z} P\!\left(\frac{z_h}{z} \right) A(z)\,.
\end{aligned}
\tag{3.18}
$$

On the first line, separating out the integral over z_n identifies the remainder as A. This shows that the amplitude A for inclusive jet production satisfies the DGLAP evolution. Furthermore, for $R = R_0$, A is simply equal to the fragmentation function, yielding the correct boundary condition.

The derivation above extends to TMD fragmentation with the WTA axis by splitting the parton shower into three segments:

(a) $\vartheta_i > R$: all branches yield separate jets and are summed over, since we consider inclusive jet production. Splittings modify $x = 2E_J/\sqrt{s}$ but do not affect z_h because the latter is defined relative to the jet energy.

(b) $R \geq \vartheta_i > k_T/E_J$: splittings take place inside the jet and thus do not modify x but will affect z_h. Because of $\vartheta_i > k_T/E_J$ and the strong ordering in angles, the WTA axis and fragmenting hadron must at this point in the shower still follow the same branch.

(c) $k_T/E_J \geq \vartheta_i$: The first splitting sets the angle (or equivalently $\boldsymbol{k}$) between the WTA axis and the hadron. Subsequent splittings modify z_h but cannot change this angle due to the strong angular ordering. All of these emissions are summed over.

We can directly repeat the above parton shower analysis in eq. (3.14) and eq. (3.18), from which it follows that in (a) there is DGLAP evolution in x from $\mu = \sqrt{s}$ down to $\mu = E_J R$, and in (c) there is a DGLAP evolution in z_h from $\mu = k_T$ to the initial scale $\mu \sim \Lambda_{\mathrm{QCD}}$ of the fragmentation functions. For (b), strong ordering in angles implies that the clustering tree of any jet algorithm of the k_T family (not just C/A and anti-k_T) coincides with the parton shower tree. For $R \geq \vartheta > k/E_J$ only the branch that will yield the WTA axis and produce the hadron needs to be integrated over, which corresponds to imposing $z_i > \frac{1}{2}$ and leads to the modified anomalous dimension in eq. (B.41). This justifies the evolution equations in eq. (3.11) and the scales in eq. (3.10).

3.1.4 Evolution with the broadening axis

While pointing out the practical advantages of the WTA scheme, the first phenomenological analysis of recoil-free jets, ref. [85], treated the WTA and broadening axis on an almost equal footing. I will now show (at least, for TMD in-jet fragmentation) that the broadening axis defined in section sec. 2.1.2 fails in satisfying a simple evolution picture, making the WTA scheme a preferred option to eliminate recoil. In particular, I will show that resumming logarithms of $k_T/(E_J R)$ with the broadening axis takes on a much more complicated form than for the WTA axis, because even at LL accuracy the axis finding does not have a simple recursive structure. I will need to consider at least two splittings, since when the jet consists of only two particles the broadening axis is along the most energetic one, just like the WTA.

Let me start from the case where all the particles lie in a plane, as this simplified configuration already gives some intuition of the increased complexity of the evolution with the broadening axis. According to the definition in eq. (2.12), one needs to find the unit vector $\hat{n}$ that minimizes eq. (2.11). The assumption of small jet radius justifies the approximation in eq. (2.13): in this case $\hat{n}$ is parametrized by an angle φ, and the broadening yields

$$B(\varphi) = \sum_i z_i |\vartheta_i - \varphi| \,. \tag{3.19}$$

Since this function is piecewise linear, its minimum coincides with the direction of one of the particles, $\varphi = \vartheta_i$. In the parton shower picture, we want to track the axis along the showering tree (fig. 3.4, left). To determine for a given splitting which of the two daughters takes control of the axis, requires comparing

$$B_\ell = z_r(\vartheta_\ell - \vartheta_r) + \sum_{i \in L} z_i(\vartheta_i - \vartheta_\ell) + \sum_{i \in R} z_i(\vartheta_\ell - \vartheta_i) \,,$$
$$B_r = z_\ell(\vartheta_\ell - \vartheta_r) + \sum_{i \in L} z_i(\vartheta_\ell - \vartheta_r) + \sum_{i \in R} z_i(\vartheta_r - \vartheta_i) \,. \tag{3.20}$$

Here L and R identify the subset of particles to the left and to the right of the splitting. Subtracting the two lines in eq. (3.20) from one another gives

$$B_\ell < B_r \quad \Leftrightarrow \quad z_\ell + z_L > z_r + z_R \,, \tag{3.21}$$

where z_L and z_R are the energy fractions of L and R. In contrast to the WTA axis, it is thus not sufficient to compare z_ℓ and z_r, as the other branches still enter in eq. (3.21). It is still possible to determine the broadening axis with a recursive procedure, as long as one also keeps track of the total energy on the
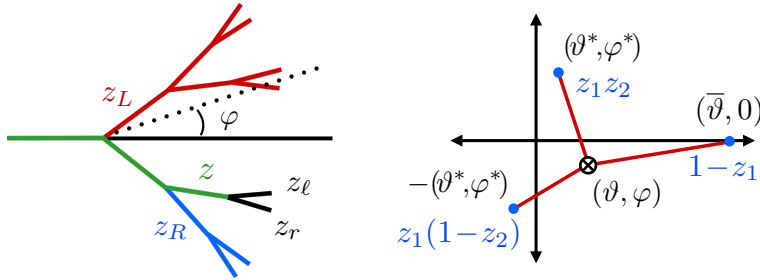
Figure 3.4 Left: parton shower picture for TMD in-jet fragmentation with the broadening jet axis, in the planar limit. Here all momentum fractions are relative to the parton initiating the jet. When the branch along which the axis lies (green) splits, the energy fractions z_L and z_R of the left (red) and right (blue) affect which daughter (black) gets the axis. Right: the general angular-ordered three-particle configuration consists of a pair and a third particle that is far away (blue dots). The position of the broadening axis depends on the angular distances (red lines). The origin of the coordinate system is centered between the two nearby particles and the ϑ axis is chosen such that the third particle lies on it.

left/right of the axis. The resulting two-variable DGLAP evolution is discussed in [2], but I stress that it is only valid in the planar limit.

I now move on to the non-planar case and consider the simplest non-trivial configuration of three particles, arising from two splittings. I will show that even in the strongly-ordered angular limit, the position of the broadening axis depends sensitively on the energy fraction of the initial splitting. In other words, the broadening axis does not behave in a Markovian manner with respect to a history in the strongly-ordered angular limit. This is in contrast to the WTA axis, whose position in this limit only depends on the branching that is currently occurring. Without the Markovian condition, the transverse momentum with respect to the broadening axis is not expected to admit a simple LL resummation.

The position of the axis in the non-planar configuration is specified by two angles (ϑ, φ), while the relative position of the three particles requires three parameters. After the first splitting, the broadening axis simply is along the particle with energy fraction $z_1 > \frac{1}{2}$. Let us consider the case that this splits into a pair of particles with energy fractions $z_2 z_1$ and $(1 - z_2)z_1$, and choose the coordinate system illustrated in the right panel of fig. 3.4. Using that for narrow jets the angular-separation measure of two particles is flat, $d\Omega \approx d\vartheta^2 + d\varphi^2$, the broadening is

$$B(\vartheta, \varphi) = z_2 z_1 \sqrt{(\vartheta - \vartheta^*)^2 + (\varphi - \varphi^*)^2} + (1 - z_2)z_1 \sqrt{(\vartheta + \vartheta^*)^2 + (\varphi + \varphi^*)^2}$$

$$+ (1 - z_1)\sqrt{(\vartheta - \overline{\vartheta})^2 + \varphi^2}. \tag{3.22}$$

Strong angular ordering corresponds to taking the limit $\overline{\vartheta} \to \infty$, and searching for a local minimum within the convex hull of the three particles requires setting derivatives with respect to (ϑ, φ) to zero in the domain

$$\vartheta^*, \varphi^* > 0, \qquad -\varphi^* < \varphi < \varphi^*, \qquad -\vartheta^* < \vartheta < \overline{\vartheta}. \tag{3.23}$$

It is convenient to switch to the variables

$$\xi_\pm = \frac{\vartheta \pm \vartheta^*}{\varphi \pm \varphi^*}, \tag{3.24}$$

for which the condition of a local minimum takes the following form,

$$\xi_- - \xi_+ = \frac{1 - z_1}{z_2 \, z_1} \sqrt{1 + \xi_+^2}, \qquad z_2^2(1 + \xi_-^2) = (1 - z_2)^2(1 + \xi_+^2). \tag{3.25}$$

A solution exists for

$$\frac{2z_1 - 1}{2z_1} < z_2 < \frac{1}{2z_1}, \tag{3.26}$$

which is given by

$$\xi_+(z_1, z_2) = \frac{-1 + 2z_1 - 2z_1^2 z_2}{\sqrt{-1 + 4z_1 - 4z_1^2 - 4z_1^2 z_2 + 8z_1^3 z_2 + 4z_1^2 z_2^2 - 8z_1^3 z_2^2}},$$

$$\xi_-(z_1, z_2) = \frac{1}{z_2}\sqrt{1 - 2z_2 + (1 - z_2)^2 \xi_+^2(z_1, z_2)}. \tag{3.27}$$

As in the planar case, the position of the broadening axis depends not just on two daughters of the splitting, but also the other particle (through z_1). However, unlike the planar case, the broadening axis does not have to lie on a particle, though it will do so for values of z_2 outside the bounds in eq. (3.26). Indeed, these boundaries exactly correspond to the condition that the momentum fractions of all of the partons are less than half, since the broadening axis will be along a parton if its momentum fraction is larger than half.

The picture is still slightly more complicated, because I have not yet imposed eq. (3.23), which shrinks the solution space (in particular, we know that it should vanish in the planar limit $\varphi^* \to 0$). The analytic expressions obtained from eq. (3.27) are rather complicated, but I illustrate the effect in fig. 3.5. The right panel shows the solution space shrinking depending on the ratio φ^*/ϑ^*; the left panel shows the position of the broadening axis for $\varphi^*/\vartheta^* = 1$, with different paths corresponding to different values of z_1. This dependence on z_1 explicitly shows that the Markovian condition is violated.
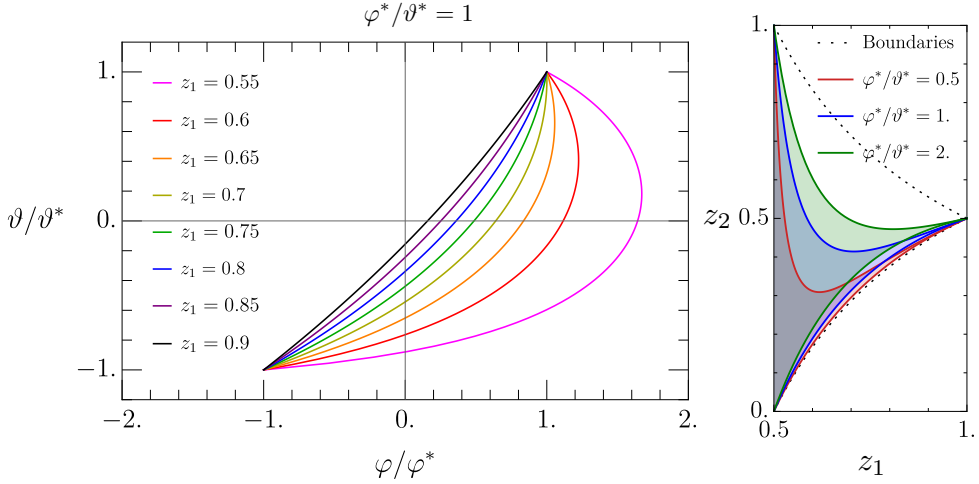
Figure 3.5 Left: the position of the broadening axis for $\varphi^*/\vartheta^* = 1$ is mapped out. The curves correspond to different z_1 values, showing that the Markovian condition is violated, and run over the allowed z_2 range. Right: the region in (z_1, z_2) where the broadening axis does *not* lie on a particle, shown for different values of φ^*/ϑ^*. The dotted boundaries correspond to solutions of (3.26) without taking into account the additional constraints from eq. (3.23).

In conclusion, I have shown that even at leading-logarithmic order, the position of the broadening axis generically (and nontrivially) depends on particles other than the daughters of the splitting under consideration. It is therefore clear that there is no simple DGLAP evolution that describes this parton shower picture, though the evolution can of course be calculated by simulating the *full* shower.

3.2 Phenomenological study

3.2.1 Jet shape

The framework that I sketched in the previous sections is fairly general, in the sense that the double differential cross section contains in principle all the information about the energy fraction and transverse momentum dependence of hadrons fragmenting in jets. When it comes to phenomenology, this is often too much information. One chooses what features of the cross section are worth investigating, projecting them onto two-dimensional plots. Furthermore, some of the kinematical regions we get predictions for could be in fact experimentally inaccessible, such as low hadron transverse momenta or jet energies. Moreover,

large sources of theoretical and experimental uncertainty, such as the extraction
of FFs, could nullify the effort to increase the perturbative accuracy. These
considerations play an important role in choosing the focus of the analysis.

That the framework heavily relies on factorization only makes the situation
more delicate. Assuming wide separation between each of the energy scales
in eq. (3.3) allows for resumming logarithms of any of their ratios, but it is
important to know what power corrections are left aside: I will always ignore
$\Lambda_{\mathrm{QCD}}/k_T$ and large-R corrections, but provide a transition between the two
regimes $k_T \sim E_J R$ and $k_T \ll E_J R$ in order to cover all of the interesting
perturbative range. How to implement the transition is not obvious, and allows
for different prescriptions.

Finally, resummation is implemented by evolving the perturbative ingredi-
ents from an initial to a final scale. Since the procedure deals by definition
with contributions beyond the working perturbative order, any choice of scales
yields results that are formally equivalent up to higher-order corrections. How-
ever, these corrections are in fact large (or we would not need resummation
in the first place) so the choice does matter. Assessing the theoretical error
induced by this choice is important, and the standard method to do so is *scale
variation*. There is general consensus in the field on the large degree of arbi-
trariness involved in scale variation, thus it is good practice to always specify
clearly the procedure followed.

In ref. [83] we mainly focused on the jet shape, that shows most of the
characteristic features of absence of recoil while limiting the non-perturbative
input required. In the rest of this section and the following, I will discuss the
considerations introduced above in the context of this specific observable.

The jet shape is the average fraction of the jet energy at a specific angle ϑ
with the axis. It can be obtained from the cross section differential in transverse
momentum of eq. (3.5), by expressing $\boldsymbol{k}$ in terms of ϑ using eq. (3.2), summing
over hadron species h and averaging over z_h,

$$\frac{\mathrm{d}\langle z_h \rangle}{\mathrm{d}E_J \, \mathrm{d}\vartheta} = \frac{2\pi\vartheta E_J^2}{\sigma} \sum_h \int_0^1 \mathrm{d}z_h \, z_h \, \frac{\mathrm{d}\sigma_h}{\mathrm{d}E_J \, \mathrm{d}\boldsymbol{k} \, \mathrm{d}z_h} \, . \tag{3.28}$$

The overall factor is the Jacobian due to switching from $\boldsymbol{k}$ to ϑ, and the full
cross section σ that gives the normalization[1]. In the region $\sqrt{s} \gg E_J R \gg
k_T \gg \Lambda_{\mathrm{QCD}}$, eqs. (3.5), (3.6) and (3.7) combine to explicitly yield

$$\frac{\mathrm{d}\langle z \rangle}{\mathrm{d}E_J \, \mathrm{d}\vartheta} = \frac{2\pi\vartheta E_J^2}{\sigma} \sum_{i,j,k} \int_{x_J}^1 \frac{\mathrm{d}x}{x} \, H_i\Big(\frac{E_J}{x}, \mu\Big) \int_0^1 \mathrm{d}y \, y \, B_{ij}(x, E_J R, y, \mu)$$

---

[1]In fact, the results of sec. 3.2.3 use a different normalization, which I will specify later.

$$\times \int_0^1 \mathrm{d}z\, z\, C_{jk}\big(\boldsymbol{k}(\vartheta), z, \mu\big) \sum_h \int_0^1 \mathrm{d}z_h\, z_h\, d_{k\to h}(z_h, \mu)\,. \qquad (3.29)$$

Here I used that the (first) Mellin moment of a product is the product of the individual moments to separate the integrals in the hadron fraction. The lower limit $x_J = 2E_J/\sqrt{s}$ is the jet energy fraction.

The dependence on the FFs drops out because of the momentum sum rule in eq. (2.26), which is particularly convenient because it removes one of the largest sources of theoretical uncertainty. There is a drawback however, since neutral hadrons are hard to detect (they escape calorimeters), reducing the overall resolution. To avoid this issue, the jet shape can also be defined on subsets S of particles, such as charged particles or charged pions, restricting the sum over h in eq. (3.28). In that case the sum rule cannot be used to eliminate the fragmentation functions completely. However, the required non-perturbative input is rather limited, as it reduces to one non-perturbative number for each parton flavor (the first moment of the FF), which describes the average energy of a parton that goes into S.

In the complementary regime $\sqrt{s} \gg E_J R \sim k_T \gg \Lambda_{\mathrm{QCD}}$, eq. (3.6) is unjustified and one uses instead eqs. (3.5) and (3.8) to get

$$\frac{\mathrm{d}\langle z\rangle}{\mathrm{d}E_J\, \mathrm{d}\vartheta} = \frac{2\pi\vartheta E_J^2}{\sigma} \sum_{i,k} \int_{x_J}^1 \frac{\mathrm{d}x}{x}\, H_i\Big(\frac{E_J}{x}, \mu\Big)$$

$$\times \int_0^1 \mathrm{d}z\, z\, J_{ik}\big(x, E_J R, \boldsymbol{k}(\vartheta), z, \mu\big) \sum_h \int_0^1 \mathrm{d}z_h\, z_h\, d_{k\to h}(z_h, \mu)\,, \quad (3.30)$$

capturing the full $k_T/(E_J R)$ dependence. All the considerations for the maximally-factorized case remain valid.

Resummation is formally included through the evolution kernels

$$\mathcal{G}_{i\to h}(x, E_J R, \boldsymbol{k}, z_h, \mu) = \sum_j \int_x^1 \frac{\mathrm{d}x'}{x'} U_{ij}\Big(\frac{x}{x'}; \mu, \mu_B\Big) \mathcal{G}_{j\to h}(x', E_J R, \boldsymbol{k}, z_h, \mu_B)\,,$$

$$\mathcal{D}_{i\to h}(\boldsymbol{k}, z_h, \mu) = \sum_j \int_{z_h}^1 \frac{\mathrm{d}z}{z} U'_{ij}\Big(\frac{z_h}{z}; \mu, \mu_C\Big) \mathcal{D}_{j\to h}(\boldsymbol{k}, z, \mu_C)\,, \qquad (3.31)$$

solutions of eq. (3.11). The operators U and U' perform respectively the standard DGLAP and modified evolution discussed in sec. 3.1.3, and the convolution structure reflects the form of the evolution equations. By taking moments of the evolution kernels and inserting them in eq. (3.29), it is straightforward to get expressions that also account for the evolution.

3.2.2 Numerical implementation

I will now present some detail of my numerical implementation. All the one-loop and evolution ingredients are known from the literature, and in principle the previous section provides all the equations needed to implement the jet shape at NLO + LL. In practice, a number of subtleties remain to be addressed: first, the perturbative ingredients are formulated as an expansion in plus distributions, whose evolution is not straightforward; second, one needs to combine the factorization formulae for $k \ll E_J R$ and $k \sim E_J R$, and provide an uncertainty estimate. I will examine these aspects in turn, starting with how I solved the evolution equations numerically.

The starting point for all the numerical results shown in sec. 3.2.3 is the double differential cross section. I worked with the cumulative distribution in transverse momentum $\boldsymbol{k}$,

$$\int_{k<k_c} \mathrm{d}\boldsymbol{k} \, \frac{\mathrm{d}\sigma_h}{\mathrm{d}\boldsymbol{k} \, \mathrm{d}E_J \, \mathrm{d}z_h} = \pi \int_0^{k_c} \mathrm{d}k_T^2 \, \frac{\mathrm{d}\sigma_h}{\mathrm{d}\boldsymbol{k} \, \mathrm{d}E_J \, \mathrm{d}z_h} \,, \qquad (3.32)$$

differentiating the result at the end of the computation. This does not complicate the evolution, because the kernels in eq. (3.31) (or equivalently, the anomalous dimensions) do not involve $\boldsymbol{k}$. In fact, it is necessary to choose the scales of the evolution in terms of k_c, because $C_{ij}^{(0)}(\boldsymbol{k}) \propto \delta^2(\boldsymbol{k})$ would cause the distribution to vanish unless $\boldsymbol{k} = 0$. By contrast, $C_{ij}^{(0)}(k_c) \propto \theta(k_c)$ as function of k_c. This choice is referred to as *cumulative* scale settings, contrasting *differential* scale settings.

The resummation was implemented in the form presented in eq. (3.11): I started from the fragmentation functions d at some initial scale μ_d and evolved them to $\mu_C \sim k_c$, where they match onto the TMD fragmentation function $\mathcal{D}$. Here the convolution variable of the evolution is the energy fraction of the hadron z. I then evolved the TMD fragmentation function using the modified DGLAP to $\mu_B \sim E_J R$, with the convolution variable still effectively being the energy fraction of the hadron. At the μ_B scale, they match onto the fragmenting jet function $\mathcal{G}$. Finally I evolved using standard DGLAP up to $\mu_H \sim \sqrt{s}$, with the convolution variable now being the energy fraction of the hard parton which initiates the jet, denoted by x. At this point the corrections from the hard function are included. Due to the matrix nature of the factorization formulae, the various evolution/matching steps do not commute. The evolution is performed independently for each point of a linear grid in the jet energy fraction E_J, which is finally integrated over. Each term in the NLO corrections $H^{[1]}, C^{[1]}, B^{[1]}, J^{[1]}$ only has a nontrivial dependence on x or z but not both, so these evolutions factorize and are carried out separately.

All RGEs were solved using the classic Runge-Kutta method in the evolution basis and accounted for heavy quark thresholds. Using the singlet/nonsinglet decomposition

$$d_\Sigma = \sum_f (d_f + d_{\bar{f}}) , \qquad d_f^+ = d_f + d_{\bar{f}} - \frac{1}{n_f} d_\Sigma , \qquad d_f^- = d_f - d_{\bar{f}} , \quad (3.33)$$

evolution couples the gluon FF to only the singlet d_Σ, and nonsinglet distributions $d^\pm$ evolve independently. However, I adopted different strategies depending on the observable. The jet shape in eq. (3.28) is the first moment in z_h, so in this case it is natural to perform the evolution in Mellin space, where it becomes multiplicative. To this purpose, the one-loop anomalous dimensions for (modified) DGLAP evolution in Mellin space were given in ref. [83]. When inclusive over all hadrons, I could use the sum rule to remove input from fragmentation functions, while for charged pions I took the first moment of existing parameterizations provided by the latest DSS [121] global fit. Even at LL, the presence of NLO fixed-order ingredients justifies the usage of their more recent NLO sets. As a different observable, we considered the cross section differential in the hadron energy fraction z_h, varying cuts on the transverse momentum k_c. In this case I carried out the evolution directly in z space.

Small-R resummation in e^+e^- collisions poses the additional issue of evolving distributions in the convolution variable, such as $\delta(1-x)$, rather than functions (for the convolutions in z there is no problem, as such distributions are smeared by their convolution with FFs). I solved this issue by taking the zero truncated moment of the distribution and exploiting that such a truncated moment itself satisfies a DGLAP evolution equation with modified splitting functions [189]. This is simply due to the rearrangement

$$\int_{x_0}^1 \mathrm{d}x \int_x^1 \frac{\mathrm{d}x'}{x'} P_{ij}(x') \mathcal{G}_j\left(\frac{x}{x'}\right) = \int_{x_0}^1 \frac{\mathrm{d}x'}{x'} \frac{x_0}{x'} P_{ij}\left(\frac{x_0}{x'}\right) \int_{x'}^1 \mathrm{d}x \, \mathcal{G}_j(x) , \qquad (3.34)$$

where I omitted the non-relevant arguments. To get the evolved spectrum I then differentiated the evolved truncated moment. Finally, because the jet shape turns off sharply at the endpoint $\vartheta = R$, it was necessary to resum threshold logarithms of $1 - x_J$ in order to correctly describe this region. I won't discuss this subtlety here, and I point the interested reader to [2].

I now describe how the jet shape predictions are extended from $k_c \ll E_J R$ to $k_c \lesssim E_J R$. A way to smoothly transition between eq. (3.29) and eq. (3.30), is schematically performing the matching

$$\sigma = H(\sqrt{s}) \otimes_x U(\sqrt{s}, E_J R) \otimes_x \Big[B(E_J R) \otimes_z U'(E_J R, k_c) \otimes_z C(k_c) \otimes_z d(k_c)$$

$$+ J(E_J R) \otimes_z d(E_J R) - B(E_J R) \otimes_z C(E_J R) \otimes_z d(E_J R) \Big] , \qquad (3.35)$$

where the evolution kernels in eq. (3.31) run between the scales in parenthesis, and the arguments of the functions indicate the canonical scale at which they are evaluated. The symbol $\otimes$ denotes Mellin convolution over the jet energy fraction or hadron energy fraction. The formula is read as follows: the first term within square brackets contains leading logarithms of the ratio $k_c/(E_J R)$ (via the evolution kernel U'), but misses power corrections of the same quantity. Vice versa, the second term includes power corrections (via the coefficients J) but misses LLs beyond NLO. Summing the two contributions includes both classes of terms, but implies some double counting: the overlap is obtained leaving out power corrections (by using the maximally factorized formula) and logarithms (by not including the evolution kernel) at the same time, which is precisely the term subtracted in eq. (3.35).

Let me note that eq. (3.35) is not the only possible prescription to implement a transition. In general, a way to interpolate between two regimes I and II is named *profile*. A simple profile is given by a weight function f,

$$\sigma(y) = \sigma^{\mathrm{I}}(y) f(y; a) + \sigma^{\mathrm{II}}(y)[1 - f(y; a)], \qquad (3.36)$$

where y are kinematical variables and a profile parameters, that reduces to 1 in the kinematical region dominated by I and to 0 in the one dominated by II. A more elegant prescription is using profile *scales*, choosing the scales $\mu_i(y, a)$ as functions of the kinematics, see e.g. [17, 190]. By doing this, one controls the speed at which resummation is performed across the whole kinematical range, and can gradually switch it off in the region where logarithms are under control. A reason why eq. (3.35) is appealing compared to these alternatives is that it does not involve additional parameters, as it captures two classes of terms that are already present in the all order QCD expression.

In our case, we found no clear reason to transition between the two regimes with profile scales, and we chose as standard configuration

$$\mu_H = \sqrt{s}, \qquad \mu_B = 2E_J \tan(R/2), \qquad \mu_C = k_c, \qquad (3.37)$$

which differs slightly from the canonical scales in eq. (3.10). In particular, keeping the tangent (rather than just the angle R) retains some subleading corrections in the small-R expansion underpinning eq. (3.5), improving the behavior of the cross section in the vicinity of the $\vartheta \sim R$ endpoint.[2] To avoid $\alpha_s(\mu_C)$ from hitting the Landau pole, I used the following profile for the scale μ_C,

$$\mu_C(k_c) = \frac{k_0}{2}\left(1 + \frac{k_c^2}{k_0^2}\right) \qquad \text{if} \quad k_c \leq k_0, \qquad (3.38)$$

---

[2]The same corrections were retained in our expression for the NLO ingredients, where the relation $p_T R \leftrightarrow 2E_J \tan \frac{R}{2}$ was used to convert the pp jet definition (that uses azimuthal angles and pseudo-rapidity) to the e^+e^- case (that uses angles).

where $k_0 = 1$ GeV. Of course in this region non-perturbative corrections to eq. (3.7) will be important, and our numerical predictions are just indicative.

Finally, following common lore to estimate the perturbative uncertainty, I varied the scales by a factor 2 (and $1/2$) around their central value. Specifically, I first only varied the profile scale μ_C around its central value, then varied μ_B and μ_C at the same time, and then varied all the three scales together. This probes the resummation uncertainties related to logarithms of $k_c/(E_J R)$, R and fixed-order uncertainty, respectively. In addition, I varied the profile parameter k_0 up and down by a factor of 2, and took the final uncertainty to be the quadrature of the four cases.

3.2.3 Results

Having specified our definition and numerical procedure, in this section I finally show results for the jet shape, differential in angle or transverse momentum, and the fragmentation spectrum with a cut on angle or transverse momentum. The default setup is as follows: $e^+e^- \to$ jets at a center of mass energy of $\sqrt{s} = 1$ TeV. The jets are identified using (the e^+e^- version of) anti-k_T with $R = 0.4$ and the WTA recombination scheme, and are required to have jet energy $E_J > 200$ GeV. The value of the jet radius is a fair compromise between suppressing power corrections in R and experimental significance, while the cut on jet energy leaves out spurious jets, formed by clusters of soft radiation. Predictions obtained from HERWIG 7.1.1 and PYTHIA 8.226, through a RIVET analysis [191] are compared to the analytic results based on the framework above. The cumulant jet shape I show is obtained by integrating eq. (3.28) over the jet energy, and has the following default normalization,

$$Z(\vartheta) = \left(\frac{\mathrm{d}\langle z\rangle}{\mathrm{d}\vartheta}\right) \Big/ \left(\int_{\vartheta_{\min}}^{R} \mathrm{d}\vartheta \, \frac{\mathrm{d}\langle z\rangle}{\mathrm{d}\vartheta}\right),$$

$$Z(k_T) = \left(\frac{\mathrm{d}\langle z\rangle}{\mathrm{d}k_T}\right) \Big/ \left(\int_{k_{\min}}^{k_{\max}} \mathrm{d}k_T \, \frac{\mathrm{d}\langle z\rangle}{\mathrm{d}k_T}\right), \tag{3.39}$$

with $\vartheta_{\min} = 0.1$ and $k_{\min} = 20$ GeV, $k_{\max} = 100$ GeV. The lower cut on angle (transverse momentum) imposes that the normalization is not dominated by hadronization effects, while the upper cut on transverse momentum reduces the impact of threshold effects on normalization.

Fig. 3.6 shows results for the jet shape. The central region of the distribution follows an (approximate) power law, where deviations from a simple $1/\vartheta$ are due to the resummation of logarithms of R/ϑ and the running of the coupling constant. Plotting $\vartheta Z(\vartheta)$ rather than $Z(\vartheta)$ highlights these deviations. Analytic and MC predictions agree well in this region, and my predictions have
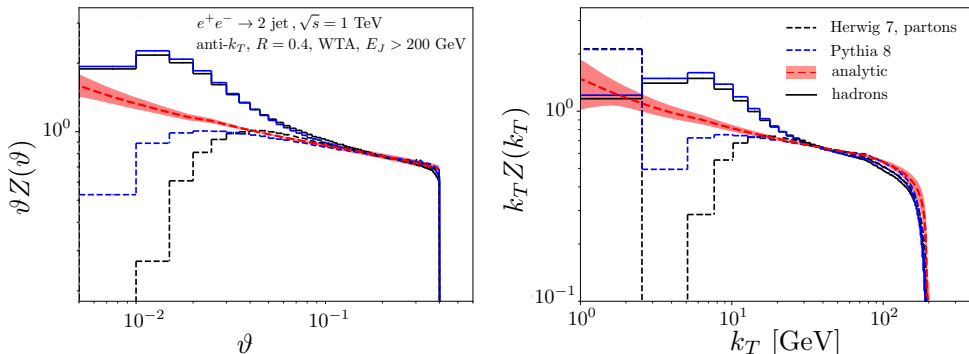
Figure 3.6 Jet shape in e^+e^- collisions, as a function of the angle (left) and transverse momentum (right), defined with the WTA jet axis, as predicted by Herwig (black) and Pythia (blue) at hadron (solid) and parton (dashed) level, compared to my analytic prediction (red). Here and in the following $e^+e^- \to 2$ jets refers to the MC setting *before* the parton shower, while our measurement is *inclusive* on the number of jets.

the added benefit of a theory uncertainty estimate. The power-law behavior extends to the edge of the jet for the angular distribution, but has a smooth turnoff for the transverse momentum distribution (right panel) due to the effect of the jet energy distribution on eq. (3.2). In particular, reliable predictions near the endpoint require the resummation of threshold logarithms, discussed in [2]. Moving on to the small k_T region, one notes that the parton-level distribution is peaked near $k_T = 0$ because the WTA axis is always along a particle. The adjacent "dead cone" is due to the shower cut off[3], and is filled with radiation by the hadronization model. This effect is not visible with standard axes, whose position is smeared by soft radiation, suggesting that the WTA axis is particularly useful for studying this non-perturbative physics. Note that HERWIG and PYTHIA differ before hadronization, but agree well after including it. The purely perturbative calculation is not valid in this region; extending the predictions there would require developing a non-perturbative model to supplement the factorization ingredients with $\Lambda_{\mathrm{QCD}}/k_T$ corrections. The plot suggests that non-perturbative effects already become important for $k_T \lesssim 10$ GeV. The reason for this is the denominator of eq. (3.1): a hadron with $z_h \sim 0.1$ and $k_T = 10$ GeV has a transverse momentum of $p_{hT} = z_h k_T = 1$ GeV.

---

[3]Event generators regulate the collinear singularity with a minimum angle for each emission, analog to R_0 in eq. (3.15). Since the WTA axis lies on a particle, nothing is found at $\vartheta < R_0$
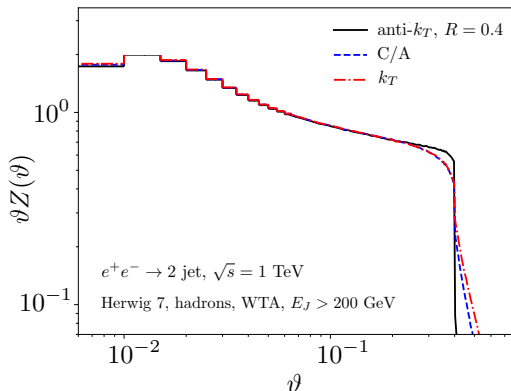
Figure 3.7 The jet shape at hadron level as function of angle for the e^+e^- anti-k_T (black), Cambridge/Aachen (blue dashed) and k_T algorithm (red dot-dashed).

Next we investigate in fig. 3.7 the dependence of the jet shape on the specific jet algorithm, comparing the (e^+e^- version of) anti-k_T, Cambridge/Aachen and k_T algorithms, using the WTA recombination scheme. There are only differences at the very edge of the jet, and they are rather small. Since the WTA axis is robust, these differences are due to particles at the edge of the jet being clustered into it or not. As expected, anti-k_T has the sharpest edge (since it clusters energetic particles first) while k_T the softest edge. The NLO analytic calculation yields identical predictions for the three cases, so the good agreement gives some indirect evidence that higher-order corrections are under control. The differences between algorithms would most likely become larger when there are many jets in an event, e.g. when the cut on E_J is loosened or pp collisions are considered.

In the left panel of fig. 3.8, I show MC results for the jet shape with anti-k_T, for different radii $R = 0.2, 0.4$ and 1. Exclusive k_T is also shown, which clusters the whole event into two jets, and thus corresponds to $R \sim \pi/2$. The WTA axis is the same, independent of R, which is why the distributions overlap. For larger values of ϑ the collinear approximation no longer holds, and the distribution even rises due to a Jacobian factor. Specifically, one would expect a constant energy density from soft radiation, i.e. $\mathrm{d}E/\mathrm{d}\Omega = \mathrm{d}E/(\mathrm{d}\varphi\mathrm{d}\vartheta\sin\vartheta) \sim$ constant, implying that $\vartheta\mathrm{d}E/\mathrm{d}\vartheta \sim \vartheta/(\sin\vartheta)$ rises. This is not the case for the jet shape using the standard jet axis, as shown in the right panel of fig. 3.8, because the axis will reposition itself depending on all the radiation in the jet. This figure also clearly shows that the jet shape with standard jet axis exhibits Sudakov double logarithms instead of a power-law dependence on ϑ.

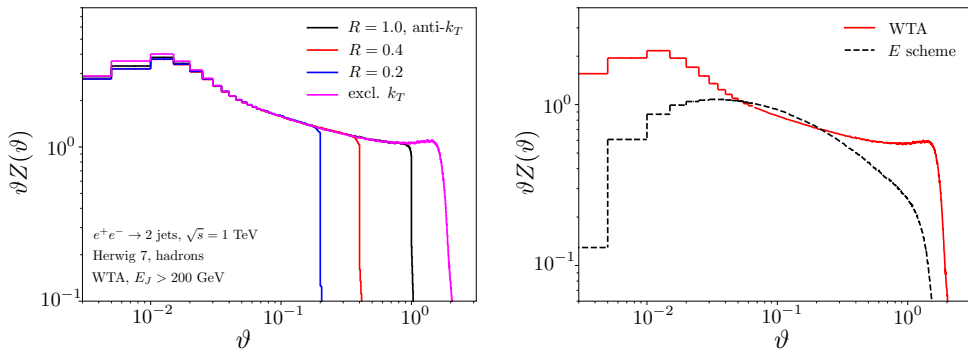The jet shape distributions shown so far go down to angles smaller than the

Figure 3.8 Left: the jet shape as function of the angle for different values of the jet radius R, and for exclusive k_T (two jets). The curves are normalized in $\theta = [0.1, 0.2]$. Right: the jet shape for exclusive k_T as function of angle with the WTA axis (red) and standard jet axis (black dashed).

typical size of a calorimeter cell ($\vartheta \approx 0.1$ at the LHC). The left panel of fig. 3.9 demonstrates that limited angular resolution does not change the jet shape. Specifically, the jets were reclustered into subjets of radius $r < R$, and the jet shape recalculated using these subjets as input, instead of hadrons. The distributions overlap as long as the angle is above the subjet radius scale, and below the subjet radius the distribution drops off, except for the contribution from $\vartheta = 0$. These features are easily explained by the WTA axis always lying on a particle (in this case, a subjet). Alternatively, a more granular angular resolution can be achieved tracking specific particles. The right panel of fig. 3.9 shows that the jet shape is essentially unaltered when defined on all hadrons or only on charged pions. As discussed in sec. 3.2.1, this distribution would benefit by increased resolution but would be likely more sensitive to hadronization effects, and requires a few non-perturbative parameters to implement in the analytic calculation.

Next I consider the effect of a cut on transverse momentum on the fragmentation spectrum of charged pions, see fig. 3.10. For $z_h > 0.5$, the WTA axis is along the hadron and the distribution is insensitive to the cut, which is why this region is not shown. In fact, the effects of the cut are clearly visible at small z_h but already negligible for $z_h > 0.3$, suggesting that hadrons with this energy fraction almost always control the axis. The analytic curves exhibit a similar qualitative behavior as those obtained using HERWIG, as is particularly clear in the subpanels which show the ratio to the most-inclusive cut on k_T. The difference in absolute normalization indicates that the intrisically-nonperturbative fragmentation spectrum used by HERWIG differs from the DSS global fit.
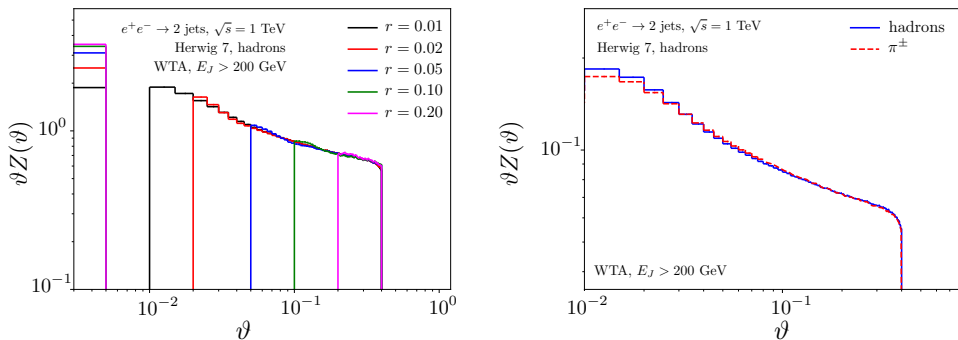
Figure 3.9 Left: the jet shape using subjets (instead of hadrons) as input. The lowest bin gets its contribution from $\vartheta = 0$. All the jet shapes were normalized by the same factor, taken to be the area of the $r = 0.01$ curve in $\vartheta = [0.1, 0.4]$. Right: the jet shape using all particles (blue) and only charged pions (red dashed) as input. The red-dashed pion distribution has been normalized to the blue curve for all particles to emphasize the similarity in the shape.

3.3 Outlook

Before moving on to a second application of recoil-free jets, I will comment on the findings presented in this chapter and discuss the natural extensions of this work. The physical process that I considered was fragmentation of hadrons inside jets, whose transverse momentum dependence I mainly described through the study of the jet shape, defined relative to the WTA axis.

As already noted, what makes the framework interesting from a theoretical point of view is that it yields purely collinear observables. Despite the presence of multiple scales, the factorization picture is relatively simple, because it does not involve rapidity divergences and non-global logarithms. This allowed me to sensibly describe the jet shape across the whole perturbative range in transverse momentum, by just combining two of the factorization regimes using a natural prescription. In view of future extensions, the observable being purely collinear will also make it easier to calculate the perturbative ingredients to higher orders, although two-loop calculations involving jet algorithms are largely unexplored territory.

Regarding phenomenological interest, the results I showed in sec. 3.2.3 highlighted two prominent features: the first one is the aforementioned power-law behavior of the jet shape, resulting from the absence of Sudakov double logarithms. Such a definite scaling is highly promising in view of precision physics as it delivers a clear prediction to compare with experiments. The second one is the stability of the axis: the WTA clustering procedure is highly robust,
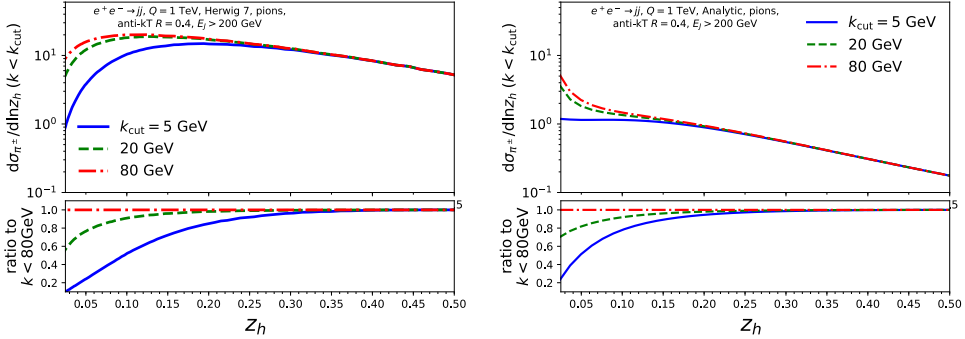
Figure 3.10 The fragmentation spectrum of charged pions with a cut on their transverse momentum, from Monte Carlo (left) and through the analytic calculation (right). The lower panels shows the ratio to the "most-inclusive" cut $k_{\mathrm{cut}} = 80$ GeV.

as single low-energy emissions barely affect the jet direction. As relevant examples, I showed with MC simulations that reclustering into subjets, varying algorithm within the k_T family, or summing over charged pions rather than all hadrons cause only minor alterations to the jet shape. This stability would help overcome common problems in a "real" collider, such as finite angular resolution and limited tagging efficiency.

The first natural extension of the work would be pp collisions, in order to obtain predictions for the LHC. The perturbative ingredients required by the analysis are the same, with the factorization formula in eq. (3.5) supplemented by the convolutions with two collinear PDFs. An interesting question is whether these convolutions could smear out the relevant features of the jet shape. The MC simulation in fig. 3.11 shows this is not the case, presenting results at the 13 TeV LHC. Now $z_h = p_{T,h}/p_{T,J}$, is the transverse momentum fraction and in place of ϑ we quantify the distance to the jet axis through $\Delta R = \sqrt{(\varphi_h - \varphi_J)^2 + (y_h - y_J)^2}$, where φ and y are the azimuthal angle and rapidity. Specifically, the plot shows the pp version of the jet shape $Z(\Delta R)$, normalized to 1 in the region $[0.1, R]$. The same (approximate) power-law behavior observed for the e^+e^- case is also evident for pp collisions. Also shown is the jet shape after soft drop with $z_{\mathrm{cut}} = 0.1$ and $\beta = 2$. Due to the large β, this grooming is rather mild, so only affects the region close to the jet boundary.

In the pp case, convolution with the PDFs would introduce a new source of error, but since these are relatively well constrained, I expect the perturbative uncertainty to still play a dominant role. Using the recoil-free jet shape to precision QCD test would most likely require to extend the fixed-order accuracy to NNLO, and investigate evolution beyond LL.

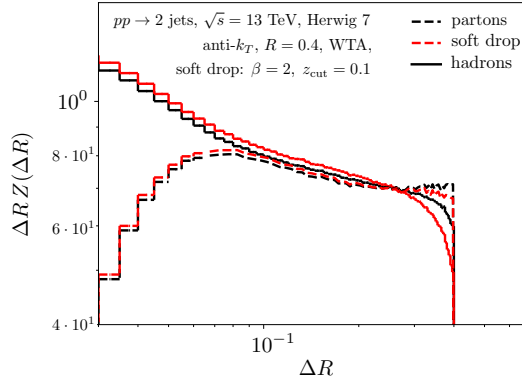In addition to the intrinsic interest for the TMD community and the possible

Figure 3.11 Jet shape at the LHC for jets with $p_{T,J} > 200$ GeV at hadron (solid) and parton level (dashed), using all particles (black) or after applying soft drop (red). The shape shows the same main features as the analog e^+e^- observable.

precise QCD measurement, the observables presented here are promising for studying the quark-gluon plasma, since the medium produces so much low-energy radiation that it is essential to remove that source of contamination. Another possible direction is to consider recoil-free axes for more complicated observables, for instance those used to tag boosted heavy objects.

4

Transverse Momentum Distributions from recoil-free jets

The structure of the proton has been a fundamental research topic for a long time. Besides intrinsic interest in the complex interplay of gluons and quarks in a bound state, an increasingly detailed description of the nucleon is demanded to achieve high precision at hadron colliders such as the LHC, and therefore important in the search for new short-distance physics. Since the early days of the parton model, the main focus has been on the collinear PDFs that I discussed in sec. 2.2.1. However, the precision of the LHC and the advent of the electron-ion collider (EIC) have raised attention on differential cross sections that probe TMDs. In particular, the EIC will enable the extraction of TMDs with unmatched precision, with SIDIS playing an important role [192–194]. In the rest of the thesis, I will present applications of jets to the study of TMD-PDFs, with DIS being the main focus. The analysis of the present chapter will build again on the properties of the WTA axis. Similar to in-jet fragmentation, I will show that the absence of recoil causes a major simplification in the factorization structure, which in turn makes it possible to achieve a remarkable level of theoretical precision.

Traditional processes involving a transverse momentum measurement are dihadron production in e^+e^- collisions, γ^*/Z boson production in pp, and SIDIS [123–126, 128–130]. Since a transverse momentum measurement can also be thought of as the measurement of an angle, the factorization formulae for these processes involve two TMDs. In the case of SIDIS, the factorization in eq. (2.25) gets complicated by the presence of non-perturbative physics in both the initial and final state of the process. Measuring a perturbatively calculable jet instead of a hadron would in principle remove the main source of final-state non-perturbative uncertainty, allowing for a cleaner extraction of the TMDPDFs.[1]

---

[1]In practice, of course, when the transverse momentum is small the jet functions themselves are affected by hadronization corrections. I will extensively comment on this in the outlook.

With this motivation in mind, in [1] we investigated TMD factorization for jet production. There we proved that a class of processes, including DIS+jet, obeys the same factorization formulae valid for single hadrons, with the TMDFF replaced by a TMD jet function. Not only do the formulae look similar, but they involve the exact same ingredients except for the jet function. This is very convenient, because as I discussed in sec. 2.2, these ingredients are known at NNLO+N^{3}LL. With the WTA axis, this applies independent of the jet radius, providing a simple and comprehensive framework. In ref. [3] we supplemented our analysis with numerical predictions for $e^+e^- \to$ dijet and DIS+jet. We found that even for moderate values of the jet radius parameter ($R \gtrsim 0.5$) using the large-R limit of the jet function gives an excellent approximation of the TMD cross section. We could then determine numerically the NNLO jet function in this limit, achieving N^{3}LL accuracy.

The rest of the chapter is based on the two works mentioned above. Sec. 4.1 presents the framework: building on the mode analysis, I discuss factorization for the various hierarchies between the relevant angles and the jet radius, compute the one-loop ingredients and describe the extraction of the two-loop function. In sec. 4.2 I show numerical predictions for e^+e^- and ep collisions, and comment on the results.

4.1 Theoretical framework

4.1.1 Kinematics and modes

In the following I will consider two different processes, $e^+e^- \to 2$ jets and DIS+jet. Although the main phenomenological focus is on the latter, the former provides a useful testing ground of the theoretical framework: lepton collisions allow for studying the jet functions without worrying about parton distributions, and in sec. 4.2 I will show plots also for this process.

In the case of $e^+e^- \to$ dijet, the main physical quantity I consider is the transverse momentum decorrelation. It is defined as

$$\boldsymbol{q} = \frac{\boldsymbol{p}_1}{z_1} + \frac{\boldsymbol{p}_2}{z_2}, \qquad (e^+e^- \to \text{dijet}) \qquad (4.1)$$

where $\boldsymbol{p}_i$ are the jet transverse momenta measured with respect to a common direction and $z_i = 2E_i/\sqrt{s}$ are their energy fractions, $\sqrt{s}$ is the center-of-mass energy of the collision. For factorization to be valid, I will always assume

$$q_T \equiv |\boldsymbol{q}| \ll \frac{\sqrt{s}}{2} \,. \qquad (4.2)$$

A related quantity is the *angular* decorrelation, shown in the right panel of fig. 4.1,

$$\vartheta = \arctan\left(\frac{2q_T}{\sqrt{s}}\right) \approx \frac{2q_T}{\sqrt{s}} \ll 1, \qquad (e^+e^- \to \text{dijet}) \qquad (4.3)$$

where the final expression exploits eq. (4.2). This makes it explicit that we consider configurations where jets are almost back to back. The angular decorrelation is similar to the azimuthal decorrelation in hadronic collisions, calculated at NLL accuracy in refs. [195–198].

In principle, the definitions in eqs. (4.1) and (4.3) depend on the direction with respect to which the jet transverse momenta are measured. However, differences induced by this choice are suppressed by powers of q_T^2/s, thus they do not matter in the effective-theory description. Of course, the definition *is* sensitive to the details of the jet algorithm: the default will be the WTA axis with anti-k_T, but I will also consider the standard jet axis and other clustering algorithms of the k_T family.
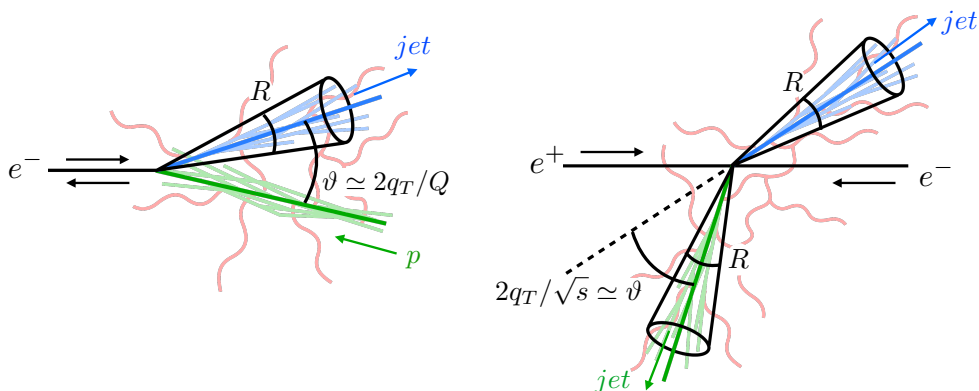

Figure 4.1 Sketch of the TMD processes I consider in this chapter: DIS+jet in the Breit frame (left) and dijet production from e^+e^- collisions (right). The angle ϑ is assumed small, but can compete with the jet radius R.

The kinematics for DIS+jet in the Breit Frame (fig. 4.1) is analogous to the one discussed in sec. 2.2.2 for SIDIS, with the straightforward replacement hadron → jet. Explicitly, the transverse momentum reads

$$\boldsymbol{q} = \frac{\boldsymbol{P}_J}{z} + \boldsymbol{q}_{\text{in}}, \qquad (\text{DIS+jet}) \qquad (4.4)$$

where $\boldsymbol{P}_J$ is the transverse momentum of the jet with respect to the beam axis, $\boldsymbol{q}_{\text{in}}$ is the transverse momentum of the initial-state quark in the proton,

and $z = 2E_J/Q$ is the jet energy normalized to (minus) the virtuality of the photon Q^2. The choice of Breit frame is suggested by existing experimental analyses at HERA, the only large electron-proton collider that operated so far: in particular, measurements of DIS+jet [199–202] were preferentially carried out in this frame. In analogy with eq. (4.3), I define a corresponding angle ϑ,

$$\vartheta = \arctan\left(\frac{2q_T}{Q}\right) \simeq \frac{2q_T}{Q} \ll 1 \,. \qquad \text{(DIS+jet)} \qquad (4.5)$$

I use the same symbols $\boldsymbol{q}$ and ϑ for similar quantities in DIS+jet and $e^+e^- \to$ dijet. This should not generate confusion, since they play the very same role in factorization formulae.

I now turn to presenting the modes that enter the SCET analysis. I will describe dijet production for definiteness, but everything I will say also applies to DIS+jet, where the incoming proton beam takes the place of one of the jets in the anticollinear direction. While the angle ϑ is always assumed small, I will consider in turn the three hierarchies $R \ll \vartheta$, $R \sim \vartheta$ and $R \gg \vartheta$. In fact, the case of small jets has rather limited practical utility, as there is no room for reconstructing such narrow jets in a detector with limited angular resolution. However, this is an interesting case to consider theoretically, as it will provide a useful consistency check of the framework.

Let me discuss this starting from the simplest case $R \sim \vartheta$. As I already described in sec. 1.3.2, in TMD dijet production the small angle ϑ plays the role of power-counting parameter. The transverse momentum measurement imposes the SCET$_\text{II}$ picture, with soft and collinear modes scaling as

$$p_\text{c} \sim \sqrt{s}\,(\vartheta^2, 1, \vartheta)\,, \qquad p_\text{s} \sim \sqrt{s}\,(\vartheta, \vartheta, \vartheta)\,, \qquad (4.6)$$

in the usual $p = (p_+, p_-, p_\perp)$ lightcone decomposition, with the anticollinear mode obtained from the collinear one by exchanging $p_+ \leftrightarrow p_-$.

The situation is slightly more involved if $R \ll \vartheta \ll 1$. The additional hierarchy produces the new modes

$$p_\text{c2} \sim \sqrt{s}\,(R^2, 1, R)\,, \qquad (4.7)$$

whose virtuality is suppressed by the small ratio R/ϑ with respect to eq. (4.6). This regime will involve refactorizing the collinear functions, with R/ϑ corrections expanded away. Intuitively, jet production decouples from the transverse momentum dependence, because collinear splittings within the jet alter the transverse momentum by a power-suppressed amount. One also expects the fine details of the jet algorithm to become irrelevant, because the jet is essentially shrunk to a pencil of radiation.

The most interesting configuration is the opposite hierarchy, $\vartheta \ll R$. Here the jet definition is expected to be maximally relevant, and indeed the difference between recoil-free jets and standard jets shows up dramatically. Let me start from standard algorithms, where the situation is much more involved. The corresponding framework was formulated in [203, 204] (see also [205, 206]): I will not explore the phenomenology of this case, but describe the picture to point out its complexity.

Consider first radii of order unity, $\vartheta \ll R \sim 1$. Energetic emissions outside the jets are not allowed, because these would lead to $\vartheta \sim R$. Because the standard jet axis balances the momentum of soft and collinear radiation inside the jet, momentum conservation implies that q_T is determined by only the transverse momentum of *soft* radiation *outside* the jets. In particular, the angle of energetic emissions inside the jet is unrestricted. Since $R \sim 1$, these emissions are hard, thus the collinear mode is absent. Each hard emission induces a soft Wilson line that can emit radiation outside the jet, and the observable is dominated by non-global logarithms of $\sqrt{s}R/q_T$.

When $\vartheta \ll R \ll 1$, the transverse momentum is still determined by only the soft radiation outside the jet, but the rightmost inequality induces collinear modes whose angular size is set by R. In addition, there will be a mode with scaling

$$p_{\rm cs} \sim \vartheta/R\,(1, R^2, R)\,, \tag{4.8}$$

fixed by the requirement that it resolves the jet boundary and contributes to the q_T measurement. This mode is referred to as *collinear-soft*, as its components have the typical relative collinear scaling, but is less energetic than collinear radiation. Because $R \ll 1$, no hard emissions are allowed, and soft radiation does not resolve the jet. However, each collinear emission produces a collinear-soft Wilson line, in direct analogy to the soft Wilson lines generated by hard emissions for $R \sim 1$.

The complications introduced by the above picture are manageable, but they burden the theoretical description. In particular, getting precise predictions would require resumming non-global logarithms. The problem has large practical relevance, since the large-R case could be the most useful for studying the small intrinsic transverse momentum of quarks and gluons in the proton. Fortunately, measuring transverse momenta relative to the WTA axis avoids all the complications above. The key observation is that soft radiation does resolve the jet boundary, but does not affect the direction of the WTA axis, hence there is no distinction between soft emissions inside or outside of the jet. In other words, without recoil, a broad jet containing a large amount of soft radiation still describes purely collinear dynamics. Since $R \gg \vartheta$, collinear

Case\Mode	coll	coll$_2$	csoft	soft
$\vartheta \sim R \ll 1$	$(1, \vartheta^2, \vartheta)$			$(\vartheta, \vartheta, \vartheta)$
$R \ll \vartheta \ll 1$	$(1, \vartheta^2, \vartheta)$	$(1, R^2, R)$		$(\vartheta, \vartheta, \vartheta)$
$\vartheta \ll R$ (WTA)	$(1, \vartheta^2, \vartheta)$			$(\vartheta, \vartheta, \vartheta)$
$\vartheta \ll R \ll 1$ (Std)				$(\vartheta, \vartheta, \vartheta)$
$\vartheta \ll R \sim 1$ (Std)		$(1, R^2, R)$	$\vartheta/R(1, R^2, R)$	$(\vartheta, \vartheta, \vartheta)$

Table 4.1 The parametric scaling of the momenta $(p_-, p_+, p_\perp)/\sqrt{s}$ corresponding to the IR modes in SCET, for the various hierarchies between ϑ and R. For $\vartheta \ll R$ the modes differ between the Winner-Take-All (WTA) and standard (Std) jet axes.

radiation does not resolve the jet boundary, thus the modes are still the ones in eq. (4.6). One could expect the same collinear-soft modes in eq. (4.8), as for standard jets. However, by the same reasoning as before, their only effect is a total recoil on the system. Consequently, these additional modes do not need to be considered, since they will simply be removed by the zero-bin subtraction due to their overlap with the soft mode. Ultimately, in this case the jet radius does not play any role in the mode analysis; in particular, whether $R \ll 1$ or $R \sim 1$ does not matter, as long as the radius is larger than the angular decorrelation.

   In the next subsection I will discuss the factorization arising from these modes, translating into equations what I described in words here. Since I considered several different cases, a recap of the modes is perhaps useful, see table 4.1.

4.1.2 Factorization and evolution

I now move on to the factorization analysis, starting with dijet production in e^+e^- scattering, where $\vartheta \approx 2q_T/\sqrt{s} \sim R \ll 1$. This is the simplest case since there are only two scales, $\sqrt{s}$ and q_T. The cross section differential in the momentum decorrelation $\boldsymbol{q}$ and the jet energy fractions $z_i = 2E_{J,i}/\sqrt{s}$ factorizes as

$$\frac{\mathrm{d}\sigma_{e^+e^- \to JJX}}{\mathrm{d}z_1 \, \mathrm{d}z_2 \, \mathrm{d}\boldsymbol{q}} = \sigma_0^{e^+e^-}(s) \, H_{e^+e^-}(s, \mu) \int \frac{\mathrm{d}\boldsymbol{b}}{(2\pi)^2} \, e^{-i\boldsymbol{b}\cdot\boldsymbol{q}}$$

$$J_q^{\mathrm{alg}}(z_1, \boldsymbol{b}, \tfrac{\sqrt{s}}{2}\mathcal{R}, \mu, \zeta) \, J_{\bar{q}}^{\mathrm{alg}}(z_2, \boldsymbol{b}, \tfrac{\sqrt{s}}{2}\mathcal{R}, \mu, \zeta) \left[1 + \mathcal{O}\left(\frac{q_T^2}{s}\right)\right], \quad (4.9)$$

The hard function $H_{e^+e^-}$ encodes the hard scattering process, in which a quark-anti-quark pair is produced. It contains virtual corrections, but no real radiation because that would result in $q_T \sim \sqrt{s}$. The result up to two loop is

shown in eq. (B.32); for convenience, I have extracted the tree-level cross section $\sigma_0^{e^+e^-}$, which contains a sum over quark flavors. The jet functions describe the fraction z_i of energy of the initial (anti-)quark that goes into the jet, as well as their transverse momentum through its Fourier conjugate, the impact parameter $\boldsymbol{b}$. They depend on the jet algorithm, as indicated by the superscript, but this does not affect their anomalous dimension, as required by RGE consistency. Here I introduced the modified jet radius parameter

$$\mathcal{R} = 2\tan(R/2) \tag{4.10}$$

that reduces to R for small radii. By simple geometrical considerations, it follows that $\mathcal{R}$ (rather than R) in the preferential quantity that enter the expressions for transverse momenta.

The corresponding factorization formula for the cross section of DIS+jet is given by

$$\frac{\mathrm{d}\sigma_{ep\to eJX}}{\mathrm{d}Q^2\,\mathrm{d}x\,\mathrm{d}z\,\mathrm{d}\boldsymbol{q}} = \sum_q \sigma_{0,q}^{\mathrm{DIS}}(x,Q^2)\,H^{\mathrm{DIS}}(Q^2,\mu) \int \frac{\mathrm{d}\boldsymbol{b}}{(2\pi)^2}\,e^{-i\boldsymbol{b}\cdot\boldsymbol{q}}$$

$$F_q(x,\boldsymbol{b},\mu,\zeta)\,J_q^{\mathrm{alg}}\left(z,\boldsymbol{b},\frac{Q\mathcal{R}}{2},\mu,\zeta\right)\left[1+\mathcal{O}\left(\frac{q_T^2}{Q^2}\right)\right]. \tag{4.11}$$

which is differential in the di-lepton invariant mass Q^2, Bjorken x, the energy fraction z of the jet, and the jet transverse momentum $\boldsymbol{q}$. It is the same as the formula for SIDIS, eq. (2.35), with just the replacement $D_{q\to h}\to J_q$. As I discussed in sec. 4.1.1, this occurs because in absence of recoil the jet radius does not interfere with the mode picture of SIDIS. By RGE consistency, they have the same dependence on the UV and rapidity scales μ,ζ as the TMDFFs, and similar to those I assume that a square root of the soft function has been absorbed in the jet, yielding a quantity which is free of rapidity divergences.

The difference between eqs. (4.9) and (4.11) is fairly modest: the hard function is replaced by the one for DIS, but the two are related by crossing symmetry,

$$H_{e+e-}(Q^2,\mu) = |C_V(Q^2,\mu)|^2\,, \qquad H^{\mathrm{DIS}}(Q^2,\mu) = |C_V(-Q^2,\mu)|^2\,; \tag{4.12}$$

one of the jet functions is replaced by a TMDPDF, and the sum over quark flavors must be explicitly included because both $\sigma_{0,q}^{\mathrm{DIS}}$ and F_q depend on flavor (J_q does not, as long as we can treat quarks as massless). By universality of collinear physics, the jet functions are the same for the two processes.

I now consider the case where the small size of the jet radius induces an additional hierarchy, $R\ll\vartheta\ll 1$. In the rest of this chapter, for the purpose of generality, I will denote with E the energy of the parton producing the jet

with (up to power corrections), $E = \sqrt{s}/2$ for dijet production and $E = Q/2$ for DIS+jet. The factorization in this case is an extension of eqs. (4.9) and (4.11). The two scales $E\mathcal{R} \ll q_T$ in the jet functions can be separated through the refactorization

$$J_i^{\text{alg}}(z, \boldsymbol{q}, E\mathcal{R}, \mu, \zeta) = \sum_j \int \frac{\mathrm{d}z'}{z'} \, \mathbb{C}_{i \to j}(z', \boldsymbol{q}, \mu, \zeta) \, \mathcal{J}_j\Big(\frac{z}{z'}, \frac{2z}{z'} E\mathcal{R}, \mu\Big)$$

$$\times \big[1 + \mathcal{O}(E^2\mathcal{R}^2/q_T^2)\big]. \quad (4.13)$$

This is analogous to the matching of TMDFFs onto collinear FFs in eq. (2.36) for large transverse momentum, and indeed the matching coefficients coincide. Intuitively, only collinear radiation at angular scales ϑ, encoded in $\mathbb{C}_{i \to j}$, can affect q_T. However, subsequent splittings down to angles of order R will change the parton j with momentum fraction z' into a jet with momentum fraction z. This is described by the semi-inclusive jet function $\mathcal{J}_j$, which has been calculated to $\mathcal{O}(\alpha_s)$ in refs. [163, 188] (my notation matches that of ref. [188], and explicit expressions are collected in appx. B.2.2). The distinction between WTA and standard jet axis is irrelevant, since $\vartheta \gg R$, and indeed the $\mathcal{J}_j$ are the same for the two schemes. The additional RG evolution between the natural scales $\mu_J \sim q_T$ and $\mu_{\mathcal{J}} \sim E\mathcal{R}$ sums single logarithms of $\mu_J/\mu_{\mathcal{J}} \sim q_T/(E\mathcal{R}) \sim \vartheta/R$, although the improvement granted by resummation is expected to be irrelevant for phenomenologically relevant choices of R.

Finally, I describe the case of large radius, starting from WTA jets. From the discussion summarized in table 4.1, the hierarchy $R \gg \vartheta$ leaves the SCET modes unaltered: rather than a refactorization, the situation is described by simply taking the analytical limit of the jet functions,

$$J_i^{\text{WTA}}(z, \boldsymbol{q}, E\mathcal{R}, \mu, \zeta) = \delta(1-z) \, \mathscr{J}_i(\boldsymbol{q}, \mu, \zeta) \big[1 + \mathcal{O}\big(q_T^2/(E\mathcal{R})^2\big)\big]. \quad (4.14)$$

All collinear radiation has been clustered into the jet, implying that there is no dependence on the jet radius in this limit. For the same reason, one can extract $\delta(1-z)$, as all the energy is enclosed by the jet. The form of eq. (4.14) is remarkably simple. Furthermore, by dimensional analysis, the dependence of $\mathscr{J}$ on $E\mathcal{R}$ is entirely determined by the dependence on the scales μ, ζ, which in turn is known by RGE consistency. In practice, determining $\mathscr{J}$ reduces to computing one constant: in sec. 4.1.5, I will use this fact to extract the two-loop expression for $\mathscr{J}$ numerically.

For completeness, let me quote the factorization formulae for the standard axis when $R \gg \vartheta$. These are based on [203, 204], and I will show for brevity only the $e^+e^- \to$ dijet case. When $\vartheta \ll R \sim 1$ there is only a soft mode, and

$$\frac{\mathrm{d}\sigma^{\mathrm{std}}_{e^+e^- \to JJX}}{\mathrm{d}\boldsymbol{q}} = \sum_{m=2}^{\infty} \mathrm{tr}_c\Big\{ \mathcal{H}_m(\{n_i\}, \sqrt{s}, \mathcal{R}) \otimes \mathcal{S}_m(\{n_i\}, \boldsymbol{q}, \mathcal{R}) \Big\} \Big[1 + \mathcal{O}\Big(\frac{q_T^2}{Q^2}\Big) \Big].$$

(4.15)

I have eliminated the measurement of the momentum fractions of the jets, since $z_i = 1$ in this limit. $\mathcal{H}_m$ denotes the hard function with m real emissions inside the jets, along the light-like directions n_i: as discussed in the previous section, one needs considering an arbitrary number of such emissions. The soft function $\mathcal{S}_m$ describes the transverse momentum q_T of soft radiation outside the jets, produced by the Wilson lines along the directions n_i. The color indices identify the representation of the hard emissions/Wilson lines connecting the hard and soft function, and tr_c denotes the trace over these color indices. Finally, $\otimes$ denotes integrals over the light-like directions n_i.

The last case is the hierarchy $\vartheta \ll R \ll 1$ for standard jets. It features additional collinear and collinear-soft modes (last row in table 4.1), whose refactorization yields

$$\frac{\mathrm{d}\sigma^{\mathrm{std}}_{e^+e^- \to JJX}}{\mathrm{d}\boldsymbol{q}} = \sigma_0^{e^+e^-}(s)\, H_{e^+e^-}(s, \mu) \int \frac{\mathrm{d}\boldsymbol{b}}{(2\pi)^2}\, e^{-i\boldsymbol{b}\cdot\boldsymbol{q}}\, S(\boldsymbol{b})$$
$$\times \Big[\sum_{m=2}^{\infty} \mathrm{tr}_c\Big\{ \mathcal{J}_m(\{n_i\}, \tfrac{\sqrt{s}}{2}\mathcal{R}) \otimes \mathcal{U}_m(\{n_i\}, \boldsymbol{b}, \mathcal{R}) \Big\} \Big]^2 \Big[1 + \mathcal{O}\Big(\frac{q_T^2}{Q^2}\Big) \Big]. \quad (4.16)$$

The hard and soft function are the same as for $\vartheta \sim R$. The jet function $\mathcal{J}_m$ describes m collinear emissions inside a jet along light-like directions n_i, and the collinear-soft function $\mathcal{U}_m$ describes the resulting q_T from collinear-soft emissions of these Wilson lines.

In the case $R \sim \vartheta$, the RGE is identical to the one of TMDs. For DIS, this is evident from the factorization formulae in eqs. (4.11) and (2.31), and we can reuse the evolution equations (2.38) for the jet functions. Explicitly,

$$\mu\frac{\mathrm{d}}{\mathrm{d}\mu} J_i^{\mathrm{alg}}(z, \boldsymbol{b}, ER, \mu, \zeta) = +\gamma_i(\mu, \zeta) J_i^{\mathrm{alg}}(z, \boldsymbol{b}, ER, \mu, \zeta), \qquad (4.17)$$

$$\zeta\frac{\mathrm{d}}{\mathrm{d}\zeta} J_i^{\mathrm{alg}}(z, \boldsymbol{b}, ER, \mu, \zeta) = -\mathcal{D}_i(\boldsymbol{b}, \mu) J_i^{\mathrm{alg}}(z, \boldsymbol{b}, ER, \mu, \zeta). \qquad (4.18)$$

Since the anomalous dimensions do not involve z, this results extends trivially to the large-R limit (4.14) when using the WTA axis. As for the small-R case described by eq. (4.13), the matching coefficients $\mathbb{C}_{i \to j}$ are responsible for the double scale evolution, while the semi-inclusive jet functions have DGLAP evolution [188], in direct analogy with the matching to collinear FFs.

4.1.3 One-loop calculation of the jet functions

The predictions presented in ch. 3 built on analytical expressions available in the literature. As a consequence, I kept hidden one of the fundamental parts of our research activity: computing perturbative ingredients in the effective theory. To make amends, I will now show in detail the one-loop calculation of the TMD jet functions that enter the factorization formulae presented in sec. 4.1.2.

There are two natural ways to set up the calculation: either in momentum space or in impact-parameter space. The level of complexity is similar: the calculation in momentum space heavily relies on plus distributions involving two variables, but has the advantage that the angular cut imposed by the jet radius naturally translates to a cut in transverse momentum. Vice versa, working in impact parameter space only requires handling regular functions, but the angular cut generates integrals that are much harder to carry out. I will perform the calculation in momentum space, while the impact parameter calculation can be found in [3].

In the following I will focus on the quark jet function, since the processes I consider involve at leading power only quarks. The starting point is the matrix-element definition in terms of SCET operators,

$$
J_q^{\text{alg}}(z, E\mathcal{R}, \boldsymbol{q}) = \frac{z}{2N_c} \text{tr} \bigg\{ \frac{\overline{\slashed{n}}}{2} \langle 0 | \delta(2E\mathcal{R} - \overline{n} \cdot \mathcal{P}) \, \delta^{(2)} (z\boldsymbol{q} - \mathcal{P}_\perp) \, \chi_n(0) | JX \rangle
$$
$$
\times \langle JX | \overline{\chi}_n(0) | 0 \rangle \bigg\} . \quad (4.19)
$$

The delta functions fix the large and perpendicular momentum component of the measured quantities, the final state J carries the details of the jet algorithm, and the normalization is such that at tree level

$$
J_q^{[0]}(z, E\mathcal{R}, \boldsymbol{q}) = \delta(1 - z)\delta^{(2)}(\boldsymbol{q}) . \quad (4.20)
$$

The one-loop jet function requires computing the four SCET diagrams in eq. (2.6), where all the lines are collinear, summing over phase-space cuts. This can be done either with SCET Feynman rules, or by computing the matrix element (4.19) on QCD fields. Letting $\ell = (\ell_+, \ell_-, 0)$ be the incoming quark momentum and labeling k the loop momentum, one gets for the first diagram

$$
\frac{z}{2N_c} \text{tr} \left[\frac{\overline{\slashed{n}}}{2} \otimes \text{\raisebox{-3pt}{\includegraphics[height=18pt]{diagram}}} \otimes \right] = -\frac{g_s^2 \mu^{2\varepsilon} C_F}{4\ell^4} \int \frac{\mathrm{d}^d k}{(2\pi)^d} \, (2\pi)\delta^+\big((\ell - k)^2\big) \, (2\pi)\delta^+\big(k^2\big)
$$
$$
\times \text{tr}\big[\overline{\slashed{n}}\slashed{\ell}\gamma_\mu(\slashed{\ell} - \slashed{k})\gamma^\mu\slashed{\ell}\big]\delta_{\text{meas}}(z, \boldsymbol{q}, E\mathcal{R})
$$

$$= + 2g_s^2 \mu^{2\varepsilon} C_F \int \frac{\mathrm{d}^d k}{(2\pi)^{d-2}} \, \delta^+ \big((\ell - k)^2 \big) \, \delta^+ \big(k^2 \big)$$

$$\times \left[(1 - \varepsilon) \frac{\ell_+ - k_+}{\ell_+^2} \right] \delta_{\mathrm{meas}}(z, \boldsymbol{q} E\mathcal{R}) \, , \qquad (4.21)$$

where the cut through the loop imposes the two on-shell conditions δ^+, while δ_{meas} enforces the measurement, including the effects of the jet algorithm. The other diagrams in eq. (2.6) involve gluon insertions on Wilson lines: the definition eq. (1.159) yields the eikonalized Feyman rule

$$\text{} \quad = g_s \frac{n^\mu}{n \cdot (k - i\Delta)} t_a \, , \qquad (4.22)$$

where k is the outgoing gluon momentum, n is the reference direction, and Δ is the rapidity regulator, which in the spirit of [207] is implemented on Wilson lines. This fixes the rapidity divergences in the soft and collinear functions, while their product must be regular in the $\Delta \to 0$ limit. Repeating the steps in eq. (4.21) for the other diagrams, summing over diagrams and cuts yields

$$J_q^{[1]}(z, \boldsymbol{q}, E\mathcal{R}) = 4 C_F \left(\frac{\overline{\mu}^2 e^{\gamma_E}}{4\pi} \right)^\varepsilon \int_0^\infty \frac{\mathrm{d}\ell_+}{2\pi \ell_+} \int \frac{\mathrm{d}^d k}{(2\pi)^d} \delta^+(k^2) \delta^+ \big((\ell - k)^2 \big)$$

$$\left[\frac{\ell_- - k_-}{k_- - i\Delta_-} + \text{h.c.} + (1 - \varepsilon) \left(1 - \frac{k_+}{\ell_+} \right) \right] \delta_{\mathrm{meas}}(z, \boldsymbol{q}, E\mathcal{R}) \, , \quad (4.23)$$

where the hermitian conjugate refers to the previous term, $\overline{\mu}$ is the $\overline{\text{MS}}$ scale defined in eq. (1.20), and as a reminder, the superscript [1] denotes the first coefficient in the $\alpha_s/(4\pi)$ expansion.

To proceed, I identify $\ell_- = 2E$, rewrite the phase space measure as

$$\mathrm{d}^d k = \tfrac{1}{2} \mathrm{d}k_+ \, \mathrm{d}k_- \mathrm{d}^{d-2} k_\perp = E \, \mathrm{d}k_+ \, \mathrm{d}x \, \mathrm{d}^{d-2} k_\perp \, , \qquad (4.24)$$

where $x = 1 - k_-/\ell_-$ represents the energy fraction of the quark after splitting, and fix the two + components with the on-shell conditions,

$$J_q^{[1]}(z, \boldsymbol{q}, E\mathcal{R}) = 16\pi C_F \left(\frac{\overline{\mu}^2 e^{\gamma_E}}{4\pi} \right)^\varepsilon \int_0^1 \mathrm{d}x \int \frac{\mathrm{d}^{2-2\varepsilon} k_\perp}{(2\pi)^{2-2\varepsilon} k_\perp^2} \, \delta_{\mathrm{meas}}(z, \boldsymbol{q}, E\mathcal{R})$$

$$\times \left[\frac{(1 + x^2)(1 - x)}{(1 - x)^2 + \delta^2} - (1 - x)\varepsilon \right] . \qquad (4.25)$$

Here I introduced the dimensionless rapidity regulator $\delta = \Delta_-/E$. The measurement function expands as

$$\delta_{\mathrm{meas}}(z, \boldsymbol{q}, E\mathcal{R}) = \sum_{\mathrm{case}} \delta \left(z - \frac{E_{J\mathrm{case}}}{E} \right) \delta^{(2)}(\boldsymbol{q} - \boldsymbol{q}_{\mathrm{case}}) \, \Theta_{\mathrm{case}}(E\mathcal{R}) \, , \qquad (4.26)$$

where at one loop I need to consider the three cases

case	algorithm	Θ_{case}	$E_{J\text{case}}$	$q_{T\text{case}}^2$
(a) q,g in	Std	$\theta\big(x(1-x)E\mathcal{R} - k_\perp\big)$	E	0
	WTA			$\dfrac{k_\perp^2}{\max^2(x, 1-x)}$
(b) g out	Std/WTA	$\theta\big(k_\perp - x(1-x)E\mathcal{R}\big)$	Ex	$\dfrac{k_\perp^2}{x^2}$
(c) q out	Std/WTA	$\theta\big(k_\perp - x(1-x)E\mathcal{R}\big)$	$E(1-x)$	$\dfrac{k_\perp^2}{(1-x)^2}$

Table 4.2 Constraints imposed by the jet algorithm and energy/transverse momentum measurements, for different schemes (standard, WTA) and cases.

(a) both partons are inside the jet;

(b) the gluon is outside the jet;

(c) the quark is outside the jet.

The explicit expressions for $E_{J\text{case}}$ and $\boldsymbol{q}_{\text{case}}$ depend on the jet algorithm, and easily follow from the recombination prescriptions of eq. (2.3) (standard axis) and eq. (2.10) (WTA axis), while the phase-space cut imposed by the jet was given in eq. (2.7), with $\omega = 2E$. These constraints are summarized in table 4.2. At one loop, the scheme dependence is very modest: the clustering order does not matter (so all the algorithms of the k_T family yield the same result) and the difference between standard and WTA schemes shows up only in the transverse momentum measurement, when both particles are clustered in the jet. In particular, this implies that the semi-inclusive jet functions $\mathcal{J}$ in eq. (4.13) are the same for the two schemes, because they do not involve a transverse momentum measurement.

I will now solve in turn the remaining integrations for the different cases. In fact, it is evident from table 4.2 that the constraints for the quark/gluon case are symmetric for $x \leftrightarrow 1 - x$, and so is the integrand $(4.25)^2$, thus one can always combine (b) and (c).

Starting from the configuration of both particles inside the jet, standard jet axis, the dependence on the transverse momentum trivially factors out and the calculation reduces to the one performed in ref. [188] for the semi-inclusive quark jet function. After integration over the transverse momentum,

$$J_{q(a)}^{\text{std},[1]}(z, q_T^2, E\mathcal{R}) = -\frac{2C_F}{\pi} \left(\frac{\bar{\mu}^2}{E^2\mathcal{R}^2}\right)^\varepsilon \frac{e^{\varepsilon\gamma_E}}{\varepsilon\Gamma(1-\varepsilon)}\, \delta(1-z)\, \delta(q_T^2)$$

---

[2]This is a consequence of $q \to qg$ being the only vertex describing one-loop quark splitting, and fails at higher loops.

$$\times \int_0^1 \mathrm{d}x \, x^{-2\varepsilon}(1-x)^{1-2\varepsilon}\left[\frac{1+x^2}{(1-x)^2} - \varepsilon\right]. \tag{4.27}$$

Here I could set the rapidity regulator $\delta = 0$ because convergence issues at the endpoint $x = 1$ are already fixed by dimensional regularization, and I switched to distribution space in the norm q_T^2 using azimuthal symmetry,

$$\int_0^{2\pi} \mathrm{d}\varphi \, \delta^{(2)}(\boldsymbol{q}) = \pi\delta(q_T^2). \tag{4.28}$$

After this clarification, I will drop the arguments of the jet function for brevity. The remaining integral over the energy fraction is a combination of Euler's Beta functions, whose ε-expansion yields

$$J_{q(a)}^{\mathrm{std},[1]} = \frac{2C_F}{\pi}\,\delta(1-z)\,\delta(q_T^2)\left[\frac{1}{\varepsilon^2} + \frac{1}{\varepsilon}\left(\overline{L}_R + \frac{3}{2}\right) + \frac{1}{2}\overline{L}_R^2 + \frac{3}{2}\overline{L}_R + \frac{13}{2} - \frac{3\pi^2}{4}\right], \tag{4.29}$$

where

$$\overline{L}_R = \ln\left(\frac{\overline{\mu}^2}{E^2\mathcal{R}^2}\right). \tag{4.30}$$

Next, I consider the cases where only one particle is inside the jet, that are independent of the jet algorithm. One can use $x \to 1 - x$ to combine the case where the gluon is outside the jet with the case where the quark is outside. Both the integrals over transverse momentum and energy fraction are fixed by the δ functions enforcing the measurement, resulting in

$$J_{q(b)+(c)}^{[1]} = \frac{2C_F}{\pi}\,\frac{\overline{\mu}^{2\varepsilon}}{(q_T^2)^{1+\varepsilon}}\,\frac{z^{-2\varepsilon}\,e^{\varepsilon\gamma_E}}{\Gamma(1-\varepsilon)}\,\theta\left(z - 1 + \frac{q_T}{E\mathcal{R}}\right)\left[\frac{2}{1-z+\delta} - 3 + \frac{2}{z} - \varepsilon\right]. \tag{4.31}$$

Here the rapidity regulator is needed, but I simplified the expression using

$$\frac{1-z}{(1-z)^2 + \delta^2} = \frac{1}{(1-z)+\delta} + \mathcal{O}(\delta). \tag{4.32}$$

This is valid in the sense of distributions, meaning that (up to $\mathcal{O}(\delta)$ corrections) they both yield the same result when integrated on $[y, 1]$, with y generic. Now in view of (UV and rapidity) renormalization, eq. (4.31) needs to be expanded in ε and δ. One would like to perform separate expansions in terms of plus distributions, using

$$\frac{\overline{\mu}^{2\varepsilon}}{(q_T^2)^{1+\varepsilon}} = -\frac{1}{\varepsilon}\delta(q_T^2) + \mathcal{L}_0(q_T, \overline{\mu}) - \varepsilon\mathcal{L}_1(q_T, \overline{\mu}) + \mathcal{O}(\varepsilon^2),$$

$$\frac{1}{1 - z + \delta} = -\delta(1 - z) \ln \delta + \mathcal{L}_0(1 - z) + \mathcal{O}(\delta) \tag{4.33}$$

(definitions and basic properties of plus distributions and collected in appx. A.2). Unfortunately this is too naive, as the step function in eq. (4.31) connects the z and q_T dependence (in particular, it is undefined when both $z \to 1$ and $q_T \to 0$ limits are taken), signaling that the result has to be treated as a genuine two-dimensional distribution. Instead, I find

$$\frac{\bar{\mu}^{2\varepsilon}}{q_T^{2+2\varepsilon}} \frac{1 - z}{1 - z + \delta} \theta\Big(z - 1 + \frac{q_T}{E\mathcal{R}}\Big) = \delta(q_T^2)\Big\{\overline{L}_R \mathcal{L}_0(1 - z) - 2\mathcal{L}_1(1 - z)$$

$$+ \delta(1 - z)\Big[-\frac{1}{2\varepsilon^2} + \frac{1}{\varepsilon}\Big(\ln \delta - \frac{1}{2}\overline{L}_R\Big) - \frac{1}{4}\overline{L}_R^2\Big]\Big\}$$

$$- \mathcal{L}_0(q_T, \bar{\mu})\Big[\delta(1 - z)\ln \delta - \mathcal{L}_0(1 - z)\Big] - \mathcal{L}_0^{\text{cut}}\big(q_T, E\mathcal{R}(1 - z)\big)\mathcal{L}_0(1 - z). \tag{4.34}$$

This identity was obtained by switching to cumulative distributions in both variables, then expanding in δ, next[3] expanding in ε, and finally identifying term by term the differential distributions that reproduce the cumulative counterpart. The last term is not simply a product of two one-dimensional distributions, since its argument still involves both transverse momentum and energy fraction. Note that eq. (4.34) has a double pole that an expansion like eq. (4.33) could have never generated. With this trick, I obtain

$$J_{q(b)+(c)}^{[1]} = \frac{2C_F}{\pi}\Big\{\delta(q_T^2)\delta(1 - z)\Big[-\frac{1}{\varepsilon^2} + \frac{1}{\varepsilon}\Big(2\ln \delta - \overline{L}_R\Big) - \frac{1}{2}\overline{L}_R^2 + \frac{\pi^2}{12}\Big]$$

$$+ \Big(-3 + \frac{2}{z} + 2\mathcal{L}_0(1 - z)\Big)\Big[\mathcal{L}_0(q_T, \bar{\mu}) - \mathcal{L}_0^{\text{cut}}\big(q_T, E\mathcal{R}(1 - z)\big)$$

$$+ \overline{L}_R\delta(q_T^2)\Big] - 2\ln \delta\, \mathcal{L}_0(q_T, \bar{\mu})\delta(1 - z)$$

$$- 2\delta(q_T^2)\Big[\Big(-3 + \frac{2}{z}\Big)\ln(1 - z) + 2\mathcal{L}_1(1 - z)\Big]\Big\}. \tag{4.35}$$

The last case I need to consider is when two particles are in the jet, but using the WTA axis, where the transverse momentum dependence becomes nontrivial. By symmetrizing the integrand in $x \leftrightarrow 1 - x$,

$$J_{q(a)}^{\text{WTA}[1]} = \frac{2C_F}{\pi} \frac{e^{\varepsilon\gamma_E}}{\Gamma(1 - \varepsilon)} \frac{\bar{\mu}^{2\varepsilon}}{(q_T^2)^{1+\varepsilon}} \delta(1 - z) \int_{\frac{1}{2}}^1 \mathrm{d}x\, x^{-2\varepsilon}\theta\big((1 - x)E\mathcal{R} - q_T\big)$$

---

[3]The expansion in δ should precede the one in ε since we want the former to only regulate rapidity divergences. If the result is expanded in ε first, virtual diagrams do not vanish, but provide a tower of logarithms of δ to cancel against real emissions.

$$\times \left[\frac{2}{1-x} - 3 + \frac{2}{x} - \varepsilon \right]. \quad (4.36)$$

Again, I have dropped the rapidity regulator, because the upper integration limit is regulated by ε. At this stage one would be tempted to expand $x^{-2\varepsilon}$ under integral, and the $x \to 1$ endpoint seems regulated by the step function, but the previous case taught us to have extra care. Indeed this operation would be wrong, as it will miss a ε pole coming from the $x \to 1$ *and* $q_T \to 0$ limits. The correct way to proceed is using again eq. (4.34), which yields

$$J_{q(a)}^{\text{WTA}[1]} = \frac{2C_F}{\pi} \delta(1-z) \left\{ \delta(q_T^2) \left[\frac{1}{\varepsilon^2} + \frac{1}{\varepsilon} \left(\overline{L}_R + \frac{3}{2} \right) + \frac{1}{2} \overline{L}_R^2 + \frac{3}{2} \overline{L}_R + \frac{7}{2} \right. \right.$$
$$\left. - 2\ln^2 2 - \frac{5\pi^2}{12} \right] - \mathcal{L}_1^{\text{cut}} \left(q_T, \frac{E\mathcal{R}}{2} \right) + \left(2\ln 2 - \frac{3}{2} \right) \mathcal{L}_0^{\text{cut}} \left(q_T, \frac{E\mathcal{R}}{2} \right)$$
$$\left. + \theta \left(\frac{E\mathcal{R}}{2} - q_T \right) \frac{1}{q_T^2} \left[3 \frac{q_T}{E\mathcal{R}} + 2\ln \left(1 - \frac{q_T}{E\mathcal{R}} \right) \right] \right\}. \quad (4.37)$$

It is natural to compare this intermediate result with the standard-jet analog in eq. (4.29). Contrary to that expression, the WTA axis makes the transverse momentum dependence highly nontrivial, since the axis tracks the momentum of the most energetic particle. However, the pole structure and logarithmic dependence coincides for the two algorithms, as required by RGE consistency.

I can now sum over cases, combining the expressions in eqs. (4.29) and (4.37) with (4.35), to obtain the bare quark jet function at one loop

$$J_q^{[1]} = \frac{2C_F}{\pi} \left\{ \delta(1-z) \left[\delta(q_T^2) \left(\frac{2}{\varepsilon} \ln \delta + \frac{3}{2\varepsilon} + \frac{3}{2} \overline{L}_R \right) - 2\ln \delta \, \mathcal{L}_0(q_T, \mu) + \Delta_q^{\text{axis}}(q_T^2) \right] \right.$$
$$+ \left(\frac{2}{z} - 3 + \mathcal{L}_0(1-z) \right) \left[\delta(q_T^2) \overline{L}_R + \mathcal{L}_0(q_T, \mu) - \mathcal{L}_0^{\text{cut}}(q_T, E\mathcal{R}(1-z)) \right]$$
$$\left. - 2 \left[\left(-3 + \frac{2}{z} \right) \ln(1-z) + 2\mathcal{L}_1(1-z) \right] \delta(q_T^2) \right\}. \quad (4.38)$$

The dependence on the algorithm occurs via the functions Δ_q^{axis}. Explicitly,

$$\Delta_q^{\text{std}}(q_T^2) = \delta(q_T^2) \left(\frac{13}{2} - \frac{2\pi^2}{3} \right),$$
$$\Delta_q^{\text{WTA}}(q_T^2) = \delta(q_T^2) \left(\frac{7}{2} - 2\ln^2 2 - \frac{\pi^2}{3} \right) + \left(2\ln 2 - \frac{3}{2} \right) \mathcal{L}_0^{\text{cut}} \left(q_T, \frac{E\mathcal{R}}{2} \right)$$
$$+ \theta \left(\frac{E\mathcal{R}}{2} - q_T \right) \frac{1}{q_T^2} \left[\frac{3q_T}{E\mathcal{R}} + 2\ln \left(1 - \frac{q_T}{E\mathcal{R}} \right) \right] - \mathcal{L}_1^{\text{cut}} \left(q_T, \frac{E\mathcal{R}}{2} \right).$$
$$(4.39)$$

The additional terms in the WTA result are power corrections in $E\mathcal{R}/q_T$,

$$\Delta_q^{\text{WTA}}(q_T^2) = \Delta_q^{\text{std}}(q_T^2) \left[1 + \mathcal{O}\left(\frac{E^2 \mathcal{R}^2}{q_T^2} \right) \right] . \tag{4.40}$$

This implies that the dependence on the jet algorithm vanishes in the regime $R \ll \vartheta$, as predicted from the factorization formula in eq. (4.13): as I already commented on, the semi-inclusive jet function $\mathcal{J}_j$ that enter there are independent of the jet axis.

4.1.4 Renormalization and refactorization

The jet functions I computed in the previous section are still affected by UV and rapidity divergences. In this short section I will comment on the UV renormalization, rapidity renormalization and expansion of the jet functions in presence of additional hierarchies with the jet radius.

Because they enter in the same factorization formula as the usual TMDs, cancellation of divergences follows an identical pattern. First, renormalization in $\overline{\text{MS}}$ is performed by including the one-loop UV renormalization factor known from the TMD case,

$$Z_q^{[1]} = -2C_F \frac{1}{\varepsilon} \left(\frac{1}{\varepsilon} + \ln \frac{\zeta}{\mu^2} + \frac{3}{2} \right) , \tag{4.41}$$

and relabeling $\overline{\mu} \to \mu$ in eq. (4.38).

Next, it is necessary to account for the overlap of soft and collinear modes. A simple way to compute the zero bin Z_b is taking the soft limit $k^- \ll \ell_-$ at the integrand level in eq. (4.23) (or $x \to 1$ in eq. (4.25)): since these expressions already embed the collinear limit, the result returns the overlap between the two modes. The constraints in table 4.2 have to be expanded accordingly, which implies that the dependence on $\mathcal{R}$ disappears, only the case of one particle in the jet contributes, and the calculation reduces to the one performed for hadron TMDs in [208]. We know from this case that the zero bin simply coincides with the soft function itself, whose expansion up to $\mathcal{O}(\alpha_s^2)$ is

$$Z_{\text{b},q}(q_T^2, \mu, \zeta) = S_q(q_T^2, \mu, \zeta) = \frac{1}{\pi} \delta(q_T^2) + \frac{\alpha_s C_F}{\pi^2} \Bigg\{ \mathcal{L}_1(q_T, \mu)$$
$$- \mathcal{L}_0(q_T, \mu) \ln \left(\frac{4E^2 \delta \overline{\delta}}{\mu^2} \right) \delta(q_T^2) \left[-\frac{1}{\varepsilon^2} + \frac{1}{\varepsilon} \ln \left(\frac{4E^2 \delta \overline{\delta}}{\mu^2} \right) + \frac{\pi^2}{12} \right] \Bigg\} . \tag{4.42}$$

Then, rapidity renormalization follows from absorbing a square root of the soft function in the jet functions, as described for hadron TMDs in eq. (2.33).

By combining the three steps, the renormalized TMD jet functions read

$$J_q(z, \boldsymbol{q}, E\mathcal{R}, \mu, \zeta) = Z_q(\mu) \, S_q^{-\frac{1}{2}}(\boldsymbol{q}, \mu, \zeta) \otimes J_q(z, \boldsymbol{q}, E\mathcal{R}) \,, \tag{4.43}$$

where $\otimes$ denotes Laplace convolution over the transverse momentum. Explicitly, this yields the one-loop result

$$
\begin{aligned}
J_q^{[1]}(z, q_T^2, &E\mathcal{R}, \mu, \zeta) = \\
&\frac{2C_F}{\pi} \bigg\{ \delta(1-z) \Big[\frac{3}{2} L_R \delta(q_T^2) - \mathbf{l}_\zeta \, \mathcal{L}_0(q_T, \mu) - \mathcal{L}_1(q_T, \mu) + d_q^{\text{axis}}(q_T^2) \Big] \\
&+ \Big(\frac{2}{z} - 3 + \mathcal{L}_0(1-z) \Big) \Big[L_R \delta(q_T^2) + \mathcal{L}_0(q_T, \mu) - \mathcal{L}_0^{\text{cut}}\big(q_T, E\mathcal{R}(1-z)\big) \Big] \\
&- 2 \Big[\Big(\frac{2}{z} - 3 \Big) \ln(1-z) + 2\mathcal{L}_1(1-z) \Big] \delta(q_T^2) \bigg\} \,,
\end{aligned}
\tag{4.44}
$$

where the logarithms are

$$L_R = \ln\left(\frac{\mu^2}{E^2 \mathcal{R}^2} \right) \qquad \mathbf{l}_\zeta = \ln \frac{\mu^2}{\zeta} \tag{4.45}$$

and d^{axis} are simply related to the expressions in eq. (4.40) via

$$d_q^{\text{axis}}(q_T^2) = \Delta_q^{\text{axis}}(q_T^2) - \frac{\pi^2}{12} \,, \tag{4.46}$$

the additional term $\pi^2/12$ due to the soft function in eq. (4.42).

From the final expression (4.44), one can study the two cases $R \ll \vartheta$ and $R \gg \vartheta$. In the small-R limit, expanding the distributions simply requires dropping the cut superscript, the dependence on the axis vanishes, and I get

$$
\begin{aligned}
J_q^{[1]}(z, q_T^2, E\mathcal{R}, \mu, \zeta) \to &\frac{2C_F}{\pi} \bigg\{ \delta(1-z) \Big[\delta(q_T^2) \Big(\frac{3}{2} L_R + \frac{13}{2} - \frac{3\pi^2}{4} \Big) - \mathbf{l}_\zeta \mathcal{L}_0(q_T, \mu) \\
&- \mathcal{L}_1(q_T, \mu) \Big] + \Big(\frac{2}{z} - 3 + \mathcal{L}_0(1-z) \Big) \Big[L_R \delta(q_T^2) + \mathcal{L}_0(q_T, \mu) \Big] \\
&- 2\delta(q_T^2) \Big[\Big(\frac{2}{z} - 3 \Big) \ln(1-z) + 2\mathcal{L}_1(1-z) \Big] \bigg\}.
\end{aligned}
\tag{4.47}
$$

Comparison with eq. (B.28) and (B.30) shows this result to correctly reproduce the right-hand side of eq. (4.13), thus providing a nontrivial one-loop check of the factorization framework.

I now move on to the large-R limit and consider explicitly the WTA case, where the factorization picture is unaltered and the function simplifies as in eq. (4.14). Expanding distributions in this limit requires some extra care: when

in doubt, it is safer to perform the expansion in cumulant space and map the result back to distribution space. In particular,

$$\mathcal{L}_0(1-z)\mathcal{L}_0^{\rm cut}\big(q_T, ER(1-z)\big) \underset{R\ll\vartheta}{\to} -2\mathcal{L}_1(1-z)\delta(q_T^2)$$

$$+ \mathcal{L}_0(1-z)\mathcal{L}_0^{\rm cut}\Big(q_T, \frac{ER}{2}\Big) - \frac{1}{2}\delta(1-z)\mathcal{L}_1^{\rm cut}\Big(q_T, \frac{ER}{2}\Big), \quad (4.48)$$

and the expansion yields the result

$$\mathscr{I}_q(q_T^2, \mu, \zeta) = \frac{2C_F}{\pi}\left[\delta(q_T^2)\Big(\frac{7}{2} - \frac{5\pi^2}{12} - 3\ln 2\Big) - \mathcal{L}_0(q_T, \mu)\Big(\frac{3}{2} + 1_\zeta\Big) - \mathcal{L}_1(q_T, \mu)\right].$$
$$(4.49)$$

This easily transforms to impact parameter space,

$$\mathscr{I}_q(\boldsymbol{b}, \mu, \zeta) = \frac{2C_F}{\pi}\left[\frac{7}{2} - \frac{5\pi^2}{12} - 3\ln 2 - \frac{1}{2}L_\mu^2 + L_\mu 1_\zeta + \frac{3}{2}L_\mu\right], \quad (4.50)$$

where

$$L_\mu = \ln\Big(\frac{b^2\mu^2}{4e^{-2\gamma_E}}\Big). \quad (4.51)$$

Eq. (4.50) confirms the large-R factorization at one loop, showing explicitly that the dependence on z vanishes and the dependence on $\boldsymbol{b}$ (or $\boldsymbol{q}$) is purely logarithmic. In the next section I will confirm this fact at two loop.

4.1.5 Two-loop extraction of the large-radius jet function

As I showed in detail in sec. 4.1.3, calculations involving jet algorithms are nontrivial. In particular, the cuts imposed by the recombination procedure seriously increases the complexity of the integrals. For two particles the situation is manageable, but the general two-loop case gets highly complicated. On the other hand, resumming logarithms at N³LL provides no real advantage if this precision is not matched by a corresponding level of fixed-order accuracy.

If the analytic two-loop calculation seems out of reach, one can still aim at a numerical extraction. In sec. 4.2, I will show the large-R limit captures the dominant part of the perturbative corrections, which justifies focusing on this limit. The large-R WTA jet function is completely determined at two loops by known anomalous dimensions, except for a constant $j^{[2]}$. Explicitly,

$$\mathscr{I}_q^{[2]}(\boldsymbol{b}, \mu, \zeta) = \left\{C_F^2\left[\frac{L_\mu^4}{2} - (3+21_\zeta)L_\mu^3 + \Big(21_\zeta^2 + 61_\zeta - \frac{5}{2} + 6\ln 2 + \frac{5\pi^2}{6}\Big)L_\mu^2\right.\right.$$

$$+ \left(\left(14 - 12 \ln 2 - \frac{5\pi^2}{3} \right) \mathrm{l}_\zeta + \frac{45}{2} - 18 \ln 2 - \frac{9\pi^2}{2} + 24\zeta_3 \right) L_\mu \Big]$$

$$+ C_F C_A \left[-\frac{22}{9} L_\mu^3 + \left(\frac{11}{3} \mathrm{l}_\zeta - \frac{35}{18} + \frac{\pi^2}{3} \right) L_\mu^2 + \left(\frac{404}{27} - 14\zeta_3 \right) \mathrm{l}_\zeta \right.$$

$$+ \left. \left(\left(\frac{134}{9} - \frac{2\pi^2}{3} \right) \mathrm{l}_\zeta + \frac{57}{2} - 22 \ln 2 - \frac{11\pi^2}{9} - 12\zeta_3 \right) L_\mu \right]$$

$$+ C_F n_f T_F \left[\frac{8}{9} L_\mu^3 + \left(\frac{2}{9} - \frac{4}{3} \mathrm{l}_\zeta \right) L_\mu^2 - \frac{112}{27} \mathrm{l}_\zeta \right.$$

$$+ \left. \left(-\frac{40}{9} \mathrm{l}_\zeta - 10 + 8 \ln 2 + \frac{4\pi^2}{9} \right) L_\mu \right] \Big\} + j^{[2]} . \tag{4.52}$$

This expression was obtained directly from the evolution equations: a solution of eq. (4.18) is

$$\mathscr{J}_q(\boldsymbol{b}, \mu, \zeta) = \exp \left[\mathcal{D}_\mu(\mu, \boldsymbol{b})(\mathrm{l}_\zeta - L_\mu) \right] \hat{\mathscr{J}}_q(\boldsymbol{b}, \mu) , \tag{4.53}$$

where $\hat{\mathscr{J}}_q$ does not depend on ζ, and expands as

$$\hat{\mathscr{J}}_q(\boldsymbol{b}, \mu) = \sum_{n=0}^{\infty} \left(\frac{\alpha_s}{2\pi} \right)^n \sum_{k=0}^{2n} \hat{\mathscr{J}}_q^{[n,k]} L_\mu^k . \tag{4.54}$$

I can now insert this expansion in eq. (4.17) and recursively solve for the first two perturbative orders, using the expressions for the anomalous dimensions in appx. B.3.2. Finally, logarithms of ζ are included via eq. (4.53).

There is a shortcut to this procedure, which takes advantage of the cross section being independent of the renormalization scale: by solving

$$\frac{\mathrm{d}}{\mathrm{d}\mu} H_{e^+ e^-}(s, \mu) \hat{\mathscr{J}}_q^2(\boldsymbol{b}, \mu) = 0 \tag{4.55}$$

order by order in perturbation theory, I also reproduce eq. (4.52) from the logarithmic structure of the two-loop hard function in eq. (B.32).

Knowing the logarithmic dependence, it is now possible to aim at extracting the constant. The method to do so numerically is well known [209], and exploits that event generators have factorization built in: as long as the assumptions underpinning factorization are valid, the description they provide should be exact in the limit of infinite number of events. Therefore, one simulates a large number of collisions using the same two-loop hard function as in eq. (4.9) and clustering parton jets with the WTA algorithm. Of course this is better done from $e^+ e^- \to$ dijet, since the TMDPDFs do not enter this process.
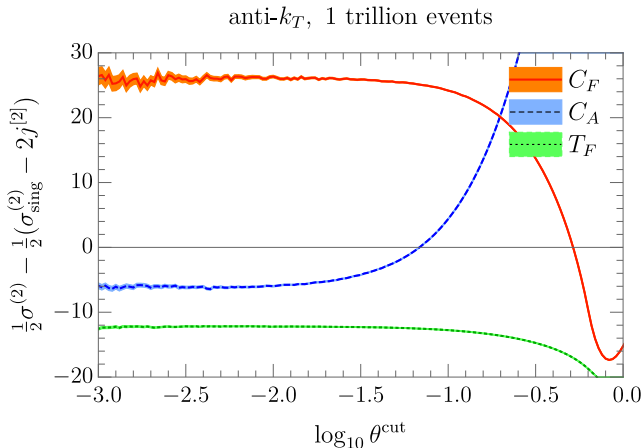
Figure 4.2 The difference between the $\mathcal{O}(\alpha_s^2)$ contribution to e^+e^- cross section with a cut on the angular decorrelation $\vartheta \leq \vartheta^{\mathrm{cut}}$, obtained from EVENT2 and from the factorization formula in eq. (4.9). The figure shows the (e^+e^- version of) the anti-k_T algorithm, and the curves correspond to the different color structures, see eq. (4.57). The error bands indicate the statistical uncertainty. The missing two-loop constant in the quark jet function is the value of the plateau at small ϑ^{cut}.

The constant follows from the difference between the simulated two-loop cross section and the analytic prediction for the singular cross section,

$$\frac{1}{2}\sigma^{(2)} - \frac{1}{2}(\sigma^{(2)}_{\mathrm{sing}} - 2j^{[2]}),\qquad(4.56)$$

where $\sigma^{(2)}_{\mathrm{sing}}$ is the factorized expression from eq. (4.9), and the factor 2 in front of $j^{[2]}$ comes from having two jets. If factorization is valid and power corrections are negligible, then $\sigma^{(2)}$ and $\sigma^{(2)}_{\mathrm{sing}}$ cancel, leaving out $j^{[2]}$.

Fig. 4.2 shows the difference (4.56) for the anti-k_T jet algorithm. In [3] we extracted this using the EVENT2 generator, run with $n_f = 5$ and an infrared cutoff $\rho = 10^{-12}$, generating 10^{12} events. The quantity is plotted as a function of a cut on the angular decorrelation, $\vartheta \leq \vartheta^{\mathrm{cut}}$. A sharper cut delivers a more accurate description, since the factorization formula is valid up to ϑ corrections, but lowers the precision, as fewer events will pass the cut. The different curves correspond to the C_F^2, $C_F C_A$ and $C_F T_F$ color structures, with the bands indicating the statistical uncertainty. From varying the infrared cutoff we concluded that the cross section obtained from EVENT2 can be trusted for $\log_{10} \vartheta^{\mathrm{cut}} > -3$, corresponding to the plotted range.

The clear plateau at small values for ϑ^{cut} confirms the factorization formula to predict the singular part of the cross section correctly, and the value of the plateau corresponds to the missing two-loop constant $j^{[2]}$. The decomposition of $j^{[2]}$ in terms of the three color structures is given by

$$j^{[2]} = j^{[2]}_{C_F} + j^{[2]}_{C_A} + \frac{n_f}{5} j^{[2]}_{T_F} \,, \tag{4.57}$$

i.e. the group theory factors are included in the constants. The result was extracted by fitting the plateau to a constant, assuming $n_f = 5$, and the generalization to arbitrary number of flavors only involves rescaling $j^{[2]}_{T_F}$. The best range for this fit is not a priori clear, since one has no control over the power corrections at large ϑ^{cut}, not included in the factorization picture. We chose to consider the fit range $-3 \leq \log_{10} \vartheta^{\text{cut}} \leq \log_{10} \vartheta^{\text{cut}}_{\max}$, varying $\log_{10} \vartheta^{\text{cut}}_{\max}$ between -2.9 and -2 in steps of 0.02 (this corresponds to the size of the binning). We performed a different fit in each window, including the uncertainty from the EVENT2 integration. Finally, we took the lowest and highest value obtained in this way as the error, and their average as the central value, leading to

$$\text{anti-}k_T : j^{[2]}_{C_F} = 25.3 \pm 0.6 \,, \quad j^{[2]}_{C_A} = -6.3 \pm 0.2 \,, \quad j^{[2]}_{T_F} = -12.5 \pm 0.3 \,,$$
$$C/A : j^{[2]}_{C_F} = 24.5 \pm 0.6 \,, \quad j^{[2]}_{C_A} = -6.7 \pm 0.2 \,, \quad j^{[2]}_{T_F} = -12.5 \pm 0.2 \,,$$
$$k_T : j^{[2]}_{C_F} = 12.2 \pm 1.1 \,, \quad j^{[2]}_{C_A} = -9.3 \pm 0.2 \,, \quad j^{[2]}_{T_F} = -13.0 \pm 0.3 \,. \tag{4.58}$$

While these constants are remarkably similar for anti-k_T and C/A, they differ substantially for k_T.

4.2 Phenomenological study

4.2.1 Numerical implementation and non-perturbative model

In the following, I will use the framework that I set up in the previous sections to obtain numerical predictions for the cross section differential in transverse momentum. The region of interest for TMDs is small q_T, for which the regimes $\vartheta \sim R$ and $\vartheta \ll R$ are most relevant. For this reason I exclusively focus on the WTA axis, which is well behaved in the large-R limit. The case of $e^+e^- \to$ dijet will be a testing ground for the perturbative convergence, and allow me to explore the dependence on the jet radius R and cut on the jet energy fraction z. In the case of DIS+jet, I will provide numerical predictions for HERA and the EIC, and investigate the sensitivity of the cross section to non-perturbative effects.

In [3], we built on ARTEMIDE[4] to obtain resummed predictions for these processes. ARTEMIDE is a Fortran code to compute factorized TMD cross sections, performing resummation through the double-scale evolution of TMDs described in sec. 2.2.3 and based on the framework of [147, 148].

In brief, the main logical steps are the following: first, TMDs are built in b space at the initial scales (μ_i, ζ_i). In the example of SIDIS, the program interfaces to user-provided existing sets of collinear PDFs/FFs, and performs the matching to TMDs described by eq. (2.36). Independently, the evolution kernels in eq. (2.45) are computed from the anomalous dimensions (also in b space). The TMDs evolved to the scale (μ_f, ζ_f) are then assembled by combining these two ingredients, which provides the integrand of eq. (2.35); next, the result is Fourier transformed to q_T space. Finally, a high-level, process-dependent module includes the hard function and possibly performs the integration or binning over the kinematic variables (in the case of SIDIS, these are virtuality Q^2, hadron fraction z, Bjorken x and transverse momentum q_T).

The current version of ARTEMIDE provides cross sections for Drell-Yan and SIDIS. However, its modular structure allowed me to extend it to processes involving jets, with a limited amount of modification. Specifically, I added $e^+e^- \to$ dijet and jet-SIDIS high-level modules, and a jet-TMD low-level module that provides our perturbative input for the quark jet functions in $\boldsymbol{b}$-space.

The initial scales for TMD evolution are set as

$$(\mu_i, \zeta_i) = \left(\frac{2e^{-\gamma_E}}{b} + 2 \text{ GeV} , \zeta(\mu_i) \right), \tag{4.59}$$

where $\zeta(\mu_i)$ is given by the ζ-prescription(2.46), and μ_i corresponds to the saddle point eq. (2.43), while the shift at 2 GeV avoids hitting the Landau pole at large b. The final scales are

$$(\mu_f, \zeta_f) = \begin{cases} (\sqrt{s}, s) & e^+e^- \\ (Q, Q^2) & \text{DIS+jet} \end{cases} \tag{4.60}$$

An additional, important ingredient is the non-perturbative model used for TMDs, which I now describe. The matching of TMDs to collinear distributions is strictly valid only at large q_T, while at small transverse momentum (large b) non-perturbative effects become important. Rather than using a full parametrization for the TMDs, at first approximation one can still use the factorized expression, but correct the PDFs with a function f_{NP},

$$F_{p \to i}(x, \boldsymbol{b}, \mu, \zeta) = \sum_j \mathcal{C}_{i \leftarrow j}(x, \boldsymbol{b}, \mu, \zeta) f_{\text{NP}}(x, \boldsymbol{b}) f_{p \to j}(x, \mu). \tag{4.61}$$

---

[4]Web-page: http://avladimirov.net/index.php/projects/artemide
Repository: https://github.com/VladimirovAlexey/artemide-public

In particular, I use the non-perturbative model from [210], that was specifically formulated for the optimal TMDs considered here. Their ansatz is

$$f_{\text{NP}}(x, b; \lambda_i) = \exp\left(-\frac{\lambda_1(1-x) + \lambda_2 x + \lambda_3 x(1-x)b^2}{\sqrt{1 + \lambda_4 x^{\lambda_5} b^2}}\right), \qquad (4.62)$$

which in particular assumes flavor independence.

The TMD evolution kernel also receives non-perturbative corrections, which are modeled by modifying the rapidity anomalous dimension $\mathcal{D}_q$ as

$$\mathcal{D}_q(\mu, \boldsymbol{b}) = \mathcal{D}_q^{\text{res}}\big(\mu, b^*(\boldsymbol{b})\big) + g(\boldsymbol{b}). \qquad (4.63)$$

Here $\mathcal{D}_q^{\text{res}}$ resums logarithms present in the anomalous dimension itself, see e.g. [148] for details, and

$$b^*(\boldsymbol{b}) = \sqrt{\frac{b^2 B_{\text{NP}}^2}{b^2 + B_{\text{NP}}^2}}, \qquad g(\boldsymbol{b}) = c_0\, b\, b^*(\boldsymbol{b}), \qquad (4.64)$$

where c_0 and B_{NP} are parameters of the model, whose main effect is preventing the anomalous dimension from blowing up in proximity of the Landau pole.

The same work [210] carried out a simultaneous fit of the coefficients λ_i, c_0 and B_{NP}, extracted form Drell-Yan scattering and Z boson production. Their fit was performed at N^{3}LL accuracy, and to be consistent, I will always run the evolution at this order of accuracy, even though the jet function for generic R is only calculated at one-loop order (an exception is given by plots showing the perturbative convergence, that use by definition lower-order ingredients).

Having described the setup, I finally turn to showing predictions.

4.2.2 Momentum decorrelation in e^+e^- collisions

Even if the most promising application of the framework is the extraction of TMDs via DIS+jet at the future EIC, there are different reasons to study $e^+e^- \to$ dijet. First, the transverse momentum/angular decorrelation is an interesting observable by its own. Although the contamination by soft radiation has a reduced impact in lepton collision, using the WTA axis grants an advantage, as it provides precise predictions over the whole range of jet radii. Second, the absence of PDFs makes e^+e^- collision a useful testing ground, allowing one to study the framework in a clean environment. In this spirit, I will investigate how varying the parameters of the analysis impacts on the cross section. Finally, there is a third, interesting reason that makes the e^+e^- case relevant. The jet functions I computed are perturbative objects, but of course, for small transverse momenta $q_T \sim \Lambda_{\text{QCD}}$, non-perturbative effects can cause
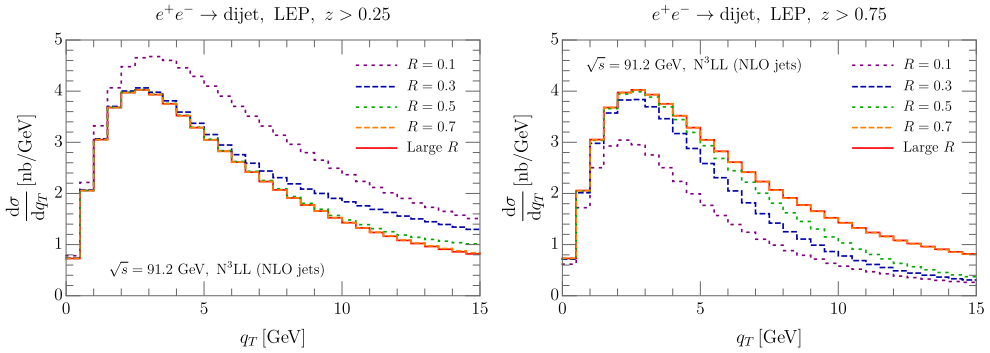
Figure 4.3 Dependence of the cross section differential in the transverse momentum decorrelation on the jet radius parameter R, for cuts on jet energy fraction $z > 0.25$ (left) and $z > 0.75$ (right). Results employ the NLO jet function computed in the regime $R \sim \vartheta$, and the large-R result (red solid) is shown for comparison.

large corrections. However, this can be addressed by exploiting the universality of non-perturbative physics: specifically, data from e^+e^- collisions could be used to fit a model for non-perturbative corrections to the jet function to be later applied to DIS.

With this motivation in mind, I consider the following setup and experiments:

- Belle II: $\sqrt{s} = 10.52$ GeV, 4 quark flavors.

- LEP: $\sqrt{s} = 91.1876$ GeV, 5 quark flavors.

The Belle analysis omits b-jets: my calculation of the jet function does not include quark mass effects, that will be dominant at such center-of-mass energy. Experimentally, these will be relatively easy to distinguish from light-quark jets and remove from the analysis. I account for both the photon and Z-boson contribution, describing the Z resonance via the effective replacement in eq. (1.50): of course, this causes a minor correction for Belle, but is fundamental to obtain the correct size of the cross section at LEP. In both cases, I will restrict the plotted q_T range to the region where the power corrections to the factorization theorem are reasonably under control. By default, I set the non-perturbative parameters of the evolution kernel to

$$B_{\mathrm{NP}} = 2.5 \text{ GeV}^{-1}, \qquad c_0 = 0.037, \tag{4.65}$$

but will study their variation at the end of this section.

I start the analysis by studying the dependence on the jet radius parameter R in fig. 4.3 for LEP. The cross section is shown for various jet radii, ranging
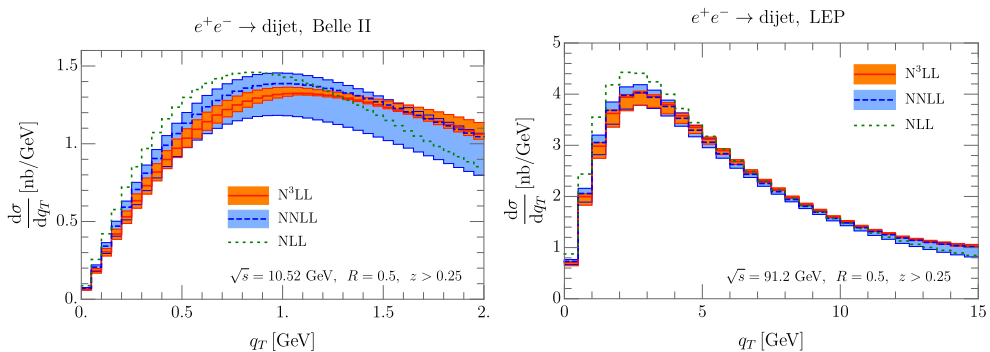
Figure 4.4 Perturbative convergence of the cross section differential in transverse momentum decorrelation, for Belle II (left) and LEP (right), for jet radius $R = 0.5$ and jet energy fraction $z > 0.25$. The N^{3}LL result is obtained with the prescription in eq. (4.66). The bands encode the perturbative uncertainty, as described in the text.

from $R = 0.1$ to 0.7, using the factorization formulae for $\vartheta \sim R$ in sec. 4.1.2. I consider two representative cuts on the jet energy fraction: $z > 0.25$ (left panel) and $z > 0.75$ (right panel). For comparison, the large-R limit is also shown, using the one-loop jet functions in eq. (4.50). The hard function is always included at two-loop order, and resummation performed at N^{3}LL accuracy.

As expected, as R increases the results approach the $\mathcal{R} \to \infty$ limit. Surprisingly, however, the convergence to this limit occurs very fast. In both cases, the cross section for $R = 0.7$ is indistinguishable from the large-R result, and for $z > 0.25$ the difference is even minimal for $R = 0.5$. This means that in the factorization in eq. (4.14) the power corrections $\mathcal{O}(\vartheta/R) \sim \mathcal{O}(q_T^2/(ER)^2)$ have a limited impact even for $\vartheta \lesssim R$. This observation will be used in the rest of the analysis, to justify including the two-loop jet function in the large-R limit, as this will capture the dominant two-loop fixed-order contribution. Explicitly, results are combined according to

$$\left(\frac{d\sigma}{dq_T}\right)^{\text{N}^3\text{LL}} = \left(\frac{d\sigma}{dq_T}\right)^{\text{NLO}} + \left(\frac{d\sigma}{dq_T}\right)^{\text{NNLO}}_{\mathcal{R}\to\infty} - \left(\frac{d\sigma}{dq_T}\right)^{\text{NLO}}_{\mathcal{R}\to\infty}, \qquad (4.66)$$

where NLO and NNLO indicate the order of the jet function. Each term uses the NNLO hard function, and resummation is included at N^{3}LL accuracy. The above approximation contains all large logarithms of ϑ (or equivalently, $q_T/(ER)$) at N^{3}LL accuracy. It reduces to NNLL accuracy for $\vartheta \sim R \ll 1$, since it misses some $\mathcal{O}(\vartheta/R)$ corrections. However, fig. 4.3 showed that their effect is small, except in the tail region where the cross section will be also affected by $\mathcal{O}(q_T/\sqrt{s})$ corrections.

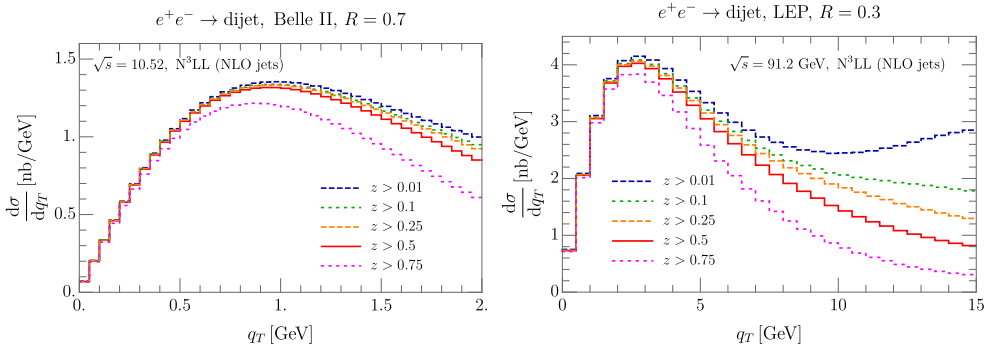Next, I study the perturbative convergence of the TMD cross section in

Figure 4.5 Dependence of the transverse momentum decorrelation distribution on the cut on jet energy fraction z, for Belle II with $R = 0.7$ (left panel) and LEP with $R = 0.3$ (right panel). The dependence on this cut is larger for smaller R, as discussed in the text. In both cases, the results for $z > 0.5$ (solid red curve) exactly coincide with the large-R limit, see footnote.

fig. 4.4. I take $R = 0.5$, $z > 0.25$ and show results for the cross section for Belle II (left panel) and LEP (right panel) at NLL, NNLL and N³LL. The perturbative uncertainty is estimated by varying the scales μ_i in eqs. (4.59) and (4.60) up and down by a factor 2 around their central value and taking the envelope. The band obtained by this procedure at NLL is artificially small and not shown. As expected, the N³LL correction is small compared to the NNLL one, and the uncertainty bands overlap and are reduced at higher order.

To provide a complementary picture with respect to fig. 4.3, fig. 4.5 investigates the dependence of the cross section on the cut on the jet energy fraction $z > z_{\text{cut}}$ for a fixed value of the jet radius. I show results for Belle II with $R = 0.7$ (left panel) and LEP with $R = 0.3$ (right panel), imposing $z > z_{\text{cut}}$ and varying $z_{\text{cut}} = 0.01$ to $z_{\text{cut}} = 0.75$. As in fig. 4.3, we use NLO jet functions. For $R = 0.7$ the dependence on the cut on z is relatively mild, which reflects the fact that in the large-R limit the jet function is proportional to $\delta(1 - z)$, and thus independent of this cut. For $R = 0.3$ there is a stronger dependence, and at very small (large) values of z the cross section shows unphysical features. This is not surprising, since the cross section diverges as $z_{\text{cut}} \to 0$ (every single low-energy particle originates a different jet) and has large logarithms of $1 - z_{\text{cut}}$ for $z_{\text{cut}} \to 1$. Regardless of the jet radius, for $z_{\text{cut}} = 0.5$ the cross section coincides with the large-R result. This is due to a one-loop accident.[5]

---

[5]At one loop, the initial quark undergoes a single splitting. When integrating over $0.5 < z < 1$, each phase-space configuration contributes to the cross section with exactly one jet: either a jet containing two particles, or a jet containing the most energetic particle. In addition, due to the WTA recombination prescription, the resulting jet axis is the same in
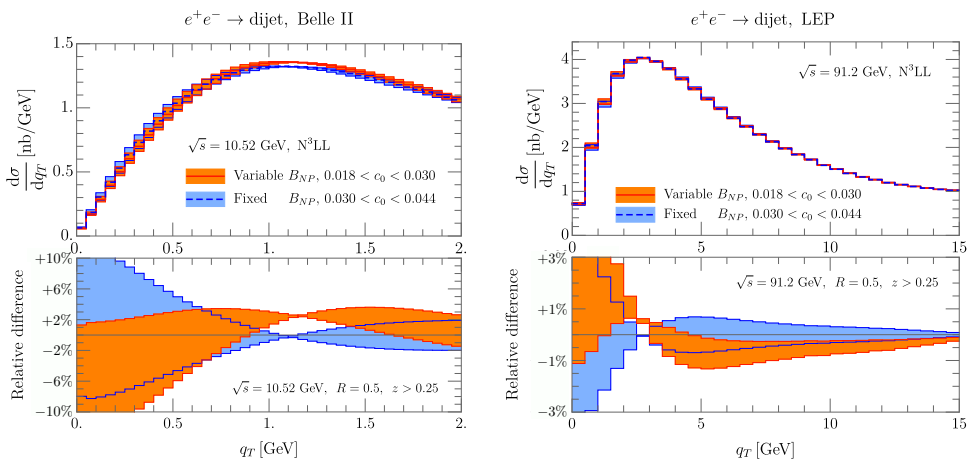
Figure 4.6 Estimate of the sensitivity of the TMD to nonperturbative effects in the rapidity resummation at Belle II (left) and LEP (right). We vary the parameter c_0 in the range of its statistical uncertainty, testing both the fixed and variable B_{NP} schemes of ref. [210]. Results are obtained with the prescription in eq. (4.66).

As a final plot, fig. 4.6 shows the sensitivity of the cross sections to B_{NP} and c_0, that parametrize the non-perturbative contribution to the rapidity evolution, see eqs. (4.63) and (4.64). We considered both the "fixed B_{NP}" and "variable B_{NP}" schemes used in [210], and varied the parameters within the statistical errors listed in their table 4. In practice, we found that the B_{NP} variation is subdominant, so we simply plot variations of c_0. As one would expect, the sensitivity to nonperturbative effects is much larger at Belle, commensurate with its smaller center-of-mass energy, and increases at low transverse momenta. The conclusions obtained from the two schemes are compatible with each other. The situation is similar for LEP, though the relative variation is substantially lower (below 1% for most of the range in q_T).

Finally, I investigated the impact of the choice of jet algorithm, specifically, the impact of the different two-loop constants in eq. (4.58). The difference with respect to anti-k_T is negligible for C/A ($< 0.1\%$) and very small for the k_T algorithm ($< 1\%$).

4.2.3 Predictions for DIS+jet

In this section I will show representative results for TMD measurements with jets in DIS. I consider the two configurations

---

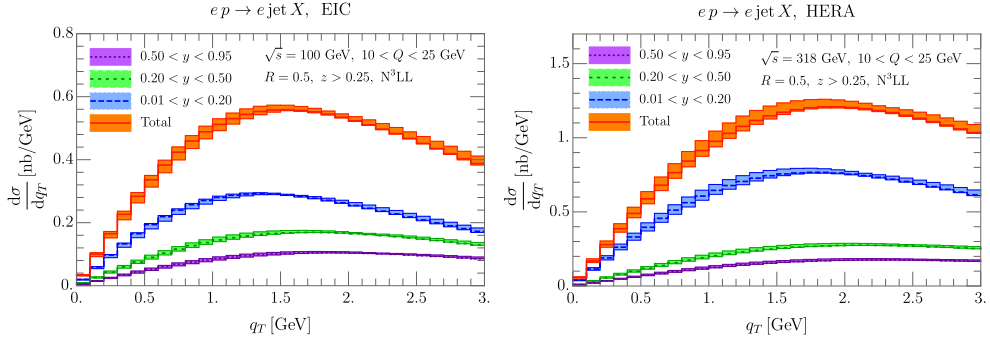either case, independent of R. Thus it must in particular coincide with the large-R limit.

Figure 4.7 TMD cross section for SIDIS with jets at the EIC (left) and at HERA (right), with $10 < Q < 25$ GeV and different intervals in elasticity within the range $0.01 < y < 0.95$. Results are obtained with the prescription in eq. (4.66).

- HERA: $\sqrt{s} = 318$ GeV,

- EIC: $\sqrt{s} = 100$ GeV.

The above value for the center-of-mass energy of EIC is an assumption[6]. I take $10 \leq Q \leq 25$ GeV and study the transverse momentum distribution for $q_T \leq 3$ GeV, ensuring that power corrections of order q_T^2/Q^2 to the factorization formula can be neglected. In this kinematic range, quark mass effects are expected to be negligible, so they are ignored in the analysis. Working in the Breit frame, I impose a cut on the jet energy fraction $z > 0.25$ and set the jet radius to $R = 0.5$. The e^+e^- study in the left panel of fig. 4.3 shows that in this case the large-R approximation works extremely well, so I include again the two-loop, large-R jet function extracted in sec. 4.1.5, using eq. (4.66). The TMDPDFs were built starting from the NNPDF 3.1 PDFs [113] with $\alpha_s(M_Z) = 0.118$, using the matching in eq. (4.61).

The results are shown in fig. 4.7, for different intervals in the elasticity y in the range $0.01 < y < 0.95$. In each case, as for the convergence plots in fig. 4.4, the uncertainty band is obtained by independently varying the scales μ_i and μ_f up and down by a factor of 2 around their central values, and taking the envelope. Roughly half of the contribution to the cross section comes from low elasticity ($y < 0.2$). The variation in shape between the different elasticity intervals is modest; at high elasticity, the peak of the distribution is slightly shifted towards larger transverse momenta.

---

[6]At the time of the publication [3], the technical details of the EIC were still largely under discussion. Electrons with energy 20 GeV scattering on protons with 100 GeV actually results in $\sqrt{s} = 89$ GeV, and all the following considerations remain true for such a value.
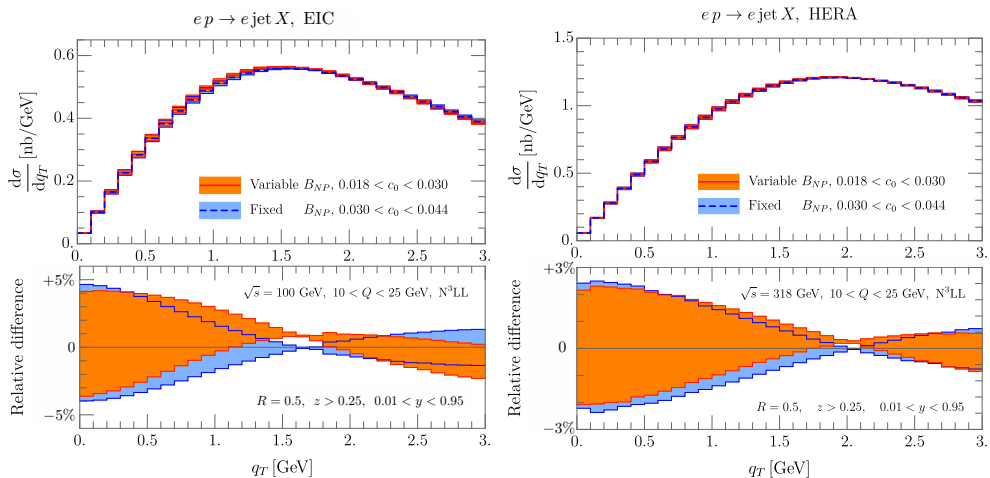
Figure 4.8 Sensitivity of the cross section to nonperturbative effects at the EIC (left) and HERA (right). This is estimated by varying the parameter c_0, that controls the nonperturbative contribution to the evolution kernel, within its current statistical uncertainty [210]. Results are obtained with the prescription in eq. (4.66).

I now investigate the sensitivity of our jet observable to non-perturbative initial-state hadronic physics. Assessing this aspect is particularly important, as a large sensitivity denotes a high discrimination power in the extraction of TMDPDFs. A first impression can be obtained by varying the parameters B_{NP}, c_0 and λ_i (see eqs. (4.63), (4.64) and (4.62)) that enter the non-perturbative model. In principle, these parameters are highly correlated, and a full error estimate would require taking data with a large number of replicas, along the lines of the original analysis in ref. [210]. In practice, the non-perturbative uncertainty is dominated by the variation of the single parameter c_0, describing non-perturbative corrections to the rapidity anomalous dimension. Therefore, a realistic estimate of the size of NP effects can be obtained by simply varying c_0 within its statistical uncertainty, which we show in fig. 4.8. The effect of such a variation is not large (below 5% at the EIC and 3% at HERA), but not negligible, and increases at small q_T. This plot suggests that such a measurement can likely be used to improve our knowledge of the non-perturbative part of the evolution kernel, parametrized by c_0, which is particularly relevant because it is universal.

Finally, I explored the dependence of NP effects on the choices of R, z_{cut} and the range in Q and y, finding that their size is not affected by different choices of kinematical cuts.

4.3 Outlook

In this chapter, I showed how the study of the transverse momentum distribution of the proton can benefit from using jets (instead of hadrons) as final state. A clear advantage is that the jet momentum can be calculated in perturbation theory, while the fragmentation of hadrons is an intrinsically non-perturbative process.

The main theoretical result is that the cross section for dijet production in e^+e^- collisions and DIS with a jet in the final state admits the same factorization as for hadronic TMD measurements, simply replacing a TMDFF by our TMD jet function. In general, this factorization depends on the jet radius R and recombination scheme. The cross section for the standard jet axis does *not* satisfy the usual TMD factorization at large jet radii. Critically, instead, this happens for all values of R when the WTA scheme is used: once more, recoil-free jets induce a major simplification of the factorization picture through a better separation of soft and collinear physics.

This theoretical simplification translated into a practical advantage, as it allowed me to rely on existing results for hadrons at almost every stage of the analysis: I could reuse most of the perturbative ingredients; run the same evolution; build on the ARTEMIDE code. The evidence that the large-R limit of the jet functions well approximates the full predictions finally allowed me to achieve N³LL accuracy in this limit, the same as for the hadronic TMD cases.[7]

Using $e^+e^- \rightarrow$ dijet as testing ground, I verified the perturbative convergence of our numerical predictions, achieving perturbative uncertainties of order 5% in the peak of the distribution at N³LL. In DIS, I showed that our cross sections have similar sensitivity to non-perturbative effects as the corresponding hadronic case, without the burden of additional non-perturbative effects from fragmentation. Our predictions are particularly interesting for the EIC, where measurements involving jets have been recently considered from both a theoretical and experimental perspective [213–216].

The main question still to be answered is whether the smaller non-perturbative uncertainty compensates for new sources of error introduced by the jet measurement. For instance, the position of the jet axis is less precisely measured than a single charged hadron, where the angular resolution of the tracker is superior. Defining the jets on only charged hadrons would mitigate this issue, and it was recently shown that the shape of the distribution is essentially unaltered [217]. In addition, the results depend on the considered range of energy fraction, $z > z_{\text{cut}}$, which also enter the definition of transverse momentum

---

[7]Similar result were also obtained in [211,212] for the transverse energy-energy correlation, setting up a framework to reuse the known TMD ingredients in the back-to-back limit.

$\boldsymbol{q} = \boldsymbol{P}_J/z$. This should be marginal since we showed the large-R limit, where all the energy goes into the jet, to be a solid approximation for the finite-R case. In order to assess the impact of these effects on our predictions, it would be useful to perform a dedicated Monte Carlo study.

Finally, in the limit of small transverse momenta $q_T \sim \Lambda_{\mathrm{QCD}}$, the jets themselves receive non-perturbative corrections. Such effects could be modeled with an analysis similar to the one of sec. 4.2.1 for hadron TMDs, or systematically described from QFT principles. Developing such a model for TMD recoil-free jets would be a necessary step in view of extraction of TMDPDFs. The non-perturbative parameters required by the model could then be fitted from $e^+e^- \to$ dijet collisions and applied to the DIS+jet, exploiting universality of non-perturbative physics. Interestingly, jet measurements at HERA showed that for inclusive jet spectra at large radii, hadronization corrections are very small ($\sim 1\%$) [199]. This, and the fact that our framework is highly accurate at large-R, would make it very interesting to compare our predictions against existing HERA data.

5

Transverse Momentum Distributions from groomed jets

In the previous two chapters I explored the potential of the Winner-Take-All recombination scheme to study the transverse momentum distributions of hadrons and jets. I emphasized how the resulting jet axis is only sensitive to collinear physics, simplifying factorization. When describing hadrons fragmenting in jets, the cross section exhibits characteristic features which are stable under perturbations of the jet constituents; when studying the TMD of jets themselves, it allows for extracting TMDs with remarkable precision.

As I discussed in sec. 2.1.3, recoil-free jets have a famous competitor when it comes to eliminating sources of contamination inside the jets: grooming techniques have proven themselves highly successful, drastically reducing the effects of pileup and the underlying event in a variety of contexts. For the specific example of soft drop, factorization analyses were carried out in [218–222], and resummation predictions obtained for different groomed observables, see [223–227].

Fragmentation inside groomed jets was studied in refs. [176, 177]. These works showed that applying soft drop to the spectra of fragmenting hadrons grants some of the benefits already observed in ch. 3 with the WTA scheme: it removes the smearing caused by Sudakov double logarithms and makes the observable insensitive to non-global logarithms (but an important difference is that their framework involves rapidity divergences). This shows that soft drop can also simplify the theoretical description, although it often introduces additional hierarchies of scales that may require restricting the analysis to a certain kinematical range.

In the present chapter, I will consider the application of grooming to the extraction of TMDPDFs, based on my paper [4]. There we performed an analysis along the same lines of ch. 4, considering dijet production in e^+e^- collisions and jet measurements in DIS experiments, but using soft drop instead of recoil-free jets. The original motivation is similar, as using jets instead of hadrons

reduces the final-state non-perturbative uncertainty. In this regard, soft drop promises a further advantage, since, as I showed in fig. 2.3, it dramatically decreases hadronization effects within the jet. The price one pays is that the mode picture is complicated by the presence of the grooming parameter z_{cut}, and in general factorization is more involved than for hadron TMDs. However, in the limit of large jet radius relevant to EIC phenomenology, one can retrieve the familiar factorization structure by selecting collimated jets, which is done by imposing an upper cut on the groomed jet mass.

As in ch. 4, my main focus will be on cross sections differential in transverse momentum (decorrelation) q_T. The following analysis will show this quantity to exhibit very promising features: the main effect of grooming on the shape of the distribution is shifting the peak towards lower values of transverse momentum, where power corrections to factorization, $\sim q_T/Q$, are smaller; although the framework requires a small cut in jet mass, the predictions are stable under different choices of cut; finally, the NNLL predictions are in excellent agreement with Monte Carlo simulations. The sensitivity to hadronization corrections is similar to the case of recoil-free jets, but not surprisingly (given the convergence plot 4.4), the error on this observable is dominated by the perturbative uncertainty, estimated through scale variation. Reducing this uncertainty would require calculating (or extracting numerically) the missing two-loop ingredients.

This chapter follows the usual separation in three sections: in sec. 5.1 I will present the theoretical framework, discussing modes, factorization and evolution; in sec. 5.2 I will show predictions for $e^+e^- \to$ dijet and DIS+jet, with the former process playing again the role of testing ground, and in sec. 5.3 I will conclude, commenting on possible next steps. Many of the relevant ingredients have been already discussed in the previous chapter, and I will emphasize similarities and differences with respect to the recoil-free case.

5.1 Theoretical framework

5.1.1 Kinematics and modes

The processes I will focus on are again dijet production and DIS+jet, but crucially, the jets are now defined using the soft drop grooming procedure, discussed in sec. 2.1.3. Specifically, I consider the case $\beta = 0$ in eq. (2.16), where the grooming condition tests only the energy fraction of the splittings. Explicitly, in the e^+e^- case, grooming stops as soon as an emission passes the condition

$$\frac{\min(E_i, E_j)}{E_i + E_j} > z_{\mathrm{cut}} \,. \tag{5.1}$$

In general, experimental analyses use typical values $z_{\rm cut} \sim 0.1$, and this is the size that I will have in mind when discussing hierarchies and modes. To the purpose of factorization, this value allows one to safely assume $z_{\rm cut} \ll 1$.

In view of applications to the EIC, in the case of DIS, I consider again the Breit frame described in sec. 2.2. The definitions of transverse momentum decorrelation in $e^+e^- \to$ dijet, and jet transverse momentum in DIS+jet, are formally identical to eqs. (4.1) and (4.4),

$$\boldsymbol{q} = \frac{\boldsymbol{p}_1}{z_1} + \frac{\boldsymbol{p}_2}{z_2} \quad (e^+e^- \to \text{ dijet}), \qquad \boldsymbol{q} = \frac{\boldsymbol{P}_J}{z} + \boldsymbol{q}_{\rm in} \quad (\text{DIS+jet}), \qquad (5.2)$$

but the jet transverse momenta $\boldsymbol{p}_1, \boldsymbol{p}_2$ and $\boldsymbol{P}_J$ are defined after grooming, so they result by construction from the sum of the transverse momenta of only the jet constituents that survive soft drop. Similarly, z_i and z are the energy fractions of the *groomed* jets. Since these are in general smaller than the ungroomed counterpart, the resulting $\boldsymbol{q}$ is intrinsically larger than the analogous quantities defined for standard (or recoil-free) jets. I define the normalized groomed jet mass as

$$e = \left(\frac{m_J}{2E}\right)^2, \qquad (5.3)$$

where $E = \sqrt{s}/2$ (dijet) or $E = Q/2$ (DIS) and the jet mass is the norm of the jet four-momentum, see eq. (2.4), but defined again on only the particles that pass grooming. As already discussed, imposing an upper cut on jet masses, $m_J < 2E\sqrt{e_{\rm cut}}$, selects collimated jet configurations. This is opposite to the cut on thrust considered in sec. 1.2.2, where $T < T_c$ *discarded* collimated events. In the following I will always consider $e_{\rm cut} \ll 1$: since the IR limit coincides with $e \to 0$, most of the events occur at small jet mass, so even a stringent cut on the mass retains a significant fraction of the total cross section. At the same time, I will restrict the analysis to large jet radii, $R \sim 1$, so that the jet radius does not interfere with factorization. As I already commented on, large radii are preferred in electron-proton colliders.

The multiple scales in the problem lead to a rich spectrum of possible hierarchies of momenta, which are all consistent with maintaining $q_T/E, e_{\rm cut}$, $z_{\rm cut} \ll 1$. The modes induced by different hierarchies in the EFT fall in three classes: energetic modes that always pass soft drop; wide-angle, soft modes that explicitly fail soft drop; and those modes which live at the border, whose emissions can either pass or fail the grooming condition. I will now describe these modes and discuss the resulting factorization picture, considering dijet production for definiteness. A key point of the following discussion is that the jet axis aligns to the total transverse momentum inside the groomed jet.

Therefore, the measured transverse momentum is the total transverse momentum outside the groomed jets. Since the jets radius is large (ideally, infinite) this coincides with the total transverse momentum of the *dropped* radiation.

If the three small scales are roughly of the same size, $\frac{q_T}{E} \sim \sqrt{e_{\text{cut}}} \sim z_{\text{cut}}$, we get the standard SCET$_{\text{II}}$ modes

$$p_c \sim E(\lambda^2, 1, \lambda), \qquad p_s \sim E(\lambda, \lambda, \lambda), \qquad \lambda = \frac{q_T}{E}. \qquad (5.4)$$

As in the hadron TMD case, the scaling of soft radiation is determined by the transverse momentum measurement, the two modes have the same virtuality, and the framework is affected by rapidity divergences. In this case, in principle, soft emissions may or may not fail soft drop, while collinear emissions always pass. However, by selecting the collinearity via e_{cut}, we restrict to those configurations that are unaffected by recoil: soft emissions with transverse momentum $\sim q_T$ inside the groomed jet would result in too large a jet mass, thus they must always be groomed away, then the groomed jet is free of soft radiation. Therefore, the dijet transverse momentum is still determined by the *global* soft radiation. This reasoning argues for the jet function to be the same as for hadron production.

To examine further hierarchies between the three small scales, it is useful to introduce the Lund plane, a powerful graphical and conceptual tool to visualize modes and get physical intuition for the factorization/resummation picture. The Lund plane describes IR radiation in terms of its energy fraction z and angle ϑ relative to the energetic particle that emitted it, in logarithmic coordinates $\ln \frac{1}{z}, \ln \frac{1}{\vartheta}$. At leading logarithmic accuracy, we can think of the emissions as strongly ordered in energy and angle, thus a measurement is set by the leading emission. Imposing a cumulant measurement draws a line in the plane, vetoing emissions on one side of the line. What makes this representation particularly convenient is that at LL the phase space for a single emission is simply $\mathrm{d}z/z \, \mathrm{d}\vartheta/\vartheta$, as already noted in eq. (1.83). As a consequence, the allowed area in the Lund plane is interpreted as the probability of one emission.[1] This procedure allows for determining Sudakov form factors at LL by simply computing the vetoed areas; however, rather than exploiting this feature, I will focus here on the utility of the Lund plane in identifying the modes in the EFT.

The intuition is that modes live at the boundary between the vetoed and allowed regions. Specifically, new modes appear at the intersection of either a line parametrizing the measurement and the axes, or two lines describing the

---

[1] The paradox of a formally infinite area is resolved by noting that the total cross section is devoid of large logarithms, so the vetoed and allowed regions must complement to zero. This corresponds to the cancellation of IR poles between real and virtual diagrams.
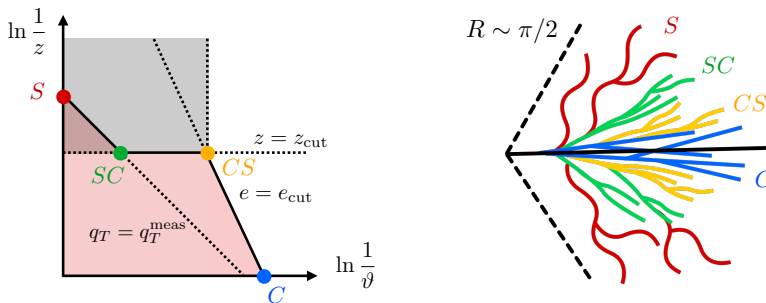
Figure 5.1 Left: representation of the modes in the Lund plane $\ln \frac{1}{z}, \ln \frac{1}{\vartheta}$ for the hierarchy $1 \gg z_{\text{cut}} \gg q_T/E \sim \sqrt{e_{\text{cut}}}$. Emissions in the red-shaded area are vetoed by the event kinematics, while the ones in the gray-shaded area are soft dropped. A graphical representation of the jet is given on the right, with lower-energy emissions drawn as wavier lines.

measurement. Such emissions are special in that they give the largest possible contribution to one or more of the measured quantities. In the spirit of the EFT, one identifies points in the Lund plane up to power corrections, so any separation represents in fact hierarchical separation.

To see the picture at work, let me examine the relevant hierarchy

$$1 \gg z_{\text{cut}} \gg q_T/E \sim \sqrt{e_{\text{cut}}}, \tag{5.5}$$

where the angular decorrelation q_T/E is now much smaller than the soft drop parameter. For definiteness, we can imagine the jet mass eE to be of the same size as the transverse momentum, although in view of factorization it only matters that e is much smaller than the soft-drop cut. The corresponding Lund-plane picture is given on the left of fig. 5.1, on which I now comment extensively: the soft drop condition $z = z_{\text{cut}}$ draws a horizontal line, while transverse momentum and jet mass measurements have slope dictated by respectively $q_T/E \sim z\vartheta$ and $e \sim z\vartheta^2$. The area corresponding to groomed emissions is shaded in grey. Note that because soft drop reclusters jets with the C/A algorithm (based on purely angular distance measure) no emission will be dropped whose angle is smaller than the groomed jet radius set by the emission passing the test (hence the vertical line). The vetoed region is shaded in red: emissions are vetoed if they set too large a jet mass, unless they are groomed away (grey shaded area); or, they are prohibited if they result in a transverse momentum larger than measured. As already stressed, only particles external to the groomed jet contribute to the transverse momentum measurement, so only groomed radiation is subjected to the veto (segments

that do not play a role in enforcing vetoes are denoted by dotted lines). The four vertices delimiting the resulting polygon give the modes of the analysis: soft and collinear modes have respectively the largest angle and largest energy fractions, and live therefore on the axes; other two modes arise from the interplay of the two measurements and the grooming condition, and they are referred to as collinear-soft (CS) and soft collinear (SC).

The Lund plane makes it evident which measurement each mode knows about. In particular, no mode determines the jet mass and transverse momentum at the same time, meaning that the dependence on the two variables will be completely factorized (even if eq. (5.5) assumed them to be of the same size!). Finally, their virtuality $\mu \sim E\vartheta z$ is easily computed by solving for the intersection of each pair of lines. This yields the scaling

$$
\begin{aligned}
\text{soft}: \quad & p_s^\mu \sim q_T(1,1,1); \\
\text{collinear}: \quad & p_c^\mu \sim E(\lambda_c^2, 1, \lambda_c),\ \lambda_c = \sqrt{e}; \\
\text{soft} - \text{collinear}: \quad & p_{sc}^\mu \sim E z_{\text{cut}}(\lambda_{sc}^2, 1, \lambda_{sc}),\ \lambda_{sc} = q_T/(E z_{\text{cut}}); \\
\text{collinear} - \text{soft}: \quad & p_{cs}^\mu \sim E z_{\text{cut}}(\lambda_{cs}^2, 1, \lambda_{cs}),\ \lambda_{cs} = \sqrt{e/z_{\text{cut}}}\,.
\end{aligned}
\tag{5.6}
$$

To briefly recap the role of each mode (see also fig. 5.1, right): collinear radiation (blue) form the energetic core of the jet. It contributes to the mass and always passes grooming; collinear-soft emissions (yellow) may or may not pass grooming. If they do, they contribute to the mass measurement despite the lower energy, because of the larger angle; soft-collinear radiation (green) saturates the grooming condition, and contributes to the transverse momentum measurement; so does soft radiation (red), that also fails soft drop.

The four modes in fig. 5.1 are largely separated, either in virtuality (C,CS,SC) or in rapidity (S,SC). Relaxing some of the hierarchies in eq. (5.5) results in pairs of modes to collapse into a single one: this corresponds to a refactorization of the theory, as power corrections in the ratio of characteristic scales can no longer be neglected. To elucidate this, I will briefly consider two possible situations,

$$
1 \gg z_{\text{cut}} \sim \sqrt{e_{\text{cut}}} \gg q_T/E \sim \sqrt{z_{\text{cut}} e_{\text{cut}}},
\tag{5.7a}
$$

$$
1 \gg z_{\text{cut}} \sim q_T/E \gg \sqrt{e_{\text{cut}}}\,.
\tag{5.7b}
$$

In the first case, the separation in virtuality between the CS and SC modes vanishes, and the two merge into a single collinear-soft mode that knows about both transverse momentum and jet mass (fig. 5.2 left). Physically, relaxing the cut on jet mass allows soft-collinear emissions that set the transverse momentum decorrelation to enter the groomed jet without necessarily spoiling its

mass. In the second case, asking $z_{\text{cut}} \sim q_T/E$ removes the separation in energy and angle between S and SC modes, which then collapse into a single kind of emission. This means that no radiation will automatically fail soft drop.
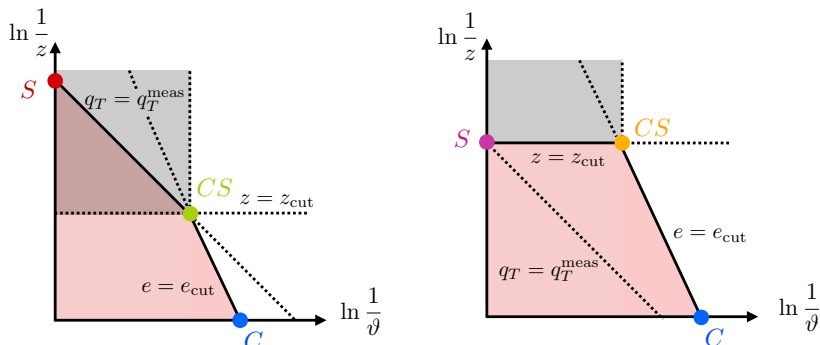

Figure 5.2 Mode picture in the Lund plane for $1 \gg z_{\text{cut}} \sim \sqrt{e_{\text{cut}}} \gg q_T/E \sim \sqrt{z_{\text{cut}} e_{\text{cut}}}$ (left) and $1 \gg z_{\text{cut}} \sim q_T/E \gg \sqrt{e_{\text{cut}}}$ (right). In these two scenarios, the SC mode in fig. 5.1 coalesces with respectively the CS mode and the S mode, causing a refactorization of the theory.

One can imagine several more hierarchies, but most of them will have limited practical relevance. For instance, the simple situation in eq. (5.4) corresponds to the SC, CS, C modes merging into a single kind of collinear radiation. Which regimes are worth considering is driven by phenomenological interest: some of the hierarchies may never occur for sensible values of the parameters (such as large z_{cut}) or might describe a corner of phase space where very few events occur (such as large e). In fact, Monte Carlo simulations (PYTHIA 8) predict most of the events to fall in the kinematic regime in eq. (5.5), which will be the focus of sec. 5.2.

5.1.2 Factorization and evolution

I now move on to the factorization analysis. The factorization theorem for small groomed jet mass was formulated in [218, 219], and the refactorization will naturally follow by assuming the validity of the mode picture presented above.

In presence of the modes (5.4), the factorization formula for $e^+e^- \to$ dijet is

$$\frac{\mathrm{d}\sigma_{e^+e^- \to JJX}}{\mathrm{d}e_1 \, \mathrm{d}e_2 \, \mathrm{d}\boldsymbol{q}} = \sigma_0^{e^+e^-}(s) \, H_{e^+e^-}(s, \mu) \int \frac{\mathrm{d}\boldsymbol{b}}{(2\pi)^2} \, e^{-i\boldsymbol{b}\cdot\boldsymbol{q}}$$

$$\mathcal{J}_q^\perp(e_1, \sqrt{s}, z_{\text{cut}}, \boldsymbol{b}, \mu, \zeta) \, \mathcal{J}_{\bar{q}}^\perp(e_2, \sqrt{s}, z_{\text{cut}}, \boldsymbol{b}, \mu, \zeta) \left[1 + \mathcal{O}\left(\frac{q_T^2}{s}\right)\right]. \quad (5.8)$$

This is similar to eq. (4.9), but exhibits some important differences. It features the same hard and soft function as the ungroomed case, with the latter reabsorbed in the jet functions following the usual pattern of eq. (2.33). The cross section is differential in the jet masses e_i, and not in the energy fraction of the jets (whose dependence is trivial, since I consider the large-R limit). Besides this quantity, the jet functions depend on the grooming parameter and the transverse momentum (via the impact parameter $\boldsymbol{b}$). The same considerations valid in dijet production yield the analogous formula for SIDIS,

$$
\frac{\mathrm{d}\sigma_{ep\to eJX}}{\mathrm{d}Q^2\,\mathrm{d}x\,\mathrm{d}e\,\mathrm{d}\boldsymbol{q}} = \sum_q \sigma^{\mathrm{DIS}}_{0,q}(x,Q^2)\,H^{\mathrm{DIS}}(Q^2,\mu)\int\frac{\mathrm{d}\boldsymbol{b}}{(2\pi)^2}\,e^{-i\boldsymbol{b}\cdot\boldsymbol{q}}
$$

$$
F_q(x,\boldsymbol{b},\mu,\zeta)\,\mathcal{J}_q^\perp(e,Q,z_{\mathrm{cut}},\boldsymbol{b},\mu,\zeta)\left[1+\mathcal{O}\!\left(\frac{q_T^2}{Q^2}\right)\right]. \quad (5.9)
$$

Again, this is very similar to eq. (4.11). Instead of a regular jet function we now have a groomed jet function, and the hypothesis of small jet mass enforces the same factorization formula as for the hadronic case, at the price that its validity is restricted to large jet radii.

I now proceed to the hierarchy in eq. (5.5), that constitutes the most relevant case in view of the analysis below. Following the mode picture in fig. 5.1, one predicts the jet function $\mathcal{J}_i^\perp$ in eqs. (5.8) and (5.9) to refactorize into three terms,

$$
\mathcal{J}_i^\perp(e,Q,z_{\mathrm{cut}},\boldsymbol{b},\mu,\zeta) = \int\mathrm{d}e'\,S_{\mathrm{cs},i}(e-e',Qz_{\mathrm{cut}},\mu)\,J_i(e',Q,\mu)
$$

$$
S_{\mathrm{sc},i}^\perp(Q,z_{\mathrm{cut}},\boldsymbol{b},\mu,\zeta)\left[1+\mathcal{O}\!\left(\frac{e}{z_{\mathrm{cut}}^2},\frac{q_T^2}{Q^2z_{\mathrm{cut}}^2}\right)\right], \quad (5.10)
$$

where the e^+e^- case requires only relabeling $Q\to\sqrt{s}$. The two functions carrying jet mass dependence appear in Laplace convolution, since this variable is additive, and reduce to a simple product in Laplace space. The collinear-soft function also knows about grooming, while the jet function[2] J depends on only the mass. This is a consequence of the collinear modes always surviving grooming. The collinear-soft function inherits (up to power corrections) all the transverse momentum dependence of the jet function on the left-hand side, and in particular it will obey the same double-scale evolution typical of TMDs. Being independent of the groomed jet mass, it does not enter the convolution (although in momentum space it would enter the factorization formula (5.9) in convolution with the TMDPDF). Operator definitions and one-loop results for

---

[2]Not to be confused with the jet functions in ch. 4 for ungroomed jets.

the three ingredients figuring here are collected in appx. B.1 and appx. B.2.3 respectively.

Finally, I can consider the two hierarchies in eq. (5.7), represented in fig. 5.2. In these situations the expansion in eq. (5.10) is too radical, as power corrections in respectively jet mass and transverse momentum need to be retained. In the case of larger jet mass, eq. (5.7a), one has instead

$$\mathcal{J}_i^\perp(e, Q, z_{\rm cut}, \boldsymbol{b}, \mu\zeta) = \int {\rm d}e'\, S_{{\rm cs},i}^\perp(e - e', Q z_{\rm cut}, \boldsymbol{b}, \mu, \zeta)\, J_i(e', Q, \mu)$$
$$\times \left[1 + \mathcal{O}(q_T/(Q z_{\rm cut})) \right],$$

with a single collinear-soft function describing the transverse momentum dependence *and* carrying jet mass dependence, which now captures power corrections in the ratio $\sqrt{e}/z_{\rm cut}$. Consistency of factorization implies the (multiplicative) relation

$$S_{{\rm cs},i}^\perp(e - e', Q z_{\rm cut}, \boldsymbol{b}, \mu, \zeta) = S_{{\rm cs},i}(e - e', Q z_{\rm cut}, \mu)\, S_{{\rm sc},i}^\perp(Q, z_{\rm cut}, \boldsymbol{b}, \mu, \zeta)$$
$$\times \left[1 + \mathcal{O}(\sqrt{e}/z_{\rm cut}) \right], \quad (5.11)$$

describing the refactorization of the modes that merge when passing from fig. 5.1 to the left panel of fig. 5.2.

Last, in the case described by eq. (5.7a) (or fig. 5.2, right panel), the factorization still looks like (5.10), but the soft-collinear function is now replaced by a groomed soft function which depends on both the transverse momentum and the soft drop parameter. This regime does not require the double-scale evolution discussed in sec. 2.2.3, since the two modes with large separation in rapidity coalesced to a single point.

In the rest of this section, I will discuss the RGE of the ingredients that enter the refactorization formula in eq. (5.10). The TMD jet functions on the left-hand side of the equation must satisfy the double-scale evolution of TMDFFs, since their evolution must match the one of the TMDPDF in eq. (5.9). As I already noted, on the right-hand side the transverse momentum dependence is described by only the soft-collinear function; thus, for RGE consistency, also $S_{{\rm sc},q}^\perp$ has identical evolution. Explicitly,

$$\mu \frac{{\rm d}}{{\rm d}\mu} S_{{\rm sc},i}^\perp(Q, z_{\rm cut}, \boldsymbol{b}, \mu, \zeta) = +\gamma_i(\mu, \zeta) S_{{\rm sc},i}^\perp(Q, z_{\rm cut}, \boldsymbol{b}, \mu, \zeta),$$
$$\zeta \frac{{\rm d}}{{\rm d}\zeta} S_{{\rm sc},i}^\perp(Q, z_{\rm cut}, \boldsymbol{b}, \mu, \zeta) = -\mathcal{D}_i(\boldsymbol{b}, \mu) S_{{\rm sc},i}^\perp(Q, z_{\rm cut}, \boldsymbol{b}, \mu, \zeta). \quad (5.12)$$

Because of the refactorization of the jet function, the resummation in eq. (5.12) does not capture large logarithms of $\sqrt{e}$ and $\sqrt{e z_{\rm cut}}$, which can still spoil the

convergence of the perturbative series. This is achieved with the evolution (only in virtuality) of the other ingredients in eq. (5.10), which I now present. Such evolution is conveniently described in Laplace space. Taking s to be the Laplace conjugate of the normalized groomed jet mass, then

$$\widetilde{G}_i(s) = \int_0^\infty \mathrm{d}e \, \exp(-e\,s)\, G_i(e)\,, \qquad (5.13)$$

where G_i generally denotes either $S_{\mathrm{sc},i}$ or J_i. In this space, factorization is just multiplicative, and evolution simply reads

$$\mu \frac{\mathrm{d}}{\mathrm{d}\mu} \widetilde{G}_i(\mu) = \gamma_i^G(\mu)\, \widetilde{G}(\mu) = \left[\Gamma_i^G\big(\alpha_s(\mu)\big) \ln \frac{\mu^2}{\widetilde{m}_G^2} + \Delta\gamma_i^G(\alpha_s(\mu)) \right] \widetilde{G}(\mu), \quad (5.14)$$

where the anomalous dimensions differ between the two functions (and from the UV anomalous dimension of TMDs, γ_i in eq. (5.12)). The second equality explicitly shows the cusp/non-cusp decomposition of the anomalous dimension, originating from the double-logarithmic dependence of the functions on μ. This is similar to the TMD case, eq. (2.40), but with the important difference that the anomalous dimensions do not depend on the rapidity scale ζ. Finally, $\widetilde{m}_G$ are the natural scales in Laplace space, formally obtained by conjugation from the natural scales in distribution space,[3]

$$m_J = Q\,\sqrt{e} \quad \rightarrow \quad \widetilde{m}_J = Q/\sqrt{s\,e^{-\gamma_E}}\,, \qquad (5.15)$$

$$m_{S_{\mathrm{cs}}} = Q\,\sqrt{z_{\mathrm{cut}}e} \quad \rightarrow \quad \widetilde{m}_{S_{\mathrm{cs}}} = Q\,\sqrt{z_{\mathrm{cut}}}/\sqrt{s\,e^{-\gamma_E}}\,. \qquad (5.16)$$

Consistent with the factorization structure, and the groomed jet mass being additive (rather than multiplicative), RGE does not mix different flavors. This allows eq. (5.14) to be solved analytically, as I now show explicitly. Using that in $\overline{\mathrm{MS}}$ scheme the anomalous dimensions depend on μ only through the strong coupling, one finds

$$\widetilde{G}_i(\mu) = \exp\big(K_i^G(\mu,\mu_0)\big) \left(\frac{\mu_0}{\widetilde{m}_G} \right)^{2\omega_i^G(\mu,\mu_0)} \widetilde{G}_i(\mu_0)\,, \qquad (5.17)$$

where the kernels

$$K_i^G(\mu,\mu_0) = 2\int_{\alpha_s(\mu_0)}^{\alpha_s(\mu)} \frac{d\alpha_s}{\beta(\alpha_s)} \Gamma_i^G(\alpha_s) \int_{\alpha_s(\mu_0)}^{\alpha_s} \frac{d\alpha_s'}{\beta(\alpha_s')} + \int_{\alpha_s(\mu_0)}^{\alpha_s(\mu)} \frac{d\alpha_s}{\beta(\alpha_s)} \Delta\gamma_i^G(\alpha_s),$$

$$\omega_i^G(\mu,\mu_0) = \int_{\alpha_s(\mu_0)}^{\alpha_s(\mu)} \frac{d\alpha_s}{\beta(\alpha_s)} \Gamma_i^G(\alpha_s)\,, \qquad (5.18)$$

---

[3]It is customary to include factors e^{γ_E}, arising when Laplace transforming plus distributions, in the argument of logarithms in Laplace space.

are determined order by order in perturbation theory from the cusp/non-cusp anomalous dimensions, as well as the beta function in eq. (1.33). The evolution in eq. (5.14) combines trivially for the two function I need, yielding

$$\widetilde{S}_{\mathrm{cs},i}(s,\mu)\,\widetilde{J}_i(s,\mu) = \exp\left\{K_i^J(\mu,\mu_J) + K_i^{S_{\mathrm{cs}}}(\mu,\mu_{\mathrm{cs}}) + \omega_i^J(\mu,\mu_J)\left[\gamma_E + L_J(\mu_J,s)\right]\right.$$
$$\left. + \omega_i^{S_{\mathrm{cs}}}(\mu,\mu_{\mathrm{cs}})\left[\gamma_E + L_{\mathrm{cs}}(\mu_{\mathrm{cs}},s)\right]\right\}\widetilde{S}_{\mathrm{cs},i}(\mu_{\mathrm{cs}},s)\,\widetilde{J}_i(\mu_J,s)\,. \quad (5.19)$$

Here I omitted non-relevant arguments, and defined

$$L_J = \ln\frac{\mu_J^2}{\widetilde{m}_J^2}\,, \qquad L_{\mathrm{cs}} = \ln\frac{\mu_{\mathrm{cs}}^2}{\widetilde{m}_{S_{\mathrm{cs}}}^2}\,, \qquad (5.20)$$

that depend on the Laplace parameter s through the natural scales (5.15). The expression of the kernels for these ingredients up to NLL for can be found in [4]. Expressing the result in terms of the groomed jet mass requires taking the inverse Laplace transform of eq. (5.19), which in general is challenging. It becomes easy if the dependence of the fixed-order functions on the mass is purely logarithmic, since the logarithms (5.20) are obtained from eq. (5.19) by formally differentiating with respect to the kernels ω^G. In this case, after solving the inverse Laplace transform,

$$\mathcal{J}_i(e,Q,z_{\mathrm{cut}},\mu) = \exp\left[K_i^{S_{\mathrm{cs}}}(\mu,\mu_{\mathrm{cs}}) + K_i^J(\mu,\mu_J)\right]\widetilde{S}_{\mathrm{cs},i}(L_{\mathrm{cs}}\to\partial_{\omega_{\mathrm{cs}}})\widetilde{J}_i(L_J\to\partial_{\omega_J})$$
$$\left(\frac{\mu_{\mathrm{cs}}^2}{Q^2 z_{\mathrm{cut}}e}\right)^{\omega_i^{S_{\mathrm{cs}}}(\mu,\mu_{\mathrm{cs}})}\left(\frac{\mu_J^2}{Q^2 e}\right)^{\omega_i^J(\mu,\mu_J)}\frac{\exp\left\{\gamma_E\left[\omega_i^{S_{\mathrm{cs}}}(\mu,\mu_{\mathrm{cs}}) + \omega_i^J(\mu,\mu_J)\right]\right\}}{\Gamma\left(1 - \omega_i^{S_{\mathrm{cs}}}(\mu,\mu_{\mathrm{cs}}) - \omega_i^J(\mu,\mu_J)\right)}\,.$$
$$(5.21)$$

Here I denote with $\mathcal{J}$ the evolved product of the jet and collienar-soft functions, and $\widetilde{S}_{\mathrm{cs},i}, \widetilde{J}_i$ should now be thought of as differential operators, derived from the Laplace-space ingredients using the replacement rule in brackets.

Performing the evolution of the jet quantity defined in eq. (5.11) in the scenario described by fig. 5.1 amounts therefore to: 1) computing the jet in eq. (5.21), evolved from the natural scales $(\mu_{\mathrm{cs}},\mu_J)$ to the hard scale μ, and 2) performing the double-scale evolution of the soft-collinear function from $(\mu_{\mathrm{cs}},\zeta_{\mathrm{cs}})$ to the hard scale. The two evolutions do not mix; this means in particular that the jet function in eq. (5.21) will not alter the shape of the transverse momentum distribution (although it is of course fundamental to get the correct normalization).

5.1.3 Hadronization effects

The main goal of the framework described above is the extraction of TMD-PDFs in electron-proton collisions. As already remarked in sec. 4.3, measuring

jets instead of hadrons removes one of the sources of final-state uncertainty (the poor knowledge of TMDFF entering SIDIS), but at small transverse momentum the jet functions themselves are not immune to hadronization effects. Although soft drop reduces the impact of hadronization on jets, further improvement could be obtained from a model that parametrizes the impact of non-perturbative physics on the jet. In sec. 4.2.1, I briefly described the non-perturbative model used for the TMDPDF, based on the ansatz (4.62). For perturbative ingredients, it is often possible to act more systematically, and set up a QFT-based description to incorporate non-perturbative corrections to leading power in an expansion in Λ_{QCD}, see e.g. [228–231]. This approach has the advantage of describing hadronization corrections from first principles, up to few parameters that are fixed by universality of non-perturbative physics.

Hadronization corrections to TMDs have been extensively studied from a field theory perspective, see [14,232–235], while a hadronization model for cross sections differential in groomed jet mass was recently introduced in ref. [236]. A quantitative description of hadronization effects was beyond the scope of [4], but in the following I will summarize the qualitative analysis that was proposed there. The focus is on those corrections that may alter the shape of the q_T distribution, rather than impacting only the normalization.

Let me start from the hierarchy in fig. 5.1. In principle, any of the functions that appear in eq. (5.10) (as well as the soft function reabsorbed in S_{cs}) receives hadronization corrections, although their magnitude will be larger for those ingredients whose virtuality is closer to Λ_{QCD}. In the case of the soft function, hadronization effects are described through an expansion (in impact parameter space)

$$
\begin{aligned}
S(\boldsymbol{b}) &= \langle 0|T[Y_n Y_{\bar{n}}^\dagger(\boldsymbol{b})]\overline{T}[Y_{\bar{n}} Y_n^\dagger(0)]|0\rangle \\
&= S^{\mathrm{pert}}(\boldsymbol{b})\big[1 + b^2 \textstyle\sum_a C_a^{(s)}(b)\langle 0|O^a|0\rangle + \mathcal{O}(b^4 \Lambda_{\mathrm{QCD}}^4)\big]\,,
\end{aligned} \tag{5.22}
$$

where the sum runs over a complete set of local operators that have the same quantum numbers as the soft function S^{pert} computed in perturbation theory. In practice, this can be described by introducing a single parameter Ω_{s},

$$
S(\boldsymbol{b}) = S^{\mathrm{pert}}(\boldsymbol{b}) + b^2\, \Omega_{\mathrm{s}} + \mathcal{O}(b^4 \Lambda_{\mathrm{QCD}}^4)\,, \tag{5.23}
$$

which is universal and can be fitted from experiment. This sort of contribution is referred to as *shift* hadronization correction, since in transverse momentum space it can be reabsorbed in a shift of the argument of the perturbative function, $S^{\mathrm{pert}}(q_T) \to S^{\mathrm{pert}}(q_T - \Omega_s)$.

In the SCET$_{\mathrm{II}}$ picture of interest here, the soft-collinear function has the same virtuality as the soft function and will therefore carry non-perturbative

corrections of roughly the same size. As discussed in sec. 5.1.1, soft-collinear emissions contribute to the cross section only if they fail soft drop (otherwise, their large plus momentum component would drive the jet mass out of the measurement region). Given the angular scaling of this mode, which is much larger than the collinear-soft and collinear modes forming the groomed jet, the phase-space region available is effectively unconstrained. Hence, the correction in this case also causes a simple shift, and is implemented in the same manner as in the case of the global soft function, yielding

$$SS_{\mathrm{sc}}^{\perp}(\boldsymbol{b}) = \left[1 + b^2(\Omega_{\mathrm{s}} + \Omega_{\mathrm{sc}})\right] S^{\perp,\mathrm{pert}} S_{\mathrm{sc}}^{\perp,\mathrm{pert}}(\boldsymbol{b}) + \mathcal{O}(b^4 \Lambda_{\mathrm{QCD}}^4). \qquad (5.24)$$

Note that in this regime hadronization effects in the collinear-soft sector are the largest source of non-perturbative corrections, since this mode carries the lowest virtuality, $\mu_{\mathrm{cs}} \sim Q\sqrt{ez_{\mathrm{cut}}}$. However, this radiation does not contribute to the transverse momentum measurement, so such effects do not modify the shape of the q_T spectrum.

The situation becomes more interesting in the regime of eq. (5.7a). Here a single collinear-soft mode with same virtuality as the soft one determines the jet mass and transverse momentum at the same time, and may or may not pass soft drop. In this situation the analysis follows the lines of [236]. There, hadronization effects were described through non-perturbative gluon emissions. Concerning the shift correction, one has to distinguish two possible scenarios (fig. 5.3):

1. Collinear-soft (cs) particles pass soft drop
   If cs particles pass soft drop they do not contribute to q_T, as the groomed jet axis (just like the standard axis) balances the transverse momentum of all the emissions inside the jet. Non-perturbative emissions with cs scaling contribute to q_T when they lie outside the groomed jet. In this case, one needs to calculate the catchment area of the groomed jet that is determined by the angular distance of the cs subjet that passed soft drop. Ref. [236] did this at NLL using a coherent branching formalism, factorizing a purely non-perturbative function from the calculable perturbative effects.

2. Collinear-soft particles fail soft drop
   In this case, collinear modes are the only ones that pass soft drop, so non-perturbative radiation with cs scaling has unconstrained phase space, by the same logic as for the soft and the soft-collinear functions. This generates again a simple shift correction. Interesting corrections come from the collinear non-perturbative emissions lying outside the catchment region, that is now determined by the collinear modes alone. However,

the size of these collinear effects is suppressed by the large virtuality of the collinear radiation.
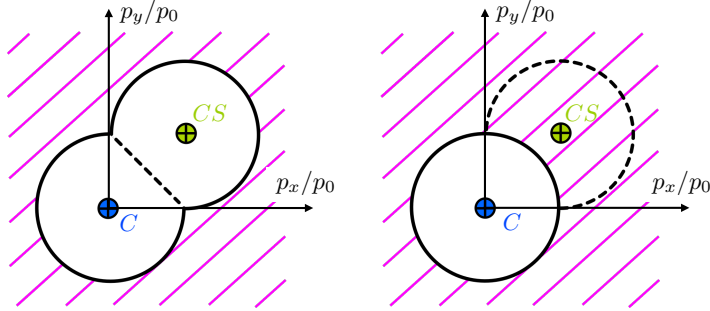

Figure 5.3 Catchment area (in transverse momentum) for collinear-soft non-perturbative emissions. If perturbative cs emissions pass soft drop (left), non-perturbative cs emission must lie out of the collinear and cs subjets. If they fail soft drop (right), then the vetoed area coincides with the collinear subjet, and the catchment area is effectively unconstrained (the angular size of collinear emissions is negligible).

In this regime another kind of hadronization effect arises, due not to non-perturbative emissions directly changing q_T, but rather to modifications of the soft-drop condition. Specifically, a non-perturbative emission from a cs subjet might reverse the outcome of the soft-drop test on that branch. In presence of a non-perturbative cs emission with momentum k and a perturbative cs emission with momentum p, the complete measurement function writes

$$\Theta^{p\pm k} = \Theta\left(\frac{p_0 + k_0}{E_J} - z_{\text{cut}}\right)\delta^{(2)}(\boldsymbol{q} - \boldsymbol{p} \pm \boldsymbol{k})\,. \tag{5.25}$$

The $\pm$ sign indicates whether the perturbative cs subject gains or loses a non-perturbative momentum after hadronization. At leading power, the measurements expand as

$$\Theta^{p+k} \approx \Theta^p_{\text{SD}}\delta^{(2)}(\boldsymbol{q} - \boldsymbol{p}) + \frac{k_-}{E_J}\Theta^{\text{b.c.}}(\vartheta_k, \vartheta_p, \Delta\phi)\delta^p_{\text{SD}}\delta^{(2)}(\boldsymbol{k} - \boldsymbol{p})\,,$$

$$\Theta^{p-k} \approx \Theta^p_{\text{SD}}\delta^{(2)}(\boldsymbol{q} - \boldsymbol{p}) - \frac{k_-}{E_J}\overline{\Theta}^{\text{b.c.}}(\vartheta_k, \vartheta_p, \Delta\phi)\delta^p_{\text{SD}}\delta^{(2)}(\boldsymbol{k} - \boldsymbol{p})\,, \tag{5.26}$$

with

$$\Theta^p_{\text{SD}} = \Theta\left(\frac{p_-}{2E_J} - z_{\text{cut}}\right)\,, \qquad \delta^p_{\text{SD}} = \delta\left(\frac{p_-}{2E_J} - z_{\text{cut}}\right)\,, \tag{5.27}$$

while $\Theta^{\text{b.c.}}$ gives the phase space for the non-perturbative emission to get clustered with the cs subjet, see fig. 5.4, and $\overline{\Theta}^{\text{b.c.}}$ is its complement. The leading
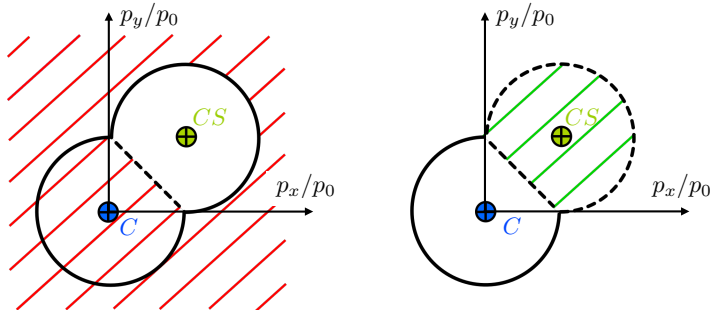

Figure 5.4 Phase space (in transverse momentum) for loss (left) or gain (right) of a collinear-soft non perturbative emission. Such an emission may revert the outcome of the soft-drop test, causing *boundary* corrections.

power correction scales as $q^-/E_J \sim q_T z_{\text{cut}}/E$, which for typical values of $z_{cut} \sim 0.1$ is comparable to the q_T^2/E^2 correction that one gets from the shift terms.

5.2 Phenomenological study

5.2.1 Implementation

I will now comment on some of the details of the implementation of the framework above. Similar to the recoil-free analysis of ch. 4, numerical predictions are based on ARTEMIDE, which takes care of the double-scale evolution and the integration over the kinematics. For this application, I supplemented the code with a module for groomed jets, which includes the perturbative jet functions and evolves them in virtuality.

The distribution in transverse momentum is obtained by integrating the cross section in eq. (5.8) over the jet mass,

$$\frac{\mathrm{d}\sigma}{\mathrm{d}\boldsymbol{q}}(e_{\text{cut}}) = \int_0^{e_{\text{cut}}} \mathrm{d}e_1 \int_0^{e_{\text{cut}}} \mathrm{d}e_2 \, \frac{\mathrm{d}\sigma}{\mathrm{d}\boldsymbol{q}\,\mathrm{d}e_1\,\mathrm{d}e_2}\,, \tag{5.28}$$

with the default value $e_{\text{cut}} = 0.01$. In the regime $z_{\text{cut}} \ll q_T/E \sim e_{\text{cut}}$ that is the focus of the analysis, switching to the cumulant simply amounts to using the integrated jet functions

$$\mathcal{J}_j(e_{\text{cut}}, Q, z_{\text{cut}}, \boldsymbol{q}, \mu, \zeta) = \int_0^{e_{\text{cut}}} \mathrm{d}e \, \mathcal{J}_j(e, Q, z_{\text{cut}}, \boldsymbol{q}, \mu, \zeta)\,, \tag{5.29}$$

rather than the differential counterpart shown in eq. (5.21). The one-loop jet function and collinear-soft function were computed in [218]. As discussed in sec. 5.1.2, the evolution in virtuality is performed analytically, from the initial scales

$$\mu_J = 2E\sqrt{e_{\rm cut}}\,, \qquad \mu_{\rm cs} = 2E\sqrt{e_{\rm cut}\,z_{\rm cut}} \tag{5.30}$$

up to the final hard scale 2E ($\sqrt{s}$ for e^+e^-, Q for DIS+jet). When using cumulant scale setting (namely choosing the scales as a function of $e_{\rm cut}$, rather than e) all the manipulations that lead to eq. (5.21) from the unevolved, differential jet function are still valid for the integrated function.

When replacing the default values $z_{\rm cut} = 0.2$, $e_{\rm cut} = 0.01$, the scale of lowest virtuality evaluates to $\mu_{\rm cs} \simeq 4.1$ GeV for e^+e^- collisions at the Z-boson mass, and to $\mu_{\rm cs} \simeq 1.8$ GeV for DIS, at the lower value $Q = 40$ GeV I consider. Especially in the second case, a significant part of the evolution occurs below the bottom quark mass, so that setting $n_f = 5$ is unjustified. Instead, I use a scheme with variable number of flavors, namely I run four-flavor evolution of the jet functions up to $m_b = 4.75$ GeV and switch to $n_f = 5$ at the bottom threshold. A subtlety to take into account is that the kernels ω^G that appear in eq. (5.18) compose additively, but the K^G do not,

$$\omega_i^G(\mu_1, \mu_3) = \omega_i^G(\mu_1, \mu_2) + \omega_i^G(\mu_2, \mu_3)\,,$$
$$K_i^G(\mu_1, \mu_3) = K_i^G(\mu_1, \mu_2) + K_i^G(\mu_2, \mu_3) + 2\omega_i^G \ln \frac{\mu_2}{\mu_3}\,. \tag{5.31}$$

This effect can impact up to $\sim 20\%$ on the normalization of the cross section, thus it must be included when getting predictions with absolute normalization.

The other fundamental ingredient in eq. (5.10) is the soft-collinear function $S_{\rm sc}^\perp$, that was computed at one-loop accuracy in [4]. Equivalently to the case of recoil-free jets, the double-scale evolution in eq. (5.12) is performed adopting the ζ-prescription discussed in sec. 2.2.3. In particular, the initial scales coincide with eq. (4.59), and are chosen so as to cancel the dependence on μ. However, an important difference is that the final scale for groomed jets is now

$$(\mu_f, \zeta_f) = \begin{cases} (\sqrt{s}, z_{\rm cut}^2 s) & e^+e^- \\ (Q, z_{\rm cut}^2 Q^2) & {\rm DIS+jet} \end{cases} \tag{5.32}$$

The need for the additional factors $z_{\rm cut}$ in the final rapidity scale is easily understood from the Lund plane picture in fig. 5.1: the separation in rapidity between the S and SC modes interrupts at $z = z_{\rm cut}$ (in the case of TMDs, it extends all the way to $z = 1$). Of course, in the case of DIS+jet, the evolution of the TMDPDF is unaltered, as grooming only applies to jets.

Finally, I used again the non-perturbative model of [210] for the TMD-PDF and its evolution. Including corrections due to hadronization inside the groomed jets, as described in sec. 5.1.3, would guarantee a further improvement. However, as the next section will show, the theory uncertainty due to scale variation is rather large for this observable, suggesting that improving the perturbative accuracy should be prioritized.

5.2.2 Numerical predictions

I now move on to showing numerical predictions for TMDs involving groomed jets. As in the analysis using recoil-free jets, I will use the case of $e^+e^- \rightarrow$ dijet as a way to assess the validity of our framework in an environment which is cleaner because the initial-state TMDPDF is absent. To this aim, besides numerical predictions, I will show Monte Carlo simulations obtained using PYTHIA 8 [25] and FASTJET 3 [79].

According the factorization formula eq. (5.10), as long as one remains within the hierarchy in eq. (5.5), then the exact cutoff on the groomed jet mass will only influence the overall normalization and not the shape of the TMD distribution. Fig. 5.5 (left) test this prediction against simulations, by comparing the normalized TMD distributions for various values of e_{cut}. Here and in the following labels, I use the shortcut notation $\mathrm{d}\sigma = \mathrm{d}\sigma/\mathrm{d}q_T$. The shape is fairly stable under variations of the cut on jet mass: the relative difference on each bin in transverse momentum is of order 5% when varying the cut by two orders of magnitude.

In addition, fig. 5.5 (right) investigates the validity of the large-radius approximation, by simulating events at $\sqrt{s} = 50$ GeV for different values of $R \simeq 1$. As long as the radius is sufficiently large, the shape and normalization of the cross section around the peak region are independent of the specific value. Note that the plot preserves the relative normalization of the curves. Significant deviations occur in the tail, where the assumption $q_T \ll \sqrt{s}$, and in particular $q_T/\sqrt{s} \ll z_{\text{cut}}$, also gradually lose validity. These tests validate the factorization framework in sec. 5.1.2 and justify focusing on the regime in fig. 5.1.

In fig. 5.6, I show analytic results for the NLL cross section (normalized) against PYTHIA simulations, for $\sqrt{s} = 50$ and 100 GeV. For the purpose of comparison, hadronization effects in the simulation are turned off, and the parameter c_0 of the non-perturbative model is set to 0 (B_{NP} is not, such that the soft scale, scaling as $1/b$, does not hit the Landau pole). Rather than the ζ-prescription that I use elsewhere, these predictions are obtained with the Rapidity Renormalization Group evolution of [129]. Although, as I am about to discuss, the theoretical uncertainty of the cross section for these
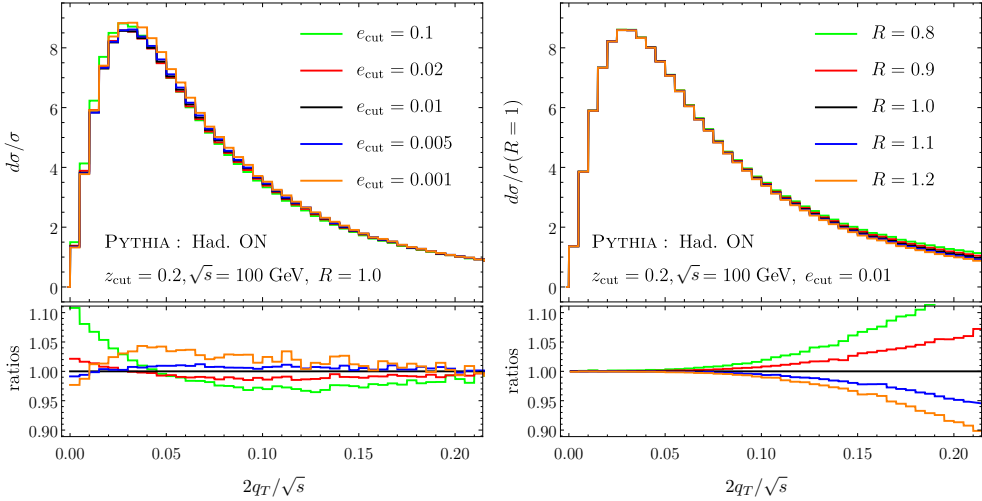
Figure 5.5 Left: the normalized cross sections for different values of the jet mass cutoff parameter e_{cut}. We also include the corresponding ratios with respect to the case $e_{\text{cut}} = 0.01$. Right: The cross section for fixed $e_{\text{cut}} = 0.01$ and for different values of the jet radius R, normalized with respect to $R = 1$.
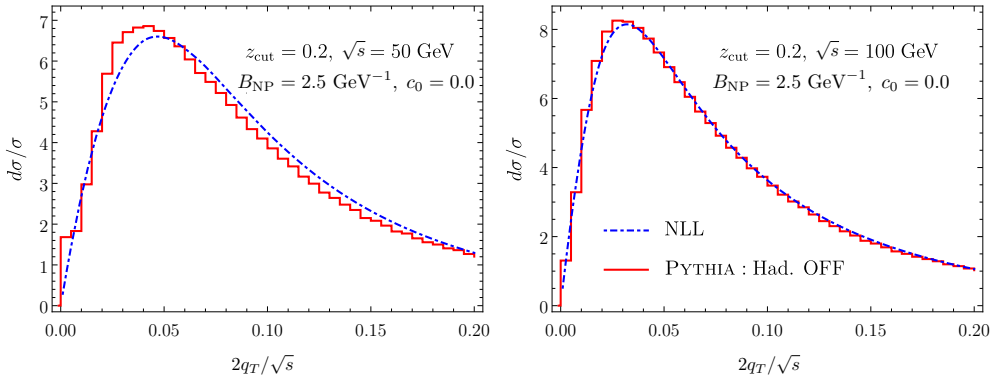

Figure 5.6 Comparison between NLL predictions (here obtained with the rapidity RG approach) and Monte Carlo parton-level simulations, for e^+e^- collisions at the two center-of-mass energies $\sqrt{s} = 50$ GeV (left) and $\sqrt{s} = 100$ GeV (right).

energies at NLL is quite large, agreement with the simulations is very good for the canonical choice of scales (i.e., central line in fig. 5.6). As expected, the agreement gets even better at the larger center-of-mass energy, since the scale separation is wider and power corrections to factorization smaller.
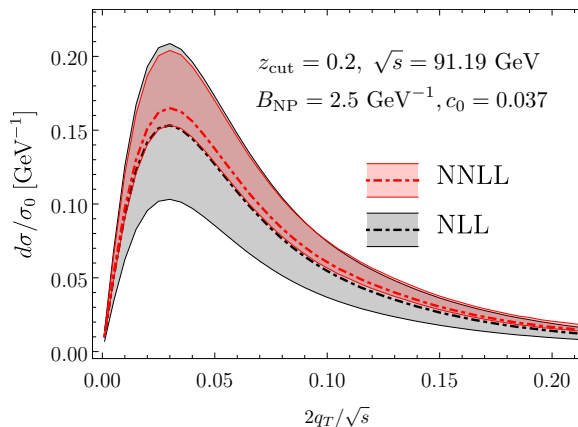
Figure 5.7 Transverse momentum decorrelation for $e^+e^- \to$ dijet with center of mass energy at the Z mass.

In fig. 5.7 I give the NNLL predictions including a theoretical uncertainty band. Numerical results are obtained with the ζ prescription, using the settings discussed in sec. 5.2.1, and the NLL prediction is shown for comparison. To estimate the theoretical uncertainty I first vary all the factorization scales of a factor 2 (0.5) around their canonical value, then separately take the envelope of the variations involved in rapidity evolution, μ, μ_{sc}, and of the ones involved only in the virtuality evolution of the jet function, μ_{cs}, μ_J. The final error bands are the quadrature of the two contributions: the reason for this prescription is that rapidity and virtuality evolutions are in principle uncorrelated. It is reassuring that the theory error decreases by approximately a factor of two when moving from NLL to NNLL. The uncertainty is somewhat larger than one might expect for a NNLL calculation, and is practically dominated by the scale variations in the jet function. This is ascribed to the small values of the collinear-soft scale, $\mu_{cs} \sim Q\sqrt{e_{\text{cut}}z_{\text{cut}}}$, which approaches the non-perturbative regime even for values of $\sqrt{s} \sim M_Z$. One might attempt to reduce the uncertainty by increasing either e_{cut} or z_{cut}, but caution is needed not to invalidate the corresponding hierarchy. I will show in a moment that in DIS, when only the mass of one jet is measured, the error band decreases.

I now turn to describing numerical results for the TMD spectrum of groomed jets in DIS, using the factorization theorem in eq. (5.9). As for recoil-free jets in sec. 4.2.3, the analysis is performed for two center-of-mass energies, EIC: $\sqrt{s} = 100$ GeV and HERA: 318 GeV. For both energies, $y = Q^2/(xs)$ and $Q = \sqrt{-q^2}$ are integrated over in the regions $0.01 < y < 0.95$ and $40 < Q < 50$ GeV. For the TMDPDFs, I use again the fits obtained from Drell-Yan data in [210] with the use of the ζ-prescription.
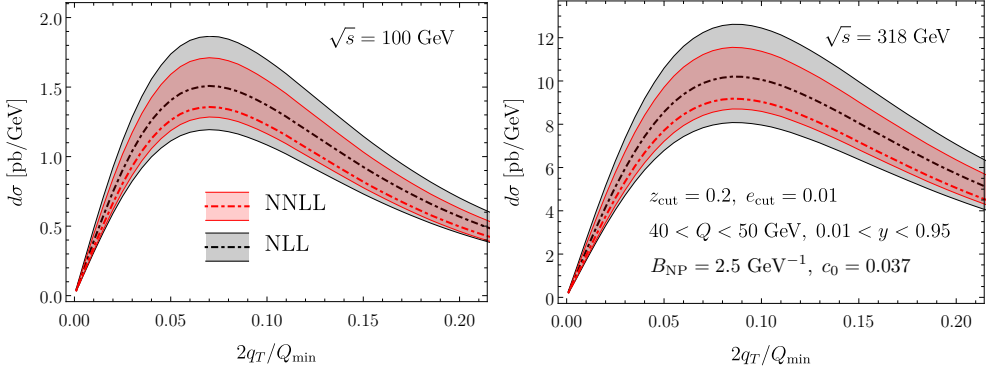
Figure 5.8 Transverse momentum spectrum for DIS+jet, at the two center-of-mass energies of HERA and EIC.

In fig. 5.8 I show the results for NLL and NNLL accuracies for the two center of mass choices, including theoretical uncertainties. Theoretical scale variations are estimated as for the electron-positron case, with the important difference that the TMDPDF does not have additional evolution in virtuality (besides the double-scale evolution of TMDs). The groomed jet parameters are also the same as in the di-lepton case: $\beta = 0$, $z_{\mathrm{cut}} = 0.2$, and $e_{\mathrm{cut}} = 0.01$. As before, there is good perturbative convergence between the NLL and NNLL results. In the presence of a single groomed jet, the size of the NLL error band is lower ($\sim 30\%$ at peak, compared to $\sim 50\%$ of the e^+e^- case). The NNLL band is still large, and in particular very asymmetric: this is a consequence of the upper curve being dominated by the lower variation of $\mu_{\mathrm{cs}} \sim 0.9$ GeV, that touches the non-perturbative region. The absolute value of theoretical scale variation is improvable with higher logarithmic accuracy (ideally, N^{3}LL), which however needs the explicit calculation of several jet and soft matrix elements at two loops, including their anomalous dimensions.

Finally, I investigate the size of the uncertainty due to the hadronic initial state and the non-perturbative effects induced by TMD evolution. Identical to the analysis for recoil-free jets, I do so by varying the parameters of the non-perturbative model in our NNLL result. The effects are shown in fig. 5.9, considering both *variable* and *fixed* B_{NP} schemes (for details on the difference, see [210]). The variation for this kinematics is small, order $\sim 5\%$: the sensitivity to initial-state physics is similar to using recoil-free jets, but much smaller than the theoretical uncertainties highlighted in fig. 5.8. This implies that in order to constrain TMD distributions using groomed jets in DIS, we need a better control over the theoretical uncertainties. However, it confirms
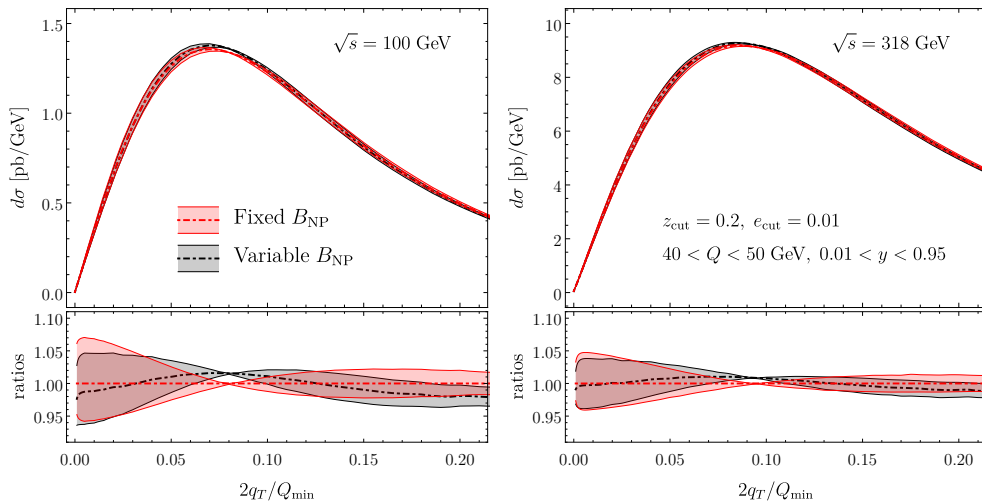
Figure 5.9 The NNLL cross-section including modeling of the initial hadronic state effects fitted from Drell-Yan processes using two different scenes: fixed and variable B_{NP}.

the potential of the framework as an alternative to hadrons or recoil-free jets to study TMDPDFs.

5.3 Outlook

In this chapter, I have presented a framework to compute the transverse momentum (decorrelation) spectrum in $e^+e^- \to$ dijet and DIS+jet, where the fat jets are groomed using the soft-drop algorithm. As I showed in ch. 4, recoil-free jets lead to the same factorization formula as for hadrons over the whole kinematic range; achieving a similar result with groomed jets needed additional assumptions on the kinematics. Specifically, one requires that the jets are large, and – at the same time – selects collimated jets with a jet mass cut. On the one hand, these assumption reduce the theoretical scope of the framework. On the other hand, they do not pose serious limits to its applicability at the EIC, since experimental analyses at *e-p* colliders prefer large jets, and most of the events fall in the low-mass region.

Having specified the caveats above, soft-drop jets have two of the main theoretical simplifications accomplished by their recoil-free equivalent: insensitivity to non-global logarithms and identical rapidity evolution as for hadrons. The price of grooming, compared to the WTA scheme, is the larger theoretical error: the uncertainty shown through scale variation ($10\% \sim 20\%$) surpasses the

sensitivity to initial-state non-perturbative physics ($\sim 5\%$). This additional error originates from the lower perturbative accuracy (NNLL vs N^{3}LL) and the richer mode structure in the effective theory. Therefore, uncertainty can be mitigated either by pushing the calculation to higher logarithmic accuracy, or by extending the EFT description to other regimes. Since most of the scale uncertainty ultimately comes from the small value of e_{cut}, loosening the cut on jet mass is an interesting option. This is still compatible with factorization, but requires one to treat the regime shown on the right panel of fig. 5.1.

At the same time, grooming provides an additional advantage of cutting off sources of contamination inside the jets. Simulations using PYTHIA, see again fig. 2.3, show that soft drop greatly reduces the impact of the underlying event, as well as final-state hadronization effects. In particular, hadronization corrections at low q_T are significantly smaller than for the case of a standard jet axis. Moreover, soft drop is a well-established technique that can build on solid experimental and theoretical grounds: for instance, as I briefly described in sec. 5.1.3, a model exists to account for hadronization effects within the jet, which at present is still lacking for the recoil-free counterpart.

Ultimately, in chapters 4 and 5 I presented two alternatives to deepen the study of TMDs that elaborate on the same idea: jets are in principle better probes than final-state hadrons, since they are calculable objects in perturbation theory. Under what conditions this statement holds true, and what is the best jet definition to achieve the goal, remain interesting open questions.

6

Conclusions

The present thesis investigated the use of alternative jets to study transverse momentum dependent distributions. Both quantities, discussed in ch. 2, are intrinsic QCD objects, whose definition acquires precise meaning only in the context of factorization. For this reason, I devoted ch. 1 to review the soft and collinear limit of the theory. The main protagonist in the applications I presented is the Winner-Take-All recombination scheme, the most widely used instance of a recoil-free jet. In ch. 3, I applied this sequential jet algorithm to describing the transverse momentum dependence of hadrons fragmenting inside jets. Measuring the transverse momentum with respect to the recoil-free jet axis (rather than a standard axis) resulted in a purely collinear observable, whose characteristic features are stable under perturbations in the final state. Extending the analysis to hadrons will allow for applications at the LHC, in both proton-proton and heavy-ion collisions. In ch. 4, the same WTA scheme was used to develop a framework for DIS+jet valid to N^3LL, a remarkable level of precision. Such a framework offers a promising channel in view of extraction of TMDPDFs at the future EIC. Finally, in ch. 5 I studied again DIS with *soft-drop* jets, which allowed for a direct comparison of grooming and recoil-free techniques. While groomed jets minimize the impact of contamination within an established framework, they suffer from a more involved factorization picture.

Standing the comparison with jet grooming is in fact one of the biggest challenges faced by recoil-free jets. Similar to grooming, recoil-free algorithms aim at limiting the effects of contamination inside the jet, especially originating from the underlying event. In theory, this mitigation is guaranteed by the direction of the recoil-free axis being insensitive to soft emissions. Besides the aforementioned ref. [85], the reduction of contamination was quantified and compared to grooming techniques in [237] (see also [238] for a study of the relative angle between the two). On this front, especially in the case of DIS+jet, progress remains to be done to quantify the effectiveness of the WTA scheme in removing soft contamination. A specific Monte Carlo analysis would

help in this direction.

However, the absence of recoil has a clear and striking advantage in the large simplification of factorization formulae. This property is achieved through an improved separation of collinear from soft physics, since soft emissions do not perceive the jet boundary as a sharp cut. In TMD fragmentation inside jets, this fact makes the observable completely insensitive to the soft sector; in DIS+jet and dijet production, it leads to the same soft physics as in hadron production; in both cases, it eliminates non-global logarithms. The resulting simplified framework is not only desirable theoretically, but has also important consequences in phenomenology, see the respective outlooks in sec. 3.3 and sec. 4.3. Around the time of writing this thesis, a further application of the WTA recombination scheme to vector boson-jet production [217] confirmed the high potential of this alternative jet definition. In presence of several dedicated phenomenological analyses (see also [239]), WTA jets appear to be mature enough to stand the test of experiment.

Transverse momentum dependent processes are the natural place where the absence of recoil can play a significant advantage, since soft radiation has a much larger impact on the small transverse momenta than on their large longitudinal component. This immediately requires handling multi-scale processes and multi-differential cross sections. The analyses presented here largely benefited by the Soft Collinear Effective Theory formulation, which makes it immediate to translate the (sometimes intricate) mode picture into factorization formulae and Renormalization Group Equations. Multi-differential quantities also call for precision physics: in the past decade, QCD experienced the *NNLO revolution*, an outburst of breakthrough perturbative calculations at two-loop order and beyond. At this frontier, jet observables still lag behind, since managing the phase-space constraints imposed by jet algorithms quickly becomes complicated beyond one loop. In ch. 4, I showed how we extracted a two-loop jet function in the large radius limit using standard numerical techniques, which was a fundamental step to achieve N^3LL precision. In the cases of in-jet fragmentation (ch. 3) and groomed jets (ch. 5), the level of perturbative accuracy is indeed what currently limits the theoretical precision.

Finally, much interesting physics hides in the region of small transverse momentum, where non-perturbative corrections may be large. Therefore, WTA jets would largely benefit from the formulation of a hadronization model, along the lines sketched in sec. 5.1.3 for the case of groomed jets. As I discussed in sec. 4.3, one important question is whether non-perturbative corrections to recoil-free jets could flaw the increased precision they promise in the study of TMDs. Further studies in this direction, and the presence of a hadronization model, would significantly improve the robustness of the framework.

A

Conventions and formulae

A.1 Lightcone coordinates

Given two lightlike, linearly independent vectors $n, \overline{n}$ such that

$$n^2 = 0, \qquad \overline{n}^2 = 0, \qquad n \cdot \overline{n} = 2, \tag{A.1}$$

and two orthogonal, spacelike vectors $n_\perp^i$, the ordered set $(n, \overline{n}, n_\perp^i)$ forms a basis of Minkowsky space. A generic vector v decomposes as

$$v^\mu = \frac{v \cdot \overline{n}}{2} n^\mu + \frac{v \cdot n}{2} \overline{n}^\mu + v_\perp^\mu, \tag{A.2}$$

where $v_\perp^\mu = v \cdot n_\perp^1 \, n_\perp^{1,\mu} + v \cdot n_\perp^2 \, n_\perp^{2,\mu}$. In components, one represents

$$v = (v_+, v_-, \vec{v}_\perp) \tag{A.3}$$

where $v_+ = v \cdot n$ and $v_- = v \cdot \overline{n}$. The Lorentz metric in lightcone coordinates is

$$g^{\mu\nu} = \frac{n^\mu \overline{n}^\nu + n^\nu \overline{n}^\mu}{2} + g_\perp^{\mu\nu}, \tag{A.4}$$

so a dot product yields

$$v \cdot w = \frac{1}{2} v^+ w^- + \frac{1}{2} v^- v^+ - \vec{v}_\perp \cdot \vec{w}_\perp. \tag{A.5}$$

A convenient choice is

$$n = (1, 0, 0, 1), \quad \overline{n} = (1, 0, 0, -1). \tag{A.6}$$

For given n, the choice for $\overline{n}$ is clearly not the unique solution of eq. (A.1), and in fact reparametrization invariance in SCET deals exactly with this freedom.

In the case of a collinear scaling, I use the convention that the minus lightcone component is the large component, so a collinear momentum will scale

$$p = (p_+, p_-, \vec{p}_\perp) \sim Q(\lambda^2, 1, \lambda) \,. \tag{A.7}$$

This convention (although common in SCET literature) is by far not universal, and so is the choice of normalization in the third expressions of eq. (A.1), thus care is required when comparing different sources.

A.2 Plus distributions

Dimensional regularization is a brilliant way to fix UV and IR divergences without destroying the symmetries of gauge theories, but it still complicates intermediate stages of the calculations. Most often, the full ε dependence of observables is superfluous, and it is sufficient to retain only finite terms in the power expansion. For practical purpose, it is usually convenient to perform this expansion at the level of *integrands*: this is where *plus distributions* arise.

For illustration purpose, consider the integral

$$\int_0^{x_0} \frac{\mathrm{d}x}{x^{1+\varepsilon}} = -\frac{x_0^{-\varepsilon}}{\varepsilon} = -\frac{1}{\varepsilon} \sum_{k=0}^{\infty} \frac{(-\varepsilon \ln x_0)^k}{k!} \,. \tag{A.8}$$

Clearly, we cannot reproduce the power expansion on the right-hand side by naively expand $x^{-1-\varepsilon}$ under integral around $\varepsilon = 0$, as the first term in the expansion, $\mathrm{d}x/x$, would diverge. If an expansion in terms of regular functions is doomed to fail, we can still expand in terms of *distributions*. Similar to the Dirac delta, one can define plus distributions, $\mathcal{L}(x)$, by specifying their action on a generic smooth function $f(x)$ with support $[0,1]$,

$$\mathcal{L}_n(x) \equiv \left[\frac{\ln^n x}{x}\right]_+ \; : \; \int_0^1 \mathrm{d}x \, f(x) \mathcal{L}_n(x) = \int_0^1 \mathrm{d}x \, \frac{\ln^n(x)}{x} \big[f(x) - f(0) \big] \,. \tag{A.9}$$

Practically, subtracting the value of the smooth function at $x = 0$ regularizes the singularity at the endpoint. This definition generalizes to an arbitrary integration range by requiring compatibility with basic integration rules,

$$\int_0^{x_0} \mathrm{d}x \, f(x) \mathcal{L}_n(x) = \int_0^{x_0} \mathrm{d}x \, \frac{\ln^n(x)}{x} \big[f(x) - f(0) \big] - f(0) \int_{x_0}^1 \mathrm{d}x \, \frac{\ln^n(x)}{x} \,, \tag{A.10}$$

and plus distributions reduce to the regular counterpart when integrated over intervals that do not contain the singular point $x = 0$. Given this definition, expanding under integral sign

$$\frac{1}{x^{1+\varepsilon}} = -\frac{1}{\varepsilon}\delta(x) + \sum_{k=0}^{\infty} (-\varepsilon)^k \mathcal{L}_k(x) \tag{A.11}$$

correctly reproduces the right-hand side of eq. (A.8). Of course this strategy is of little use when the integral is easily solved at all orders, but becomes valuable when integrating against a complicated smooth function $f(x)$, where an all-order analytic solution could be out of reach. Furthermore, differential distributions correspond to integrands by definition: in this case, an expansion in terms of plus distributions is the only way to get a result at finite order in ε. For this reason, plus distributions are essentially unavoidable when handling differential cross sections that receive contributions from the IR region.

When considering transverse momentum measurements, I derive plus distributions in the transverse momentum q_T from eq. (A.9),

$$\mathcal{L}_n(q_T, q_0) = \frac{1}{q_0^2} \, \mathcal{L}_n\!\left(\frac{q_T^2}{q_0^2}\right), \tag{A.12}$$

such that

$$\int_0^{p_T^2} \mathrm{d}q_T^2 \, f(q_T^2) \mathcal{L}_n(q_T, q_0) = \int_0^{p_T^2/q_0^2} \mathrm{d}x \, f(q_0^2 x) \mathcal{L}_n(x) \,. \tag{A.13}$$

Related "cut" distributions are defined as

$$\mathcal{L}_n^{\mathrm{cut}}(q_T, q_0) = \mathcal{L}_n(q_T, q_0) \theta(q_0 - q_T) \,. \tag{A.14}$$

A.3 Transforms

When measuring some some final-state physical quantities, the resulting differential cross sections often factorize as a convolution of functions, rather than a simple product. In this case, it is often convenient to perform a transform to a space where factorization (and evolution) are multiplicative. Usually, this largely simplifies the manipulations at intermediate steps, and the complexity is confined to taking a final antitransform.

When an energy fraction is measured, the factorization ingredients usually enter the cross section in a Mellin convolution

$$[f \otimes g](x) = \int_x^1 \frac{\mathrm{d}x'}{x'} f\!\left(\frac{x}{x'}\right) g(x') \,. \tag{A.15}$$

This is the case of integrated PDFs and FFs, as well as many of the ingredients that appear in ch. 3. It is immediate to show that the Mellin convolution is symmetric and associative. The Mellin transform is defined as

$$\overline{f}(N) = \int_0^1 \mathrm{d}x \, x^N \, f(x) \,, \tag{A.16}$$

and the $\overline{f}$ for integer N take the name of *Mellin moments*. Under Mellin transform,

$$\overline{f \otimes g}(N) = \overline{f}(N)\,\overline{g}(N)\,. \tag{A.17}$$

Transforming back to momentum space requires solving

$$f(x) = \frac{1}{2\pi i} \int_{c-i\infty}^{c+i\infty} \mathrm{d}N\, x^{-N-1} \overline{f}(N)\,, \tag{A.18}$$

where c determines a vertical path in the complex plane that does not cross singularities. Efficiently solving the transform is a nontrivial numerical problem, which requires a smart choice of path.

Additive vector quantities, like transverse momenta, usually enter factorization formulae though Laplace convolutions,

$$\frac{\mathrm{d}\sigma}{\mathrm{d}\boldsymbol{q}} = \int \mathrm{d}\boldsymbol{p}\, F(\boldsymbol{q})\, G(\boldsymbol{p}-\boldsymbol{q}). \tag{A.19}$$

This is the case for all TMD cross sections studied in sec. 2.2 and 4.1.2. Like Mellin convolutions, Laplace convolutions are symmetric and associative. I define the Fourier transform as

$$F(\boldsymbol{b}) = \int \mathrm{d}\boldsymbol{q}\, F(\boldsymbol{q})\, e^{+i\boldsymbol{b}\cdot\boldsymbol{q}}\,, \tag{A.20}$$

where $\boldsymbol{b}$ is the impact parameter, thus the inverse transform reads

$$F(\boldsymbol{q}) = \int \frac{\mathrm{d}\boldsymbol{b}}{(2\pi)^2} F(\boldsymbol{b})\, e^{-i\boldsymbol{b}\cdot\boldsymbol{q}}\,. \tag{A.21}$$

In presence of angular symmetry, the Fourier transform reduces to

$$F(b) = \pi \int_0^\infty \mathrm{d}q_T^2\, J_0(bq_T)\, F(q_T)\,, \tag{A.22}$$

where J_0 is the Bessel function. In particular, the Fourier transform of the plus distributions in eq. (A.12) yields

$$\int \mathrm{d}\boldsymbol{q}\, \mathcal{L}_n(q_T,\mu)\, e^{+i\boldsymbol{b}\cdot\boldsymbol{q}} = \frac{\pi}{n!} \ln^n \left(\frac{b^2\mu^2}{4e^{-2\gamma_E}} \right)\,. \tag{A.23}$$

Finally, in case of jet mass measurements, the cross section factorizes as a one-dimensional Laplace convolution. If $e = m_J^2/(4E^2)$ is the normalized jet mass, I define the Laplace transform as

$$\widetilde{F}(s) = \int_0^\infty \mathrm{d}e\, \exp(-s\,e) F(e)\,, \tag{A.24}$$

so that the corresponding inverse transform reads

$$F(e) = \frac{1}{2\pi i} \int_{\gamma-i\infty}^{\gamma+i\infty} \mathrm{d}e \, \exp(+s\,e)\widetilde{F}(s)\,. \tag{A.25}$$

Laplace transforms of the first plus distributions yield

$$\int_0^\infty \mathrm{d}e \, \exp(-s\,e)\,\mathcal{L}_0(e) = -\ln(s\,e^{\gamma_E})\,,$$

$$\int_0^\infty \mathrm{d}e \, \exp(-s\,e)\,\mathcal{L}_1(e) = \frac{1}{2}\ln^2(s\,e^{\gamma_E}) + \frac{\pi^2}{12}\,. \tag{A.26}$$

A.4 Electroweak parameters

This section gathers expressions for the constants that enter eq. (1.50), used to include the Z-boson contribution to the cross section for $e^+e^- \to$ hadrons.

Basic trigonometric functions of the electroweak mixing angle ϑ_W are

$$\sin\vartheta_W = 0.23119, \qquad \cos\vartheta_W = 0.87681\,. \tag{A.27}$$

The mass of the EW bosons is

$$M_Z = 91.1876 \text{ GeV}\,, \qquad M_W = M_Z\cos\vartheta_W = 80.379 \text{ GeV} \tag{A.28}$$

and the decay width of the Z

$$\Gamma_Z = 2.4952 \text{ GeV}\,. \tag{A.29}$$

Finally, the vector and axial couplings for the particle species κ are a function of the electric charge Q and isospin T^3,

$$v_\kappa = \frac{T_\kappa^3 + 2Q_\kappa\sin^2\vartheta_W}{2\sin\vartheta_W\cos\vartheta_W}\,, \qquad a_\kappa = -\frac{T_\kappa^3}{2\sin\vartheta_W\cos\vartheta_W}\,. \tag{A.30}$$

B

Perturbative Ingredients

This appendix collects the perturbative expressions presented in the main text, and the complementary factorization and evolution ingredients needed to obtain numerical results. To make the thesis self-contained, I include the definitions of the collinear/soft functions in terms of SCET operators.

B.1 Function definitions

This section collects expressions for the soft and collinear functions, defined as matrix elements of SCET operators. In the following $|X\rangle$ denotes an inclusive state, and is therefore implicitly summed over. I will focus on the operator definitions relevant to the two applications discussed in ch. 4 and ch. 5, that were relevant to computing the missing perturbative ingredients in [3, 4]. For the definitions relevant to the in-jet fragmentation process discussed in ch. 3, see [83].

The definitions of integrated quark PDFs and FFs in position space are respectively

$$f_{p \to i}(x) = \int \frac{\mathrm{d}\xi}{2\pi} e^{-ixp^+\xi_-} \, \mathrm{tr}\left\{ \langle p| \frac{\overline{n}}{2} \chi_{n,i}\left(\frac{\xi_-}{2}\right) |X\rangle \langle X| \overline{\chi}_{n,i}\left(-\frac{\xi_-}{2}\right) |p\rangle \right\}, \qquad \text{(B.1)}$$

$$d_{i \to h}(z) = \frac{1}{2N_c} \int \frac{\mathrm{d}\xi}{2\pi} e^{-izp^+\xi_-} \, \mathrm{tr}\left\{ \langle 0| \frac{\overline{n}}{2} \chi_{n,i}\left(\frac{\xi_-}{2}\right) |hX\rangle \langle hX| \overline{\chi}_{n,i}\left(-\frac{\xi_-}{2}\right) |0\rangle \right\}. \qquad \text{(B.2)}$$

Their transverse momentum dependent counterpart in impact parameter space yields

$$F_{p \to i}(x, \boldsymbol{b}) = \int \frac{\mathrm{d}\xi}{2\pi} e^{-ixp^+\xi_-} \, \mathrm{tr}\left\{ \langle p| \frac{\overline{n}}{2} \chi_{n,i}\left(\frac{\xi}{2}\right) |X\rangle \langle X| \overline{\chi}_{n,i}\left(-\frac{\xi}{2}\right) |p\rangle \right\}, \qquad \text{(B.3)}$$

$$D_{i \to h}(z, \boldsymbol{b}) = \frac{1}{2N_c} \int \frac{\mathrm{d}\xi}{2\pi} e^{-izp^+\xi_-} \, \mathrm{tr}\left\{ \langle 0| \frac{\overline{n}}{2} \chi_{n,i}\left(\frac{\xi}{2}\right) |hX\rangle \langle hX| \overline{\chi}_{n,i}\left(-\frac{\xi}{2}\right) |0\rangle \right\}. \qquad \text{(B.4)}$$

The difference between the definition of integrated and TMD distributions is that in the latter the fields are evaluated at the position $\pm\xi/2$, which involves a space separation $\boldsymbol{b}$ in the transverse direction.

The soft function for SIDIS is given (in position space) by the following vacuum matrix element of soft Wilson lines,

$$S_q(\boldsymbol{b}) = \frac{1}{N_c}\operatorname{tr}_c\langle 0|\overline{T}\big[\widetilde{Y}_{\bar{n}}^{\dagger}Y_n\big](0^+,0^-,\boldsymbol{b})T\big[Y_n^{\dagger}\widetilde{Y}_{\bar{n}}\big](0)|0\rangle, \qquad (B.5)$$

where the coordinates in brackets indicate the position of both Wilson lines, T ($\overline{T}$) denotes (anti-)time ordering, and the Wilson lines are defined as

$$Y_n(x) = P\exp\left[+ig_s\int_{-\infty}^{0}\mathrm{d}s\, n\cdot A(x+s\,n)\right], \qquad (B.6)$$

$$\widetilde{Y}_{\bar{n}}(x) = P\exp\left[-ig_s\int_{0}^{\infty}\mathrm{d}s\,\bar{n}\cdot A(x+s\,\bar{n})\right].$$

As amply discussed in the main text, the same soft function enters for processes involving jets (instead of hadrons) in the final state. In the case of TMD dijet/dihadron production, eq. (B.5) simply involves two outgoing Wilson lines rather than one incoming and one outgoing line.

The matrix element definition of the TMD recoil-free jet function was given in eq. (4.19) in the main text. Moving on to groomed jets, the definitions for the ingredients entering the refactorization eq. (5.10), describing the most hierarchical regime of interest, are given in the following: first, the jet function reads

$$J_q(e,Q) = \frac{(2\pi)^3}{N_c}\operatorname{tr}\left\{\langle\frac{\not{\bar{n}}}{2}\chi_n(0)\delta(2E-\bar{n}\cdot\mathcal{P})\delta^{(2)}(\boldsymbol{\mathcal{P}}_{\perp})\delta(e-\mathcal{E})\bar{\chi}_n\rangle\right\}, \qquad (B.7)$$

where the action of the operator $\mathcal{E}$ on a state returns its jet mass. Second, the collinear soft function is defined as

$$S_{\mathrm{cs}}(e,Qz_{\mathrm{cut}}) = \frac{1}{N_R}\operatorname{tr}\left\{\langle T(U_n^{\dagger}W_t)\mathcal{M}_e^{SD}\bar{T}(W_t^{\dagger}U_n)\rangle\right\}. \qquad (B.8)$$

Here W_t is a collinear-soft Wilson line, whose reference direction t differs in general from collinear analogous n, and U_n arises from the BPS field redefinitions. These are needed to decouple collinear from collinear-soft physics, in the same manner as discussed in sec. 1.3.4 for the standard ultrasoft-collinear decoupling. The invariant measurement function is

$$\mathcal{M}_e^{\mathrm{SD}} = \delta\big(e-(1-\Theta_{\mathrm{SD}})\,\mathcal{E}\big), \qquad (B.9)$$

which imposes only the radiation that passes soft drop to contribute to the measured groomed jet mass. Finally, the soft-collinear function is defined by the matrix element

$$S_{\text{sc}}^{\perp}(\boldsymbol{q}, Q z_{\text{cut}}) = \frac{1}{N_R} \text{tr} \Big\{ \langle T(U_n^{\dagger} W_t) \mathcal{M}_{\perp}^{\text{SD}} \bar{T}(W_t^{\dagger} U_n) \rangle \Big\}, \qquad \text{(B.10)}$$

and the groomed jet measurement function, $\mathcal{M}_{\perp}^{\text{SD}}$ is given in terms of the label momentum operator, $\mathcal{P}$,

$$\mathcal{M}_{\perp}^{SD} = \Theta_{\text{SD}} \times \delta^2(\boldsymbol{q} - \Theta_{\text{SD}} \boldsymbol{\mathcal{P}}_{\perp}). \qquad \text{(B.11)}$$

Soft-collinear emissions only contribute to the transverse momentum measurement if they fail soft-drop, as is enforced by the Θ_{SD} term.

B.2 Fixed-order ingredients

I expand the fixed-order ingredients in powers of $\alpha_s/(4\pi)$, defining

$$F = \sum_{k=0}^{\infty} \left(\frac{\alpha_s}{4\pi} \right)^k F^{[k]}. \qquad \text{(B.12)}$$

B.2.1 Ingredients for in-jet fragmentation

In the following, I collect the one-loop factorization ingredients needed to obtain the numerical result for in-jet fragmentation presented in ch. 3. All these ingredients were first calculated in [83] with proton-proton collisions in mind, and here I show the e^+e^- equivalent used in the analysis above.

The TMD matching coefficients that enter in eq. (3.6) are given by

$$C_{ij}^{[0]}(k_T, z, \mu) = \frac{1}{\pi} \delta_{ij} \, \delta(k_T^2) \, \delta(1-z), \qquad \text{(B.13)}$$

$$C_{qq}^{(1)}(k_T, z, \mu) = \frac{2C_F}{\pi} \theta\Big(\frac{1}{2} - z\Big) \Big\{ \mathcal{L}_0(k_T, \mu) \frac{1+z^2}{1-z}$$
$$+ \delta(k_T^2) \Big[\frac{2(1+z^2)}{1-z} \ln\big(z(1-z)\big) + 1 - z \Big] \Big\}, \qquad \text{(B.14)}$$

$$C_{qg}^{[1]}(k_T, z, \mu) = \frac{2C_F}{\pi} \theta\Big(\frac{1}{2} - z\Big) \Big\{ \mathcal{L}_0(k_T, \mu) \frac{1+(1-z)^2}{z}$$
$$+ \delta(k_T^2) \Big[\frac{2(1+(1-z)^2)}{z} \ln\big(z(1-z)\big) + z \Big] \Big\}, \qquad \text{(B.15)}$$

$$C_{gg}^{[1]}(k_T, z, \mu) = \frac{C_A}{\pi} \theta\Big(\frac{1}{2} - z\Big) \Big\{ \mathcal{L}_0(k_T, \mu) \frac{2(1-z+z^2)^2}{z(1-z)}$$

$$+ \delta(k_T^2) \frac{4(1-z+z^2)^2}{z(1-z)} \ln\big(z(1-z)\big) \bigg\}, \tag{B.16}$$

$$C_{gq}^{[1]}(k_T, z, \mu) = \frac{2T_F}{\pi} \theta\Big(\frac{1}{2} - z\Big) \bigg\{ \mathcal{L}_0(k_T, \mu)\big(z^2 + (1-z)^2\big)$$

$$+ \delta(k_T^2)\Big[2\big(z^2 + (1-z)^2\big) \ln\big(z(1-z)\big) + 2z(1-z)\Big] \bigg\}, \tag{B.17}$$

Here E is the jet energy and $\mathcal{R} = 2\tan(R/2)$. The boundary coefficients that enter the same equation are

$$B_{ij}^{[0]}(x, E\mathcal{R}, y, \mu) = \delta_{ij}\, \delta(1-x)\delta(1-y)\,, \tag{B.18}$$

$$B_{qq}^{[1]}(x, E\mathcal{R}, y, \mu)$$
$$= \frac{2C_F}{\pi}\bigg(-\delta(1-y)\bigg\{ 2(1+x^2)\Big[\mathcal{L}_0(1-x)\ln\Big(\frac{E\mathcal{R}}{\mu}\Big) + \mathcal{L}_1(1-x)\Big] + 1-x\bigg\}$$
$$+ \delta(1-x)\theta\Big(y-\frac{1}{2}\Big)\bigg\{ 2(1+y^2)\Big[\mathcal{L}_0(1-x)\ln\Big(\frac{E\mathcal{R}y}{\mu}\Big) + \mathcal{L}_1(1-y)\Big] + 1-y\bigg\}\bigg)\,,$$

$$B_{qg}^{[1]}(x, E\mathcal{R}, y, \mu)$$
$$= \frac{2C_F}{\pi}\bigg(-\delta(1-y)\bigg\{ 2\frac{1+(1-x)^2}{x}\ln\Big(\frac{E\mathcal{R}(1-x)}{\mu}\Big) + x\bigg\}$$
$$+ \delta(1-x)\bigg\{ \theta\Big(y-\frac{1}{2}\Big)\Big[2\frac{1+(1-y)^2}{y}\ln\Big(\frac{E\mathcal{R}y(1-y)}{\mu}\Big) + y\Big]\bigg\}\bigg)\,, \tag{B.19}$$

$$B_{gg}^{[1]}(x, E\mathcal{R}, y, \mu)$$
$$= \frac{2C_A}{\pi}\bigg(-\delta(1-y)\frac{4(1-x+x^2)^2}{x}\bigg\{ \mathcal{L}_0(1-x)\ln\frac{E\mathcal{R}}{\mu} + \mathcal{L}_1(1-x)\bigg\}$$
$$+ \delta(1-x)\theta\Big(y-\frac{1}{2}\Big)\frac{4(1-y+y^2)^2}{y}\Big[\mathcal{L}_0(1-y)\ln\frac{E\mathcal{R}y}{\mu} + \mathcal{L}_1(1-y)\Big]\bigg)\,, \tag{B.20}$$

$$B_{gq}^{[1]}(x, E\mathcal{R}, y, \mu)$$
$$= \frac{4T_F}{\pi}\bigg(-\delta(1-y)\bigg\{ (x^2+(1-x)^2)\ln\frac{E\mathcal{R}(1-x)}{\mu} + x(1-x)\bigg\}$$
$$+ \delta(1-x)\theta\Big(y-\frac{1}{2}\Big)\Big[(y^2+(1-y)^2)\ln\frac{E\mathcal{R}y(1-y)}{\mu} + y(1-y)\Big]\bigg)\,. \tag{B.21}$$

The matching coefficients in eq. (3.8), describing the regime $k_T \sim E_J R$,

$$J_{ij}^{[0]}(x, E\mathcal{R}, k_T, z, \mu) = \frac{1}{\pi}\delta_{ij}\,\delta(k_T^2)\delta(1-x)\delta(1-z)\,, \tag{B.22}$$

$$J_{qq}^{[1]}(x, E\mathcal{R}, k_T, z, \mu)$$

$$= \frac{2C_F}{\pi} \Bigg(\mathcal{L}_0(k_T, \mu)\delta(1-x)\,\theta\Big(\frac{1}{2} - z\Big)\theta(E\mathcal{R} - k_T)\,\frac{1+z^2}{1-z}$$

$$- \delta(k_T^2)\delta(1-z)\Big\{ 2(1+x^2)\Big[\mathcal{L}_0(1-x)\ln\Big(\frac{E\mathcal{R}}{\mu}\Big) + \mathcal{L}_1(1-x)\Big] + 1 - x\Big\}$$

$$+ \delta(k_T^2)\delta(1-x)\Big\{ \theta\Big(z - \frac{1}{2}\Big)\Big[2(1+z^2)\Big[\mathcal{L}_0(1-z)\ln\Big(\frac{E\mathcal{R}z}{\mu}\Big) + \mathcal{L}_1(1-z)\Big]$$

$$+ 1 - z\Big] + \theta\Big(\frac{1}{2} - z\Big)\Big[2\frac{1+z^2}{1-z}\ln\big(z(1-z)\big) + (1-z)\Big]\Big\}\Bigg) \qquad \text{(B.23)}$$

$$J_{qg}^{[1]}(x, E\mathcal{R}, k_T, z, \mu)$$

$$= \frac{2C_F}{\pi} \Bigg(\mathcal{L}_0(k_T, \mu)\delta(1-x)\,\theta\Big(\frac{1}{2} - z\Big)\theta(E\mathcal{R} - k_T)\,\frac{1+(1-z)^2}{z}$$

$$- \delta(k_T^2)\delta(1-z)\Big\{ 2\frac{1+(1-x)^2}{x}\ln\Big(\frac{E\mathcal{R}(1-x)}{\mu}\Big) + x\Big\}$$

$$+ \delta(k_T^2)\delta(1-x)\Big\{ \theta\Big(z - \frac{1}{2}\Big)\Big[2\frac{1+(1-z)^2}{z}\ln\Big(\frac{E\mathcal{R}z(1-z)}{\mu}\Big) + z\Big]$$

$$+ \theta\Big(\frac{1}{2} - z\Big)\Big[2\frac{1+(1-z)^2}{z}\ln\big(z(1-z)\big) + z\Big]\Big\}\Bigg), \qquad \text{(B.24)}$$

$$J_{gg}^{[1]}(x, E\mathcal{R}, k_T, z, \mu)$$

$$= \frac{2C_A}{\pi} \Bigg(\mathcal{L}_0(\mu, k_T)\delta(1-x)\,\theta\Big(\frac{1}{2} - z\Big)\theta(E\mathcal{R} - k_T)\,\frac{2(1-z+z^2)^2}{z(1-z)}$$

$$- \delta(k_T^2)\delta(1-z)\,\frac{4(1-x+x^2)^2}{x}\Big\{ \mathcal{L}_0(1-x)\ln\frac{E\mathcal{R}}{\mu} + \mathcal{L}_1(1-x)\Big\}$$

$$+ \delta(k_T)\delta(1-x)\Big\{ \theta\Big(z - \frac{1}{2}\Big)\frac{4(1-z+z^2)^2}{z}\Big[\mathcal{L}_0(1-z)\ln\frac{E\mathcal{R}z}{\mu}$$

$$+ \mathcal{L}_1(1-z)\Big] + \theta\Big(\frac{1}{2} - z\Big)\frac{4(1-z+z^2)^2}{z(1-z)}\ln\big(z(1-z)\big)\Big\}\Bigg), \qquad \text{(B.25)}$$

$$J_{gq}^{[1]}(x, E\mathcal{R}, k_T, z, \mu)$$

$$= \frac{2T_F}{\pi} \Bigg(\mathcal{L}_0(k_T, \mu)\delta(1-x)\,\theta\Big(\frac{1}{2} - z\Big)\theta(E\mathcal{R} - k_T)\,\big(z^2 + (1-z)^2\big)$$

$$- 2\delta(k_T^2)\delta(1-z)\Big\{ \big(x^2 + (1-x)^2\big)\ln\frac{E\mathcal{R}(1-x)}{\mu} + x(1-x)\Big\}$$

$$+ 2\delta(k_T^2)\delta(1-x)\Big\{ \theta\Big(z - \frac{1}{2}\Big)\Big[\big(z^2 + (1-z)^2\big)\ln\frac{E\mathcal{R}z(1-z)}{\mu} + z(1-z)\Big]$$

$$+ \theta\Big(\frac{1}{2} - z\Big)\Big[\big(z^2 + (1-z)^2\big)\ln\big(z(1-z)\big) + z(1-z)\Big]\bigg\}\bigg). \qquad \text{(B.26)}$$

When $E\mathcal{R} \gg k_T$, by dropping power corrections in the ratio $k_T/E\mathcal{R}$, one immediately checks the refactorization in terms of matching coefficients and boundary functions, as predicted by eq. (3.9).

B.2.2 Ingredients for TMD recoil-free jets

I use the following shortcut notation for logarithms,

$$L_\mu = \ln\Big(\frac{b^2\mu^2}{4e^{-2\gamma_E}}\Big), \quad L_R = \ln\Big(\frac{\mu^2}{E^2\mathcal{R}^2}\Big), \quad \mathbf{l}_X = \ln\Big(\frac{\mu^2}{X}\Big), \qquad \text{(B.27)}$$

where $X \in \{\zeta, s, Q^2\}$.

I computed the TMD quark jet functions that enter in dijet production and DIS+jet in sec. 4.1.3, with the final result presented in eq. (4.44). Their large-radius limit is given in eq. (4.49) in the main text. To check one-loop refactorization in the small-R limit, one needs the one-loop TMD matching coefficients to FFs,

$$\mathbb{C}^{[0]}_{i\to j}(z, \boldsymbol{b}, \mu) = \delta_{ij}\delta(1-z),$$

$$\mathbb{C}^{[1]}_{q\to q}(z, \boldsymbol{b}, \mu) = 2C_F\Big[(1+z^2)\mathcal{L}_0(1-z)\big(2\ln z - L_\mu\big) \qquad \text{(B.28)}$$

$$+ \delta(1-z)\Big(-\frac{1}{2}L_\mu^2 + L_\mu \mathbf{l}_\zeta - \frac{\pi^2}{12}\Big) + 1 - z\Big],$$

$$\mathbb{C}^{[1]}_{q\to g}(z, \boldsymbol{b}, \mu) = 2C_F\Big[\frac{1 + (1-z)^2}{z}\big(2\ln z - L_\mu\big) + z\Big], \qquad \text{(B.29)}$$

which I defined here with an extra z^2 factor with respect to common choices in the literature [103, 135, 136], consistent with the matching equation eq. (2.36). The second ingredient of refactorization is the semi-inclusive quark jet function computed at NLO in [188],

$$\mathcal{J}_q^{[0]}(z, 2zE\mathcal{R}, \mu) = \delta(1-z),$$

$$\mathcal{J}_q^{[1]}(z, 2zE\mathcal{R}, \mu) = \qquad\qquad\qquad\qquad\qquad\qquad\qquad\qquad \text{(B.30)}$$

$$2C_F\Big[\delta(1-z)\Big(\frac{13}{2} - \frac{2\pi^2}{3} + \frac{3}{2}L_R\Big) + (L_R - 2\ln z)\Big((1+z^2)\mathcal{L}_0(1-z)$$

$$+ \frac{1+(1-z)^2}{z}\Big) - 2\frac{1+(1-z)^2}{z}\ln(1-z) - 2(1+z^2)\mathcal{L}_1(1-z) - 1\Big]. \quad \text{(B.31)}$$

The hard function for electron-positron annihilation up to two loop is [240, 241]

$$H^{[0]}_{e^+e^-}(s, \mu) = 1,$$

$$H_{e^+e^-}^{[1]}(s, \mu) = 2C_F\left(-\mathbf{l}_s^2 - 3\mathbf{l}_s^2 - 8 + \frac{7\pi^2}{6}\right),$$

$$H_{e^+e^-}^{[2]}(s, \mu) = 2C_F\Bigg\{C_F\bigg[\mathbf{l}_s^4 + 6\mathbf{l}_s^3 + \left(25 - \frac{7\pi^2}{3}\right)\mathbf{l}_s^2 + \left(\frac{93}{2} - 5\pi^2 - 24\zeta_3\right)\mathbf{l}_s$$

$$+ \frac{511}{8} - \frac{83\pi^2}{6} - 30\zeta_3 + \frac{67\pi^4}{60}\bigg] + C_A\bigg[-\frac{11}{9}\mathbf{l}_s^3 + \left(-\frac{233}{18} + \frac{\pi^2}{3}\right)\mathbf{l}_s^2$$

$$+ \left(-\frac{2545}{54} + \frac{22\pi^2}{9} + 26\zeta_3\right)\mathbf{l}_s - \frac{51157}{648} + \frac{1061\pi^2}{108} + \frac{313}{9}\zeta_3 - \frac{4\pi^4}{45}\bigg]$$

$$+ n_f T_F\bigg[\frac{4}{9}\mathbf{l}_s^3 + \frac{38}{9}\mathbf{l}_s^2 + \left(\frac{418}{27} - \frac{8\pi^2}{9}\right)\mathbf{l}_s + \frac{4085}{162} - \frac{91\pi^2}{27} + \frac{4}{9}\zeta_3\bigg]\Bigg\},$$

$$\text{(B.32)}$$

while the DIS counterpart is related to e^+e^- at the level of the amplitude by $s \to -Q^2$, leading to

$$H_{\text{DIS}}(Q^2, \mu) = H_{e^+e^-}(Q^2, \mu) - \frac{\alpha_s\pi C_F}{2} + \frac{\alpha_s^2 C_F}{8}\bigg[C_F\left(2\mathbf{l}_{Q^2}^2 + 6\mathbf{l}_{Q^2} + 16 - \frac{4}{3}\pi^2\right)$$

$$+ C_A\left(-\frac{11}{3}\mathbf{l}_{Q^2} - \frac{233}{18} + \frac{\pi^2}{3}\right) + n_f T_F\left(\frac{4}{3}\mathbf{l}_{Q^2} + \frac{38}{9}\right)\bigg] \qquad \text{(B.33)}$$

up to $\mathcal{O}(\alpha_s^3)$ corrections.

B.2.3 Additional ingredients for TMD groomed jets

Besides eq. (B.27), the shortcut notation for the logarithms that enter the expressions for groomed jets is

$$L_J = \ln\left(\frac{\mu^2\tilde{s}}{Q^2}\right), \quad L_{\text{cs}} = \ln\left(\frac{\mu^2\tilde{s}}{Q^2 z_{\text{cut}}}\right), \qquad \text{(B.34)}$$

where s denotes here the Laplace variable conjugate to the normalized groomed jet mass, and $\tilde{s} = s\,e^{\gamma_E}$.

As remarked in ch. 5, requiring small groomed jet mass and large jet radius results in the same hard and soft functions as for hadrons (or recoil-free jets). The additional ingredients needed to describe the jet function in eq. (5.10) were either known from the literature or computed in [4]. Here I will limit myself to presenting the results; see that reference for a calculation of the soft-collinear and collinear-soft functions.

At LO, all the ingredients presented here are normalized to 1. The one-loop quark jet function was computed in [219]. In Laplace space,

$$\tilde{J}_q^{[1]}(s, Q; \mu) = 2C_F\left(L_J^2 + \frac{3}{2}L_J - \frac{\pi^2}{3} + \frac{7}{2}\right), \qquad \text{(B.35)}$$

while the collinear-soft function simply reads

$$S_{\mathrm{cs}\,q}^{[1]}(s, Qz_{\mathrm{cut}}, \mu) = -2C_F L_{\mathrm{cs}}^2 \,. \tag{B.36}$$

The soft-collinear function does not depend on the groomed jet mass, but does depend on the transverse momentum. In impact parameter space,

$$\tilde{S}_{\mathrm{sc},q}^{\perp\,[1]}(\boldsymbol{b}, Qz_{\mathrm{cut}}, \mu, \zeta) = 2C_F\Big(L_\mu \mathbf{l}_\zeta - \frac{1}{2}L_\mu^2 - \frac{\pi^2}{12}\Big) \,. \tag{B.37}$$

Note that when defining TMDs according to the ζ prescription of [146, 147] there is no explicit dependence on the scale Qz_{cut}, although this is the natural final scale for the rapidity evolution.

B.3 Anomalous dimensions

In this section I collect the results for the ingredients necessary to Renormalization Group Evolution. I will focus on the applications of recoil-free jets presented in ch. 3 and 4, while the complementary evolution ingredients for groomed jets can be found in [4, 219].

B.3.1 (Modified) splitting kernels

The QCD splitting kernels expand as

$$P_{ij}(z, \mu) = \sum_{k=1}^{\infty} \Big(\frac{\alpha_s}{\pi}\Big)^k P_{ij}^{(k-1)}(z) \,. \tag{B.38}$$

The lowest-order results are

$$\begin{aligned}
P_{qq}^{(0)}(z) &= C_F\Big[\frac{1+z^2}{(1-z)_+} + \frac{3}{2}\delta(1-z)\Big], \\
P_{qg}^{(0)}(z) &= C_F\frac{1+(1-z)^2}{z}, \\
P_{gq}^{(0)}(z) &= n_f T_F\big[z^2 + (1-z)^2\big], \\
P_{gg}^{(0)}(z) &= 2C_A\Big[\frac{z}{(1-z)_+} + \frac{1-z}{z} + z(1-z)\Big] + \frac{\beta_0}{2}\delta(1-z) \,.
\end{aligned} \tag{B.39}$$

DGLAP evolution is conveniently performed in Mellin space. To this aim, the Mellin moments of the splitting functions are

$$\overline{P}_{qq}^{(0)}(N) = C_F\Big[-2H(N) - \frac{1}{N+1} - \frac{1}{N+2} + \frac{3}{2}\Big],$$

$$\overline{P}_{qg}^{(0)}(N) = C_F\Big[\frac{2}{N} - \frac{2}{N+1} + \frac{1}{N+2}\Big]\,,$$

$$\overline{P}_{gg}^{(0)}(N) = C_A\Big[-2H(N+1) + \frac{2}{N} - \frac{4}{N+1} + \frac{2}{N+2} - \frac{2}{N+3}\Big] + \frac{\beta_0}{2}\,,$$

$$\overline{P}_{gq}^{(0)}(N) = n_f T_F\Big[\frac{1}{N+1} - \frac{2}{N+2} + \frac{2}{N+3}\Big]\,. \tag{B.40}$$

The TMD functions $\mathcal{D}_{ij}$ introduced in eq. (3.6) obey modified evolution, as discussed in sec. 3.1.3,

$$P'_{ij}(z,\mu) = P_{ij}(z,\mu)\,\theta\big(z - \tfrac{1}{2}\big)\,. \tag{B.41}$$

In Mellin space, the one-loop modified splitting kernels as derived in [83] are

$$\overline{P}_{qq}^{\prime(0)}(N) = \overline{P}_{qq}^{(0)}(N) - C_F\big[-H_{1/2}(N) - H_{1/2}(N+2) + 2\ln 2\big]\,,$$

$$\overline{P}_{qg}^{\prime(0)}(N) = \overline{P}_{qg}^{(0)}(N) - C_F\,2^{-N-2}\,\frac{5N^2 + 17N + 16}{N(N+1)(N+2)}\,,$$

$$\overline{P}_{gg}^{\prime(0)}(N) = \overline{P}_{gg}^{(0)}(N) - C_A\Big[-2H_{1/2}(N+1) + 2\ln 2$$

$$+ 2^{-N-2}\,\frac{5N^3 + 33N^2 + 68N + 48}{N(N+1)(N+2)(N+3)}\Big]\,,$$

$$\overline{P}_{gq}^{\prime(0)}(N) = \overline{P}_{gq}^{(0)}(N) - n_f T_F\,2^{-N-2}\,\frac{N^2 + 5N + 8}{(N+1)(N+2)(N+3)}\,, \tag{B.42}$$

where the harmonic numbers are defined for integer N as

$$H(N) = \sum_{i=1}^{N}\frac{1}{i}\,, \qquad H_{1/2}(N) = \sum_{i=1}^{N}\frac{1}{i\,2^i}\,, \tag{B.43}$$

and elsewhere by analytic continuation.

B.3.2 TMD anomalous dimensions

In the following I collect the cusp, non-cusp, and rapidity anomalous dimensions defined in eq. (2.40) and eq. (2.41), up to the order needed to reach $\mathrm{N^3LL}$ accuracy. Refs. [108, 149–153] provided the cusp part,

$$\Gamma_q^{[0]} = 4C_F\,,$$

$$\Gamma_q^{[1]} = C_F\Big[C_A\Big(\frac{268}{9} - \frac{4\pi^2}{3}\Big) - \frac{80}{9}n_f T_F\Big]\,,$$

$$\Gamma_q^{[2]} = C_F\Big[C_A^2\Big(\frac{490}{3} - \frac{536\pi^2}{27} + \frac{88}{3}\zeta_3 + \frac{44\pi^4}{45}\Big) + C_F n_F T_F\Big(-\frac{220}{3} + 64\zeta_3\Big)$$

$$+ C_A n_f T_F \Big(-\frac{1672}{27} + \frac{160\pi^2}{27} - \frac{224}{3}\zeta_3 \Big) - \frac{64}{27}(n_f T_F)^2 \Big],$$

$$\Gamma_q^{[3]} = 20702 - 5171.9\, n_f + 195.5772\, n_f^2 + 3.272344\, n_f^3 \,. \tag{B.44}$$

and the non-cusp,

$$\gamma_q^{V\,[0]} = -6C_F \,,$$

$$\gamma_q^{V\,[1]} = C_F \Big[C_F \Big(-3 + 4\pi^2 - 48\zeta_3 \Big) + C_A \Big(-\frac{961}{27} - \frac{11\pi^2}{3} + 52\zeta_3 \Big)$$

$$+ n_f T_F \Big(\frac{260}{27} + \frac{4\pi^2}{3} \Big) \Big] \,,$$

$$\gamma_q^{V\,[2]} = C_F \Big[C_F^2 \Big(-29 - 6\pi^2 - 136\zeta_3 - \frac{16\pi^4}{5} + \frac{32\pi^2}{3}\zeta_3 + 480\zeta_5 \Big)$$

$$+ C_F C_A \Big(-\frac{151}{2} + \frac{410\pi^2}{9} - \frac{1688}{3}\zeta_3 + \frac{494\pi^4}{135} - \frac{16\pi^2}{3}\zeta_3 - 240\zeta_5 \Big)$$

$$+ C_A^2 \Big(-\frac{139345}{1458} - \frac{7163\pi^2}{243} + \frac{7052}{9}\zeta_3 - \frac{83\pi^4}{45} - \frac{88\pi^2}{9}\zeta_3 - 272\zeta_5 \Big)$$

$$+ C_F n_f T_F \Big(\frac{5906}{27} - \frac{52\pi^2}{9} + \frac{1024}{9}\zeta_3 - \frac{56\pi^4}{27} \Big) + (n_f T_F)^2 \Big(\frac{19336}{729} - \frac{80\pi^2}{27}$$

$$- \frac{64}{27}\zeta_3 \Big) + C_A n_f T_F \Big(-\frac{34636}{729} + \frac{5188\pi^2}{243} - \frac{3856}{27}\zeta_3 + \frac{44\pi^4}{45} \Big) \Big] \,, \tag{B.45}$$

as well as the rapidity anomalous dimension,

$$\mathcal{D}_q^{[1]} = \frac{\Gamma_q^{[0]}}{2} L_\mu \,,$$

$$\mathcal{D}_q^{[2]} = \frac{\Gamma_q^{[0]} \beta_0}{4} L_\mu^2 + \frac{\Gamma_q^{[1]}}{2} L_\mu + \mathcal{D}_q^{[2]}(0) \,,$$

$$\mathcal{D}_q^{[3]} = \frac{\Gamma_q^{[0]} \beta_0^2}{6} L_\mu^3 + \Big(\frac{1}{2}\Gamma_q^{[1]}\beta_0 + \frac{1}{4}\Gamma_q^{[0]}\beta_1 \Big) L_\mu^2 + \Big(2\beta_0 \mathcal{D}_q^{[1]}(0) + \frac{1}{2}\Gamma_q^{[2]} \Big) L_\mu + \mathcal{D}_q^{[3]}(0) \,. \tag{B.46}$$

The first two coefficients of the QCD beta function, that enter here, are given by

$$\beta_0 = \frac{11}{3} C_A - \frac{4}{3} n_f T_F \,,$$

$$\beta_1 = \frac{34}{3} C_A^2 - \frac{20}{3} C_A n_f T_F - 4 C_F n_f T_F \,, \tag{B.47}$$

and the constants read

$$\mathcal{D}_q^{[2]}(0) = C_F C_A \Big(\frac{404}{27} - 14\zeta_3 \Big) - \frac{112}{27} C_F n_f T_F \,,$$

$$\mathcal{D}_q^{[3]}(0) = C_F \left[C_A^2 \left(\frac{297029}{1458} - \frac{1598\pi^2}{243} - \frac{6164}{27}\zeta_3 - \frac{77\pi^4}{270} + \frac{44\pi^2}{9}\zeta_3 + 96\zeta_5 \right) \right.$$

$$+ C_A n_f T_F \left(- \frac{62626}{729} + \frac{412\pi^2}{243} + \frac{904}{27}\zeta_3 - \frac{2\pi^4}{27} \right)$$

$$\left. + (n_f T_F)^2 \left(\frac{3712}{729} + \frac{64}{9}\zeta_3 \right) + C_F n_f T_F \left(- \frac{1711}{27} + \frac{304}{9}\zeta_3 + \frac{8\pi^4}{45} \right) \right].$$

$$(B.48)$$

Finally, the zeta-prescription within the "optimal TMD" method [147, 148] is determined up to two loop by the implicit equation

$$\ln \frac{\mu^2}{\zeta_\mu} = \frac{1}{2}L_\mu - \frac{3}{2} + \frac{\alpha_s}{4\pi} \left[\frac{\beta_0}{9}L_\mu^2 + C_F \left(- \frac{3}{4} + \pi^2 - 12\zeta_3 \right) \right.$$

$$\left. + C_A \left(\frac{649}{108} - \frac{17\pi^2}{12} + \frac{19}{2}\zeta_3 \right) + n_f T_F \left(- \frac{53}{27} + \frac{\pi^2}{3} \right) \right].$$

$$(B.49)$$

Setting $\zeta(\mu) = \zeta_\mu$ cancels the logarithmic dependence of TMDs at the initial scale.

Transverse Momentum Distributions with Recoil-Free Jets – Summary

As is customary, the present summary aims at making the content of this thesis accessible to a broader audience. Therefore, I will present my results from a more general viewpoint than necessary.

Fundamental physics

Fundamental physics investigates some of the most astounding features of the Universe, and addresses some of the questions about Nature that have triggered human imagination for millennia. What is the origin of the Universe? How did celestial objects form? What is the essence of space and time? What is matter made of? And more generally, is it possible to reduce the vast spectrum of observed phenomena to a few, fundamental laws?

Although science does not deliver ultimate answers, it undeniably achieved tremendous progress in understanding Nature. To present knowledge, the Universe was born as an unimaginably hot and dense aggregate of matter and radiation. The progressive cooling and expansion of this original core produced all the astronomical structures that exist today. As a result, almost all the matter we observe, from atoms to galaxies, is made of just three ingredients: electrons, protons and neutrons. As far as we know, the electron is an irreducible point-like entity – a *fundamental* particle – while protons and neutrons have a rich internal structure in terms of *quarks* and *gluons*.

Although driven by empirical observation, this advancement was made possible by the parallel development of theoretical models. The existence of the Big Bang or an expanding universe is simply absurd according to the classical laws of gravity. However, these ideas were theorized soon after the formulation of General Relativity, that ties gravitation to the fabric of space and time. Similarly, the modern description of atoms in terms of electrons orbiting a nucleus explicitly violates the classical theory of electromagnetism, but suddenly acquires meaning if the latter is combined with the somewhat bizarre principles of quantum mechanics.

Despite our progress in understanding the Universe, and spectacular experimental verifications of striking theoretical predictions (the discovery of the

Higgs boson and the detection of gravitational waves, just to mention two recent results) there are of course aspects of Nature that we do not comprehend. For instance, the rate at which the Universe accelerates, or the speed at which galaxies rotate, are not compatible with the amount of matter we observe in the sky. This makes us postulate the existence of *dark matter*, whose origin we do not yet understand, and which has escaped so far any attempt of direct detection.

Particle physics

The topics explored in this thesis belong to the broad realm of particle physics. The status of the field is encompassed in the Standard Model (SM), a comprehensive theory of the fundamental particles and their mutual interactions. The SM is a triumph of fundamental physics, as it describes every physical phenomenon whose origin we know (with the important exception of gravity). Besides the electron, ordinary matter includes two kind of quarks (named *up* and *down*) and a neutrino. These four particles form a *generation*; they are accompanied by two other generations, which are essentially more exotic and heavier copies of the first one. What classical physics portrayed as *forces*, is explained in the SM as an exchange of other particles: for instance, the electrostatic repulsion between two electrons is in fact due to the exchange of *photons*. The SM introduces two additional interactions: *weak*, mediated by the Z and W bosons, and *strong*, mediated by gluons; the two adjectives refer to their strength in nuclear phenomena, relative to electromagnetism. How particles interact follows precise laws: for example, neutrinos communicate with electrons only through the exchange of weak bosons; besides gluons themselves, only quarks sense the strong interaction. These seemingly arbitrary rules follow in reality a precise pattern of symmetries, which make the SM much more than a catalog of particles. A spectacular example is the unification of the electromagnetic and weak interactions, that are in fact two manifestations of one symmetry of nature.

Despite a long history of theoretical and experimental successes, the Standard Model has also a number of open problems. For instance, it does not explain why the Universe is full of matter but contains essentially no antimatter, or what the nature of *dark* matter is. This motivates the search for physics beyond the Standard Model. A preferential tool to extend the frontiers of fundamental physics are particle accelerators: by means of intense electromagnetic fields, beams of particles are brought to exceptionally high energies and are made to collide; sophisticated detectors examine the products to infer the nature of the collisions. Einstein's equation $E = mc^2$ allows for converting energy into mass, and larger energies make it possible to create heavier parti-

cles: the search for new particles might not have succeeded yet simply because we have not reached a sufficiently high energy to produce them. This logic lead the scientific community to invest in increasingly big and powerful particle accelerators, such as the Large Hadron Collider (LHC) at CERN, that are in themselves impressive technical achievements. The last three chapters of this thesis show predictions for physical processes that occur in particle accelerators. To simplify, we calculate what fraction of collision events show specific features, such as the presence of a certain particle within a selected energy range. By comparing predictions to experiment – how many of these events were actually counted by particle detectors – we hope to find a discrepancy that would falsify the current theory and leave room to new hypotheses.
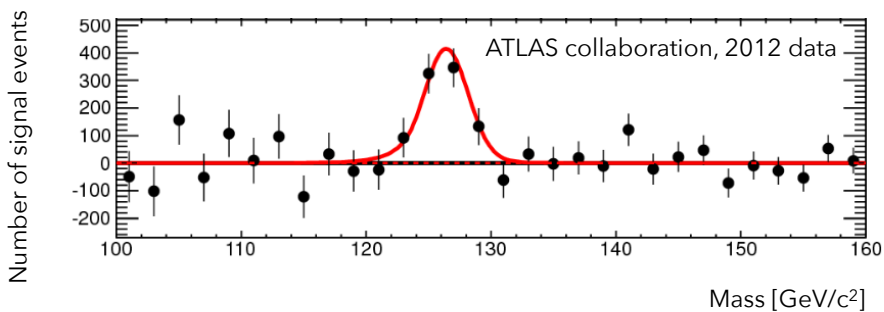

Figure 1 Simplified graph based on the data from the ATLAS collaboration that lead to the discovery of the Higgs boson in 2012. After subtracting the background, the measured number of events (black data points) is compatible with the theoretical prediction including a new particle (red). If claiming the existence of a fundamental particle on this basis seems too bold, consider that the probability that the bump is due to a random statistical fluctuation is less than one in three million.

Quantum Chromodynamics

The branch of the Standard Model investigated by this thesis is *Quantum Chromodynamics* (QCD), the theory of the strong interaction between quarks and gluons. The somewhat pompous name is inherited from *Quantum Electrodynamics*, the current theory of electromagnetism. The prefix Chromo- refers to the existence of three kinds of charge, whimsically named *colors*. Specifically, one has *red*, *blue* and *green* quarks, although the distinction has no practical relevance, since Nature only allows for "color-neutral" combinations. *Color confinement* is in fact the most striking feature of QCD: we cannot single out and observe quarks and gluons, but only study them indirectly, inside

aggregates named *hadrons*, of which protons and neutrons are examples.

Because of the nature of QCD, hadrons are very complicated objects. A proton can be roughly depicted as a bound system of two up quarks and a down quark. However, this description is largely incomplete, since these three quarks continuously exchange a multitude of gluons, and short-lived quark-antiquark pairs unceasingly create and annihilate inside the hadron. Clarifying this complex interplay is an interesting problem by its own. However, there is a second fundamental reason to deepen our knowledge of the proton structure: the LHC collides protons, and understanding their composition is mandatory in order to describe what comes out of the collisions.

Figure 2 Left: an impression of the internal structure of the proton, resulting from the incessant interaction of a large number of quarks, antiquarks, and gluons. Right: the main focus of this thesis is the transverse momentum of the hadron constituents, which describes their dynamics in the plane perpendicular to the direction of motion.

The main theoretical result that the thesis builds upon is factorization. In general, we can imagine a high-energy collision in QCD to occur in different steps: first, a small number of energetic quarks and gluons is produced in a hard scattering; next, these particles propagate in different directions, emitting a large amount of *colored* radiation; finally, because of color confinement, this radiation converts into the hadrons that we observe in the detectors. The emitted radiation is preferentially *collinear*, namely propagating in the direction of the initial particle, or *soft*, meaning it carries low energy. Factorization theorems give this picture a rigorous meaning, such that to determine the rate of collision events we can take the product of hard, soft, and collinear functions which describe the various type of particles in the event. This separation is essential, because the hard function can be calculated for each collision, while soft and collinear functions can be reused for many different processes.

Transverse momentum distributions with recoil-free jets

This thesis proposes new ways to probe the internal structure of hadrons. Historically, the main focus has been on the *longitudinal momentum*, namely on the dynamics of quarks and gluons in the direction of motion of the hadron. Describing the *transverse momentum* (fig. 2) is a relevant generalization: it collects more information about the hadron, moving towards a three-dimensional representation.

Because of color confinement, we cannot directly measure the transverse momentum of quarks and gluons inside the hadron: what we do instead is inferring it from the transverse momentum of some of the collision products. The main proposal of this doctoral work is using to this goal the transverse momentum of *jets*. Jets are collimated sprays of particles that populate the final state of collision events, and arise from the several collinear splittings undergone by energetic quarks and gluons. By collectively describing such a spray as one entity, we attempt at reconstructing the energetic particle that originated it, and extract precious information about the first moments after the collision. Practically, this collective description is achieved by sequentially recombining particles that lie close to each other. Since there is no unique way to do so, there are many possible definitions of jets: in particular, one needs to specify a direction for the final object, the *jet axis*.
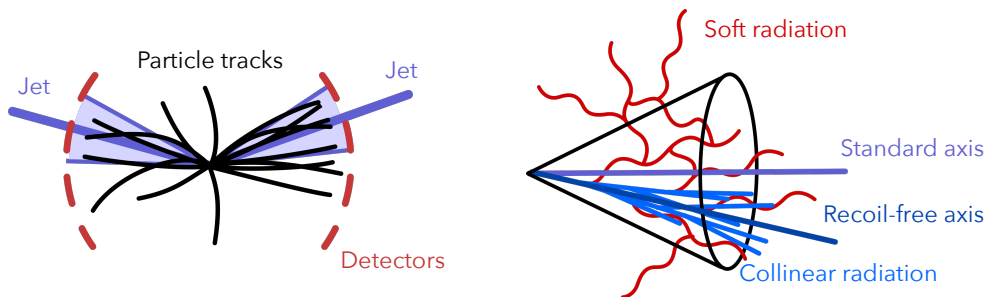

Figure 3 Left: sketch of the final state of a collision event, where sprays of collimated hadrons are described as jets. Right: the direction (axis) of standard jets is affected by soft radiation, which is a source of contamination from the rest of the event. Recoil-free jets track instead the energetic core of collinear radiation.

Traditional jet definitions are sensitive to *recoil*, a shift of the axis induced by soft radiation. The problem with recoil is that soft radiation communicates between different parts of the event: a jet may end up capturing soft emissions originated from other jets or from the proton beams, which expose it to every sort of contamination. Recoil occurs principally in the transverse direction, so

this effect is particularly relevant for the transverse momentum studied here. An interesting solution is using *recoil-free* jets, whose axis is by definition insensitive to soft radiation. An alternative is *jet grooming*, a technique to identify and remove soft radiation from within the jet. While the latter is an already well-established method, the thesis focuses on investigating the potential of recoil-free jets.

Results

To this end, the present work extensively discusses two applications of recoil-free jets to collider processes, and an application of groomed jets for comparison. The first one is the study of hadrons produced inside jets: in this case, one can extract the transverse momentum from the angle between the hadron and the jet. The angular distribution shows a characteristic power-law shape, a peculiar feature that could be tested at the LHC. For this purpose, it is promising that the numerical predictions are robust when accounting for some common experimental issues, such as the limited resolution of particle detectors. The absence of recoil plays a fundamental role, because soft radiation would otherwise smear out the salient features of the distribution.

The second application aims at the future Electron-Ion Collider. By smashing protons with beams of electrons, this facility will provide an excellent way to probe the internal structure of the hadron. Traditionally, in this process, the transverse momentum of the proton constituents has been inferred from that of a single final-state particle. This thesis proposes measuring instead the transverse momentum of a whole jet. The idea is appealing because jets are under better theoretical control than single particles, enabling a more precise study of the proton structure. However, our favorite theoretical tool, factorization, does not work well for standard jets, or requires assumptions that are hardly met in real experiments. Recoil-free jets provide a crucial advantage in that they have a neat factorization picture without calling for further assumptions. The resulting predictions reach a level of theoretical accuracy which is not often achieved in jet analyses.

Finally, the same process – electron-proton collisions with a measured jet – is also studied using *groomed* jets. The goal is again inferring the transverse momentum of the proton constituents from the transverse momentum of a jet. Grooming is a drastic procedure, because it does not simply ignore soft radiation: it eliminates most of it. As a consequence, the impact of contamination is largely reduced, which constitutes a clear advantage. However, the method introduces additional parameters (how aggressively we want to remove soft particles) that complicate the theoretical description; this limits the current precision.

The transverse momentum distributions predicted for these processes are in themselves interesting results in view of comparison with experimental data. In addition, the work presented in this thesis gives a substantial contribution to establishing recoil-free jets as a valuable alternative to standard and groomed jets. Their main advantage is a drastic simplification of the theoretical framework, because they clearly separate soft and collinear physics, often entangled with traditional jets. This theoretical simplification grants in turn improved precision to our predictions.

Acknowledgements

I would like to thank my supervisor, Wouter Waalewijn, for his steady guidance through my PhD. Wouter, most of what I learnt in the past four years about physics, good research practice, and academia, I owe to you. Your help and advice have been crucial to complete my doctorate, and I am grateful for the several opportunities of professional and personal growth you offered me, such as research visits and international collaborations. Working under the constant impression that you valued my future career was of great help to me. Not least, thanks for being so open to suggestions and understanding when problems arose, which are perhaps uncommon qualities in a supervisor. Finally, thanks for the critical and extensive feedback to the present thesis.

I would like to thank the doctoral committee members for the patience and time spent reading this thesis (I admit I could have kept it shorter!). In particular, I wish to thank my formal supervisor Eric Laenen for his feedback.

Nikhef has been an amazing working facility. I will remember the theory group as an active and stimulating place where to do physics, as well as a friendly environment where I immediately felt home. This would not have been possible without the continuous efforts of the group leaders, Eric Laenen and Robert Fleischer. And I would like to personally thank my present and past colleagues: my long-term office mates Darren, Emanuele, Michael and Nathan; my fellow PhD students Gillian, Sabrina, Jacopo, Jorinde, Jort, Eleftheria, Tom, Melissa, Ruben, Avanish and Rubén; the windmill *aficionados* Gilberto, Andreas and Michi (and here I must mention Darren again); and the other postdocs and staff members that to various extents I had the opportunity to interact with: Franz, Giulio, Rudi, Elena, Marieke, Bert, Piet, Jo, Eleni, Lisa, Tomas, Jake, Rhorry, Leonardo, Marco, Valerio, Jordy, Juan, Jos, Jan-Willem.

Even in such an ideal working environment, a doctorate remains a difficult challenge. I am particularly grateful to Pedro (thanks for sharing so many experiences!), Beatrix, Serafina, Sonia, Rabah, Solange, Marrit, and Olmo for their friendship and support during hard times. In different ways, you have all been fundamental to me.

Further thanks go to Antonio (four years under the same roof is a very long time!) and Roberta, it has been a pleasure to share a flat with you. Thanks to my brother Alessandro for help with the layout of this thesis, and for being

always eager to share silly jokes. And collective thanks to all my old friends in Torino, Val Sangone, or now spread across the rest of the world: it is always nice to come back together.

Finally, I would like to thank my family, and my parents in particular, for the unconditional support that they unceasingly show me, without which none of my achievements would have been possible. It is not easy to accept that your sons live far away, especially during uncertain times as the ones we live in, but your determination is to me an invaluable source of motivation.

Bibliography

[1] D. Gutierrez-Reyes, I. Scimemi, W. J. Waalewijn and L. Zoppi, *Transverse momentum dependent distributions with jets*, *Phys. Rev. Lett.* **121** (2018) 162001 [`1807.07573`].

[2] D. Neill, A. Papaefstathiou, W. J. Waalewijn and L. Zoppi, *Phenomenology with a recoil-free jet axis: TMD fragmentation and the jet shape*, *JHEP* **01** (2019) 067 [`1810.12915`].

[3] D. Gutierrez-Reyes, I. Scimemi, W. J. Waalewijn and L. Zoppi, *Transverse momentum dependent distributions in e^+e^- and semi-inclusive deep-inelastic scattering using jets*, *JHEP* **10** (2019) 031 [`1904.04259`].

[4] D. Gutierrez-Reyes, Y. Makris, V. Vaidya, I. Scimemi and L. Zoppi, *Probing Transverse-Momentum Distributions With Groomed Jets*, *JHEP* **08** (2019) 161 [`1907.05896`].

[5] D. J. Gross and F. Wilczek, *Ultraviolet Behavior of Nonabelian Gauge Theories*, *Phys. Rev. Lett.* **30** (1973) 1343.

[6] H. D. Politzer, *Reliable Perturbative Results for Strong Interactions?*, *Phys. Rev. Lett.* **30** (1973) 1346.

[7] PARTICLE DATA GROUP collaboration, M. Tanabashi et al., *Review of Particle Physics*, *Phys. Rev.* **D98** (2018) 030001.

[8] T. van Ritbergen, J. A. M. Vermaseren and S. A. Larin, *The Four loop beta function in quantum chromodynamics*, *Phys. Lett.* **B400** (1997) 379 [`hep-ph/9701390`].

[9] P. A. Baikov, K. G. Chetyrkin and J. H. Kühn, *Five-Loop Running of the QCD coupling constant*, *Phys. Rev. Lett.* **118** (2017) 082002 [`1606.08659`].

[10] A. Deur, S. J. Brodsky and G. F. de Teramond, *The QCD Running Coupling*, *Prog. Part. Nucl. Phys.* **90** (2016) 1 [`1604.08082`].

[11] S. Catani, G. Turnock, B. Webber and L. Trentadue, *Thrust distribution in e+ e- annihilation*, *Phys. Lett. B* **263** (1991) 491.

[12] S. Catani, L. Trentadue, G. Turnock and B. Webber, *Resummation of large logarithms in e+ e- event shape distributions*, *Nucl. Phys. B* **407** (1993) 3.

[13] A. V. Manohar and M. B. Wise, *Power suppressed corrections to hadronic event shapes*, *Phys. Lett. B* **344** (1995) 407 [`hep-ph/9406392`].

[14] G. P. Korchemsky and G. F. Sterman, *Nonperturbative corrections in resummed cross-sections*, *Nucl. Phys. B* **437** (1995) 415 [`hep-ph/9411211`].

[15] Y. L. Dokshitzer and B. Webber, *Calculation of power corrections to hadronic event shapes*, *Phys. Lett. B* **352** (1995) 451 [`hep-ph/9504219`].

[16] T. Becher and M. D. Schwartz, *A precise determination of α_s from LEP thrust data using effective field theory*, *JHEP* **07** (2008) 034 [`0803.0342`].

[17] R. Abbate, M. Fickinger, A. H. Hoang, V. Mateu and I. W. Stewart, *Thrust at N3LL with Power Corrections and a Precision Global Fit for alphas(mZ)*, *Phys. Rev. D* **83** (2011) 074021 [`1006.3080`].

[18] R. Abbate, M. Fickinger, A. H. Hoang, V. Mateu and I. W. Stewart, *Precision Thrust Cumulant Moments at N^3LL*, *Phys. Rev. D* **86** (2012) 094002 [`1204.5746`].

[19] M. Procura and I. W. Stewart, *Quark Fragmentation within an Identified Jet*, *Phys. Rev. D* **81** (2010) 074009 [`0911.4980`].

[20] A. Jain, M. Procura and W. J. Waalewijn, *Parton Fragmentation within an Identified Jet at NNLL*, *JHEP* **05** (2011) 035 [`1101.4953`].

[21] A. Jain, M. Procura, B. Shotwell and W. J. Waalewijn, *Fragmentation with a Cut on Thrust: Predictions for B-factories*, *Phys. Rev. D* **87** (2013) 074013 [`1207.4788`].

[22] E. Farhi, *A QCD Test for Jets*, *Phys. Rev. Lett.* **39** (1977) 1587.

[23] G. F. Sterman, *An Introduction to quantum field theory*. Cambridge University Press, 8, 1993.

[24] BELLE collaboration, R. Seidl et al., *Measurement of Azimuthal Asymmetries in Inclusive Production of Hadron Pairs in e+e- Annihilation at s**(1/2) = 10.58-GeV*, Phys. Rev. **D78** (2008) 032011 [`0805.2975`].

[25] T. Sjöstrand, S. Ask, J. R. Christiansen, R. Corke, N. Desai, P. Ilten et al., *An Introduction to PYTHIA 8.2*, Comput. Phys. Commun. **191** (2015) 159 [`1410.3012`].

[26] M. Bahr et al., *Herwig++ Physics and Manual*, Eur. Phys. J. **C58** (2008) 639 [`0803.0883`].

[27] Z. Nagy and D. E. Soper, *Effects of subleading color in a parton shower*, JHEP **07** (2015) 119 [`1501.00778`].

[28] H. T. Li and P. Skands, *A framework for second-order parton showers*, Phys. Lett. B **771** (2017) 59 [`1611.00013`].

[29] S. Höche, F. Krauss and S. Prestel, *Implementing NLO DGLAP evolution in Parton Showers*, JHEP **10** (2017) 093 [`1705.00982`].

[30] J. R. Forshaw, J. Holguin and S. Plätzer, *Parton branching at amplitude level*, JHEP **08** (2019) 145 [`1905.08686`].

[31] M. Dasgupta, F. A. Dreyer, K. Hamilton, P. F. Monni, G. P. Salam and G. Soyez, *Parton showers beyond leading logarithmic accuracy*, `2002.11114`.

[32] J. Collins, *Foundations of perturbative QCD*, Camb. Monogr. Part. Phys. Nucl. Phys. Cosmol. **32** (2011) 1.

[33] G. F. Sterman, *Mass Divergences in Annihilation Processes. 1. Origin and Nature of Divergences in Cut Vacuum Polarization Diagrams*, Phys. Rev. **D17** (1978) 2773.

[34] J. C. Collins, D. E. Soper and G. F. Sterman, *Factorization for Short Distance Hadron - Hadron Scattering*, Nucl. Phys. B **261** (1985) 104.

[35] J. C. Collins, D. E. Soper and G. F. Sterman, *Soft Gluons and Factorization*, Nucl. Phys. B **308** (1988) 833.

[36] J. C. Collins, D. E. Soper and G. F. Sterman, *Factorization of Hard Processes in QCD*, vol. 5, pp. 1–91. 1989. `hep-ph/0409313`. 10.1142/9789814503266_0001.

[37] S. Coleman and R. Norton, *Singularities in the physical region*, *Nuovo Cim.* **38** (1965) 438.

[38] E. L. Laenen, J. Sinninghe-Damsté, L. Vernazza, W. J. Waalewijn and L. Zoppi, *Towards subleading power factorisation in QED*, in preparation .

[39] A. V. Manohar and I. W. Stewart, *The Zero-Bin and Mode Factorization in Quantum Field Theory*, *Phys. Rev. D* **76** (2007) 074002 [`hep-ph/0605001`].

[40] A. V. Manohar, *Introduction to Effective Field Theories*, in *Les Houches summer school: EFT in Particle Physics and Cosmology*, 4, 2018, `1804.05863`.

[41] B. Webber, *Estimation of power corrections to hadronic event shapes*, *Phys. Lett. B* **339** (1994) 148 [`hep-ph/9408222`].

[42] B. Gavela, E. Jenkins, A. Manohar and L. Merlo, *Analysis of General Power Counting Rules in Effective Field Theory*, *Eur. Phys. J. C* **76** (2016) 485 [`1601.07551`].

[43] H. Georgi, *On-shell effective field theory*, *Nucl. Phys. B* **361** (1991) 339.

[44] C. Arzt, *Reduced effective Lagrangians*, *Phys. Lett. B* **342** (1995) 189 [`hep-ph/9304230`].

[45] B. Grzadkowski, M. Iskrzynski, M. Misiak and J. Rosiek, *Dimension-Six Terms in the Standard Model Lagrangian*, *JHEP* **10** (2010) 085 [`1008.4884`].

[46] W. Buchmuller and D. Wyler, *Effective Lagrangian Analysis of New Interactions and Flavor Conservation*, *Nucl. Phys. B* **268** (1986) 621.

[47] L. Lehman and A. Martin, *Low-derivative operators of the Standard Model effective field theory via Hilbert series methods*, *JHEP* **02** (2016) 081 [`1510.00372`].

[48] B. Henning, X. Lu, T. Melia and H. Murayama, *Hilbert series and operator bases with derivatives in effective field theories*, *Commun. Math. Phys.* **347** (2016) 363 [`1507.07240`].

[49] C. B. Marinissen, R. Rahn and W. J. Waalewijn, *..., 83106786, 114382724, 1509048322, 2343463290, 27410087742, ... Efficient Hilbert Series for Effective Theories*, `2004.09521`.

[50] C. W. Bauer, S. Fleming and M. E. Luke, *Summing Sudakov logarithms in B —> X(s gamma) in effective field theory*, Phys. Rev. D **63** (2000) 014006 [`hep-ph/0005275`].

[51] C. W. Bauer, S. Fleming, D. Pirjol and I. W. Stewart, *An Effective field theory for collinear and soft gluons: Heavy to light decays*, Phys. Rev. D **63** (2001) 114020 [`hep-ph/0011336`].

[52] C. W. Bauer and I. W. Stewart, *Invariant operators in collinear effective theory*, Phys. Lett. B **516** (2001) 134 [`hep-ph/0107001`].

[53] C. W. Bauer, D. Pirjol and I. W. Stewart, *Soft collinear factorization in effective field theory*, Phys. Rev. D **65** (2002) 054022 [`hep-ph/0109045`].

[54] M. Beneke, A. Chapovsky, M. Diehl and T. Feldmann, *Soft collinear effective theory and heavy to light currents beyond leading power*, Nucl. Phys. B **643** (2002) 431 [`hep-ph/0206152`].

[55] M. Beneke and T. Feldmann, *Multipole expanded soft collinear effective theory with nonAbelian gauge symmetry*, Phys. Lett. B **553** (2003) 267 [`hep-ph/0211358`].

[56] R. J. Hill and M. Neubert, *Spectator interactions in soft collinear effective theory*, Nucl. Phys. B **657** (2003) 229 [`hep-ph/0211018`].

[57] T. Becher, A. Broggio and A. Ferroglia, *Introduction to Soft-Collinear Effective Theory*, vol. 896. Springer, 2015, 10.1007/978-3-319-14848-9, [`1410.1892`].

[58] M. Beneke and V. A. Smirnov, *Asymptotic expansion of Feynman integrals near threshold*, Nucl. Phys. B **522** (1998) 321 [`hep-ph/9711391`].

[59] V. A. Smirnov, *Applied asymptotic expansions in momenta and masses*, Springer Tracts Mod. Phys. **177** (2002) 1.

[60] B. Jantzen, *Foundation and generalization of the expansion by regions*, JHEP **12** (2011) 076 [`1111.2589`].

[61] A. Idilbi and A. Majumder, *Extending Soft-Collinear-Effective-Theory to describe hard jets in dense QCD media*, Phys. Rev. D **80** (2009) 054022 [`0808.1087`].

[62] I. Z. Rothstein and I. W. Stewart, *An Effective Field Theory for Forward Scattering and Factorization Violation*, JHEP **08** (2016) 025 [`1601.04695`].

[63] C. W. Bauer, F. J. Tackmann, J. R. Walsh and S. Zuberi, *Factorization and Resummation for Dijet Invariant Mass Spectra*, *Phys. Rev. D* **85** (2012) 074006 [1106.6047].

[64] D. Bonocore, E. Laenen, L. Magnea, S. Melville, L. Vernazza and C. White, *A factorization approach to next-to-leading-power threshold logarithms*, *JHEP* **06** (2015) 008 [1503.05156].

[65] D. Bonocore, E. Laenen, L. Magnea, L. Vernazza and C. White, *Non-abelian factorisation for next-to-leading-power threshold logarithms*, *JHEP* **12** (2016) 121 [1610.06842].

[66] I. Moult, I. W. Stewart, G. Vita and H. X. Zhu, *First Subleading Power Resummation for Event Shapes*, *JHEP* **08** (2018) 013 [1804.04665].

[67] M. Beneke, A. Broggio, M. Garny, S. Jaskiewicz, R. Szafron, L. Vernazza et al., *Leading-logarithmic threshold resummation of the Drell-Yan process at next-to-leading power*, *JHEP* **03** (2019) 043 [1809.10631].

[68] E. Eichten and F. Feinberg, *Spin Dependent Forces in QCD*, *Phys. Rev. D* **23** (1981) 2724.

[69] K. Rabbertz, *Jet Physics at the LHC: The Strong Force beyond the TeV Scale*, vol. 268 of *Springer Tracts in Modern Physics*. Springer, Berlin, 2017, 10.1007/978-3-319-42115-5.

[70] G. F. Sterman and S. Weinberg, *Jets from Quantum Chromodynamics*, *Phys. Rev. Lett.* **39** (1977) 1436.

[71] G. P. Salam and G. Soyez, *A Practical Seedless Infrared-Safe Cone jet algorithm*, *JHEP* **05** (2007) 086 [0704.0292].

[72] I. W. Stewart, F. J. Tackmann, J. Thaler, C. K. Vermilion and T. F. Wilkason, *XCone: N-jettiness as an Exclusive Cone Jet Algorithm*, *JHEP* **11** (2015) 072 [1508.01516].

[73] I. W. Stewart, F. J. Tackmann and W. J. Waalewijn, *N-Jettiness: An Inclusive Event Shape to Veto Jets*, *Phys. Rev. Lett.* **105** (2010) 092002 [1004.2489].

[74] JADE collaboration, S. Bethke et al., *Experimental Investigation of the Energy Dependence of the Strong Coupling Strength*, *Phys. Lett. B* **213** (1988) 235.

[75] S. Catani, Y. L. Dokshitzer, M. Seymour and B. Webber, *Longitudinally invariant K_t clustering algorithms for hadron hadron collisions*, *Nucl. Phys. B* **406** (1993) 187.

[76] Y. L. Dokshitzer, G. Leder, S. Moretti and B. Webber, *Better jet clustering algorithms*, *JHEP* **08** (1997) 001 [`hep-ph/9707323`].

[77] M. Wobisch and T. Wengler, *Hadronization corrections to jet cross-sections in deep inelastic scattering*, in *Workshop on Monte Carlo Generators for HERA Physics (Plenary Starting Meeting)*, pp. 270–279, 4, 1998, `hep-ph/9907280`.

[78] M. Cacciari, G. P. Salam and G. Soyez, *The anti-k_t jet clustering algorithm*, *JHEP* **04** (2008) 063 [`0802.1189`].

[79] M. Cacciari, G. P. Salam and G. Soyez, *FastJet User Manual*, *Eur. Phys. J. C* **72** (2012) 1896 [`1111.6097`].

[80] W. M.-Y. Cheung, M. Luke and S. Zuberi, *Phase Space and Jet Definitions in SCET*, *Phys. Rev. D* **80** (2009) 114021 [`0910.2479`].

[81] S. D. Ellis, C. K. Vermilion, J. R. Walsh, A. Hornig and C. Lee, *Jet Shapes and Jet Algorithms in SCET*, *JHEP* **11** (2010) 101 [`1001.0014`].

[82] M. Dasgupta and G. Salam, *Resummation of nonglobal QCD observables*, *Phys. Lett. B* **512** (2001) 323 [`hep-ph/0104277`].

[83] D. Neill, I. Scimemi and W. J. Waalewijn, *Jet axes and universal transverse-momentum-dependent fragmentation*, *JHEP* **04** (2017) 020 [`1612.04817`].

[84] D. Bertolini, T. Chan and J. Thaler, *Jet Observables Without Jet Algorithms*, *JHEP* **04** (2014) 013 [`1310.7584`].

[85] A. J. Larkoski, D. Neill and J. Thaler, *Jet Shapes with the Broadening Axis*, *JHEP* **04** (2014) 017 [`1401.2158`].

[86] J. Thaler and K. Van Tilburg, *Identifying Boosted Objects with N-subjettiness*, *JHEP* **03** (2011) 015 [`1011.2268`].

[87] P. E. Rakow and B. Webber, *Transverse Momentum Moments of Hadron Distributions in QCD Jets*, *Nucl. Phys. B* **191** (1981) 63.

[88] S. Catani, G. Turnock and B. Webber, *Jet broadening measures in e^+e^- annihilation*, *Phys. Lett. B* **295** (1992) 269.

[89] T. Becher and G. Bell, *NNLL Resummation for Jet Broadening*, JHEP **11** (2012) 126 [1210.0580].

[90] A. J. Larkoski, I. Moult and B. Nachman, *Jet Substructure at the Large Hadron Collider: A Review of Recent Advances in Theory and Machine Learning*, Phys. Rept. **841** (2020) 1 [1709.04464].

[91] D. Krohn, J. Thaler and L.-T. Wang, *Jet Trimming*, JHEP **02** (2010) 084 [0912.1342].

[92] S. D. Ellis, C. K. Vermilion and J. R. Walsh, *Techniques for improved heavy particle searches with jet substructure*, Phys. Rev. D **80** (2009) 051501 [0903.5081].

[93] J. M. Butterworth, A. R. Davison, M. Rubin and G. P. Salam, *Jet substructure as a new Higgs search channel at the LHC*, Phys. Rev. Lett. **100** (2008) 242001 [0802.2470].

[94] M. Dasgupta, A. Fregoso, S. Marzani and G. P. Salam, *Towards an understanding of jet substructure*, JHEP **09** (2013) 029 [1307.0007].

[95] A. J. Larkoski, S. Marzani, G. Soyez and J. Thaler, *Soft Drop*, JHEP **05** (2014) 146 [1402.2657].

[96] ATLAS collaboration, M. Aaboud et al., *Measurement of the Soft-Drop Jet Mass in pp Collisions at $\sqrt{s} = 13$ TeV with the ATLAS Detector*, Phys. Rev. Lett. **121** (2018) 092001 [1711.08341].

[97] CMS collaboration, A. M. Sirunyan et al., *Measurements of the differential jet cross section as a function of the jet mass in dijet events from proton-proton collisions at $\sqrt{s} = 13$ TeV*, JHEP **11** (2018) 113 [1807.05974].

[98] G. Soyez, *Pileup mitigation at the LHC: A theorist's view*, Ph.D. thesis, IPhT, Saclay, 2018. 1801.09721. 10.1016/j.physrep.2019.01.007.

[99] M. Diehl and J. R. Gaunt, *Double parton scattering theory overview*, vol. 29, pp. 7–28. 2019. 1710.04408. 10.1142/9789813227767_0002.

[100] H. Georgi and H. Politzer, *Quark Decay Functions and Heavy Hadron Production in QCD*, Nucl. Phys. B **136** (1978) 445.

[101] R. Ellis, H. Georgi, M. Machacek, H. Politzer and G. G. Ross, *Perturbation Theory and the Parton Model in QCD*, Nucl. Phys. B **152** (1979) 285.

[102] J. C. Collins and D. E. Soper, *Parton Distribution and Decay Functions*, *Nucl. Phys. B* **194** (1982) 445.

[103] M. G. Echevarria, I. Scimemi and A. Vladimirov, *Unpolarized Transverse Momentum Dependent Parton Distribution and Fragmentation Functions at next-to-next-to-leading order*, *JHEP* **09** (2016) 004 [1604.07869].

[104] H.-W. Lin et al., *Parton distributions and lattice QCD calculations: a community white paper*, *Prog. Part. Nucl. Phys.* **100** (2018) 107 [1711.07916].

[105] Y. L. Dokshitzer, *Calculation of the Structure Functions for Deep Inelastic Scattering and e+ e- Annihilation by Perturbation Theory in Quantum Chromodynamics.*, *Sov. Phys. JETP* **46** (1977) 641.

[106] V. Gribov and L. Lipatov, *Deep inelastic e p scattering in perturbation theory*, *Sov. J. Nucl. Phys.* **15** (1972) 438.

[107] G. Altarelli and G. Parisi, *Asymptotic Freedom in Parton Language*, *Nucl. Phys. B* **126** (1977) 298.

[108] S. Moch, J. Vermaseren and A. Vogt, *The Three loop splitting functions in QCD: The Nonsinglet case*, *Nucl. Phys. B* **688** (2004) 101 [hep-ph/0403192].

[109] A. Vogt, S. Moch and J. Vermaseren, *The Three-loop splitting functions in QCD: The Singlet case*, *Nucl. Phys. B* **691** (2004) 129 [hep-ph/0404111].

[110] S. Moch, B. Ruijl, T. Ueda, J. Vermaseren and A. Vogt, *Four-Loop Non-Singlet Splitting Functions in the Planar Limit and Beyond*, *JHEP* **10** (2017) 041 [1707.08315].

[111] J. J. Ethier and E. R. Nocera, *Parton Distributions in Nucleons and Nuclei*, *Ann. Rev. Nucl. Part. Sci.* (2020) 1 [2001.07722].

[112] L. Harland-Lang, A. Martin, P. Motylinski and R. Thorne, *Parton distributions in the LHC era: MMHT 2014 PDFs*, *Eur. Phys. J. C* **75** (2015) 204 [1412.3989].

[113] NNPDF collaboration, R. D. Ball et al., *Parton distributions from high-precision collider data*, *Eur. Phys. J. C* **77** (2017) 663 [1706.00428].

[114] S. Alekhin, J. Blümlein, S. Moch and R. Placakyte, *Parton distribution functions, α_s, and heavy-quark masses for LHC Run II, Phys. Rev. D* **96** (2017) 014011 [`1701.05838`].

[115] T.-J. Hou et al., *New CTEQ global analysis of quantum chromodynamics with high-precision data from the LHC*, `1912.10053`.

[116] JAM collaboration, N. Sato, C. Andres, J. Ethier and W. Melnitchouk, *Strange quark suppression from a simultaneous Monte Carlo analysis of parton distributions and fragmentation functions, Phys. Rev. D* **101** (2020) 074020 [`1905.03788`].

[117] S. Kretzer, *Fragmentation functions from flavor inclusive and flavor tagged e+ e- annihilations, Phys. Rev. D* **62** (2000) 054001 [`hep-ph/0003177`].

[118] B. A. Kniehl, G. Kramer and B. Potter, *Fragmentation functions for pions, kaons, and protons at next-to-leading order, Nucl. Phys. B* **582** (2000) 514 [`hep-ph/0010289`].

[119] S. Albino, B. Kniehl and G. Kramer, *Fragmentation functions for light charged hadrons with complete quark flavor separation, Nucl. Phys. B* **725** (2005) 181 [`hep-ph/0502188`].

[120] D. de Florian, R. Sassot and M. Stratmann, *Global analysis of fragmentation functions for pions and kaons and their uncertainties, Phys. Rev. D* **75** (2007) 114010 [`hep-ph/0703242`].

[121] D. de Florian, R. Sassot, M. Epele, R. J. Hernández-Pinto and M. Stratmann, *Parton-to-Pion Fragmentation Reloaded, Phys. Rev. D* **91** (2015) 014035 [`1410.6027`].

[122] D. de Florian, M. Epele, R. Hernandez-Pinto, R. Sassot and M. Stratmann, *Parton-to-Kaon Fragmentation Revisited, Phys. Rev. D* **95** (2017) 094019 [`1702.06353`].

[123] J. C. Collins and D. E. Soper, *Back-To-Back Jets in QCD, Nucl. Phys. B* **193** (1981) 381.

[124] J. C. Collins, D. E. Soper and G. F. Sterman, *Transverse Momentum Distribution in Drell-Yan Pair and W and Z Boson Production, Nucl. Phys. B* **250** (1985) 199.

[125] R. Meng, F. I. Olness and D. E. Soper, *Semiinclusive deeply inelastic scattering at small q(T), Phys. Rev. D* **54** (1996) 1919 [`hep-ph/9511311`].

[126] T. Becher and M. Neubert, *Drell-Yan Production at Small q_T, Transverse Parton Distributions and the Collinear Anomaly*, Eur. Phys. J. C **71** (2011) 1665 [1007.4005].

[127] S. Aybat and T. C. Rogers, *TMD Parton Distribution and Fragmentation Functions with QCD Evolution*, Phys. Rev. D **83** (2011) 114042 [1101.5057].

[128] M. G. Echevarria, A. Idilbi and I. Scimemi, *Factorization Theorem For Drell-Yan At Low q_ T And Transverse Momentum Distributions On-The-Light-Cone*, JHEP **07** (2012) 002 [1111.4996].

[129] J.-Y. Chiu, A. Jain, D. Neill and I. Z. Rothstein, *A Formalism for the Systematic Treatment of Rapidity Logarithms in Quantum Field Theory*, JHEP **05** (2012) 084 [1202.0814].

[130] M. G. Echevarria, A. Idilbi and I. Scimemi, *Unified treatment of the QCD evolution of all (un-)polarized transverse momentum dependent functions: Collins function as a study case*, Phys. Rev. D **90** (2014) 014003 [1402.0869].

[131] T. Gehrmann, E. Glover, T. Huber, N. Ikizlerli and C. Studerus, *Calculation of the quark and gluon form factors to three loops in QCD*, JHEP **06** (2010) 094 [1004.3653].

[132] M. G. Echevarria, I. Scimemi and A. Vladimirov, *Universal transverse momentum dependent soft function at NNLO*, Phys. Rev. D **93** (2016) 054004 [1511.05590].

[133] T. Lübbert, J. Oredsson and M. Stahlhofen, *Rapidity renormalized TMD soft and beam functions at two loops*, JHEP **03** (2016) 168 [1602.01829].

[134] Y. Li, D. Neill and H. X. Zhu, *An Exponential Regulator for Rapidity Divergences*, 1604.00392.

[135] T. Gehrmann, T. Lübbert and L. L. Yang, *Calculation of the transverse parton distribution functions at next-to-next-to-leading order*, JHEP **06** (2014) 155 [1403.6451].

[136] S. Catani, L. Cieri, D. de Florian, G. Ferrera and M. Grazzini, *Vector boson production at hadron colliders: hard-collinear coefficients at the NNLO*, Eur. Phys. J. C **72** (2012) 2195 [1209.0158].

[137] S. Catani, L. Cieri, D. de Florian, G. Ferrera and M. Grazzini, *Universality of transverse-momentum resummation and hard factors at the NNLO*, Nucl. Phys. B **881** (2014) 414 [`1311.1654`].

[138] T. Gehrmann, T. Lübbert and L. L. Yang, *Transverse parton distribution functions at next-to-next-to-leading order: the quark-to-quark case*, Phys. Rev. Lett. **109** (2012) 242003 [`1209.0682`].

[139] M.-X. Luo, X. Wang, X. Xu, L. L. Yang, T.-Z. Yang and H. X. Zhu, *Transverse Parton Distribution and Fragmentation Functions at NNLO: the Quark Case*, JHEP **10** (2019) 083 [`1908.03831`].

[140] M.-X. Luo, T.-Z. Yang, H. X. Zhu and Y. J. Zhu, *Transverse Parton Distribution and Fragmentation Functions at NNLO: the Gluon Case*, JHEP **01** (2020) 040 [`1909.13820`].

[141] D. Boer and P. Mulders, *Time reversal odd distribution functions in leptoproduction*, Phys. Rev. D **57** (1998) 5780 [`hep-ph/9711485`].

[142] D. W. Sivers, *Single Spin Production Asymmetries from the Hard Scattering of Point-Like Constituents*, Phys. Rev. D **41** (1990) 83.

[143] M. Boglione and A. Prokudin, *Phenomenology of transverse spin: past, present and future*, Eur. Phys. J. A **52** (2016) 154 [`1511.06924`].

[144] A. Bacchetta, *Where do we stand with a 3-D picture of the proton?*, Eur. Phys. J. A **52** (2016) 163.

[145] M. Diehl, *Introduction to GPDs and TMDs*, Eur. Phys. J. A **52** (2016) 149 [`1512.01328`].

[146] M. G. Echevarria, A. Idilbi, A. Schäfer and I. Scimemi, *Model-Independent Evolution of Transverse Momentum Dependent Distribution Functions (TMDs) at NNLL*, Eur. Phys. J. C **73** (2013) 2636 [`1208.1281`].

[147] I. Scimemi and A. Vladimirov, *Analysis of vector boson production within TMD factorization*, Eur. Phys. J. C **78** (2018) 89 [`1706.01473`].

[148] I. Scimemi and A. Vladimirov, *Systematic analysis of double-scale evolution*, JHEP **08** (2018) 003 [`1803.11089`].

[149] S. Moch, J. Vermaseren and A. Vogt, *Three-loop results for quark and gluon form-factors*, Phys. Lett. B **625** (2005) 245 [`hep-ph/0508055`].

[150] P. Baikov, K. Chetyrkin, A. Smirnov, V. Smirnov and M. Steinhauser, *Quark and gluon form factors to three loops*, *Phys. Rev. Lett.* **102** (2009) 212002 [0902.3519].

[151] A. A. Vladimirov, *Correspondence between Soft and Rapidity Anomalous Dimensions*, *Phys. Rev. Lett.* **118** (2017) 062001 [1610.05791].

[152] Y. Li and H. X. Zhu, *Bootstrapping Rapidity Anomalous Dimensions for Transverse-Momentum Resummation*, *Phys. Rev. Lett.* **118** (2017) 022004 [1604.01404].

[153] S. Moch, B. Ruijl, T. Ueda, J. M. Vermaseren and A. Vogt, *On quartic colour factors in splitting functions and the gluon cusp anomalous dimension*, *Phys. Lett. B* **782** (2018) 627 [1805.09638].

[154] X. Liu, *SCET approach to top quark decay*, *Phys. Lett. B* **699** (2011) 87 [1011.3872].

[155] C. W. Bauer and E. Mereghetti, *Heavy Quark Fragmenting Jet Functions*, *JHEP* **04** (2014) 051 [1312.5605].

[156] M. Ritzmann and W. J. Waalewijn, *Fragmentation in Jets at NNLO*, *Phys. Rev. D* **90** (2014) 054029 [1407.3272].

[157] M. Procura and W. J. Waalewijn, *Fragmentation in Jets: Cone and Threshold Effects*, *Phys. Rev. D* **85** (2012) 114041 [1111.6605].

[158] M. Baumgart, A. K. Leibovich, T. Mehen and I. Z. Rothstein, *Probing Quarkonium Production Mechanisms with Jet Substructure*, *JHEP* **11** (2014) 003 [1406.2295].

[159] Y.-T. Chien, Z.-B. Kang, F. Ringer, I. Vitev and H. Xing, *Jet fragmentation functions in proton-proton collisions using soft-collinear effective theory*, *JHEP* **05** (2016) 125 [1512.06851].

[160] R. Bain, L. Dai, A. Hornig, A. K. Leibovich, Y. Makris and T. Mehen, *Analytic and Monte Carlo Studies of Jets with Heavy Mesons and Quarkonia*, *JHEP* **06** (2016) 121 [1603.06981].

[161] F. Arleo, M. Fontannaz, J.-P. Guillet and C. L. Nguyen, *Probing fragmentation functions from same-side hadron-jet momentum correlations in p-p collisions*, *JHEP* **04** (2014) 147 [1311.7356].

[162] T. Kaufmann, A. Mukherjee and W. Vogelsang, *Hadron Fragmentation Inside Jets in Hadronic Collisions*, *Phys. Rev. D* **92** (2015) 054015 [1506.01415].

[163] L. Dai, C. Kim and A. K. Leibovich, *Fragmentation of a Jet with Small Radius*, *Phys. Rev. D* **94** (2016) 114023 [1606.07411].

[164] Z.-B. Kang, F. Ringer and I. Vitev, *Jet substructure using semi-inclusive jet functions in SCET*, *JHEP* **11** (2016) 155 [1606.07063].

[165] D. Krohn, M. D. Schwartz, T. Lin and W. J. Waalewijn, *Jet Charge at the LHC*, *Phys. Rev. Lett.* **110** (2013) 212001 [1209.2421].

[166] W. J. Waalewijn, *Calculating the Charge of a Jet*, *Phys. Rev. D* **86** (2012) 094030 [1209.3019].

[167] H.-M. Chang, M. Procura, J. Thaler and W. J. Waalewijn, *Calculating Track-Based Observables for the LHC*, *Phys. Rev. Lett.* **111** (2013) 102002 [1303.6637].

[168] H.-M. Chang, M. Procura, J. Thaler and W. J. Waalewijn, *Calculating Track Thrust with Track Functions*, *Phys. Rev. D* **88** (2013) 034030 [1306.6630].

[169] B. T. Elder, M. Procura, J. Thaler, W. J. Waalewijn and K. Zhou, *Generalized Fragmentation Functions for Fractal Jet Observables*, *JHEP* **06** (2017) 085 [1704.05456].

[170] A. Accardi and A. Signori, *Quark fragmentation as a probe of dynamical mass generation*, *Phys. Lett. B* **798** (2019) 134993 [1903.04458].

[171] T. Kaufmann, X. Liu, A. Mukherjee, F. Ringer and W. Vogelsang, *Hadron-in-jet production at partonic threshold*, *JHEP* **02** (2020) 040 [1910.11746].

[172] R. Bain, Y. Makris and T. Mehen, *Transverse Momentum Dependent Fragmenting Jet Functions with Applications to Quarkonium Production*, *JHEP* **11** (2016) 144 [1610.06508].

[173] Z.-B. Kang, X. Liu, F. Ringer and H. Xing, *The transverse momentum distribution of hadrons within jets*, *JHEP* **11** (2017) 068 [1705.08443].

[174] Z.-B. Kang, A. Prokudin, F. Ringer and F. Yuan, *Collins azimuthal asymmetries of hadron production inside jets*, *Phys. Lett. B* **774** (2017) 635 [1707.00913].

[175] Z.-B. Kang, K. Lee and F. Zhao, *Polarized jet fragmentation functions*, 2005.02398.

[176] Y. Makris, D. Neill and V. Vaidya, *Probing Transverse-Momentum Dependent Evolution With Groomed Jets*, *JHEP* **07** (2018) 167 [1712.07653].

[177] Y. Makris and V. Vaidya, *Transverse Momentum Spectra at Threshold for Groomed Heavy Quark Jets*, *JHEP* **10** (2018) 019 [1807.09805].

[178] J. Bellm et al., *Herwig 7.1 Release Note*, 1705.06919.

[179] S. D. Ellis, Z. Kunszt and D. E. Soper, *Jets at hadron colliders at order $\alpha - s^3$: A Look inside*, *Phys. Rev. Lett.* **69** (1992) 3615 [hep-ph/9208249].

[180] M. Seymour, *Jet shapes in hadron collisions: Higher orders, resummation and hadronization*, *Nucl. Phys. B* **513** (1998) 269 [hep-ph/9707338].

[181] H.-n. Li, Z. Li and C.-P. Yuan, *QCD resummation for jet substructures*, *Phys. Rev. Lett.* **107** (2011) 152001 [1107.4535].

[182] Y.-T. Chien and I. Vitev, *Jet Shape Resummation Using Soft-Collinear Effective Theory*, *JHEP* **12** (2014) 061 [1405.4293].

[183] Z.-B. Kang, F. Ringer and W. J. Waalewijn, *The Energy Distribution of Subjets and the Jet Shape*, *JHEP* **07** (2017) 064 [1705.05375].

[184] G. Altarelli, R. Ellis, G. Martinelli and S.-Y. Pi, *Processes Involving Fragmentation Functions Beyond the Leading Order in QCD*, *Nucl. Phys. B* **160** (1979) 301.

[185] W. Furmanski and R. Petronzio, *Lepton - Hadron Processes Beyond Leading Order in Quantum Chromodynamics*, *Z. Phys. C* **11** (1982) 293.

[186] P. Nason and B. Webber, *Scaling violation in e+ e- fragmentation functions: QCD evolution, hadronization and heavy quark mass effects*, *Nucl. Phys. B* **421** (1994) 473.

[187] E. L. Berger, X.-F. Guo and J.-W. Qiu, *Inclusive prompt photon production in hadronic final states of e^+e^- annihilation*, *Phys. Rev. D* **53** (1996) 1124 [hep-ph/9507428].

[188] Z.-B. Kang, F. Ringer and I. Vitev, *The semi-inclusive jet function in SCET and small radius resummation for inclusive jet production*, JHEP **10** (2016) 125 [`1606.06732`].

[189] D. Kotlorz and A. Kotlorz, *Evolution equations for truncated moments of the parton distributions*, Phys. Lett. B **644** (2007) 284 [`hep-ph/0610282`].

[190] Z. Ligeti, I. W. Stewart and F. J. Tackmann, *Treating the b quark distribution function with reliable uncertainties*, Phys. Rev. D **78** (2008) 114014 [`0807.1926`].

[191] A. Buckley, J. Butterworth, L. Lonnblad, D. Grellscheid, H. Hoeth, J. Monk et al., *Rivet user manual*, Comput. Phys. Commun. **184** (2013) 2803 [`1003.0694`].

[192] M. Anselmino et al., *Transverse Momentum Dependent Parton Distribution/Fragmentation Functions at an Electron-Ion Collider*, Eur. Phys. J. A **47** (2011) 35 [`1101.4199`].

[193] R. D. Ball and A. Deshpande, *The proton spin, semi-inclusive processes, and measurements at a future Electron Ion Collider*, pp. 205–226. 2019. `1801.04842`. 10.1142/9789813238053_0011.

[194] E. C. Aschenauer, I. Borsa, R. Sassot and C. Van Hulse, *Semi-inclusive Deep-Inelastic Scattering, Parton Distributions and Fragmentation Functions at a Future Electron-Ion Collider*, Phys. Rev. D **99** (2019) 094004 [`1902.10663`].

[195] A. Banfi, M. Dasgupta and Y. Delenda, *Azimuthal decorrelations between QCD jets at all orders*, Phys. Lett. B **665** (2008) 86 [`0804.3786`].

[196] P. Sun, C. P. Yuan and F. Yuan, *Soft Gluon Resummations in Dijet Azimuthal Angular Correlations in Hadronic Collisions*, Phys. Rev. Lett. **113** (2014) 232001 [`1405.1105`].

[197] P. Sun, C. P. Yuan and F. Yuan, *Transverse Momentum Resummation for Dijet Correlation in Hadronic Collisions*, Phys. Rev. D **92** (2015) 094007 [`1506.06170`].

[198] L. Chen, G.-Y. Qin, S.-Y. Wei, B.-W. Xiao and H.-Z. Zhang, *Dijet Asymmetry in the Resummation Improved Perturbative QCD Approach*, Phys. Lett. B **782** (2018) 773 [`1612.04202`].

[199] ZEUS collaboration, S. Chekanov et al., *Jet-radius dependence of inclusive-jet cross-sections in deep inelastic scattering at HERA*, *Phys. Lett. B* **649** (2007) 12 [`hep-ex/0701039`].

[200] H1 collaboration, C. Adloff et al., *Measurement and QCD analysis of jet cross-sections in deep inelastic positron - proton collisions at s**(1/2) of 300-GeV*, *Eur. Phys. J. C* **19** (2001) 289 [`hep-ex/0010054`].

[201] H1 collaboration, A. Aktas et al., *Measurement of inclusive jet production in deep-inelastic scattering at high Q**2 and determination of the strong coupling*, *Phys. Lett. B* **653** (2007) 134 [`0706.3722`].

[202] H1 collaboration, F. Aaron et al., *Jet Production in ep Collisions at Low Q**2 and Determination of alpha(s)*, *Eur. Phys. J. C* **67** (2010) 1 [`0911.5678`].

[203] T. Becher, M. Neubert, L. Rothen and D. Y. Shao, *Effective Field Theory for Jet Processes*, *Phys. Rev. Lett.* **116** (2016) 192001 [`1508.06645`].

[204] T. Becher, M. Neubert, L. Rothen and D. Y. Shao, *Factorization and Resummation for Jet Processes*, *JHEP* **11** (2016) 019 [`1605.02737`].

[205] A. J. Larkoski, I. Moult and D. Neill, *Non-Global Logarithms, Factorization, and the Soft Substructure of Jets*, *JHEP* **09** (2015) 143 [`1501.04596`].

[206] S. Caron-Huot, *Resummation of non-global logarithms and the BFKL equation*, *JHEP* **03** (2018) 036 [`1501.03754`].

[207] M. G. Echevarria, I. Scimemi and A. Vladimirov, *Transverse momentum dependent fragmentation function at next–next-to–leading order*, *Phys. Rev. D* **93** (2016) 011502 [`1509.06392`].

[208] M. G. Echevarría, A. Idilbi and I. Scimemi, *Soft and Collinear Factorization and Transverse Momentum Dependent Parton Distribution Functions*, *Phys. Lett. B* **726** (2013) 795 [`1211.1947`].

[209] S. Catani and M. Seymour, *A General algorithm for calculating jet cross-sections in NLO QCD*, *Nucl. Phys. B* **485** (1997) 291 [`hep-ph/9605323`].

[210] V. Bertone, I. Scimemi and A. Vladimirov, *Extraction of unpolarized quark transverse momentum dependent parton distributions from Drell-Yan/Z-boson production*, *JHEP* **06** (2019) 028 [`1902.08474`].

[211] I. Moult and H. X. Zhu, *Simplicity from Recoil: The Three-Loop Soft Function and Factorization for the Energy-Energy Correlation*, JHEP **08** (2018) 160 [1801.02627].

[212] H. T. Li, I. Vitev and Y. J. Zhu, *Transverse-Energy-Energy Correlations in Deep Inelastic Scattering*, 2006.02437.

[213] M. Arratia, Y. Song, F. Ringer and B. Jacak, *Jets as Precision Probes in Electron-Nucleus Collisions at the Electron-Ion Collider*, 1912.05931.

[214] B. Page, X. Chu and E. Aschenauer, *Experimental Aspects of Jet Physics at a Future EIC*, Phys. Rev. D **101** (2020) 072003 [1911.00657].

[215] U. D'Alesio, F. Murgia, C. Pisano and P. Taels, *Azimuthal asymmetries in semi-inclusive J/ψ + jet production at an EIC*, Phys. Rev. D **100** (2019) 094016 [1908.00446].

[216] E.-C. Aschenauer, K. Lee, B. Page and F. Ringer, *Jet angularities in photoproduction at the Electron-Ion Collider*, Phys. Rev. D **101** (2020) 054028 [1910.11460].

[217] Y.-T. Chien, R. Rahn, S. S. van Velzen, D. Y. Shao, W. J. Waalewijn and B. Wu, *Azimuthal angle for boson-jet production in the back-to-back limit*, 2005.12279.

[218] C. Frye, A. J. Larkoski, M. D. Schwartz and K. Yan, *Precision physics with pile-up insensitive observables*, 1603.06375.

[219] C. Frye, A. J. Larkoski, M. D. Schwartz and K. Yan, *Factorization for groomed jet substructure beyond the next-to-leading logarithm*, JHEP **07** (2016) 064 [1603.09338].

[220] A. J. Larkoski, I. Moult and D. Neill, *Analytic Boosted Boson Discrimination at the Large Hadron Collider*, 1708.06760.

[221] Z.-B. Kang, K. Lee, X. Liu and F. Ringer, *The groomed and ungroomed jet mass distribution for inclusive jet production at the LHC*, JHEP **10** (2018) 137 [1803.03645].

[222] Z.-B. Kang, K. Lee, X. Liu and F. Ringer, *Soft drop groomed jet angularities at the LHC*, Phys. Lett. B **793** (2019) 41 [1811.06983].

[223] J. Baron, S. Marzani and V. Theeuwes, *Soft-Drop Thrust*, *JHEP* **08** (2018) 105 [1803.04719].

[224] A. Kardos, G. Somogyi and Z. Trócsányi, *Soft-drop event shapes in electron–positron annihilation at next-to-next-to-leading order accuracy*, *Phys. Lett. B* **786** (2018) 313 [1807.11472].

[225] A. H. Hoang, S. Mantry, A. Pathak and I. W. Stewart, *Extracting a Short Distance Top Mass with Light Grooming*, *Phys. Rev. D* **100** (2019) 074021 [1708.02586].

[226] C. Lee, P. Shrivastava and V. Vaidya, *Predictions for energy correlators probing substructure of groomed heavy quark jets*, *JHEP* **09** (2019) 045 [1901.09095].

[227] A. J. Larkoski, I. Moult and D. Neill, *Factorization and Resummation for Groomed Multi-Prong Jet Shapes*, *JHEP* **02** (2018) 144 [1710.00014].

[228] Y. L. Dokshitzer, A. Lucenti, G. Marchesini and G. Salam, *Universality of 1/Q corrections to jet-shape observables rescued*, *Nucl. Phys. B* **511** (1998) 396 [hep-ph/9707532].

[229] G. Salam and D. Wicke, *Hadron masses and power corrections to event shapes*, *JHEP* **05** (2001) 061 [hep-ph/0102343].

[230] C. Lee and G. F. Sterman, *Momentum Flow Correlations from Event Shapes: Factorized Soft Gluons and Soft-Collinear Effective Theory*, *Phys. Rev. D* **75** (2007) 014022 [hep-ph/0611061].

[231] M. Dasgupta, L. Magnea and G. P. Salam, *Non-perturbative QCD effects in jets at hadron colliders*, *JHEP* **02** (2008) 055 [0712.3014].

[232] M. Beneke and V. M. Braun, *Power corrections and renormalons in Drell-Yan production*, *Nucl. Phys. B* **454** (1995) 253 [hep-ph/9506452].

[233] M. Beneke, V. M. Braun and L. Magnea, *Phenomenology of power corrections in fragmentation processes in e+ e- annihilation*, *Nucl. Phys. B* **497** (1997) 297 [hep-ph/9701309].

[234] T. Becher and G. Bell, *Enhanced nonperturbative effects through the collinear anomaly*, *Phys. Rev. Lett.* **112** (2014) 182002 [1312.5327].

[235] I. Scimemi and A. Vladimirov, *Power corrections and renormalons in Transverse Momentum Distributions*, *JHEP* **03** (2017) 002 [1609.06047].

[236] A. H. Hoang, S. Mantry, A. Pathak and I. W. Stewart, *Nonperturbative Corrections to Soft Drop Jet Mass*, *JHEP* **12** (2019) 002 [1906.11843].

[237] A. J. Larkoski and J. Thaler, *Aspects of jets at 100 TeV*, *Phys. Rev. D* **90** (2014) 034010 [1406.7011].

[238] P. Cal, D. Neill, F. Ringer and W. J. Waalewijn, *Calculating the angle between jet axes*, *JHEP* **04** (2020) 211 [1911.06840].

[239] M. Procura, W. J. Waalewijn and L. Zeune, *Joint resummation of two angularities at next-to-next-to-leading logarithmic order*, *JHEP* **10** (2018) 098 [1806.10622].

[240] G. Kramer and B. Lampe, *Two Jet Cross-Section in e+ e- Annihilation*, *Z. Phys. C* **34** (1987) 497.

[241] T. Matsuura, S. van der Marck and W. van Neerven, *The Calculation of the Second Order Soft and Virtual Contributions to the Drell-Yan Cross-Section*, *Nucl. Phys. B* **319** (1989) 570.